STUDIES ON HYDROGENATION BEHAVIOR OF ZIRCONIUM AND URANIUM BASED ALLOYS

By

DEBABRATA CHATTARAJ

Enrolment Number: CHEM01201104022

BHABHA ATOMIC RESEARCH CENTRE, MUMBAI

A thesis submitted to the

Board of Studies in Chemical Sciences

In partial fulfillment of requirements

for the Degree of

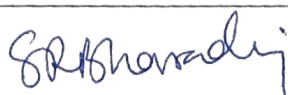## DOCTOR OF PHILOSOPHY
of
HOMI BHABHA NATIONAL INSTITUTE

August, 2016

Homi Bhabha National Institute

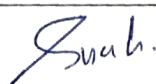## Recommendations of the Viva Voce Committee

As members of the Viva Voce Committee, we certify that we have read the dissertation prepared by Shri Debabrata Chattaraj entitled "Studies on hydrogenation behaviour of zirconium and uranium based alloys" and recommend that it may be accepted as fulfilling the thesis requirement for the award of Degree of Doctor of Philosophy.
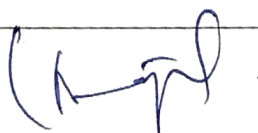
Chairman - Prof. Shyamala Bharadwaj	*SRBharadwj*	Date: 14-12-16
Guide / Convener - Dr. Smruti Dash	*Snah.*	Date: 14/12/16
Co-guide - Dr. Chiranjib Majumder	*signature*	Date: 14/12/16
Examiner - Dr. P.K. Chattaraj	*signature*	Date: 14.12-16.
Member 1- Dr. K.R.S. Chandrakumar	*Schandrm*	Date: 27-01-2017 ‡
Member 2- Dr. S.C. Parida	*signature*	Date: 27/01/2017 ⊛
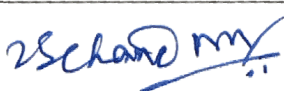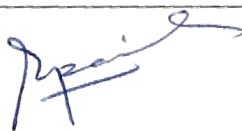
Final approval and acceptance of this thesis is contingent upon the candidate's submission of the final copies of the thesis to HBNI.

I/We hereby certify that I/we have read this thesis prepared under my/our direction and recommend that it may be accepted as fulfilling the thesis requirement.

Date:

Place:

Signature — Co-guide *signature 14.12.16*

Signature — Guide *Snah.*

⊛ I am fully satisfied with the content of the thesis and the presentation made by the student.

‡ I found the thesis work as well as the presentation made by Shri. D. Chattaraj suitable for the award of Ph.D. degree.

STATEMENT BY AUTHOR

This dissertation has been submitted in partial fulfillment of requirements for an advanced degree at Homi Bhabha National Institute (HBNI) and is deposited in the Library to be made available to borrowers under rules of the HBNI.

Brief quotations from this dissertation are allowable without special permission, provided that accurate acknowledgement of source is made. Requests for permission for extended quotation from or reproduction of this manuscript in whole or in part may be granted by the Competent Authority of HBNI when in his or her judgment the proposed use of the material is in the interests of scholarship. In all other instances, however, permission must be obtained from the author.

(Debabrata Chattaraj)

DECLARATION

I, hereby declare that the investigation presented in the thesis has been carried out by me. The work is original and has not been submitted earlier as a whole or in part for a degree / diploma at this or any other Institution / University.

(Debabrata Chattaraj)

List of Publications arising from the thesis

Journals

1. Structural and electronic properties of U_2Ti: A first principle study,

   D. Chattaraj, S.C. Parida, C. Majumder[*],

   Physica B: Condensed Matter, **2011**, 406, 4317-4321.

2. Structural, electronic and thermodynamic properties of ZrCo and $ZrCoH_3$: A first-principles study,

   D. Chattaraj, S.C. Parida, Smruti Dash, C. Majumder[*],

   International Journal of Hydrogen Energy, **2012**, 37(24), 18952-18959.

3. High temperature enthalpy increments and thermodynamic functions of U_2Ti,

   D. Chattaraj, Ram Avtar Jat, S.C. Parida, Renu Agarwal, Smruti Dash[*],

   Journal of Thermal Analysis and Calorimetry, **2013**, 112, 141-145.

4. First principles study of ZrX_2 (X=H, D, T) compounds,

   D. Chattaraj[*], S.C. Parida, Smruti Dash, C. Majumder,

   International Journal of Hydrogen Energy, **2014**, 39, 9681-9689.

5. Density functional study of vibrational, thermodynamic and elastic properties of ZrCo and $ZrCoX_3$ (X = H, D and T) compounds,

   D. Chattaraj[*], S.C. Parida, S. Dash, C. Majumder,

   Journal of Alloys and Compounds, **2015**, 629, 297-304.

6. High Temperature Enthalpy Increment and Thermodynamic Functions of ZrCo: An Experimental and Theoretical Study,

   D. Chattaraj[*], Ram Avtar Jat, S.C. Parida, Renu Agarwal, Smruti Dash,

   International Journal of Thermochimica Acta, **2015**, 614, 16-20.

7. Atomic, Electronic and Magnetic Properties of Bimetallic ZrCo clusters: A First-principles Study,

   D. Chattaraj, Saswata Bhattacharya, Smruti Dash, C. Majumder

   Journal of Applied Physics, **2016**, 120, 094301 (p. 1-6)

8. Adsorption, dissociation and diffusion of hydrogen on the ZrCo surface and subsurface: A comprehensive study using first principles approach

   D. Chattaraj[*], Nandha Kumar, Prasenjit Ghosh, C. Majumder, Smruti Dash

   (Submitted to Physical Review B, Manuscript reference number: BY12596)

Symposiums/Conferences

1) Structural and electronic properties of U_2Ti: A Density-functional study,

    Debabrata Chattaraj, Suresh Chandra Parida and Chiranjib Majumder[*],

    Proceedings of the 10th DAE-BRNS Nuclear and Radiochemistry Symposium (NUCAR - 2011), Visakhapatnam, India, February 22-26, 2011, p 188-189.

2) High temperature enthalpy increments and thermodynamic functions of U_2Ti alloy,

    D.Chattaraj, Ram Avtar Jat, S.C. Parida, R.Agarwal and Smruti Dash[*],

    Proceedings of the 18th International Symposium on Thermal Analysis (THERMANS-2012), Mumbai, India, January 31 - February 2, 2012, p. 97-99.

3) Investigation of mechanical properties and Debye temperature of U_2Ti,

    D. Chattaraj, Smruti Dash[*], S.G. Kulkarni,

    Proceedings of the DAE-BRNS 4th Interdisciplinary Symposium on Materials Chemistry (ISMC-2012), Mumbai, India, December 11-15, 2012, p. 85.

4) First Principles and Phonon Calculations of ZrCo and $ZrCo-H_2$ Systems,

    D. Chattaraj[*], C. Majumder, S.C Parida, Smruti Dash,

    Proceedings of the DAE-BRNS 4th Interdisciplinary Symposium on Materials Chemistry (ISMC 2012), Mumbai, India, December 11-15, 2012, p. 573.

5) Investigation of Thermal Properties of ZrCo: An Experimental and Theoretical Study,

    D. Chattaraj[*], Ram Avtar Jat, S.C. Parida, Renu Agarwal, Smruti Dash,

    Proceedings of DAE-BRNS 19th symposium and workshop on Thermal Analysis (THERMANS-2013), Mumbai, India, December 19-23, 2013, p-98.

6) On the Isotope Effects of $ZrCoX_3$ (X = H, D and T): A First-principles Study,

    D. Chattaraj[*], S.C. Parida, C. Majumder, Smruti Das,

    Proceedings of DAE-BRNS 19th symposium and workshop on Thermal Analysis (THERMANS-2013), Mumbai, India, December 19-23, 2013, p-58.

7) First Principles Study of Elastic Properties of ZrCo and its Hydride $ZrCoH_3$,

    D. Chattaraj[*], S.C. Parida, Smruti Das, C. Majumder,

    Proceedings of DAE-BRNS symposium on Multiscale Modeling of Materials and Devices (MMMD-2014), Mumbai, India, 30th October – 2nd November, 2014, p-99-

100.

8) Hydrogen Interactions with ZrCo Nanoclusters: A First-principles Study,

D. Chattaraj, Saswata Bhattacharya, S.C. Parida, Smruti Dash and C. Majumder[*],

Proceedings of DAE-BRNS 5th Interdisciplinary Symposium on Material Chemistry

(ISMC-2014), Mumbai, India, December 9th-13th, 2014, p-480.

9) Studies on Hydrogenation Behavior of Zirconium-Cobalt Alloy,

D. Chattaraj[*], Smruti Das, C. Majumder,

Proceedings of 27th Research Scholars' Meet (RSM-2015), Sathaye College, Vile

Parle (E), Mumbai, 20th-21st February, 2015, p. 21.

BARC Newsletter

1) On the Isotope Effects of $ZrCoX_3$ (X= H, D and T): A First-Principles Study,

D. Chattaraj[*], S.C. Parida, Smruti Dash, C. Majumder,

BARC Newsletter: Founder's Day Special Issue, 2014, P- 168-170.

(Debabrata Chattaraj)

DEDICATED TO

MY FAMILY

ACKNOWLEDGEMENTS

Modak for their moral support, diversified help, and several funs which will always be remembered.

*My sincere thanks are due to all others colleagues from **PDD** for their help, suggestion and encouragement.*

*It gives me immense pleasure to thank the members of the doctoral committee **Prof. Shymala R. Bhardwaj** (Chairman) and **Dr. S.C. Parida** (Member) and **Dr. K.R.S. Chandrakumar** (Member) for their critical review and suggestions during the progress review and presynopsis viva-voce.*

*I would like to thank **my Grandfather, Late Shri Bholanath Chattaraj** for his blessings.*

*Finally, I owe my heartfelt gratitude and indebtness to **my Parents, my In laws** and **Elder Brother, Sisters**, all my **family members** and **relatives** who have always encouraged me to follow my heart and inspired my inquisitive mind throughout my childhood and career.*

*I am forever grateful to my lovely wife, **Shreya** for being supportive, enduring and forgiving during the last six years for helping me to remember that there are more important things to do in life than the work.*

*Lastly, I am thankful to all the **unknown reviewers** of my published scientific articles/papers whose comments always upgraded my scientific thought and opened a new way of thinking.*

August, 2016   (Debabrata Chattaraj)

CONTENTS

<u>CHAPTER - 1: Introduction</u>

CHAPTER – 2: Theoretical Approach

CHAPTER - 3: Experimental Methods

CHAPTER - 4: Theoretical and Experimental Study of U$_2$Ti Alloy

CHAPTER - 5: Theoretical and Experimental Study of Zr-based Compounds

SYNOPSIS

One of the most important requirements for fusion reactor is tritium isotope (T or ^{3}H) which is going to be used along with deuterium (D or ^{2}H). Tritium is produced through nuclear reactions in a lithium-bearing blanket. Thereafter, it is extracted, purified, and stored. But, this radioactive isotope is a beta emitter. Hence, for the safe storage of this radioactive isotope, a suitable material is required to prevent the release of tritium into the environment. The solid state storage of hydrogen isotopes is quite reliable, safe and advantageous compared to gaseous or liquid form of storage. Metal hydrides are unique choice as solid state storage material for tritium. Development and delivery of such systems for tritium are of urgent requirement in the International Thermonuclear Experimental Reactor (ITER) program. Conventionally, uranium is used as "getter bed" for tritium as it has high absorption capacity at room temperature, low equilibrium pressure (<1 bar at 550–680 K) which prevents the accidental release of tritium into atmosphere, fast kinetics of hydrogen absorption–desorption and large thermal cyclic life. However, uranium hydride is pyrophoric in nature and also uranium is a nuclear material. So investigation for finding out an alternate material for tritium storage is in progress. The property of uranium can be improved by alloying it with titanium which can impart durability against powdering on hydrogenation and can reduce the pyrophoricity to a certain extent. Zirconium is also good for hydrogen isotope storage, but the main drawback is that the dissociation of hydrogen from zirconium hydride (ZrH_2) requires moderately high temperature. Presently, the intermetallic ZrCo has been found to be suitable for the safe storage of tritium. ZrCo intermetallic has good hydriding/dehydriding property which can serve as a substitution of uranium. Also it is not pyrophoric and easy to handle as it is not a

nuclear material. However, the major drawback of ZrCo is that its absorption–desorption cycle become poor on prolonged thermal cycling which is due to the disproportionation of its hydride (ZrCoH$_x$ (x $\leq$ 3) into the stable hydride phase ZrH$_2$ and the hydrogen non-absorbing phase ZrCo$_2$.

To overcome the drawbacks of this system a fundamental study of physico-chemical properties of ZrCo and its hydrides are required. Regarding hydrogen isotope storage, the isotope effect of ZrCoX$_3$ (X = H, D and T) compounds are also of prime importance and required to be explored. In literature, researchers have reported the physico-chemical properties of tritium storage alloys and their hydrides both experimentally and theoretically to a certain extent. The properties of radioactive tritides are still lacking in the literature. A comprehensive study of fundamental physico-chemical properties like structural, electronic, elastic, vibrational and thermodynamic properties of those alloys and their hydrides is the main scope of this thesis. Apart from these, a large variety of thermo-chemical and thermo-physical properties of metals, alloys and their hydrides can be calculated theoretically which can support the experimental findings. Another important aspect of hydrogen storage materials is diffusion of hydrogen through the bulk metal or alloy. The diffusion path, mechanism, activation barrier and temperature dependent diffusion coefficient are of prime importance for the gas-solid interacting systems. The investigation of diffusion phenomena may help to overcome the drawbacks related to hydrogen absorption-desorption process. The hydrogenation behavior changes with the change in dimension of the hydrogen storage materials. Thus, it is also interesting to study how hydrogen interacts with the metals and alloys in the different dimensions like bulk, surface and nanoclusters.

This thesis is divided into seven chapters as outlined below.

Chapter 1: Introduction; Chapter 2: Theoretical Approach; Chapter 3: Experimental methods; 4: Theoretical and experimental study of U_2Ti alloy 5: Theoretical and experimental study of Zr-based compounds 6: First principles study of hydrogen interaction with ZrCo surface and clusters 7: Conclusions

Chapter 1: Introduction

This chapter gives a brief introduction about the global energy demand, nuclear fusion as future source of energy and the properties of fusion reactor fuels. Different storage materials for storing tritium are discussed here along with their advantages and disadvantages. The importance of computational technique in the field of tritium storage is also presented in this chapter.

The demand for energy has been increased to meet social and economic development of human beings. The use of fossil fuels for energy supply has increased greenhouse gases concentrations in the atmosphere and that can seriously affect the environment as well as human life. Thus, the climate change is one of the most serious problems of the world and requires an immediate search of alternative sustainable fuels. The sustainable energy option available to the world with zero or low CO_2 emission are solar energy, fission with breeding, and fusion energy. Fusion has potential advantages as a safe, sustainable and environmentally attractive source of energy for electricity generation. The deuterium-tritium (D-T) reaction has been identified as the most efficient for fusion device in ITER program [1]. The hydrogen isotopes, tritium and deuterium are going to be used as fuel materials in the fusion reactor. The deuterium fuel extracted from water is universally available and essentially

inexhaustible fuel supply. Tritium has to be produced from lithium inside the reactor. Lithium is distributed in the earth's crust and the known reserves would last for more than a thousand years. As tritium is radioactive, its storage, handling and transport are important. In recent years, some selected metal hydrides are chosen as potential medium for the storage of hydrogen isotopes (H, D and T) in the solid state as it is the safest and most advantageous method over other conventional methods like gaseous and liquid storage. Hydrogen isotopes react with metals, alloys and forms hydrides. For the metal hydride to be used as a storage medium, it should satisfy certain requirements such as high hydrogen storage capacity, reversibility of absorption/ desorption pressure isotherms, wide range of equilibrium plateau pressure, small absorption heat, and first kinetics and should have small or no impurities. By investigating different properties of materials, few metals like U and Zr have been found to be suitable for tritium storage.

` Conventionally, uranium is used as getter bed for tritium as it has favorable thermodynamic and kinetic properties. However, uranium is pyrophoric and also a controlled nuclear material. Hence, an alternate material is required for this purpose. Among the alternate materials, zirconium based alloys, particularly, ZrCo alloy has been found suitable for the safe storage, supply and recovery of hydrogen isotopes in the ITER. ZrCo alloy has good hydriding/dehydriding property, not pyrophoric and easy to handle as it is not a nuclear material. However, ZrCo also has drawbacks of disproportionation due to prolong thermal cycling. Hence, both uranium and ZrCo has its own advantages and disadvantages [2]. Theoretical and computational techniques are very important in the field of tritium storage because it has manifold advantages

over the experimental procedure. The application of computational techniques in the field of tritium storage is also discussed here.

Chapter 2: Theoretical approach

This chapter depicts the density functional theory (DFT) and frozen phonon methods used for calculations of physico-chemical properties of hydrogen isotope storage materials. The fundamental aspects of the calculations and software packages have been discussed in this chapter.

All the present calculations are performed using the plane wave-pseudopotential method under the framework of DFT as implemented in the Vienna *ab-initio* simulation package (VASP) [3-4]. The electron-ion interaction and the exchange correlation energy are described under the projector-augmented wave (PAW) method and the generalized gradient approximation (GGA) of Perdew-Burke-Ernzerhof (PBE), respectively. The ionic optimization is carried out using the conjugate gradient scheme and the forces on each ion was minimized upto 5meV/Å. The k-point sampling in the Brillouin Zone (BZ) has been treated with the Monhorst-Pack scheme. Total energies of each relaxed structure using the linear tetrahedron method with Blöchl corrections are subsequently calculated. To begin with the dynamical calculations, the lattice parameters of the compounds have been optimized using VASP code and the optimized structures are used for phonon calculation. The phonon frequencies of the alloys and theirs hydrides are calculated by the PHONON program using the forces based on the VASP package. The phonon dispersion curves and temperature dependent thermodynamic functions of these compounds are obtained by using the calculated phonon frequencies.

For investigation of properties of ZrCo (110) surface and its interaction with hydrogen, all the calculations were performed using Quantum ESPRESSO software. Ultrasoft pseudopotentials were used to describe the electron-ion interactions. The climbing image nudge elastic band method (CI-NEB) was used to find out the minimum energy path (MEP), energy barriers and transition states for hydrogen dissociation and diffusion on ZrCo (110) surface. For ZrCo clusters, all calculations were performed within the spin-polarized density functional theory using the plane wave-pseudopotential approach as implemented in the VASP. To obtain the equilibrium geometries, a *cascade* genetic algorithm scheme was applied. A large number of spin states were also been considered for all these structures. The ionic optimization was carried out using the conjugate gradient scheme and the forces on each ion was minimized upto 5meV/Å. A 15x15x15 Å simulation box was considered for all calculations. The k-point sampling in the Brillouin zone (BZ) was treated with the Monhorst-Pack scheme, using Γ point. Total energies of each relaxed structure were calculated using the linear tetrahedron method with Blöchl corrections.

Chapter 3: Experimental methods

It describes the experimental methods used in this study for synthesis, characterization and measurements of thermodynamic properties of transition metal alloys. This chapter describes the principles of calorimeters for enthalpy increments and heat capacity measurements.

Both the U_2Ti and ZrCo alloys were prepared by arc-melting method and characterized by X-ray powder diffraction. The impurity analysis of U_2Ti was carried out by the X-ray fluorescence spectroscopy (XRF) and inductively coupled plasma mass spectrometry (ICPMS). The enthalpy increments of U_2Ti and ZrCo alloys were

measured using a high temperature inverse drop calorimeter (MHTC 96, SETARAM Instrumentation, France) in the temperature range 299–1169 K and 642-1497 K, respectively. The heat capacities of those alloys were calculated by differentiating the obtained enthalpy increments data. A set of thermodynamic functions for both the alloys were also calculated using experimental heat capacity data obtained in this study. The experimentally obtained thermodynamic data was also compared with the values obtained from the *ab-initio* data.

Chapter 4: Theoretical and experimental study of U_2Ti alloy

This chapter deals with the theoretical and experimental studies on U_2Ti alloy. In the theoretical part, the structural and electronic properties of U, Ti and U_2Ti under the framework of spin polarized DFT has been described. In the experimental part, synthesis, phase characterization, impurity analysis of U_2Ti alloy and measurements of its enthalpy increments are given.

Uranium is the most suitable metal for storage of tritium, but it becomes powder after absorption of hydrogen isotopes. This property of U can be improved upon by alloying it with titanium, which exhibits durability to powdering on hydrogenation [5]. Thus, U_2Ti is likely to possess a good durability to powdering. Its properties have been studied both experimentally and theoretically. U_2Ti alloy was prepared by arc melting and characterized by X-ray analysis (XRD) and impurities in it were analyzed by inductively coupled mass spectrometer (ICPMS) and X-ray fluorescence spectroscopy (XRF). The enthalpy increments of U_2Ti were measured using a high temperature inverse drop calorimeter in the temperature range of 299–1169 K. The molar heat capacity derived from enthalpy increment data was used to calculate a set

of self consistent thermodynamic functions such as entropy, Gibbs energy function, heat capacity, and Gibbs energy and enthalpy of formation values for U_2Ti.

The structural, electronic, and thermodynamic properties of U_2Ti, U, and Ti have been calculated using a plane wave (PW) based pseudopotential method under the framework of spin polarized DFT. The effect of the relativistic spin–orbit interaction on these properties has been investigated. The results were analyzed to obtain the structural parameters, lattice constants, bulk moduli, electronic specific heat, and the compound formation energy. On the basis of energetic, the enthalpy of formation of U_2Ti alloy has been calculated and found it to match reasonably with that obtained experimentally. From the density of states calculations it was seen that the nature of U_2Ti DOS and U DOS were very similar, however the energy levels of Ti lie much lower in the DOS spectrum. Due to the predominant presence of U at the Fermi energy, it might be inferred that the inclusion of Ti might not affect the hydrogenation behavior of U, but it might help to prevent the pyrophoricity of U.

Chapter 5: Theoretical and experimental study of Zr-based compounds

In this chapter the physico-chemical properties of Zr, ZrX_2, ZrCo and $ZrCoX_3$ (X= H, D and T) were studied using ab-initio method. The isotope effect of hydrides was explored here by studying the vibrational and thermodynamic properties. The enthalpy increments and heat capacity measurement of ZrCo alloy were also presented here.

The physico-chemical properties and isotope effect of Zr and its hydride ZrH_2 was investigated using *ab-initio* method. The nature of chemical bonding in ZrH_2 was analyzed through charge density distribution, electronic density of states, and electron

localization function. The results showed significant electronic charge transfer from Zr to the H site, indicating ionic bond character. Along with the isotope effect, the thermodynamic and mechanical properties of Zr, and its hydride ZrH_2 were calculated to find out hydrogenation effect on these properties. On the basis of the ZPE corrected enthalpies of formation ($\Delta_f H$ at 0 K) for all three compounds, it was found that the thermodynamic stabilities as: $ZrT_2 > ZrD_2 > ZrH_2$.

Similarly, the structural, electronic, elastic, vibrational and thermodynamic properties of ZrCo and $ZrCoH_3$ have been studied using *state of the art* first principles method and frozen phonon approach. The calculated lattice parameters of the ZrCo and $ZrCoH_3$ were found to be well in agreement with the experimental data. The volume expansion upon hydrogenation of ZrCo was found to be 22.9%. From the charge density calculation it was seen that more electronic charges are localized at the Co than Zr, thus polarizing the ZrCo bond. It has been observed that for $ZrCoH_3$, the electronic charges are localized in the decreasing order of H, Zr and Co, respectively. The ZPE corrected enthalpies of formation ($\Delta_f H$ at 0 K) for $ZrCoX_3$ (X= H, D, T) were -146.7, -158.3 and -164.1 kJ/(mole of $ZrCoX_3$) for X = H, D and T, respectively. This suggested that $ZrCoT_3$ and $ZrCoD_3$ to be more stable than $ZrCoH_3$. The elastic property calculation showed that both ZrCo and $ZrCoH_3$ were mechanically stable at ambient pressure and ductile in nature. The phonon calculation showed that the energy gap between optical and acoustic modes reduces in the order of $ZrCoT_3 > ZrCoD_3 > ZrCoH_3$. It has been concluded that isotopic effects in ZrX_2 and $ZrCoX_3$ were observed in terms of their vibrational and thermodynamic properties, but observed mechanical properties did not show isotopic effects.

The thermodynamic properties of alloys and their hydrides are important for the tritium storage purposes as these properties are related to the equilibrium pressure of that isotope. For investigating the thermodynamic properties, the ZrCo alloys was synthesized by arc melting and characterized by X-ray powder diffraction (XRD). The enthalpy increments of ZrCo alloy was carried out using a high temperature inverse drop calorimeter. Using the enthalpy increments values, the heat capacity and other thermodynamic functions of ZrCo were determined. The obtained data were compared with the theoretically calculated values and a good agreement between experimental and theoretical values was obtained. The thermodynamic data obtained in this study may be useful for design of ZrCo getter bed as well in different reactions of ZrCo.

Chapter 6: First principles study of hydrogen interaction with ZrCo surface and clusters

This chapter describes the interaction of hydrogen with ZrCo (110) surface using first principles method. It also illustrates the diffusion pathway of hydrogen on ZrCo surface as well as in bulk. The hydrogen interaction with ZrCo (m+n = 2, 4, 6 and 8) clusters is also presented here in terms of the structural, energetic and magnetic properties.

The hydrogenation behavior of metals and alloys changes with the change of its dimensions [6]. It is of great interest to study the hydrogenation behavior of ZrCo in smaller dimensions apart from bulk. The interactions of hydrogen with the ZrCo surface, particularly, the hydrogen adsorption and diffusion on ZrCo (110) surface and in the bulk have been studied using the first principles approach. The ZrCo (110) surface has been chosen as it is the most atom dense plane of CsCl type ZrCo. The hydrogen adsorption on this (110) plane has only been considered. The H_2 molecule

got adsorbed on the Co site present on the surface and decomposed with a large energy barrier of 0.85 eV. While on the top of Zr sites the H_2 molecule got repelled. The adsorption of H on ZrCo (110) surface and in the bulk is both exothermic relative to isolated hydrogen atom. The minimum energy barrier for H diffusion from Co to next Co site via Zr site, Zr to Co site and Zr to Zr site via Co site on the surface has been calculated using Nudge Elastic Band (NEB) method. The energy barrier for H diffusion from Zr site to next Zr site was found to be 0.28 eV. The diffusion pathway from bulk octahedral hole to surface was also investigated. It was concluded that in case of ZrCo surface, the H atom is stable in a bridge position of Zr and Co atoms on the ZrCo surface.

Hydrogen interactions with ZrCo nanoclusters, another dimension of ZrCo, have also been found to be interesting and need to explore fundamentally [7]. With this motif, the structural, energetics and magnetic properties of bimetallic Zr_mCo_n (m+n = 2, 4, 6 and 8) nanoclusters along with the hydrogenated species have been investigated using spin-polarized density functional theory (DFT) within the generalized gradient approximation (GGA). A plausible candidate for the ground state isomer and the other possible local minima, binding energies and magnetic moments were calculated. It has been found that Zr_2Co_2 (for tetramer), Zr_3Co_3 (for hexamer) and Zr_4Co_4 (for octamer) were the most stable isomers. In order to underscore the hydrogen storage capacity of these small clusters, the hydrogen adsorption on the stable Zr_mCo_n clusters has also been studied. The electronic structures of Zr_mCo_n clusters with and without adsorbed hydrogen were described in terms of density of states spectra and charge density contours. The magnetic moments of the Zr_mCo_n clusters were also calculated.

Chapter 7: Conclusions

Finally, the major findings of this study and the scope of this study for further investigations are discussed in chapter 7. This chapter also includes a brief description of the proposed computational studies, which, in turn will support the experimental finding in near future.

References

[1] ITER Fuel Cycle, ITER Documentation Series No. 31 (IAEA, Vienna, 1991)

[2] W.T. Shmayda, A.G. Heics, N.P. Kherani, J. Less Comm. Met. 162 (1990) 117-127.

[3] G. Kresse, J. Hafner, Phys. Rev. B 49 (1994) 14251-14269.

[4] W. Kohn, L.J. Sham, Phys. Rev. 140 (1965) 1133-1138.

[5] T. Yamamoto, S. Tanaka, M. Yamawaki, J. Nucl. Mater. 170 (1990) 140–146.

[6] S. Bredendiek-Kämper, H. Klewe-Nebenius, G. Pfennig, M. Bruns, H. J. Ache, Fresenius Z Anal. Chem. 335 (1989) 669-674.

[7] X. Sheng, G Zhao, L. Zhi, J. Phys. Chem. C 112 (2008) 17828-17834.

LIST OF FIGURES

LIST OF TABLES

CHAPTER 1

Introduction

1.1 Global Energy Demand

In recent years, the global demand of energy has increased manifold with the progress of the modern civilization. Today, a large part of the world energy demand is covered by fossil based fuels like coal, petroleum, natural gas, gasoline etc. The stock of fossil fuel is day by day decreasing while the requirement of energy is increasing. To meet the increasing demand of energy, alternative energy sources have to be explored. The energy resources available to us can be divided into two parts: (i) non-renewable and (ii) renewable energy sources. Fossil fuels are in the category of non-renewable sources of energy which is finite. It is expected that within a few decades the current stock of oil and natural gas will be exhausted. Another major issue of using fossil fuel is the emission of greenhouse gas like carbon dioxide (CO_2). The gas has major contribution in increasing the temperature and also in climate change of our earth.

The world needs energy resources which will not run out early and have a much lower environmental impact. This is possible only with the renewable energy resources. The main renewable resources are solar, wind, biomass, water, geothermal etc. [1]. Solar energy technologies produce electricity from sunlight. Electricity can also be produced by using the speed of wind using wind turbines. The biomass incorporates materials from living body. There are various types of biomass, *i.e.* plants, residue from agriculture and forestry, and the organic component of municipal and industrial wastes which are used for production of hydrocarbon based fuels. Another large source of renewable energy is hydro power. The modern technologies are now able to generate energy from water waves, currents and tides. In recent year, heat from earth, particularly from heat retained in shallow ground, hot water, rock etc. has been found as a source of energy. This is called geothermal energy which provides electricity and efficient heating and cooling. But these can not provide continuous

energy to grids because of few constraints. So, we need an energy source which can continuously supply electricity to the grids.

Recently, the World Nuclear Association has said "There is unprecedented interest in renewable energy, particularly solar and wind energy, which provide electricity without giving rise to any carbon dioxide emission. Harnessing these for electricity depends on the cost and efficiency of the technology, which is constantly improving, thus reducing costs per peak kilowatt". Renewable electricity production, from sources such as wind power and solar power, is sometimes criticized for being intermittent or variable. However, the International Energy Agency concluded that deployment of renewable technologies (RETs), when it increases the diversity of electricity sources, contributes to the flexibility of the system. However, the report also concluded: "At high levels of grid penetration by RETs the consequences of unmatched demand and supply can pose challenges for grid management. This characteristic may affect how, and the degree to which, RETs can displace fossil fuels and nuclear capacities in power generation."

In most recent, an historic agreement to combat climate change and unleash actions and investment towards a low carbon, resilient and sustainable future was agreed by various nations in Paris. The universal agreement's main aim is to keep a global temperature rise this century well below 2 degrees Celsius and to drive efforts to limit the temperature increase even further to 1.5 degrees Celsius above pre-industrial levels. The 1.5 degree Celsius limit is a significantly safer defense line against the worst impacts of a changing climate. Additionally, the agreement aims to strengthen the ability to deal with the impacts of climate change. Through this climate summit, the world is in a way of searching an alternate source of energy which will give minimum possible impact on climate.

The Intergovernmental Panel on Climate Change (IPCC) has said that if governments were supportive, and the full complement of renewable energy technologies were deployed,

renewable energy supply could account for almost 80% of the world's energy use within forty years. The chairman of the IPCC, said the necessary investment in renewable energy sector would cost only about 1% of global GDP annually. This approach could contain greenhouse gas levels to less than 450 parts per million, the safe level beyond which climate change becomes catastrophic and irreversible.

As an alternate to the fossil fuel based energy and among the renewable energy resources, nuclear energy has been considered as one of the potential source. It is a clean, cheap and continuous source of energy. It is capable of supply a large amount of energy to the grids for years. Nuclear energy is categorized into two parts (i) fission and (ii) fusion energy. The energy harvesting from fission reactors is well known and deployed worldwide. Several countries like U.S.A, France, Russia, China, Japan, Germany, India etc. are producing appreciable amount of electricity using fission reactors. In France, approximately 70-80% of total electricity comes from the nuclear power. Though the fission technology is well established, but fusion reactor is still in research and development stage. The International Thermonuclear Experimental Reactors (ITER) program [2-3] has been started by several countries to boost up the fusion reactor development.

India has embarked on a three stage nuclear power programme (as shown in the Fig.1.1), which is based on utilization of indigenous nuclear resources of modest uranium [4] and abundant thorium (~ 3,19,000 tons) [5]. The first stage involved using natural uranium (^{235}U–0.7%, fissile material and ^{238}U-99.3%, fertile material) to fuel Pressurized Heavy Water Reactors to produce electricity and producing plutonium-239 as a byproduct. Using Pressurized Heavy Water Reactors rather than Light Water Reactors was the best choice for India given its infrastructure. While Pressurized Heavy Water Reactors used unenriched uranium, Light Water Reactors required enriched uranium. Also, the components of PHWR could be domestically manufactured in India, as opposed to LWRs, which would need some

components to be imported. Furthermore the byproduct plutonium-293 would be used in the second stage.
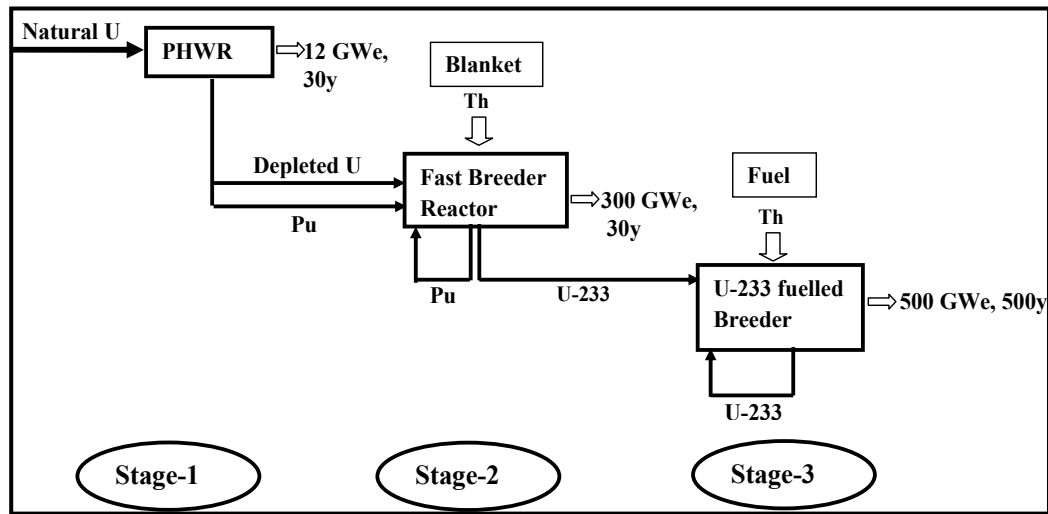
Fig. 1.1: Schematic of three stage Indian nuclear programme

The second stage involves use of plutonium-239 to produce mixed-oxide fuel, which would be used in Fast Breeder Reactors. These reactors have two processes. Firstly plutonium-293 undergoes fission to produce energy, and uranium-238 breeds to more plutonium-239. Furthermore once a sufficient amount of plutonium-239 is built up, thorium will be used in the reactor, to produce Uranium-233. This uranium is crucial for the third stage. The main purpose of stage-3 is to achieve a sustainable nuclear fuel cycle. The advance nuclear system would be used a combination of Uranium-233 and Thorium. Thus India's vast thorium would be exploited, using a thermal breeder reactor. Currently this stage is still in the research stage. Thus India is looking to simultaneously using its thorium in other technologies. The options include Accelerator Driven Systems (ADS), Advanced Heavy Water Reactor (AHWR) and Compact High Temperature Reactor (CHTR) [6].

In the fusion reactor programme, India became a full seventh partner of ITER in December 2005. The Institute for Plasma Research (IPR), which is an autonomous institute under the Department of Atomic Energy (DAE), Government of India., empowered to design,

build and deliver those contributions to ITER which have been agreed in the procurement sharing. The ITER activities of IPR have been named ITER-India, and its formal organizational structure was constituted on July 5th, 2006. IPR is carrying out research in basic and applied plasma physics. Although the institute harbours a large number of basic experimental devices for research in plasma physics, the main thrust of the research is high temperature tokamak experiments. The institute is currently in the process of building the Steady State Superconducting Tokamak (SST-1). Apart from that, several other Indian research institute also contributing directly or indirectly to the fusion reactor programme.

1.2 Nuclear Energy

The basic of nuclear fission and fusion on which fission and fusion reactors are based are discussed below.

Two different processes that involves nuclei of atoms can harness a large amount of energy without the emission of green house gases are (i) fission – the splitting of a nucleus and (ii) fusion – the joining together of two nuclei. In case of nuclear fission – electricity is generated from the energy released when heavy nuclei break apart. In case of nuclear fusion, the energy is released when two light weight nuclei fuse together. The energy extraction from fission is a well established process whereas energy production from nuclear fusion involves extraordinary scientific and engineering challenges. The Research and development (R&D) activities on fusion reactor are still in progress. The fundamental aspects for nuclear fission and fusion are discussed below.

1.2.1 Nuclear Fission

In nuclear fission reactions [7-8] (also called radioactive decay), a neutron is aimed at the nucleus of a large, unstable atom, like uranium, thorium, or other radioactive elements (Mass No (A) > 120). The extra mass of the neutron causes the radioactive nucleus to split apart, forming lighter elements, free neutrons, and great quantities of energy. The generated

neutrons cause further fission and the chain reaction propagates. This process generates a large amount of energy using which the electricity is generated. Two common fission reactions of U-235 are as follows:

$$^{235}_{92}U + ^{1}_{0}n \rightarrow\ ^{236}_{92}U \rightarrow\ ^{141}_{56}Ba + ^{92}_{36}Kr + 3^{1}_{0}n + Energy \tag{1.1}$$

$$^{235}_{92}U + ^{1}_{0}n \rightarrow\ ^{236}_{92}U \rightarrow\ ^{140}_{54}Xe + ^{94}_{38}Sr + 2^{1}_{0}n + Energy \tag{1.2}$$
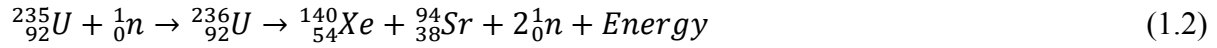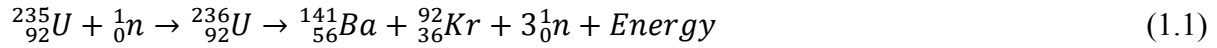
Both the reactions start when we add a single neutron to uranium-235, which forms uranium-236. Barium-141, krypton-92, xenon-140, and strontium-94 are smaller nuclei that U-236 could split into. At any poiny in the reaction the conservation of nucleons stays same. In the first reaction three neutrons were ejected, while in the second reaction only two were ejected. Although it is possible for as many as 5 neutrons to be ejected in some fission reactions, on average it is about 2.5 neutrons. These reactions are exoergic. A general type fission reaction can be written as:

$$^{235}_{92}U + ^{1}_{0}n \rightarrow\ ^{236}_{92}U \rightarrow X + Y + 2.5^{1}_{0}n + Energy \tag{1.3}$$
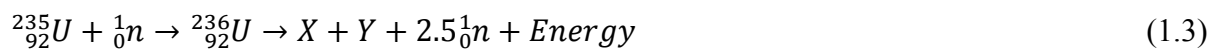
Where, X and Y represent any of the smaller nuclei that uranium-236 will split into. A pictorial representation of nuclear fission is given in Fig. 1.2.
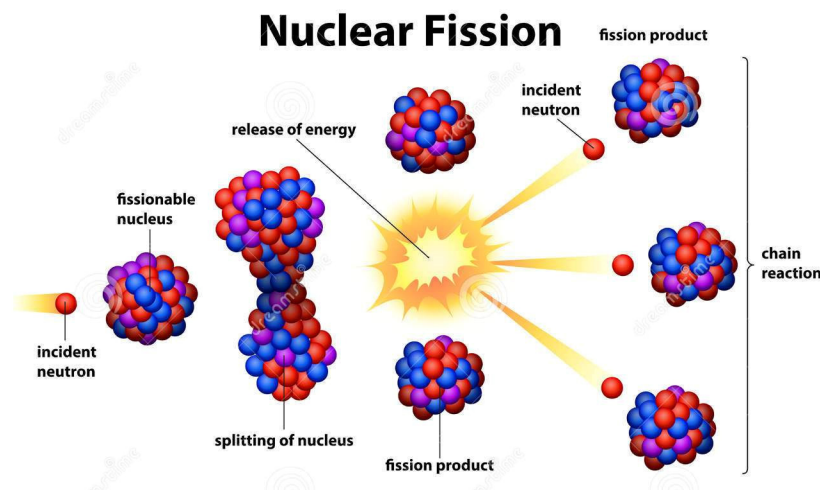
Fig. 1.2: A schematic representation of nuclear fission

1.2.2 Nuclear fusion

Nuclear fusion is a reaction where nuclei of two light atoms join together and form a stable heavier nucleus with the release of enormous amounts of energy [9-10]. A huge amount of 'activation energy' is required to make this reaction feasible. This is why fusion is called a *thermonuclear* reaction. Fusion of deuterium and tritium into helium is only one of the possible reactions that could be the basis for the fusion power reactors of the future. These reactions along with other fusion reactions are shown below:

$$_1H^2 + {}_1H^3 = {}_2He^4 + {}_0n^1 \; (+ \; 17.6 \; \text{MeV}) \tag{1.4}$$

$$_1H^2 + {}_1H^2 = {}_1H^3 + {}_1H^1 \; (+ \; 4.0 \; \text{MeV}) \tag{1.5}$$

$$_1H^2 + {}_1H^2 = {}_2He^3 + {}_0n^1 \; (+ \; 3.3 \; \text{MeV}) \tag{1.6}$$

$$_1H^2 + {}_2He^3 = {}_1H^1 + {}_2He^4 \; (+ \; 18.3 \; \text{MeV}) \tag{1.7}$$

A typical D-T type fusion reaction is shown in Fig. 1.3:
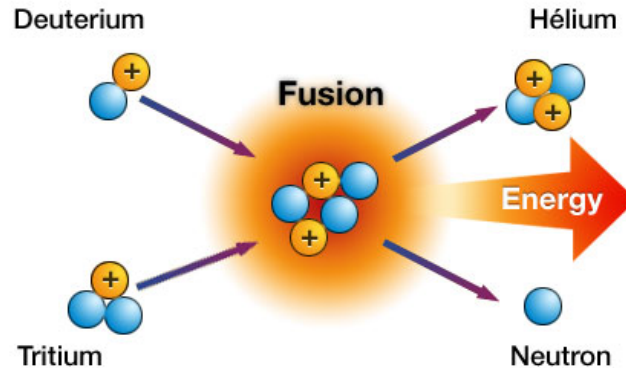
Fig. 1.3: A schematic representation of nuclear fusion

Nuclear fusion has several advantages over the nuclear fission and those are:

1) The energy release in D-T fusion reaction is one order of magnitude higher than the energy (per nucleon) released in the fission of U-235.

2) The reserves of fusionable isotopes are much larger than those of fissionable isotopes; in fact, they are essentially unlimited.

3) Fusion does not produce large amount of radioactive waste that will need to be stored.

4) The products of fusion reactions are less radioactive than the products of fission reactions. Among the products of the fusion reactions only tritium and neutrons are radioactive.

5) Fusion lies in its inherent safety.

1.3 Nuclear Reactors

Nuclear reactor is a device in which nuclear reaction particularly nuclear fission or fusion takes place, in a controlled manner, for the production of energy and neutrons. Nuclear fission is a source of energy in a nuclear reactor. In addition to energy, the fission reactions also generate neutrons which are essential for sustaining fission chain reaction. The nuclear reactor is thus a strong source of neutrons. The nuclear reactors can be classified into two types (i) fission and (ii) fusion reactor. In both the reactors, large amount of energy is released which results in the production of heat and used for electricity generation. Nuclear power reactors, only fission reactors are among the major sources of electricity in the world whereas developments of fusion reactors are in preliminary stage. Currently 446 nuclear power reactors supply about 20 percent of electricity in the world. Nuclear reactors are clean source of electricity and do not contribute to green house gas emission. If the electricity currently produced by nuclear reactors was to be produced by coal or oil or gas fired plants, there would be additional 2-3 billion tonnes of CO_2 emission into the atmosphere annually.

1.3.1 Fission Reactor

The enormous amount of energy given out in a nuclear fission reaction makes it a suitable process for the generation of electricity in a fission reactor [11-12]. The energy release from uranium is ~ 1014 J per kg whereas for coal it is ~ 107 J per kg.

Main fission reactor components are

1) Source of fissionable material (fuel rods)

2) A moderator to slow down neutrons to increase the probability of absorption by a nucleus to split into the two fission fragments and release other neutrons

3) Movable control rods absorb neutrons to maintain the reactor at a critical level to maintain a self-sustaining chain reaction and in the event of an accident can be dropped to be into reactor vessel to shut-down the fission process

4) A reflector surrounding the fuel rods and moderator to prevent the loss of neutrons thereby improving the efficiency of the reactor

5) A radiation shield surrounding the reactor vessel

6) Heat exchanger for the transfer of the energy released by the fission reactions to produce steam

7) The steam from the heat exchanger turns a turbine so that electricity is produced in an electric generator
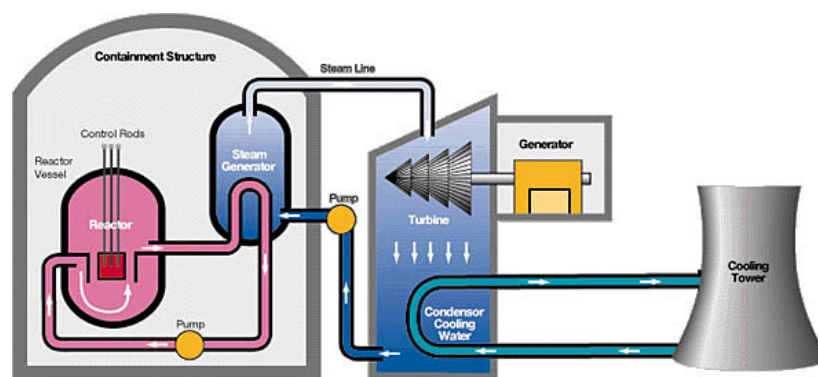
Fig. 1.4: A schematic diagram of a fission reactor

In a uranium fission reactor, the fuel is the isotope ^{235}U and not the main isotope ^{238}U found in natural uranium ore (99% ^{238}U). A ^{235}U nucleus can absorb a slow moving neutron to give a ^{236}U nucleus which then undergoes fission, but this does not happen with a ^{238}U nucleus. So the natural uranium ore must be enriched to ~ 1% ^{235}U to give a critical mass of fuel. If the amount of uranium exceeds the critical mass a sustained nuclear reaction is possible as few neutrons are lost and there are sufficient neutrons available to initiate further fission reactions. If the mass of fuel is less than the critical mass, most neutrons escape before additional fissions occur and the chain reaction is not sustained.

The uranium can't be enriched using chemical methods. The uranium must be enriched by physical means using gaseous diffusion of UF_6 in giant processing plants. The molecules of ^{235}U diffuse slightly more easily than ^{238}U molecules (due to mass differences). After about 1500 stages of diffusion a greater percentage of ^{235}U can be obtained. Also, giant gas centrifuges can be used to process the natural uranium ore.

The probability that a ^{235}U nucleus will absorb a neutron is increased if they are moving slowly. But, the neutrons emitted during fission are moving very fast. To slow down the neutrons a moderator is used. The moderator is used to elastically scatter the high-energy neutrons and thus reduce their energy. The best moderators are those which the mass of its atoms are similar to the mass of a neutron. Some materials commonly used include deuterium ^2H (heavy water), carbon (graphite), boron and beryllium.

To have a self-sustaining chain reaction, then, at least one neutron produced must cause another fission to occur. It is most important to control the number of neutrons. If the less than one neutron is available for other fissions, then the reactor is subcritical. If the number of neutrons available for other fissions is more than one, then the reactor would become supercritical which would be extremely dangerous. The number of neutrons is controlled by movable control rods and a reflector. The control rods are usually made from cadmium because cadmium atoms can easily absorb neutrons thus reducing the number of neutrons that would otherwise cause more fission. The position of the control rods is continually adjusted so the reactor is just in a critical condition. In an emergency, the control rods can be dropped into the reactor vessel to shut down the fission process. The reflector is often just water, from which neutrons are back scattered into the fuel area. The reactor must be contained within a secure vessel with adequate radiation shielding to project people working in the reactor.

The purpose of the reactor is to generate electricity. In a pressurized water reactor, the moderating water is under high pressure and circulates from the reactor to an external heat exchanger where it produces steam which drives a turbine to operate the electric generator.

1.3.2 Fusion Reactor

With the recent advances in high energy plasma physics show that nuclear fusion - the energy source of the sun and the stars, may act as the future sustainable energy source [13-14]. Such power plants would be safe and environmentally friendly. But, one of the main problems of fission reactors, namely that of a possible uncontrollable nuclear reaction is banished; also the problem of radiotoxic waste is reduced by many orders of magnitude. Fusion reactors would have almost limitless supplies of energy and could be sited anywhere in the world. Fusion is, however, still in the development stage and it is not expected that commercial power plants will start operation in near future.

The fusion reactor is totally based on fusion process which has been discussed in section 1.2.2. The aim of fusion research is to design schemes in which light nuclei approach each other frequently down to such small separations that there is a high chance of numerous reactions taking place. Under normal conditions nuclei are separated at least by the so-called atomic radius which reflects the presence of the surrounding electron cloud. Under these conditions fusion does not take place. If the atoms are heated, the motion of the electrons and the nuclei will increase until the electrons have separated. A hot gas, where nuclei and electrons are no longer bound together, is called a plasma.

Even in plasma, however, the nuclei do not come close enough to react because of mutually repulsive forces. By heating the plasma to an even higher temperature – one speaks of very hot plasma - the ions acquire an even higher velocity, or kinetic energy, and can then overcome the repulsive force. As an analogy, we can think of a fast ball rolling up a hill against the gravitational force. Clearly, the number of fusion reactions that take place will

depend on the plasma temperature and plasma density. The production of the plasma and its subsequent heating require of course energy. A successful fusion power plant requires that the power produced by the fusion reaction exceed the power required to produce and heat the plasma. The ratio of the power generated to that consumed (the fusion power amplification factor) is called the Q value. Initially, the plasma will be heated by various external sources, e.g. microwaves. With increasing temperature, however, the number of fusion reactions also increases and the fusion reaction itself heats the plasma due to the production of the energetic helium atoms (actually ions, or α particles). The kinetic energy of the helium nuclei exceeds the average kinetic energy of the nuclei of the fuel (deuterium and tritium) by orders of magnitudes. The energy is distributed to the fuel nuclei via collisions, as in a game of billiards. In fact, a point can be reached - termed ignition - when external heating is no longer necessary and the value of Q goes to infinity. In practice, however, power plant operation would probably correspond to a Q value of 20-40.

The state of very hot plasma and its nearness to the ignition condition can be characterised by the product of temperature, density and the so-called energy confinement time. The latter value describes the ability of the plasma to maintain its high temperature; in other words, it is a measure for the degree of insulation of the plasma. Ignition can only be achieved if this "fusion triple product" exceeds a certain value.

a) Magnetic confinement

The temperatures necessary to ignite plasma are between 100-200 million °C. Obviously no solid material is able to confine a medium with such a high temperature. This dilemma is solved by the fact that in the plasma, all the particles carry an electrical charge and can thus be confined by a magnetic field. (The charged particles gyrate around the magnetic field lines.) It transpires that a doughnut-shaped configuration of the magnetic field "cage" is appropriate for this purpose, although the story is actually a little more complicated: the

magnetic field lines not only have to be doughnut-shaped, they also need to have a helical twist. This scheme is referred to as magnetic confinement.
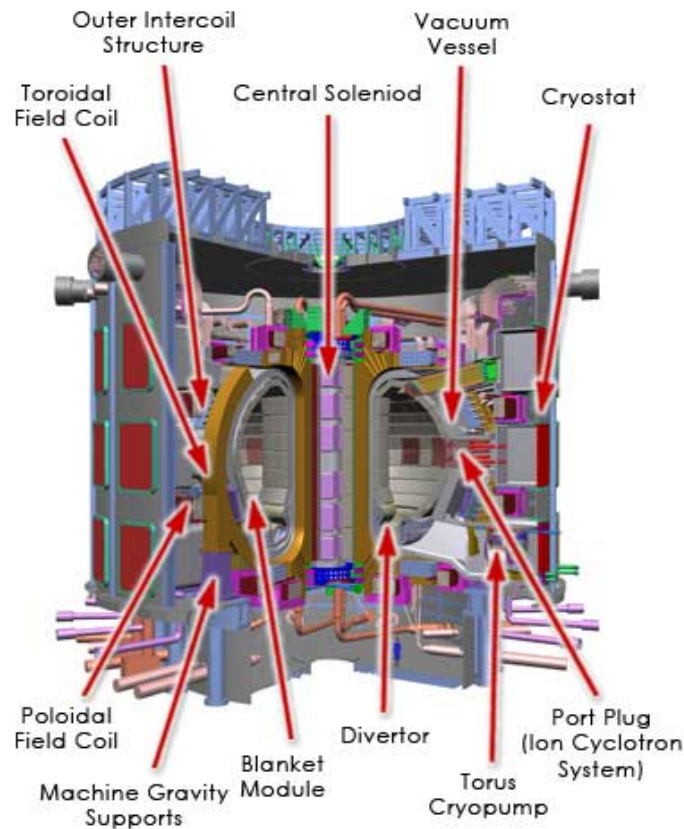
Fig. 1.5: Sketch of the ITER fusion reactor

b) Inertial confinement

In inertial confinement fusion a small pellet of deuterium and tritium fuel is compressed by so-called momentum conservation to extremely high density and temperature. (Densities of twenty times the density of lead and temperatures of 100 million °C are envisaged.) The fuel pellet is encapsulated by an layer of another material and subject to extremely intense beams of laser radiation or high energy charged particles. The outer layer heats up and evaporates. The evaporation products move outwards, but the rest of the pellet is compressed inwards, due to momentum conservation. Inertial confinement is mainly investigated in the US and France and to a lesser extent in Japan, Britain and other European countries. Since such experiments can also be used to study the physics of nuclear weapon explosions, much of this

research in the US is financed from the defence budget. Inertial fusion is considerably less developed than magnetic confinement fusion with respect to the realisation of a power plant.

c) The possible design of a fusion power plant

The various features such as steam generator, turbine and current generator will be the same as in conventional nuclear or fossil-fuelled power plants. A flow chart of the energy and material flows in a fusion plant are depicted in Fig. 1.6. The fuel deuterium and tritium is injected into the plasma in the form of a frozen pellet so that it will penetrate deeply into the centre. The neutrons leave the plasma and are stopped in the so-called blankets which are modules surrounding the plasma. The neutrons deposit all their kinetic energy as heat in the blanket. The blankets also contain lithium in order to breed fresh supplies of tritium via a nuclear reaction. The "ash" of the fusion reaction helium is removed via the divertor. This is the section of the containing vessel where the particles leaving the plasma hit the outer wall. The outer magnetic field lines of the tokamak are especially shaped so that they intersect the wall at special places, namely the divertor plates. Only a small fraction of the fuel is "burnt" so that deuterium and tritium are also found in the "exhaust" and can be re-cycled. The tritium produced in the blankets is extracted with a flushing gas - most likely helium - and delivered to the fuel cycle.

Fig. 1.6: Flow chart for a future fusion reactor

The heat produced in the blanket and the divertor is transported via water or helium to the steam generator and used to produce electricity to feed to the grid. A small fraction is used to supply electricity to the various components in the plant itself. Electrical power is required mainly for the cryo-system which produces low temperature helium for the super-conducting magnets, the current in the magnets, the current drive and the plasma heating systems. The reactor core is arranged in different layers like an onion. The inner region is the plasma, surrounded by first wall and blanket. All this is contained in the vacuum vessel. Outside the vacuum vessel are the coils for the magnetic field. Since the magnets operate at very low temperatures (superconductors), the whole core is inside a cryostat

1.4 Fuels for fusion reactor

Among the different types of fusion reactions mentioned above, D-T type fusion is found to be most favourable from the perspective of having comparatively lower threshold temperature and high energy output. Table 1.1 shows the threshold temperature of different fusion reactions. Deuterium and tritium are the main ingredients in most fusion reactions. Deuterium is a stable form of hydrogen; it is found in ordinary water. Tritium is a radioactive form of hydrogen, not found in nature.

Table 1.1: Heating requirements for selection fusion reactions

		Fusion Reaction	Threshold Temperature (^{0}C) (x 10^6)
D+D	=	$_2$He^3 + n +3.3 MeV (79 MJ/g)	400
D+D	=	T+p + 4.0 MeV (97 MJ/g)	400
D+T	=	$_2$He^4+n + 17.6 MeV (331 MJ/g)	45
D+$_2$He^3	=	$_2$He^4+p + 18.3 MeV (353 MJ/g)	350

D= deuterium; T= tritium; p=proton; n= neutron

1.4.1 Deuterium

Deuterium (symbol D or ^{2}H, also known as heavy hydrogen) is one of two stable isotopes of hydrogen. The nucleus of deuterium, called a deuteron, contains one proton and one neutron, whereas the far more common hydrogen isotope, protium (^{1}H), has no neutron in the nucleus. Deuterium has a natural abundance in Earth's oceans of about one atom in 6420 of hydrogen. Thus deuterium accounts for approximately 0.0156% (or on a mass basis 0.0312%) of all the naturally occurring hydrogen in the oceans, while the most common isotope (hydrogen-1 or protium) accounts for more than 99.98%. Deuterium occurs in trace amounts naturally as deuterium gas, written ^{2}H or D, but most natural occurrence in the universe is bonded with a typical ^{1}H atom, a gas called hydrogen deuteride (HD or ^{1}H^{2}H). For the larger amount requirement, deuterium should be produced using industrial process [15].

In theory, deuterium for heavy water could be created in a nuclear reactor, but separation from ordinary water is the cheapest bulk production process. Deuterium is produced for industrial, scientific and military purposes, by starting with ordinary water—a small fraction of which is naturally-occurring heavy water—and then separating out the heavy water by the Girdler sulfide process, ammonia-hydrogen process, distillation, or other methods.

1.4.2 Tritium

Tritium (symbol T or ^{3}H, also known as hydrogen-3) is a radioactive isotope of hydrogen [16]. The nucleus of tritium (sometimes called a triton) contains one proton and two neutrons, whereas the nucleus of protium (by far the most abundant hydrogen isotope) contains one proton and no neutrons. Tritium decays into helium-3 by beta decay as in this nuclear equation:

$$^3H \longrightarrow {}^3He + e\text{-} + \bar{\upsilon} \tag{1.8}$$

and it releases 18.6 keV of energy in the process. The electron's kinetic energy varies, with an average of 5.7 keV, while the remaining energy is carried off by the nearly undetectable

electron antineutrino. Beta particles from tritium can penetrate only about 6.0 mm of air, and they are incapable of passing through the dead outermost layer of human skin.

The deuterium is a widely available from inexhaustible resource of water. However, tritium is a fast-decaying hydrogen isotope and occurs only in trace quantities in nature and can be produced during the fusion reaction when neutrons escaping the plasma interact with the blanket. The breeder blanket has two roles to breed tritium and to convert neutron energy to heat. Lithium has been identified as the only viable element to breed tritium because of its low nuclear binding energy compared to the lighter and heavier elements in the periodic table which makes lithium to be suitable for tritium breeding than any other element. The tritium production nuclear reaction is given below:

$$_3\text{Li}^6 + {}_0\text{n}^1 = {}_2\text{He}^4 + {}_1\text{H}^3 \ (+ \ 4.8 \ \text{MeV}) \tag{1.9}$$

$$_3\text{Li}^7 + {}_0\text{n}^1 = {}_2\text{He}^4 + {}_1\text{H}^3 + {}_0\text{n}^1 \tag{1.10}$$

1.5 Different storage materials for tritium

1.5.1 Criteria for selection of tritium storage materials

Tritium being a radioactive isotope should be stored in a suitable medium to avoid its accidental release in atmosphere. Compare to gaseous or liquid state storing medium, solid state storage is found to be more advantageous. Metal hydrides are unique candidates for this purpose. There are few criteria for being a good hydrogen isotope storage material. They have been discussed as follows:

1) The material should absorb tritium (^{3}H) at room temperature and atmospheric pressure. The dissociation temperature of the tritides should be moderately high.

2) It should have very low dissociation pressure at room temperature which will prevent the release of tritium to the atmosphere under ambient condition.

3) Gravimetric capacity should be high i.e. large amount of tritium should be stored in small volume.

4) The material should have facile reversibility of hydride formation and decomposition reactions i.e. hydride should have thermal cyclic life stability.

5) It should have faster kinetics of hydrogen absorption-desorption.

6) It should have high ^{3}He (decay product) retention capacity.

7) The material should not degrade by the decay heat of beta emission.

8) The material should be resistance to chemical deactivation.

1.5.2 A Brief History of Tritium Storage Materials

While almost all metals can be made to react with hydrogen under some conditions, only a few metals do so "reversibly" at room temperature and near atmospheric pressures. These materials are generally referred to as "reversible" metal hydrides. Reversible metal hydrides can be either pure metal such as palladium, titanium, or zirconium. They can also be intermetallic compounds or alloys made up of two or more metals such as iron-titanium or lanthanum-nickel.

Reversible metal hydrides offer a number of advantages than compressed gas or a cryogenic liquid in storing hydrogen. Hydrides have an extremely high volumetric density for hydrogen. That means that a lot of hydrogen can be packed in a very small compact space. In fact, most metal hydrides can store hydrogen several times more compactly than high pressure gas and often more compactly even than liquid hydrogen. This is because the hydrogen atoms in a hydride are bound to metal atoms more closely than they can bind to themselves either as a gas or a liquid. Hydrides can store hydrogen at very low pressure, which affords a higher level of safety. Formation of hydrides often useful for separation processes. The disadvantage of hydrides is their relatively high cost and weight.

While the ability of some pure metals to absorb hydrogen was known for over several decades, the discovery of a new class of intermetallic alloys that reversibly absorb and release hydrogen did not come until the late 1960s. One of the first intermetallic alloys to be

"hydrided" was iron-titanium. Brookhaven National Laboratory reported this in 1969 (Sandrock and Huston 1981). Iron-titanium was one of the first practical metal hydrides [17-18]. It readily absorbs hydrogen at room temperature and is relatively inexpensive. However, iron-titanium has some disadvantages. It can be easily poisoned by small amounts of oxygen, and substantial heating of the material is required the first time that it is exposed to hydrogen. The initial conditions, required of a metal hydride, to first absorb hydrogen are normally referred to as its "activation" conditions. Around the same time that iron-titanium was being explored as a practical metal hydride, another important hydride material, lanthanum- nickel, was discovered [19]. This became a new and exciting reversible hydride material. Lanthanum-nickel has a high hydrogen capacity and readily absorbs hydrogen at ambient pressures. Furthermore, it can be easily activated at room temperature without additional heating and is considerably more resistant to oxygen and other hydride poisons. In the early 1970s, researchers all around the word began exploring the properties of this new reversible hydride along with its many variations. It was discovered that substituting other metals for nickel significantly change the hydrogen properties of the material. Scientists and engineers could now customize their own hydride materials and come up with operating conditions to match the needs of their application. An engineer could now select the right metal hydride material to meet a specific hydrogen storage material at optimum temperature and pressure.

The first metal hydride was tested at Savannah River Site (SRS) in 1981. A few years later, the first metal hydride applications in the tritium facilities were introduced in a new tritium loading operation. The facility required both near-term storage and compression of tritium. The hydride material chosen for this application was lanthanum-nickel-aluminum (LANA) [20-22]. By substituting a small amount of aluminum for some of the nickel in the lanthanum-nickel hydride, it was found that the operating pressure of the hydride system could be controlled. Therefore, a higher aluminum content alloy with 6% aluminum by

weight could be used for low pressure, safe storage of tritium, while a lower aluminum content alloy with only 2% aluminum by weight could be used to pump or compress tritium to higher pressures. Another advantage of using the LANA metal hydrides for this application was that pure tritium was always delivered to the loading process. In traditional tritium pumping and loading applications, if the tritium stays in the system for a prolonged period of time, some of the tritium is converted to 3-helium. Tritium naturally decays to 3- helium, a non-radioactive form of helium gas at a rate of 5.5% per year. Though this process of radioactive decay is small, over an 8-hour shift, it can produce enough helium to effect the purity of the tritium. The LANA, metal hydride is able to retain all of the decay helium and release virtually pure tritium on demand.

Another early application of metal hydrides in the tritium facilities was as a pump/separator. In 1987, a metal hydride pump/separator was put in service to provide pumping to the cryogenic distillation columns, as well as to purify inert gasses (i.e., helium, argon, nitrogen) from the hydrogen isotope stream. The pump/separator used a very low pressure hydride (palladium) that was able to efficiently separate the hydrogen isotopes from the other gasses and deliver the pure hydrogen isotopes directly to the cryogenic distillation columns. The pump/separator was also able to do this safely from tanks that were below atmospheric pressure, thereby improving the overall performance of the system [23].

In the early 1980s, the Savannah River Laboratory began a major program to develop and utilize metal hydrides in its tritium production facilities. Metal hydrides turned out to be ideally suited for tritium handling and processing. Tritium is the radioactive form, or isotope, of hydrogen, produced for defense programs by SRS for over 40 years. Tritium behaves chemically very much like normal hydrogen, except that it is radioactive and decays over time to a form of helium. It should be noted that metal hydrides were used to process tritium at other Department of Energy sites prior to the 1980s. These typically involved using mostly

uranium for tritium storage. This material has many drawbacks compared to the materials developed by SRS. Uranium hydride materials require moderately high temperatures (~700 K) to remove the tritium, which leads to tritium permeating or escaping through walls of the container. In addition the pyrophoric or flammable nature of uranium led to many safety concerns with regards to its use at SRS [24].

Also in the mid 1990s, the tritium facilities became involved in several new projects. One of these was the Tritium Facility Modernization and Consolidation Project. The goal of this project, which is referred to as Tritium Consolidation, was to reduce the overall physical size of the tritium facilities and to upgrade and modernize its capabilities. Again, to achieve the project goals, new metal hydride applications were required. A new storage bed design was developed that eliminated the need for a forced heating and cooling system, thereby minimizing the size of the facility. Another process improvement was the introduction of another class of metal hydrides, often referred to as "getters". These materials have been developed to remove small amounts of impurities from gas streams. One of the major commercial uses is to provide extremely clean gas to the semiconductor industry. These getters are typically comprised of zirconium-based metal alloys.

1.5.3 Uranium and its Alloys

Conventionally, uranium is used as a storage material for radioactive tritium. This is because it can easily absorb tritium at ~0.1 MPa below 500 K to form UT_3, and tritides exhibits a dissociation pressure lower than 10-3 Pa for holding tritium tightly at room temperature and sufficiently high at about 700 K to release tritium easily. Along with that uranium has a wide plateau in the pressure-composition isotherms. Cordfunke [25] observed a single plateau in the pressure-concentration isotherm below 700 K which spans nearly the whole range of concentration of about 0-3 U/H. However, uranium disintegrates into fine powder because of the enormous volume expansion on hydrogenation. The powder is highly

pyrophoric [26,27] and has low heat conductivity, which makes it difficult to control the temperature, and has a high possibility of explosion and contamination. Such powdering property of uranium is the main drawback for tritium storage from the safety point of view.

Therefore, there is a need to improve the hydrogen storage properties of U. One of the ideas to realize this is by alloying U with other elements. The criteria used for alloying elements include material cost, radioactivity, stability to air, storage capacity, storage pressure, loading and unloading conditions, and helium retention. So far, the hydrogen absorption–desorption properties of several uranium compounds and alloys, such as U–Al, U–Mo, U–Cr, U–Ti, U_2Ti, U_2Zr, $UZr_{2.3}$, UCo, UNi_2, UNi_5, U_6Ni, U_6Mn, U_3Si, U_6NiPd, UXAl (X = Mn, Co, Ni, Fe) and $U(Al_xNi_{1-x})_2$, have been reported in the literature [28]. Among these alloys, only U_2Ti, U_2Zr and $UZr_{2.3}$ were reported to show a good durability to powdering and prevention of pyrophoricity on hydrogenation [29,30].

1.5.4 Zirconium and its Alloys

Zirconium is a good material for hydrogen storage as it can take maximum of two H atoms per Zr atom forming the hydride ZrH_2. But it also has a limitation. ZrH_2 requires high temperature for hydrogen dissociation (> 973 K) which is not desirable for its use as a hydrogen isotope storage material. As an alternate, the intermetallic ZrCo have been found to be suitable for the safe storage, supply and recovery of hydrogen isotopes in the ITER [3, 31-34] project. ZrCo intermetallic has good hydriding/dehydriding property which can serve as a substitution of uranium [35]. ZrCo absorbs hydrogen at room temperature to form the hydride with a maximum stoichiometry of $ZrCoH_3$. The hydrogen equilibrium pressure of ZrCo hydride is around 10^{-3} Pa at room temperature and ~10^5 Pa at 673 K [36]. Also, it is not pyrophoric and easy to handle as it is not a nuclear material [31, 33]. However, the major drawback of ZrCo is that its absorption-desorption cycle become poor on prolong thermal cycling which is due to the disproportionation of its hydride ($ZrCoH_x$ (x≤3)) into the stable

hydride phase ZrH_2 and the hydrogen non-absorbing phase $ZrCo_2$. The disproportionation reaction is as follows:

$$2ZrCoX_x \rightarrow ZrX_2 + ZrCo_2 + (x-1)X_2 \qquad \text{(X= H, D and T)} \qquad (1.11)$$

Since decomposition of ZrX_2 requires much higher temperature (> 973 K) than that of ZrCo-hydride, a significant amount of hydrogen gets trapped within the storage material. This results in reduction of hydrogen storage capacity of ZrCo, which is not desirable for its use in ITER. Hence, both uranium and ZrCo has its own advantages and disadvantages [37].

1.6 Role of computational study for tritium storage

Theoretical and computational techniques are very important in the field of hydrogen storage because: (i) it reduces the cost and time of experiments by reducing the trial and error (ii) as radioactivity is concerned with the tritium storage, a special experimental facility is required for the safe handling of materials; but there is no such requirement in computations of tritium related materials and (iii) also, computational techniques can be fruitful to sort out the disadvantages of uranium and zirconium based alloys by studying different binary and ternary alloys in shorter time and with less expense. Apart from these, a large variety of thermo-chemical and thermo-physical properties of metals, alloys and their hydrides can be calculated theoretically which can support the experimental findings. The enthalpy of hydrogenation reaction for most of the metals lies within the range -40 to -45 kJ/mol H_2. The computational techniques will be useful for the selection of ideal metal hydride by calculating the enthalpy of hydrogenation reaction. Another important aspect of hydrogen storage materials is diffusion of hydrogen in the metals or alloys. The diffusion path, mechanism, activation barrier and temperature dependent diffusion coefficient etc. are of prime importance for the gas-solid interacting systems. The investigation of diffusion phenomena may help to overcome the drawbacks related to hydrogen absorption-desorption process. The hydrogenation behavior changes with the change in dimension of the hydrogen storage

materials. Thus, it is also interesting to study how hydrogen interacts with the metals and alloys in the different dimensions like bulk, surface and nanoclusters. The objective of this present thesis is focused on both theoretical and experimental studies of U_2Ti and ZrCo alloys along with the hydrides ZrX_2, $ZrCoX_3$ (X= H, D and T). Moreover, the effect of dimensionality on the hydrogenation behaviour has been illustrated by calculating the electronic structures of ZrCo based hydrides in bulk, surface and nanoclusters. The interactions of hydrogen with ZrCo alloy have been studied in the different dimensions like bulk, surface and nanoclusters using DFT.

CHAPTER 2

Theoretical Approach

2.1 Introduction

Theoretical and computational techniques are now ubiquitous part of modern science. Now a days, Modeling and computer simulations are now days widely used in various disciplines e.g. engineering, physics, chemistry, bio sciences etc. Recent development of super computers and a wide variety of software packages made the computations easier. Computational methods are especially useful where there are constraints in performing experiments. Particularly, in the field of hydrogen isotope storage, where performing experiments with tritides requires specially designed, reliable and safe experimental facility as tritium is radioactive in nature. Theoretical modeling and computational methods have been found to be very much useful not only for investigating a wide range of properties but also for interpreting the crucial experimental data. Apart from this, it has become possible to perform computational calculations to design new materials with certain desired properties for hydrogen isotope storage. This chapter will provide a broad overview of different theories and computational methods used to calculate the fundamental as well as physico-chemical properties of materials. The purpose of this chapter is not to present mathematical description of different methods but to give emphasis on the philosophy behind those methods.

The properties of matter are governed by the electrons surrounding the atomic nuclei and their interactions with one another by forming chemical bonding. The ground-state properties of a material are completely determined by the electronic charge density n($\mathbf{r}$), viz. the real space distribution of electrons around the atoms. If one has access to this charge density then one can correctly predict almost all materials properties, like bulk modulus, magnetism, etc. These calculations are said to be the *ab initio* or *first principle* calculations, because they do not contain any input from experiment. The only required information is the species in the form of the constituent atoms and their approximate geometric positions. Most of the computational methods are based on theory of quantum mechanics. The properties of

atoms and molecules, molecular interactions and motions etc. are quantitatively described by the mathematical equations of quantum mechanics. The key equation in quantum mechanics is the Schrödinger equation. But, solving this equation for many electrons system is great challenging even after the availability of fast computing facility. To meet this challenge, scientists and engineers simplified the mathematical model, developed variety of computational techniques [38]. The great effort has also been put to save the computational time and lower the computational cost. In this chapter, the basic concepts of theoretical techniques for the study of metals, alloys and their hydrides are presented. More precisely, the foundations of density functional theory calculations and direct method lattice dynamics calculations are presented.

2.2 Time Independent Schrödinger Equation

The time-independent Schrödinger equation for a crystal is a partial differential equation that describes a system of atomic nuclei and their surrounding electrons [39].

$$H\Psi(r_1, r_2, \ldots, R_1, R_2, \ldots) = E\Psi(r_1, r_2, \ldots, R_1, R_2, \ldots) \tag{2.1}$$

where H, E, and Ψ are the Hamiltonian, the electronic energy, and the many-body wave function of the system, and $\mathbf{r}_i$ and $\mathbf{R}_i$ are the positions of the electrons and ions respectively (capital indices refer to the nuclei and small indices to the electrons). The Hamiltonian of the system is given by

$$H = \sum_i \frac{\hbar^2 \nabla_i^2}{2m_e} - \sum_i \frac{\hbar^2 \nabla_I^2}{2M_I} + \frac{1}{2}\sum_{i \neq j} \frac{e^2}{|r_i - r_j|} + \frac{1}{2}\sum_{i \neq j} \frac{Z_I Z_J e^2}{|R_I - R_J|} - \sum_{i \neq j} \frac{Z_I e^2}{|r_i - R_J|} \tag{2.2}$$

where M_I and Z_I are the atomic mass and charge of the nucleus, and e is the electron charge. In the Hamiltonian above, the first two terms correspond to the kinetic energy of the electrons (T_e) and nuclei (T_N) respectively. The third and forth terms indicate the Coulomb interaction between electrons (internal potential V_{int}) and nuclei (V_{II}), respectively, and the last term corresponds to the electrons-nuclei Coulomb interactions (external potential V_{ext}). For

simplicity, atomic units will be used in the following ($\hbar = m_e = e = 1$). So, the fundamental Hamiltonian can be written as

$$H = T_e + T_N + V_{int} + V_{II} + V_{ext} \tag{2.3}$$

There are several approximations in order to solve this quantum many-body problem. Some of them are briefly explained in the following.

2.3 Born-Oppenheimer Approximation

The Born-Oppenheimer approximation [40] is an approach to simplify the Schrödinger equation of the coupled nucleus-electron system. It is based on the fact that the mass of a nucleus is almost infinity comparing to the mass of an electron and the velocity of a nucleus is much less than that of an electron, so the kinetic energy of the nuclei can be ignored in the Hamiltonian. Therefore, electrons are moving in the array of fixed nuclei with a constant potential energy (V_{II}), and the total electronic Hamiltonian becomes

$$H_{tot} = T_e + V_{int} + V_{II} + V_{ext} \tag{2.4}$$

$$H_{elec}\Psi_{elec}(r_1, r_2, \dots) = E_{elec}\Psi_{elec}(r_1, r_2, \dots) \tag{2.5}$$

In this approximation, the nuclear positions enter as parameters (this means that for different coordinates of the nuclei, the electronic wave function changes, which is the only dependence of this function on the nuclear coordinates) in the electronic wave function, so the electronic Hamiltonian and the corresponding Schrödinger equation are

$$H_{elec} = T_e + V_{int} + V_{ext} \tag{2.6}$$

We omit explicitly the parametric dependence of Ψ_{elec} on $\mathbf{R}_I$. The total energy E_{tot} is then the sum of E_{elec} and the constant nuclear repulsion term E_{nuc} which comes from the constant potential energy V_{II}

$$E_{tot} = E_{elec} + E_{nuc} \tag{2.7}$$

2.4 The Hartree and Hartree-Fock Approximation

In order to simplify Eq. 2.2, we introduce the Hartree approximation which we can solve somewhat easily [41]. In Eq. 2.2, the potential which a certain electrons feel depends on the location of all the other electrons. However, this potential can be approximated by an average single-particle potential

$$V_d(r_i) = e^2 \sum_{j \neq i} n_j \frac{[\Psi_j(r_j)]^2}{|r_i - r_j|} \qquad (2.8)$$

where n_j are the orbital occupation numbers and $\Psi_j(r_j)$ is a single-particle wave equation, *i.e.*, a solution to the one-particle wave-equation:

$$\left[-\frac{\hbar^2}{2m} \Delta^2 + V_{ext} + V_d(r_i) \right] \Psi_i r_i = \epsilon_i \Psi_i(r_i) \qquad (2.9)$$

with this simplification the set of equations now becomes separable. However, the equations are still non-linear and have to be solved self consistently by iteration. According to the Pauli exclusive principle, two electrons can not be in the same quantum state. However, the wave function in Hartree theory

$$\Psi(r_1\sigma_1, r_2\sigma_2, \dots, r_N\sigma_N) = \prod_i^N \Psi_i(r_i, \sigma_i) \qquad (2.10)$$

is not antisymmetric under the interchange of electron coordinates and accordingly does not follow the Pauli principle. Furthermore, the Hartree approximation fails to represent how the configuration of the N-1 electrons affects the remaining electrons. This defect has been rectified by Hartree-Fock theory.

The Hartree wave function neglects an important property of electrons. It neglects the fact that electrons are Fermi particles, and their wave functions must be antisymmetric with respect to interchanging any pair of particles

$$\Psi(r_1, \dots r_k, \dots r_m, \dots r_n) = -\Psi(r_1, \dots r_k, \dots r_m, \dots r_n) \qquad (2.11)$$

The Hartree wave function can be corrected by considering a linear combination of products, and the expression for Fermions can be written as a determinant. For an *n*-electron system, the Slater determinant is defined as [42]

$$\Psi(r_1, r_2, \dots r_n) = \frac{1}{\sqrt{n!}} \begin{vmatrix} \Phi_1 r_1 & \Phi_1 r_2 & \dots & \Phi_1 r_n \\ \Phi_2 r_1 & \Phi_2 r_2 & \dots & \Phi_2 r_n \\ . & . & & . \\ . & . & & . \\ . & . & & . \\ \Phi_n r_1 & \Phi_n r_2 & \dots & \Phi_n r_n \end{vmatrix} \tag{2.12}$$

each line of the determinant corresponds to a certain one-electron state, and each column to a certain position in space. The wave function changes sign when two particles (here two rows or columns of the determinant) interchange. Furthermore, if two rows or columns are identical then the determinant equals zero, which means that such a situation (two identical particles occupying the same spatial coordinates) is not physically possible.

Using the Slater determinant and the variational principle, the Hartree-Fock equation can be derived as

$$[-\frac{\Delta^2}{2} - \sum_I \frac{Z_I}{|r_i - R_J|} + \sum_I \int dr_j \Phi_j^*(r_j) \frac{1}{|r_i - r_j|} \Phi_j(r_j)]\Phi_i(r_i) -$$

$$\sum_j \int dr_j \Phi_j^*(r_j) \frac{1}{|r_i - r_j|} \Phi_i(r_j)]\Phi_j(r_i) = \epsilon_i \Phi_i^*(r_i) \tag{2.13}$$

This equation has an extra term compared to the Hartree equation. This term is called the exchange potential, since it comes from considering a constraint related to the exchange of particles. The exchange term also cancels an unphysical self-interaction of electrons in the Hartree equation.

2.5 Density Functional Theory

From the Born-Oppenheimer approximation, it follows that it is enough to solve the many-electron Schrödinger equation. The Hartree-Fock approach changes the many-body interacting problem to an independent one electron problem that can be solved. It also accounts for the anti-symmetric nature of the wave function through the exchange term.

The exact energy of a system is very hard to achieve from the exact wave function. A very important term has been introduced to reach the exact energy. The difference between exact energy and Hartree energy is called the correlation energy. Several methodologies such as the Moller-Plesset (MP) perturbation theory [43], the configuration interaction (CI) [44] approach, or the coupled cluster (CC) [45] method, were developed to include this effect. Density functional theory has been found to be efficient to solve this problem of finding quantum mechanical solution of the many-body schrödinger equation.

Hohenberg and Kohn provided the basis for DFT in 1964 and proved that all electronic properties of the system could be uniquely defined by its ground state probability density. This provided an alternative to the wave functions. However, the theorems didn't provide a practical scheme to calculate the ground state properties from electron density. The modification was provided by Kohn and Sham (1965) who reformulated the problem of calculating the total electronic energy E as a functional of the electron density ρ(r) to that of solving a set of single-particle Schrödinger like equations.

Thus,

$$E[\rho] = T[\rho] + \int \rho(\vec{r}) v_{ext}(\vec{r}) d\vec{r} + \frac{1}{2} u(\vec{r}) d\vec{r} + E_{xc}(\rho) \tag{2.14}$$

$T(\rho)$, v_{ext} and u are kinetic energy, external potential and inter electronic repulsion, respectively. E_{xc} is the exchange correlation functional which includes everything not contained in other terms. There are several approximations to calculate the correlation functional such as local density approximation (LDA), generalized gradient approximation (GGA) amongst several others. In LDA the spatial variations in density are ignored and potential at any point is calculated as that for a homogeneous electron gas with the density at that point. In GGA, the exchange and correlation energies are dependent not only on the electron density, but also on the derivatives of electron density. Recently, several hybrid

approaches have been developed that allow even more accurate calculation of energies and structures.

An extensive study by *ab initio* DFT calculations would allow us to develop a complete picture of the electronic structure of metals, alloys and their hydrides by (i) calculating the lattice parameter of the crystal structure, (ii) the systematic search for the thermodynamically stable phases of compounds by calculating the enthalpy of formation (iii) electronic partial and total density of state (DOS) and band structure calculations of alloys and their hydrides.

2.5.1 Hohenberg-Kohn Theorem

The approach of Hohenberg and Kohn is to formulate density functional theory as an *exact theory of many-body systems* [46]. The formulation applies to any system interacting particles in an external potential $v_{ext}(r)$, including any problem of electrons and fixed nuclei, where the Hamiltonian can be written as:

$$\hat{H} = -\frac{h^2}{2m_e}\sum_i \nabla_i^2 + \sum_i v_{ext}(r_i) + \frac{1}{2}\sum_{i \neq j}\frac{e^2}{|r_i - r_j|} = \hat{T} + \hat{V} + \hat{U} \tag{2.15}$$

The first theorem of Hohenberg-Kohn theorem is that *for any system of interacting particles in an external potential $V_{ext}(\mathbf{r})$ the potential $V_{ext}(\mathbf{r})$ is determined uniquely, except for a constant, by the ground state density $n_0(\mathbf{r})$.*

The second theorem of the Hohenberg-Kohn theorem is that *A universal functional for the energy E[n] in terms of the density n(\mathbf{r}) can be defined, valid for any external potential $V_{ext}(\mathbf{r})$. The exact ground state energy of the system is the global minimum of this functional and the density that minimizes the functional is the exact ground state density n0(\mathbf{r}).*

From this theorem, the total energy functional can written as

$$E_v[\rho] = \int v_{ext}(r)\rho(r)dr + F_{HK}(\rho) \tag{2.16}$$

Where $F_{HK}[\rho]$ is universal functional by construction since the kinetic energy and interaction energy of the particles are functionals only of the density and is defined as

$$F_{HK}(\rho) = (\psi, (\mathrm{T} + \mathrm{U})\psi) \tag{2.17}$$

$$T \equiv \frac{1}{2}\int \nabla\psi^*(r)\nabla\psi(r)dr \tag{2.18}$$

$$U \equiv \frac{1}{2}\int \frac{1}{|r-r^1|}\psi^*(r)\psi^*(r^1)\psi(r)\psi(r^1)drdr^1 \tag{2.19}$$

It follows that if the functional $F_{HK}[\rho]$ is known, then by minimizing the total energy of the system with respect to variations in the density function $\rho(r)$, one would find the exact ground state density and energy. This means that the energy functional equals the ground-state energy for the correct $\rho(r)$, and has a minimum, given that the number of particles of the system $N[\rho] \equiv \int \rho(r)dr$ is kept constant.

2.5.2 Self Consistent Kohn-Sham Equation

The Kohn-Sham approach (1965) is to replace the difficult interacting many body system obeying the Hamiltonian with a different auxiliary system that can be solved more easily [47]. The *ansatz* of the Kohn and Sham assumes that the ground state density of the original interacting system is equal to that of some chosen non-interacting system. This leads to independent particles for the non-interacting system that can be solved with all the difficult many-body terms incorporated into an exchange-correlation functional of the density as shown in Equation (2.20).

The set of wave functions $\psi_i(r)$ that minimize the Kohn-Sham total energy functional are given by the self-consistent solutions to the Kohn-Sham shown in (2.20) and (3.21).

$$[-\frac{\hbar^2}{2m}\nabla^2 + V_{eff}]\psi_i(r) = \epsilon_i\psi_i(r) \tag{2.20}$$

$$V_{eff} = V_{ext} + V_H + V_{xc} \tag{2.21}$$

where ε_i are the eigenvalues, $\psi_i(r)$ are the Khon-Sham orbitals and V_{eff} is the effective potential, V_H is the Hartree potential given by Equation (2.22)

$$V_H = \int \frac{\rho(r')}{|r-r'|}dr' \tag{2.22}$$

The V_{xc}, the exchange-correlation potential is the derivative of exchange-corelation energy functional with respect to the ground state density, given by Equation (2.23)

$$V_{xc}(r) = \frac{\delta E_{xc}[\rho(r)]}{\delta \rho(r)} \tag{2.23}$$

By construction, the exact ground-state density, $\rho(r)$, of an N-electron system is given by

$$\rho(r) = \sum_i |\psi_i(r)|^2 \tag{2.24}$$

As can be seen, by solving the equations one can finds the ground state density and energy of original interacting system with the accuracy limited only by the approximations in the exchange-correlation functional. If the exchange-correlation potential defined in Equation (2.23) is known, the exact ground-state density and energy of the many-body electron problem can be found by solving the single-particle Kohn-Sham equation.

2.5.3 Exchange and Correlations Functional Approximations

While the KS method provides an exact expression for the total energy, unfortunately it is still not possible to solve the KS equations, since the XC functional is not known. In this section, some approximate expressions for this functional are briefly presented.

The simplest approximation for the exchange-correlation energy is the Local Density Approximation (LDA). The basic idea of this approximation stems from a uniform electron gas. In this approximation it is assumed that the local XC energy per particle depends on the local density, and is equal to the XC energy per particle of a homogeneous electron gas (with the same density), in a neutralizing positive background. Thus the exchange-correlation energy E_{XC} is written in the following form

$$E_{xc}^{LDA} = \int \varepsilon_{xc} (\rho(r))\rho(r)dr \tag{2.25}$$

where $_{XC}(\rho(\mathbf{r}))$ is the exchange-correlation energy per particle of a uniform electron gas of density $\rho(\mathbf{r})$. Therefore E_{XC} only depends upon the value of the electronic density at each point in space (local density). The quantity $_{XC}(\rho(\mathbf{r}))$ can be further linearly decomposed into exchange and correlation contributions

$$\epsilon_{XC}(\rho(r)) = \epsilon_X(\rho(r)) + \epsilon_C(\rho(r)) \tag{2.26}$$

where the exchange part ϵ_X, represents the exchange energy of an electron in a uniform electron gas of a particular density and is given by [48].

$$\epsilon_X = -\frac{3}{4}\left(\frac{3\rho(r)}{\pi}\right)^{1/3} \tag{2.27}$$

Since there is no explicit expression for the correlation part ϵ_C, several approaches have been proposed. For example, Ceperly and Alder in 1980 used accurate numerical quantum Monte-Carlo simulations of the homogeneous electron gas to find a numerical solution for ϵ_C or Perdew and Wang who presented another accurate approximation for ϵ_C in 1992 [49].

The LDA is based on the local nature of the exchange-correlation potential and on the assumption that the density distribution does not vary too rapidly [47]. The accuracy of this simple approximation is surprisingly good and mostly leads to a correct picture of binding trends, structural parameters, bond lengths, vibrational energies, phonon spectra and other properties across the periodic table. However this method usually underestimates the band gap, and also overestimates the binding energy and underestimates the bond lengths [50]. This moderate accuracy that LDA delivers is insufficient for many applications.

The generalized gradient approximation (GGAs) for the exchange-correlation energy improves in general upon the local density description (LDA) of atoms, molecules, and solids. It goes beyond LDA by using not only the information about the density at a particular point ($\nabla\rho(r)$), but also by using the density in the local neighborhood by including the dependence on the gradient ($\nabla\rho(r)$). Within this approximation, the non-homogeneity of the true electron density is taken into account. So the XC energy is written as follows

$$E_{xc}^{GGA}(\rho) = \int \varepsilon_{xc}\left(\rho(r), \nabla\rho(r)\right)\rho(r)dr \tag{2.28}$$

In principle GGA method provides a better result for bond lengths, binding energies, band gap etc. than LDA, but in practice it has also some shortcomings.

Several studies have been made on comparing the advantages or disadvantages of the LDA versus GGA method [51]. For example, the lattice constants calculated using LDA are in general 2% smaller than the experimental ones, while GGA matches in most cases quite well or slightly overestimates the experimental values. This overestimation can lead to an underestimation of the bond strengths, in contrast to experiments and LDA.

There are many forms of GGA functionals that are used in different calculations. It is possible to construct a GGA, free of empirical parameters and starting from physical principles, e.g. the Perdew-Burke-Ernzerhof (PBE)-GGA form [52], while Becke exchange and Lee-Yang-Parr (LYP) correlation (BLYP) use parameters that are fitted to experimental data. Hybrid functionals are a group of approximations to the exchange–correlation energy functional in density functional theory that incorporate a portion of exact exchange from Hartree–Fock theory with exchange and correlation from other sources (either *ab initio* or empirical). The exact exchange energy functional is expressed in terms of the Kohn–Sham orbitals rather than the density, so is termed an implicit density functional. One of the most commonly used versions is B3LYP, which stands for Becke, 3-parameter, Lee-Yang-Parr. There are several hybrid functional like PBE0, HSE, HSE06, Meta GGA etc. that can be used in different calculations to get improved results.

2.6 Periodicity of the Crystal

In order to apply DFT to a real crystal, the KS equations should be solved for all the particles present in the system. Since there are too many particles in a real solid (roughly 1024 electrons and ions per cm^3), this will be computationally impossible. Therefore one should look for other possible approximations to solve the problem. Crystal structures are built up from a unit cell which is periodically repeated. To reduce the number of particles in a calculation, it is enough to consider only the unit cell of the crystal. It consists of atoms, whose arrangement defines the crystal's symmetry, and its repetition in three dimensions in

space generates a crystal structure. The unit cell is characterized by lattice parameters. To predict the property of a crystal it is enough to solve the KS equation for a small unit cell of a real solid.

2.6.1 The Bloch Theorem

Consider the Hamiltonian for a single particle in a potential $U(r)$

$$H = -\frac{\Delta^2}{2} + U(r) \tag{2.29}$$

According to the Bloch theory, the electrons move in a periodic potential $U(\mathbf{r})$ instead of moving in free space. This potential is generated by the periodic structure of the solid and is translational invariant.

$$U(r + R) = U(r) \tag{2.30}$$

for all lattice vectors $\mathbf{R}$ of the crystal. Bloch's theorem states that the eigenstates Φ of this Hamiltonian can be written as

$$\Phi_{nk}(r) = e^{ik.r}u_{nk}(r) \tag{2.31}$$

where it has the form of a plane wave times a function unk with periodicity of the lattice. $\mathbf{k}$ is the wave vector that is chosen in the first Brillouin zone due to the translational symmetry, n is the band index which labels different solutions for a given $\mathbf{k}$, and $u_{n\mathbf{k}}(\mathbf{r} + \mathbf{R}) = u_{n\mathbf{k}}(\mathbf{r})$ for all $\mathbf{R}$ in the crystal. Bloch's theorem is also written in another equivalent form

$$\Phi_{nk}(r + R) = e^{ik.R}\Phi_{nk}(r) \tag{2.32}$$

If $E_n(\mathbf{K})$ is an energy eigenvalue, then $E_n(\mathbf{k+G})$ is also an eigenvalue for all vectors G of the reciprocal lattice.

According to Bloch's theorem the problem of infinitely many-electrons has been turned into a problem of infinitely many k-points inside the first Brillouin zone. Since the wave functions of closely located k-points are almost identical, a small region can be sampled by one single k-point. In general it is enough to solve the K-S equation, using only a finite number of k-points, in a unit cell of the crystal and calculate the electronic part of the total

energy, to a good approximation. So choosing a sufficiently dense mesh of integration points is crucial for the convergence of the results. There are several methods for sampling the Brillouin zone with an appropriate set of k-points, such as the scheme proposed by Monkhorst and Pack in 1976 [53].

2.6.2 Energy Cut-off

The periodic functions $u_{n\mathbf{k}}$ can be expanded in plane waves

$$u_{nk}(r) = \Sigma_G \, C_{nk},_G e^{iG.r} \tag{2.33}$$

where the summation is over all reciprocal lattice vectors **G**. So the KS wave functions at each k-point are now expressed in terms of an infinite discrete plane wave basis set

$$\varphi_{nK}(r) = \Sigma_G \, C_{nK},_G e^{i(k+G).r} \tag{2.34}$$

Since it is not possible to consider an infinite basis set, the number of plane waves can be restricted by placing an upper boundary to the kinetic energy $(\mathbf{k} + \mathbf{G})2/2$ of the plane waves. This boundary is called the energy cut-off *Ecut* and the restriction is thus given by

$$|\mathbf{k} + \mathbf{G}|22 < Ecut \tag{2.35}$$

2.7 Solving Self consistent Kohn-Sham Equation

In Equation (7) the effective potential depends on the electron density $\rho(r)$, which depends on the Kohn-Sham orbitals $\psi_i(r)$, which are being searched. It means that the Kohn-Sham have to be solved iteratively until a self-consistent solution being reached. The schematic diagram is shown in Fig. 1.
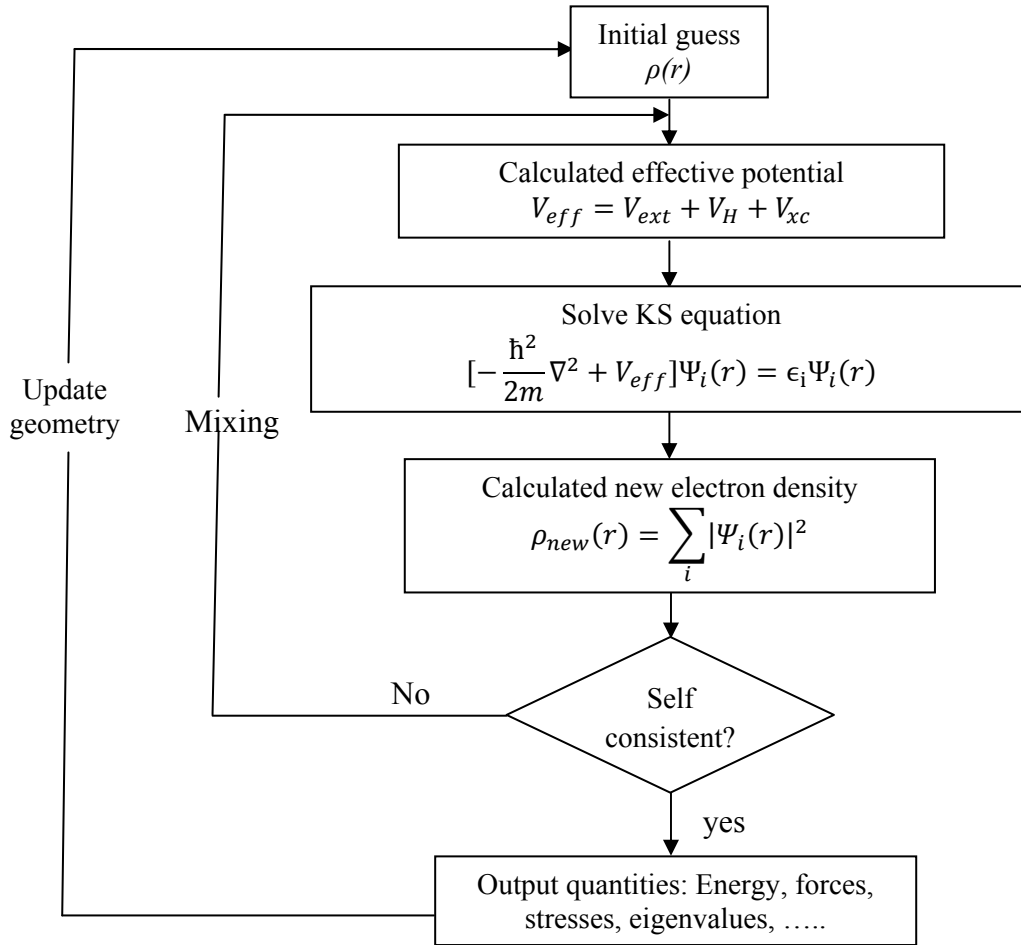
Fig. 2.1: Schematic representation of the self-consistent loop for solution of Kohn-Sham equation

2.7.1 Basis Set for Solution

For a solid state system, the effective potential in the Kohn-Sham Equation (3.20) has the periodicity of the crystalline lattice. Therefore, the Kohn-Sham orbitals, $\psi_k^n(r),$ can be written as a product of a function $u_k^n(r)$ that has the periodicity of the crystal lattice and a plane wave $e^{ik.r}$ with k being any wave vector in the first Brillouin zone, i.e.

$$\psi_k^n(r) = u_k^n(r)e^{ik.r} \tag{2.36}$$

According to the Bloch theorem, a plane wave basis set is used, the periodic function in Equation (2.36) can be written as a sum over plane waves that have the same periodicity as it. Such plane waves are those ones corresponding to reciprocal lattice vectors. Thus, the expansion of $\psi_k^n(r)$ in this basis set is

$$\psi_k^n(r) = \frac{1}{\Omega_{cell}}\sum_j C_j^n(k)e^{i(k+K_j).r} \tag{2.37}$$

Where Ω_{cell} is the volume of the primitive cell, K_j are the reciprocal lattice vectors and the parameter n is called band index. It should be pointed out that this basis set is k dependent, i.e. the eigenstates $\psi_k^n(r)$ corresponding to different k vectors are represented by different basis sets. The plane wave basis set can be truncated by setting all K_j with $K \leq K_{max}$. This means that all reciprocal lattice vectors that are inside a sphere with radius K_{max} are taken into the basis set. It is more common to specify the free electron energy corresponding to K_{max}, which is called cut-off energy

$$E_{cut} = \frac{\hbar^2 K_{max}^2}{2m} \tag{2.38}$$

However the basis set will still be intractably large for systems that contain both valence and core electrons. If we look at the radial part of a conduction electron wavefunction, we see that close to the atom core it displays a nodal behavior, while further away from the core; the wavefunction is smooth and vary as plane waves. The nodal behavior ensures orthogonality of the wavefunctions. Because the radial wavefunctions vary intensely with the smallest radii, many plane waves are required to describe this part of the wavefunction, while much lesser

number plane waves are required for the outermost parts. A smart way to reduce the number of plane waves needed is the use of pseudopotentials.

2.7.2 Pseudopotentials and Ultra-soft Pseudo Potential

In the previous section, many plane waves are needed to describe the nodal behavior close to the core region of the radial wavefunction of a conduction electron. If we treat the conduction electrons in the interstitial regions as plane waves, the energy must depend on the wavevector approximately as $\varepsilon_{\vec{k}} = \frac{\hbar^2 k^2}{2m}$ as for free electrons. Using the Hamilton operator, one can calculate the energy of an orbital at any point in space. This means that in the interstitial regions, this energy will be close to the above free electron energy. The wavefunctions' behavior close to the core does not affect the dependency of ε on *k* much, or in other words; the outer regions are mainly responsible for the chemical reactions. This leads to the idea of replacing the core potential with a .pseudopotential that gives the same wavefunctions outside the core, but simpler ones inside the core. This is why the pseudopotential best fits the outer side and nearly zero fits inside the core. An example of pseudopotential is shown in Fig. 2.2.
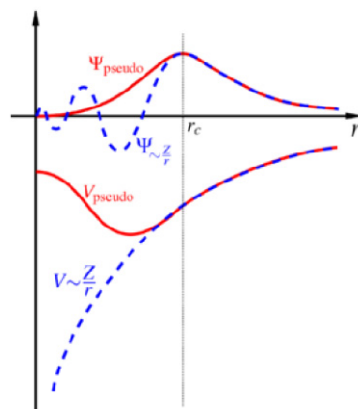
Fig. 2.2: Illustration of the real and pseudo wave-function and potential

Pseudopotential can be soft or hard. A soft pseudopotential include only the outermost electrons and requires only a few plane waves. A hard pseudopotential includes some of the

core electrons and requires hence more plane waves. Some pseudopotential is called ultrasoft, as very small number of plane waves needed to describe them [54]. Although the norm-conservaing pseudopotentials can be used in many general solid state calculations, their application is limited for systems containing first-row and transition–metal elements. The difficulty lies in the inefficiency to represent the highly localized p and d orbitals which are already nodeless. The pseudo wave function can be made softer by pushing the cutoff radius outward, but the norm-conserving constraint leaves little room for any significant improvement in the procedure.

2.7.3 Planewave Pseudopotential Method

The plane wave pseudopotential (PP) approach is used to replace the atomic all-electron potential such that the core states are eliminated. It is based on the fact that most physical properties of solids only depend on the valence electrons and one can distinguish between the core and valence electrons.

In this approximation, the core (i.e. non-valence) electrons are removed and the strong ionic potential is replaced by the weaker pseudopotential V_{pseudo} in the Schrödinger equation, that acts on a set of pseudo wave functions Ψ_{pseudo}. This approach was first introduced by Hans Hellmann in 1934 [55]. These pseudo functions are constructed in such a way that the pseudo wave function and the true wave function become identical beyond a certain radius (cut-off radius rc). As it is shown schematically in Fig. 3.2, the pseudo wave function is generated so that it has no radial nodes in the core region.

2.7.4 Projector Augmented Planewave Method

The projector augmented wave method (PAW) is an alternative which has been introduced by Blöchl in 1994 [56]. This approach is in between the all-electron and pseudopotential method. The projector augmented wave (PAW) method is a general approach to solution of the electronic structure problem that reformulates the orthogonalized plane waves (OPW),

adapting it to modern techniques for calculations of total energy, forces and stresses. Like the ultrasoft pseudopotential method, it introduces projectors and auxiliary functions. The PAW approach also defines a functional for the total energy that involves auxiliary functions and it uses advances in algorithms for efficient solution of the generalized eigenvalue problem. The PAW method is an all-electron frozen core method, which combines the features of both the ultra-soft pseudopotentials and linear augmented plane wave (LAPW) methods. It allows an easier treatment of first-row and transition metal elements, and provides access to the full wave function. In real materials, the wave function is fairly smooth in the bonding region, whereas it varies rapidly near the nucleus due to the large attractive potential. This is the main difficulty for electronic structure methods to describe the bonding region with accuracy as well as account for the large variations in the atomic core. The augmented-wave methods deal with this problem by dividing the wave function into two parts, i.e., a partial-wave expansion within an atom centered sphere and envelope functions outside the spheres. The value and derivative of the two parts are then matched at the sphere radius.

In the PAW method, one can define a smooth part of valence wavefunction $\tilde{\psi}_i^v(r)$ or an atomic orbital and a linear transformation $\psi^v = \tau \tilde{\psi}^v$ that relates the set of all electron valence functions $\tilde{\psi}_j^v(r)$ to the smooth functions $\tilde{\psi}_i^v(r)$. The transformation is assumed to be unity except with a sphere centered on the nucleus, $\tau = 1 + \tau_0$. For simplicity, we omit the superscript v, assuming that the ψs are valence states, and the labels i, j. Using the Dirac notation, the expansion of each smooth function $|\tilde{\psi}\rangle$ in partial waves m within each sphere can be written Equation (2.39),

$$|\tilde{\psi}\rangle = \sum_m C_m |\tilde{\psi}_m\rangle \qquad (2.39)$$

with the corresponding all-electron function,

$$|\psi\rangle = \tau|\tilde{\psi}\rangle = \sum_m C_m |\psi_m\rangle \qquad (2.40)$$

Hence the full wave function in all space can be written

$$|\psi\rangle = |\tilde{\psi}\rangle + \sum_m C_m\{|\psi_m\rangle - |\tilde{\psi}_m\rangle\} \tag{2.41}$$

If the transformation τ is required to be linear, then the coefficient must be given by a projection in each sphere

$$c_m = \langle \tilde{p}_m | \tilde{\psi}\rangle \pi r^2 \tag{2.42}$$

for some set of projection operators $\tilde{p}$. If the projection operators satisfy the iorthogonality condition,

$$\langle \tilde{p}_m | \tilde{\psi}_{m'}\rangle = \delta_{mm'} \tag{2.43}$$

Then the one-center expansion $\sum \;\; |\tilde{\psi}_m\rangle\langle\tilde{p}_m|\tilde{\psi}\rangle$ of the smooth function $\tilde{\psi}$ equals $\tilde{\psi}$ itself.

The requirement that the transformation in Equation (2.39) is linear leads to the following form for the operator τ

$$\tau = + \sum_m\{|\psi_m\rangle - |\tilde{\psi}_m\rangle\}\langle\tilde{p}_m| \tag{2.44}$$

Furthermore, the expressions apply equally well to core and valence states so that one can derive all-electron results by applying the expressions to all the electron states. The general form of PAW s can be cast in terms of transformation by Equation (26). For any operator $\hat{A}$ in the original all-electron problem, one can introduce a transformed operator $\hat{A}$ that operates on the smooth part of the wavefunctions

$$\tilde{A} = \tau'\hat{A}\tau = \hat{A} + \sum_{mm'} |\tilde{p}_m\rangle\{\langle\psi_m|\hat{A}|\psi_{m'}\rangle - \langle\tilde{\psi}_m|\hat{A}|\tilde{\psi}_{m'}\rangle\}\langle\tilde{p}_{m'}| \tag{2.45}$$

One acan add an operator of the form in the right hand side

$$\hat{B} - \sum_{mm'} |\tilde{p}_m\rangle\langle\tilde{\psi}_m|\hat{B}|\tilde{\psi}_{m'}\rangle\langle\tilde{p}_{m'}| \tag{2.46}$$

with no change in the expectation values. For example, one can remove Coulomb singularity for the smooth function, leaving a term that can be dealt with in the radial about each nucleolus. Now the physical quantities can be obtained from Equations (2.44) and (2.45). For example, the charge density is given by Equation (2.47)

$$\rho(r) = \tilde{\rho}(r) + \rho^1(r) - \tilde{\rho}^1(r) \tag{2.47}$$

which can be written in terms of eigenstates labeled I with occupancy f_i as

$$\tilde{\rho}(r) = \sum_i f_i \left| \tilde{\psi}_i(r) \right|^2 \tag{2.48}$$

$$\rho^1(r) = \sum_i f_i \sum_{mm'} \langle \tilde{\psi}_i | \tilde{\psi}_m \rangle \psi_m^*(r) \psi_{m'}(r) \langle \tilde{\psi}_{m'} | \tilde{\psi}_i \rangle \tag{2.49}$$

and

$$\tilde{\rho}^1(r) = \sum_i f_i \sum_{mm'} \langle \tilde{\psi}_i | \tilde{\psi}_m \rangle \tilde{\psi}_m^*(r) \tilde{\psi}_{m'}(r) \langle \tilde{\psi}_{m'} | \tilde{\psi}_i \rangle \tag{2.50}$$

Similarly, the energy functional can be written as

$$E = \tilde{E} + E^1 - \tilde{E}^1 \tag{2.51}$$

The last two terms $\rho^1(r)$ and $\tilde{\rho}^1(r)$ are localized around each atom and the integrals can be done in spherical co-ordinates with no problems from the string variables near the nucleus. They contain contributions from the core and smooth core states, respectively. In practice, the smooth core density is constructed instead of constructing a smooth core state for each core state individually unless one is interested in the physical properties that are related to the core states.

2.8 Software Packages

2.8.1 The Vienna Ab-initio Simulation Package (VASP)

The Vienna *ab-initio* simulation package (VASP) is used to perform firstprinciples total-energy calculations within the density functional theory [57-59]. The VASP simulates the electronic and atomic structures of molecules and crystals. It uses ultrasoft pseudopotentials or the projector-augmented wave method and a plane wave basis set. The expression *ab initio* means that only first-principles are used in the simulations, no experimental data are needed. VASP has a large amount of settings and specifications in the database for tailoring the calculations for different systems. The inputs to the program are text-files of which the most important are: *INCAR*, *POSCAR*, *KPOINTS* and *POTCAR*. The *INCAR* file contains the basic instructions to VASP, such as which algorithm to use, what precision is required for the result, which way to relax the structure, (conjugate gradient, MD, etc.), energy cut-off for the plane waves, the *EXC* approximation and much more. In the

POSCAR file the size of the supercell is specified along with the positions of the atoms and, if relevant, initial velocities and constraints on movement. The *KPOINTS* file controls which *k*-point scheme to use and finally the *POTCAR* file contains the atomic mass and the ultrasoft pseudopotentials or PAW potentials for the relevant atoms and the chosen *EXC* approximation from the database.

2.8.2 Quantum Espresso

QUANTUM ESPRESSO is an integrated suite of computer codes for electronic-structure calculations and materials modeling, based on density-functional theory, plane waves, and pseudopotentials (norm-conserving, ultrasoft, and projector-augmented wave) [60]. The acronym ESPRESSO stands for opEn Source Package for Research in Electronic Structure, Simulation, and Optimization. It is freely available to researchers around the world under the terms of the GNU General Public License. QUANTUM ESPRESSO builds upon newly-restructured electronic-structure codes that have been developed and tested by some of the original authors of novel electronic-structure algorithms and applied in the last twenty years by some of the leading materials modeling groups worldwide. Innovation and efficiency are still its main focus, with special attention paid to massively parallel architectures, and a great effort being devoted to user friendliness. QUANTUM ESPRESSO is evolving towards a distribution of independent and interoperable codes in the spirit of an open-source project, where researchers active in the field of electronic-structure calculations are encouraged to participate in the project by contributing their own codes or by implementing their own ideas into existing codes.

2.8.3 PHONON

DFT is a non-empirical parameter method whose applications and predictive ability in different fields known for some time. But, the results we obtain from DFT are always at 0 K which may not be viable in practical applications. Hence combination of DFT with different

techniques such as linear response method or direct methods allows us to evaluate phonon dispersion curves without empirical parameters. In the direct method the forces are calculated *via* the Hellmann-Feynman theorem using DFT-derived total energies, assuming a finite range of interaction. The phonon spectra are then derived using Newton's equation of motion in lattice dynamics calculations.

For building the crystal the best is to use PHONON [61]. The supercell with a given space group can also be created using this. The supercell can be equal to the primitive unit cell of the crystal. Next, transfer the structural data (*POSCAR*) to an *ab initio* software, for example VASP, and minimize the system energy. The optimized lattice constants, and atomic positions are then reused by PHONON to create a large supercell, which will be used to calculate phonons spectra. Transfer the crystal data from PHONON to VASP program and optimize again the large supercell. Usually it is sufficient to optimize the atomic positions only (in VASP ISIF=2). One should quickly reach the minimum, since the input structural data correspond already to the minimum. In VASP create a new POSCAR with atomic positions where one atom is displaced. For each configuration with displaced atom calculate the Hellmann-Feynman forces from a single minimization run of electronic subsystem only (NSW=1). The Hellmann-Feynman forces are then collected to a single file. Then import the generated Hellmann-Feynman file to PHONON, and calculate phonon dispersion curves, density of states, etc to calculate the finite temperature thermodynamic properties.

2.9 Computational Details of Present Studies

2.9.1 *Ab-initio* Study of U_2Ti

All calculations were performed using density functional theory [47]. In particular, we have used the plane wave–pseudopotential method as implemented in the Vienna *ab initio* simulation package (VASP) [57-59]. The total energy calculation was carried out by including the spin-orbit coupling [62] term. The atomic pseudopotentials generated using the

projector-augmented wave (PAW) method [56] was employed for U and Ti. The valence electron configurations of U and Ti were set to $6s^2 6p^6 6d^1 5f^3 7s^2$, and $3d^3 4s^1$, respectively. The energy cut off for the plane wave basis set was fixed to 500 eV. The PAW pseudopotentials are an improvement over the Vanderbilt-type ultrasoft pseudopotentials [63], especially for transition metals, [64] since they combine the elegance and computational efficiency of plane waves with the chemically appealing concept of localized functions. Total energies for each relaxed structure using the linear tetrahedron method with Blöchl corrections were subsequently calculated in order to eliminate any broadening-related uncertainty in the energies [65]. Ground state atomic geometries were obtained by minimizing the Hellman–Feynman forces [66,67] using the conjugate gradient method. The generalized gradient approximation (GGA) of Perdew and Wang [49] was used to calculate the exchange-correlation energy functional. In order to verify the magnetic nature of the systems studied in this work, we have performed the total energy calculations using the spin polarized version of density functional theory. The results suggest that all these systems are non magnetic.

To begin with, we have calculated the total energies of a series of cell volumes above and below the experimental volume. In the next step we plot the total energies as a function of cell-volume, $E(V)$. The resultant parabolic curve [E-V] was then fitted using the Murnaghan equation of state [68] to determine the theoretical equilibrium volume and the single crystal bulk moduli at temperature $T = 0$ K. The same computational steps were followed for U_2Ti, U (bulk) and Ti (bulk), to ensure that systematic errors in the energy differences will be cancelled to the greatest extent possible. The total energies (E_{tot}) of α-U, Ti and U_2Ti emerging from the energy-volume graphs was used for calculating the enthalpy of formation of U_2Ti. In particular, the enthalpy of formation $\Delta_f H$ of U_2Ti is calculated as:

$$\Delta_f H \, (U_2Ti, \, 0 \, K) = E_{tot}(U_2Ti) - 2E_{tot}(U) - E_{tot}(Ti) \tag{2.52}$$

2.9.2 *Ab-initio* Study of ZrX$_2$ (X= H, D and T) compounds

All calculations were performed using the plane wave-pseudopotential method under the framework of density functional theory as implemented in the Vienna *ab-initio* simulation package (VASP) [57-59]. The electron-ion interaction and the exchange correlation energy were described using the projector-augmented wave (PAW) [61,64] method and the generalized gradient approximation (GGA) of Perdew-Burke-Ernzerhof (PBE) [52], respectively. The valence electron configuration of Zr and H were set to $5s^14d^3$ and $1s^1$, respectively. The energy cut off for the plane wave basis set was 500 eV for all calculations performed in this study. The ionic optimization was carried out using the conjugate gradient scheme and the forces on each ion were minimized upto 5meV/Å [66,67]. The k-point sampling in the Brillouin zone (BZ) was treated with the Monhorst-Pack scheme [53], using a 6x6x6 k-mesh. Total energies of each relaxed structure using the linear tetrahedron method with Blöchl corrections were subsequently calculated in order to eliminate any broadening-related uncertainty in the energies [65].

To begin with the lattice-dynamical calculations, the lattice parameters of ZrH$_2$ have been optimized using the VASP code. For the phonon calculations, the optimized structure of ZrH$_2$ has been used. The phonon frequencies of ZrH$_2$ and its isotopic analogues were calculated by the PHONON program using the forces based on the VASP package. The PHONON package calculates the phonon frequency by supercell calculation of forces on the atoms [61]. A 3x3x2 supercell of ZrH$_2$ containing total 108 atoms have been used for the phonon calculation. A small displacement of 0.02 Å was given to the atoms present in the supercell of ZrH$_2$. The phonon dispersion curve, phonon density of states and temperature dependent thermodynamic functions of the compounds under study are obtained by using the calculated phonon frequencies. The total energy of hydrogen molecule (H$_2$) was obtained by centering a single H$_2$ molecule inside a cubic box of dimension 12Å x 13Å x14Å, cutoff

energy 500 eV, and 1x1x1 *k*-point Monkhorst-Pack mesh. The box length and cutoff energy are sufficient to converge the energy without interaction effects from periodic images. A 0.01 Å displacement was given to the atom of X_2 (X= H, D, and T) molecule to compute the Hessian matrix and vibrational frequencies (ω) at the Γ point of the isotopic species in the same cubic box. The zero point energies ($1/2\hbar\omega$) were calculated for the isotopic species using the computed vibrational frequencies (ω).

The temperature-dependent thermodynamic functions of a crystal, such as the internal energy (*E*), entropy (*S*), Helmholtz free energy (*F*) and constant volume heat capacity (C_V) are calculated from their phonon density of states as a function of frequencies using the following formulas [85] within the harmonic approximation:

$$F = 3nNk_BT \int_0^{\omega max} \ln\left\{2\sinh\frac{\hbar\omega}{2k_BT}\right\} g(\omega)d\omega \tag{2.53}$$

$$E = 3nN\frac{\hbar}{2}\int_0^{\omega max} \omega \coth\left(\frac{\hbar\omega}{2k_BT}\right) g(\omega)d\omega \tag{2.54}$$

$$S = 3nNk_B \int_0^{\omega max} \left[\frac{\hbar\omega}{2k_BT}\coth\frac{\hbar\omega}{2k_BT} - \ln\left\{2\sinh\frac{\hbar\omega}{2k_BT}\right\}\right] g(\omega)d\omega \tag{2.55}$$

$$C_V = 3nNk_B \int_0^{\omega max} \left(\frac{\hbar\omega}{2k_BT}\right)^2 \csc h^2\left(\frac{\hbar\omega}{2k_BT}\right) g(\omega)\, d\omega \tag{2.56}$$

2.9.3 *Ab-initio* Study of ZrCo and ZrCoX$_3$ (X= H, D and T) Compounds

All the present calculations are performed using the plane wave-pseudopotential method under the framework of density functional theory as implemented in the Vienna *ab-initio* simulation package (VASP) [57-59]. The electron-ion interaction and the exchange correlation energy are described under the projector-augmented wave (PAW) [56,64] method and the generalized gradient approximation (GGA) of Perdew-Burke-Ernzerhof (PBE) [52], respectively. The valence electronic configuration of Zr, Co and H are set to $5s^14d^3$, $4s^13d^8$ and $1s^1$, respectively. The energy cut off for the plane wave basis set is fixed at 500 eV. The ionic optimization is carried out using the conjugate gradient scheme and the forces on each

ion was minimized upto 5meV/Å [66,67]. The k-point sampling in the Brillouin Zone (BZ) has been treated with the Monhorst-Pack scheme [53], using a 4x4x4 k-mesh. Total energies of each relaxed structure using the linear tetrahedron method with Blöchl corrections are subsequently calculated in order to eliminate any broadening-related uncertainty in the energies [65]. To begin with the dynamical calculations, the lattice parameters of ZrCo and ZrCoH$_3$ have been optimized using VASP code and the optimized structures are used for phonon calculation.

The phonon frequencies of ZrCo and ZrCoX$_3$ (X=H, D and T) are calculated by the PHONON program [61] using the forces based on the VASP package. A 3x3x3 supercell of ZrCo containing total 54 atoms and a 3x1x2 supercell of ZrCoX$_3$ (X=H, D and T) containing 120 atoms have been used for the phonon calculations. A small displacement of 0.02 Å have been given to the atoms present in the supercell of ZrCo and ZrCoX$_3$ (X=H, D and T) compounds. The phonon dispersion curves and temperature dependent thermodynamic functions of these compounds are obtained by using the calculated phonon frequencies. The temperature-dependent thermodynamic functions of a crystal, such as the internal energy (*E*), entropy (*S*), Helmholtz free energy (*F*) and constant volume heat capacity (*C$_V$*) can be calculated from their phonon density of states as a function of phonon frequencies which is already described in section 3.9.2. The elastic properties of ZrCo and its hydride ZrCoH$_3$ were also calculated using an efficient stress-strain method implemented in VASP.

2.9.4 First Principles of ZrCo Surface

All the calculations were performed using Quantum ESPRESSO software [60], a plane wave based implementation of density functional theory, to solve the Kohn-Sham equations. The electronic exchange and correlation energy was described by the generalized gradient approximation (GGA) based parameterizations of Perdew-Burke-Ernzerhof (PBE) [52]. Ultrasoft pseudopotentials were used to describe the electron-ion interactions [63]. A plane

wave basis set with kinetic energy cutoff 40 Ry, and charge density cutoff 400 Ry were used. Marzari-Vanderbilt smearing [70] with a smearing width of 0.005 Ry was used to speed up the convergence. The k-point sampling in the Brillouin zone (BZ) has been treated with Monkhorst-Pack scheme [53]. We obtained lattice parameter of 3.18 Å for bulk BCC ZrCo, with a converged 9x9x9 mesh. This is in very good agreement with the experimental value of 3.19 Å [71]

To investigate the interactions of hydrogen on ZrCo surface, we have used the density functional theory to compute the surface energy, hydrogen adsorption and bonding energies as well as activation energies for hydrogen atom diffusion on ZrCo surface and inside the bulk. Firstly, we have ensured that the ZrCo (110) surfaces used in the entire calculations are clean. The bulk-truncated surface is flat and has no rumpling. After relaxation, the Zr and Co atoms relax in the opposite direction and results a rumpled surface. The surface rumpling is given by $d_{rum} = \frac{\Delta Z}{Z_{1,2}}$, where $\Delta Z = Z_{Zr}^{(1)} - Z_{Co}^{(1)}$ refers to the spacing of Zr and Co atoms in the top layer. For the bulk truncated ZrCo (110) surface d_{rum} is zero. Whereas the d_{rum} for the relaxed surface is high at the topmost layer about 14% and for the second layer it is about -6%. The inter planar distances of the relaxed layer was calculated by taking the average distance of Zr and Co, which changes less than 1%.

The stability of the surfaces was determined by the surface energy. The surface energy has been calculated by performing the total energy calculations for a periodic slab representing the particular surface (h k l) as well as for a bulk system as a reference using the formula given below:

$$E_{surf} = \frac{1}{2A}[E_{slab}(n) - E_{bulk}(n)] \tag{2.57}$$

Where E_{surf} is the surface energy, A is the surface area, $E_{slab}(n)$ is the energy of a slab and $E_{bulk}(n)$ is the energy of bulk. To represent the ZrCo (110) surface we have taken a six layers slab. In order to achieve best compromise between the computational cost and the accuracy

of our calculations we have used 11Å vacuum between the slabs. All the atoms are allowed to relax except one atom in the middle layer to avoid the translational motion of the slab. The surface energy of ZrCo (110) surface calculated with our model is 1.46 Jm^{-2}. Calculation with an increased number of layers (eight layers) has also given the same value which suggests that six layer slab is a good model to represent the surface.

The climbing image nudge elastic band method (CI-NEB) [72] was used to find out the minimum energy path (MEP), energy barriers and transition states for hydrogen dissociation and diffusion on ZrCo (110) surface. Once the initial and final images of a diffusion path are known, intermediate images are determined by interpolating the initial and final configurations. According to the complexity of the NEB simulation we employed 7 to 17 images in the path. After finding the TS, the energy barrier of the diffusion process was determined from the energy difference between the TS and the initial stable configuration.

2.9.5 First Principles of ZrCo Clusters

All calculations were performed within the spin-polarized density functional theory using the plane wave-pseudopotential approach as implemented in the Vienna *ab-initio* simulation package (VASP) [57-59]. The electron-ion interaction and the exchange correlation energy were described under the projector-augmented wave (PAW) [56,64] method and the generalized gradient approximation (GGA) of Perdew-Burke-Ernzerhof (PBE) [52], respectively. The valence electronic configuration of Zr, Co and H were set to $4s^2 4p^6 5s^1 4d^3$, $4s^1 3d^8$ and $1s^1$, respectively. The energy cut off for the plane wave basis set was fixed at 500 eV. Finding the ground state structure of a cluster was a challenging task. For this, several methods like, GA, basin-hopping, evolutionary algorithms were used to generate a large number of geometries. However, for small clusters one can use chemical intuition, which in other words called as educated guess structure and relax these structures to the possible nearest minima. Following this, we generated a large number of initial

geometries. To obtain the equilibrium geometries, we employed a *cascade* genetic algorithm (GA) scheme as implemented in fhi-aims code [73] and detailed in Ref. 42 and 43, where the term *cascade* means a multi-stepped algorithm where successive steps employ higher level of theory and each of the next level takes information obtained from its immediate lower level. A typical *cascade* scheme normally starts from a classical force field and goes upto density functional theory using hybrid functional [74,75]. Here since the system is not so large, we have skipped the force field optimization part and started GA using density functional theory with semi-local functional. We have optimized the geometries using PBE with lower level settings (*i.e.* tight settings) and then on top of that optimized structure the energetics are calculated with HSE06 [76] using higher level settings (*i.e.* tight settings) A large number of spin states were also been considered for all these structures. The ionic optimization was carried out using the conjugate gradient scheme and the forces on each ion was minimized upto 5meV/Å [66,67]. A suitable simulation box was considered for all the calculations. The k-point sampling in the Brillouin zone (BZ) was treated with the Monhorst-Pack scheme [53], using Γ point. Total energies of each relaxed structure using the linear tetrahedron method with Blöchl corrections were subsequently calculated in order to eliminate any broadening-related uncertainty in the energies [65].

The binding energies (E_b) of Zr_mCo_n (m+n = 2, 4, 6 and 8) clusters and hydrogen adsorption energy (E_{ads}) for their hydrogenated species were estimated from the total energy calculations using equation (2.58) and (2.59), respectively

$$E_b\,(Zr_mCo_n) = \{E_{Zr_mCo_n} - m \cdot E_{Zr-atom} - n \cdot E_{Co-atom}\}/(m + n) \qquad (2.58)$$

$$E_{ads}\,(Zr_mCo_n - 2H) = \{E_{Zr_mCo_n-2H} - m \cdot E_{Zr-atom} - n \cdot E_{Co-atom} - 2 \cdot E_H\}/(m + n +$$

$$2) \qquad (2.59)$$

CHAPTER 3

Experimental Methods

3.1 Introduction

This chapter describes the basic principles of the instrumentation or techniques and their uses to carry out the experimental work performed during the present study. In the section 3.2, the basic principle of different apparatus used for sample preparation and annealing of as cast samples has been discussed. Then fundamentals of X ray diffraction (XRD), X ray Fluorescence (XRF) and Inductively Coupled Plasma Mass Spectrometry (ICPMS) characterization techniques for samples were summarized briefly in the section 3.3. This is followed by a short description of different types of calorimeter, their working principle; calibration and discussion on high temperature inverse drop calorimeter are given in section 3.4.

3.2 Sample Preparation

The alloy preparation is the first step for the investigation of thermodynamic parameters of a multi-component system. The purity of the starting materials is also very important as very small amount of impurities may affect significantly in the results. The alloy samples were prepared under high purity argon atmosphere in an arc melting furnace and induction furnace. A brief description of arc melting furnace and induction furnace is given to understand the whole process thoroughly.

3.2.1 Arc Melting Furnace

Electrical conductivity of gases is normally poor. However, if sufficient energy is supplied to the gas, its atoms / molecules ionized into charged particles. These charged particles then make it possible for the gas to become conductive. An intense stream of electrons from the cathode flows across the gas-filled gap to the anode. As a result, arc is initiated between the electrodes. The electric arc contains extremely high heat and brightness, ideal for welding and melting of metals. Temperatures in excess of 3000°C can be attained in such a furnace.
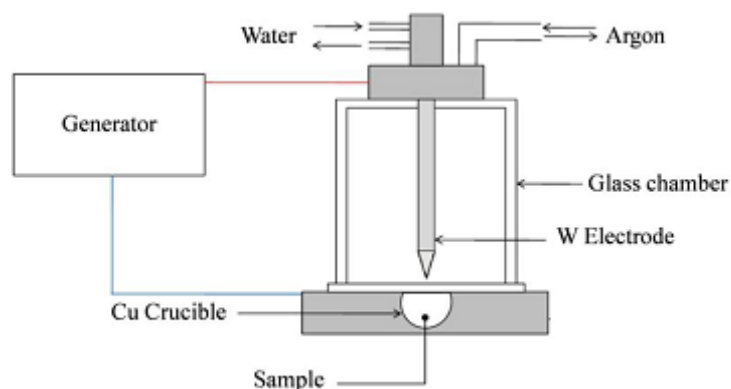
Fig. 3.1: Schematic of electric arc furnace

As illustrated in the Fig. 3.1, the electric arc furnace used during the present study consisted of a non-consumable tungsten electrode serving as a cathode and a water cooled copper hearth that acts as a sample holder and as a part of the anode [77]. For the alloy preparation, elements to be melted were placed in the copper hearth, chamber of the furnace was closed and a rotary vacuum pump was used to remove atmospheric gases. There were ports for inert gas inlet and outlet. The chamber was purged with high purity argon gas after required value of vacuum was achieved. The purging of argon in the chamber also made possible the movement of the tungsten electrode and striking of electric arc. The current of arc can be varied from 0 to 100%. To prevent the vapor loses of low melting component of alloy, very low current of about 5 to 10 A was supplied. The temperature of melt and evaporation loses of the low melting metal was achieved by controlling the current of the power supplied to generate the arc. Before melting the desired sample, a piece of Zirconium was melted by striking arc to remove any possible oxygen impurity from the chamber. Then the arc was struck on the materials to be melted under the continuous flow of argon gas. The tungsten electrode was moved around and over the alloy in order to obtain a uniform melt. The alloys obtained after melting were in the shape of buttons. The melted alloys should have a homogeneous composition because the macro-inhomogeneities, left during melting, are difficult to remove during subsequent annealing treatments. In order to achieve a homogeneous distribution of the constituent elements in the alloys, the alloys were flipped over and melted again and again. This process was repeated several times in order to achieve

maximum homogenization. The weight of each sample was measured before and after melting to keep a record of the weight losses during sample preparation. In most of the cases, the weight loss during melting was less than 1 %.

3.2.2. Homogenization Heat Treatment

Water cooling during arc melting results in stabilization of liquid state with some unwanted phases. It is like a water quenching. The annealing of these samples result in attaining equilibrium phases and growth of their crystal as well. It removes the concentration gradient, defects and the stresses that may appear during solidification due to segregation. Annealing treatment is necessary to obtain homogeneous equilibrium phase Annealing is a heat treatment where the material is taken to a high temperature, kept there for some time and then slowly cooled. During the process of annealing, homogenization of the samples is achieved through diffusion; therefore, annealing time and temperature are two important factors. Annealing is normally carried out at > 70% of the melting point as the diffusion rates of atoms are reasonable at such temperatures. High temperatures allow diffusion processes to occur fast.

3.2.3 Preparation of Alloy Sample

a) Preparation of U$_2$Ti alloy

U$_2$Ti phase was prepared by arc-melting method by taking stoichiometric mixtures of uranium and titanium metals. The ingots were arc melted six times to improve homogeneity. The cast ingots was wrapped in Ti foil and annealed in an evacuated sealed quartz tube at 850°C for 120 h and slowly cooled to room temperature. The annealed sample was cut into pieces of 4 mm x 2 mm x 1 mm using a diamond saw cutter for carrying out the calorimetric studies.

b) Preparation of ZrCo Alloy

$Zr_{0.5}Co_{0.5}(s)$ intermetallic was prepared by arc-melting technique. The stoichiometric mixtures of as received high purity zirconium (Sigma–Aldrich, purity 99.98% trace metal basis) and cobalt (Alfa Aesar, purity 99.95% metal basis) metals were used. The cast ingot was wrapped in a titanium foil and annealed in an evacuated sealed quartz tube at 973 K for 72 h and water quenched to room temperature. The annealed sample was cut into pieces of 4 mm x 2 mm x 1 mm using a diamond saw cutter for carrying out the calorimetric studies.

3.3 Material Characterization Techniques

After annealing, alloys compositions was characterized with the help of different characterization techniques. This section provides information about their working principle and uses.

3.3.1 X-ray Diffraction (XRD)

The X-ray diffraction (XRD) technique is used for characterization of different solid crystalline materials. It is a non destructive material characterization technique. The identification of phases present in equilibrium, determination of their lattice parameter and structural characterization can be carried out employing XRD measurements.

The principle of this technique is based on elastic scattering of X-rays by the crystal which consists of well defined arrays of ions /atoms or molecules. When a monochromatic beam of X-rays is impinged on the sample, the X-rays-sample interaction causes oscillation of the electronic cloud of the atoms. This oscillation results in the emission of new radiations that have the same phase and wavelength as that of the incident beam (elastic scattering). This phenomenon is called as Thomson scattering. The nucleus bearing the positive charge might also be expected to take part in the coherent scattering. According to the Thomson equation, intensity of the coherent scattering is inversely proportional to the square of the mass of the scattering particle. Therefore, nucleus with relatively large mass will not

participate in the coherent scattering. Consequently, the coherent scattering by an atom is only due to the electrons present in that atom [78]. The radiations emitted by different atoms interact and the directions in which there is a constructive interference, diffracted beams are observed. The intensity of the diffracted beam is recorded as a function of incident angle by a detector. According to the Bragg's law, constructive interference occurs only when the path difference between the rays scattered from parallel set of planes is an integer multiple of the wavelength of the radiation. The X-ray diffractogram serves as a fingerprint in the identification of the compound.

The necessary condition for diffraction to occur can be represented by the Braggs equation

$$n\lambda = 2d_{hkl}\sin\theta \tag{3.1}$$

In the Equation 3.1,

➢ n is an integer and corresponds to the order of diffraction

➢ λ is the wavelength of the incident beam of light

➢ d_{hkl} is the distance between two planes of miller indices h, k and l

➢ θ is the angle between surface of the sample and the incident beam

Fig. 2.3, shows the diffraction from a three dimensional periodic structure (Bragg diffraction) such as atoms in a crystal. Bragg diffraction is a consequence of interference between waves reflecting from different crystal planes. In case of cubic unit cell, distance between two parallel planes is given by the following relation:

$$d_{hkl} = \frac{a}{\sqrt{h^2 + k^2 + l^2}} \tag{3.2}$$

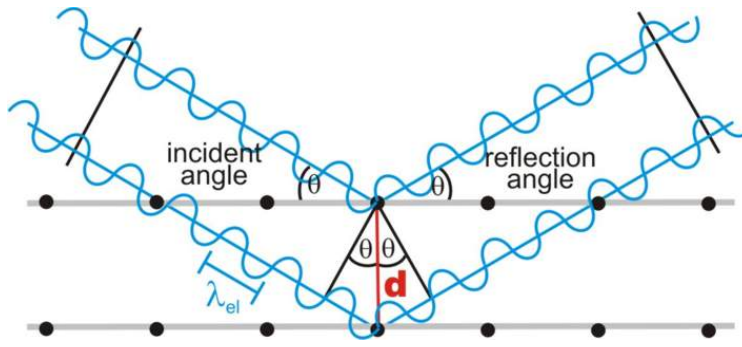a represents lattice parameter of a cubic unit cell.

Fig. 3.2: Schematic representation of Bragg diffraction

The resultant of the waves scattered by all the atoms in the unit cell, in the direction of the *hkl* reflection, is called the structure factor (F_{hkl}). The structure factor depends on both the position of each atom and its scattering factor. The intensity diffracted by a set of planes of indices *hkl* is proportional to the squared modulus of the structure factor.

$$F = Structure\ Factor = \frac{Amplitude\ of\ wave\ scattered\ by\ all\ atoms\ in\ unit\ cell}{Amplitude\ of\ wave\ scattered\ by\ an\ electron}$$

Structure factor is independent of the shape and size of the unit cell. Since, it is only the electrons that contribute to the diffraction of X-rays; therefore, contribution of light elements containing less number of electrons to the diffracted intensity will be weaker than that of heavy atoms possessing more electrons. As a result atoms with remote atomic numbers can be differentiated. However, it is difficult to distinguish the elements with close atomic numbers. The relative intensities of the reflections depend upon the atomic numbers of the atoms, the arrangement of atoms within the unit cell, the unit cell volume of the diffracting crystal and the absorption of X-rays by crystal. In X-ray diffraction pattern, from the position of the reflection observed, one can find out the size of the unit cell and at the most its space groups but not the position of the atoms or the bond length or bond angles. A block diagram of the typical powder diffractometer, consisting of an X-ray source, sample under investigation and a detector to pick up the diffracted X-rays is shown in the Fig. 2.3. The details of construction, working and application of diffractometers are discussed in several excellent books [79,80].
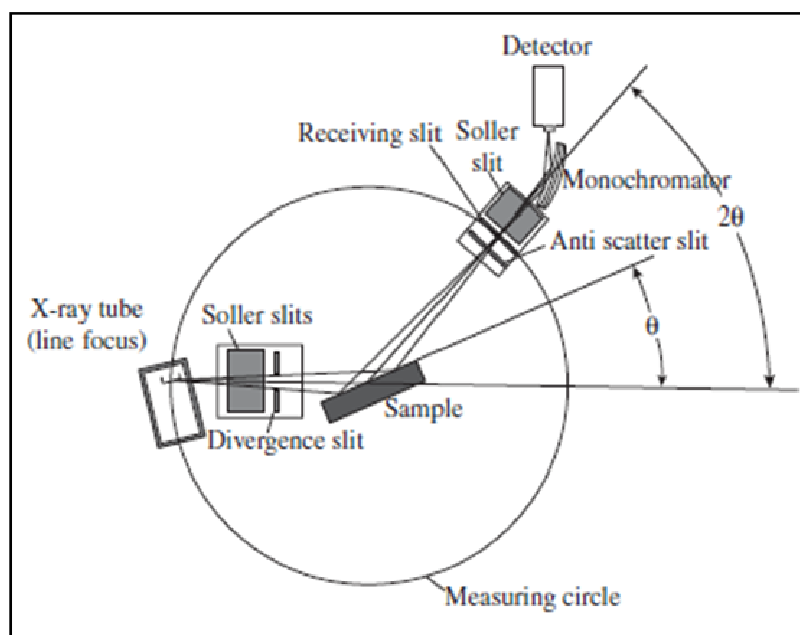
Fig. 3.3: Geometric arrangement of X-Ray diffractometer

In the studies presented in this thesis, the STOE XRD was employed to record the X-ray patterns for the compounds. Sample preparation for the XRD measurements involved crushing the sample in a mortar and pastel to obtain fine powder, sprinkling it on a double-sided tape applied on a plexi-glass sample holder, and flattening it with the help of a glass slide to obtain a smooth surface. The crushing of the sample prior to the XRD measurements helps to obtain random orientation of the grains with respect to the incident beam and avoids preferential orientation that may cause intensity variations during XRD measurements. Most of the samples investigated during the present study were easily reduced to the fine powder because of their high brittleness. In case of the alloy compositions that were difficult to crush, samples were cut from the center and polished before subjecting them to the XRD measurements. The powder XRD patterns were recorded using nickle filtered Cu-Kα radiation at 30 kV and 20 mA. The alignment and the calibration of the goniometer were performed using Silicon standard. The powdered sample was spread on a glass slide using collodion in isoamyl acetate as an adhesive. Since collodion, an organic compound made up

of carbon and hydrogen it did not interfere. Scanning speed of $2\theta = 1^0$ per min was used. The samples were scanned from 10 to 70^0. The measurement error in d values was around 0.02 Å.

3.3.2 X-ray Fluorescence (XRF)

X-ray fluorescence (XRF) is a non-destructive analytical technique used to determine the elemental composition of materials. XRF analyzers determine the chemistry of a sample by measuring the fluorescent (or secondary) X-ray emitted from a sample when it is excited by a primary X-ray source. Each of the elements present in a sample produces a set of characteristic fluorescent X-rays ("a fingerprint") that is unique for that specific element, which is why XRF spectroscopy is an excellent technology for qualitative and quantitative analysis of material composition [81].

The X-ray fluorescence process is described as follows:

1. A solid or a liquid sample is irradiated with high energy X-rays from a controlled X-ray tube.

2. When an atom in the sample is struck with an X-ray of sufficient energy (greater than the atom's K or L shell binding energy), an electron from one of the atom's inner orbital shells is dislodged.

3. The atom regains stability, filling the vacancy left in the inner orbital shell with an electron from one of the atom's higher energy orbital shells.

4. The electron drops to the lower energy state by releasing a fluorescent X-ray. The energy of this X-ray is equal to the specific difference in energy between two quantum states of the electron. The measurement of this energy is the basis of XRF analysis.

The two main types of XRF spectrometers (WD and ED) differ completely in their detection systems. EDXRF systems depend on semiconductor-type detectors which receive the entire emitted spectrum from the sample and decode it into a histogram of number of counts versus photon energy. WDXRF spectrometers, however, use an analyzing crystal to

disperse the emitted photons based on their wavelength and place the detector in the correct physical location to receive X-rays of a given energy.
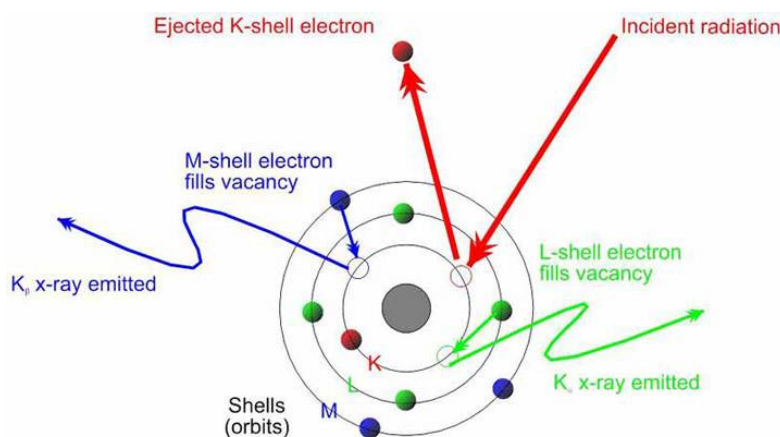

Fig. 3.4: A schematic presentation of X-ray fluorescence process

Most atoms have several electron orbitals (K shell, L shell, M shell, for example). When x-ray energy causes electrons to transfer in and out of these shell levels, XRF peaks with varying intensities are created and will be present in the spectrum, a graphical representation of X-ray intensity peaks as a function of energy peaks. The peak energy identifies the element, and the peak height/intensity is generally indicative of its concentration.

3.3.3 Inductively Coupled Plasma Mass Spectrometry (ICPMS)

Inductively coupled plasma mass spectrometry (ICP-MS) is a highly sensitive mass spectroscopy that is capable of the determination of a range of metals and several non-metals at concentrations below parts per trillion (ppt) levels [82]. Inductively coupled plasma mass spectrometry is a method used for separating and detecting the ions. In trace elemental analysis, the method has advantages compare to atomic absorption spectroscopic technique because of its better speed, precision and sensitivity. It is an analytical technique used for elemental determinations [83]. This technique is superior to detection capability of ICP-AES with the same sample throughput and the ability to obtain isotopic information.

An ICP-MS combines a high-temperature ICP (Inductively Coupled Plasma) source with a mass spectrometer. The ICP source converts the atoms of the elements in the sample to ions. These ions are then separated and detected by the mass spectrometer.

Fig. 3.5 shows a schematic representation of an ICP source in an ICP-MS. Argon gas flows inside the concentric channels of the ICP torch. The radio-frequency (RF) load coil is connected to a RF generator. As power is supplied to the load coil from the generator, oscillating electric and magnetic fields are established at the end of the torch. When a spark is applied to the argon flowing through the ICP torch, electrons are stripped off of the argon atoms, forming argon ions. These ions are caught in the oscillating fields and collide with other argon atoms, forming an argon discharge or plasma.
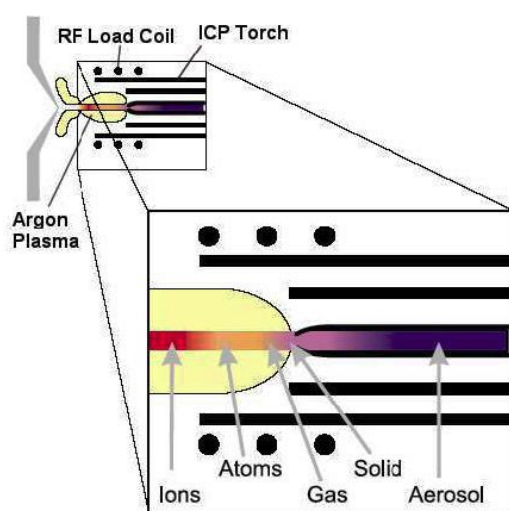
Fig. 3.5: The ICP torch showing fate of the sample

The sample is typically introduced into the ICP plasma as an aerosol, either by aspirating a liquid or dissolved solid sample into a nebulizer or using a laser to directly convert solid samples into an aerosol. Once the sample aerosol is introduced into the ICP torch, it is completely desolvated and the elements in the aerosol are converted first into gaseous atoms and then ionized towards the end of the plasma.

Once the elements in the sample are converted into ions, they are then brought into the mass spectrometer via the interface cones. The interface region in the ICP-MS transmits

the ions traveling in the argon sample stream at 1-2 torr pressure into the low pressure region of the mass spectrometer ($<1 \times 10^{-5}$ torr). This is done through the intermediate vacuum region created by the two interface cones, the sampler and the skimmer (see Fig. 3.6). The sampler and skimmer cones are metal disks with a small hole (~1mm) in the center. The purpose of these cones is to sample the center portion of the ion beam coming from the ICP torch. A shadow stop (see Fig. 3.6) or similar device blocks the photons coming from the ICP torch, which is also an intense light source. Due to the small diameters of the orifices in the sampler and skimmer cones, ICP-MS has some limitations as to the amount of total dissolved solids in the samples. Generally, it is recommended that samples have no more than 0.2% total dissolved solids (TDS) for best instrument performance and stability. If samples with very high TDS levels are run, the orifices in the cones will eventually become blocked, causing decreased sensitivity and detection capability and requiring the system to be shut down for maintenance. This is why many sample types, including digested soil and rock samples must be diluted before running on the ICP-MS.
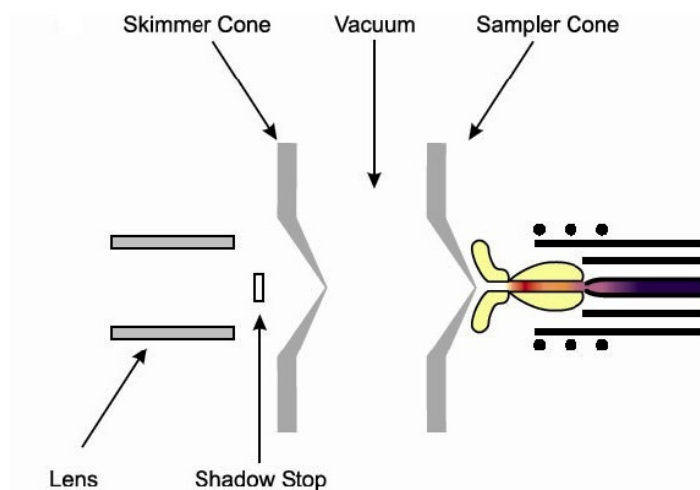

Fig. 3.6: The interface region of an ICP-MS

The ions from the ICP source are then focused by the electrostatic lenses in the system. The ions coming from the system are positively charged, so the electrostatic lens, which also has a positive charge, serves to collimate the ion beam and focus it into the

entrance aperture or slit of the mass spectrometer. Different types of ICP-MS systems have different types of lens systems. The simplest employs a single lens, while more complex systems may contain as many as 12 ion lenses. Each ion optic system is specifically designed to work with the interface and mass spectrometer design of the instrument.

Once the ions enter the mass spectrometer, they are separated by their mass-to-charge ratio. The most commonly used type of mass spectrometer is the quadrupole mass filter (See Fig. 3.7). In this type, 4 rods (approximately 1 cm in diameter and 15-20 cm long) are arranged as in Fig. 3. In a quadrupole mass filter, alternating AC and DC voltages are applied to opposite pairs of the rods. These voltages are then rapidly switched along with an RF-field. The result is that an electrostatic filter is established that only allows ions of a single mass-to-charge ratio (m/e) pass through the rods to the detector at a given instant in time. So, the quadrupole mass filter is really a sequential filter, with the settings being change for each specific m/e at a time. However, the voltages on the rods can be switched at a very rapid rate. The result is that the quadrupole mass filter can separate up to 2400 amu (atomic mass units) per second. This is why the quadrupole ICP-MS is often considered to have simultaneous multi-elemental analysis properties.
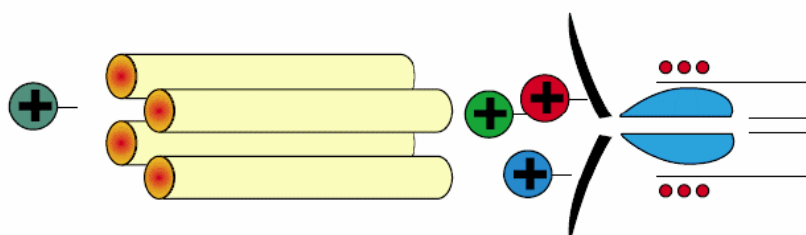

Fig. 3.7 Schematic of quadrupole mass filter

One of the great advantages to ICP-MS is extremely low detection limits for a wide variety of elements (see Table 3.1). Some elements can be measured down to part per quadrillion ranges while most can be detected at part per trillion levels. The table below shows some common detection limits by element.

Table 3.1: ICP-MS detection limit of elements

Element	Detection Limit (ppt)
U, Cs, Bi	Less than 10
Ag, Be, Cd, Rb, Sn, Sb, Au	10-50
Ba, Pb, Se, Sr, Co, W, Mo, Mg	50-100
Cr, Cu, Mn	100-200
Zn, As, Ti	400-500
Li, P	1-3 ppb
Ca	Less than 20 ppb

3.4 Calorimeter

The calorimeter is an instrument to measure any type of heat change: calori-meter, i.e. metering the calories or the heat change. It has unique ability to measure heat capacity as well as heat associated with the system itself.

The selection of calorimeter depends on the following factors

1. The rate of reaction under study

2. The magnitude of heat effect to be measured

3. The temperature of the experiment

4. The extent of accuracy desired

5. Corrosiveness of the substance involved

3.4.1 Different types of Calorimeter

There are different types of calorimeters, based on the nature of measurements to be made; heat content and heat capacity, enthalpy of fusion and transformation, and enthalpy of formation and reaction. Calorimeters can be also classified as solution calorimeter, mixing calorimeter, scanning calorimeter or reaction calorimeter. However, a most widely accepted

and meaningful classification of calorimeters based on three main variables: the temperature of the calorimeter (T_c), the temperature of its surroundings (T_s), and the heat produced per unit time (Q). According to this classification there are four different types of calorimeters which are described below.

(a) Isothermal Calorimeter

Isothermal calorimeter is the one in which temperature of the system is maintained constant and equal to the calorimetric block, $T_c = T_s$ = constant. The heat change, Q, is measured by measuring change in the physical property of some other material acting as surrounding to the system being investigated e.g. ice calorimeter and diphenyl ether calorimeter. Change in volume of the surrounding material due to heat exchanged with the system, is used to measure the heat change of the system. Hultgren et al. [84] used this calorimeter for measuring the heat content of metals and alloys.

(b) Adiabatic Calorimeter

In an adiabatic calorimeter temperature of the surrounding and the system are maintained equal i.e. $T_c = T_s$, but T_c and T_s vary. Physical or chemical changes of the system changes its temperature. In order to maintain $T_c = T_s$, a measured quantity of heat is given either to the system or to the calorimetric block around the system acting as surrounding. The compensated heat is the measure of heat change of the system under investigation. To minimise heat losses both system and surrounding are thermally insulated. Such calorimeters have mainly been built for the determination of heat capacities, but also enthalpies of transformation and reaction.

(c) Isoperibol Calorimeter

In an isoperibol calorimeter the surrounding is maintained at a constant temperature, and the change in temperature of the system is monitored. Heat exchange between the system and the surrounding is maintained by thermally insulating the system. The temperature variation of

the system reflects the heat changes taking place in the system. These calorimeters measure the temperature change in the reacting solution [85].

(d) Heat Flow Calorimeter

In case of heat flow calorimeter, instead of measuring the temperature of the system, the heat flow between the system and the surrounding due to temperature difference between them is measured. Initially the temperature of system and surrounding are same. The surrounding temperature T_s is maintained constant but T_c varies because of the heat change taking place in the system. In this calorimeter there is a deliberate heat exchange between the system and the surrounding which is channelized through a thermopile. Thermopile develops a voltage difference due to this heat flow and the electrical signal due to this voltage difference is a measure of the heat changes occurring in the system. A specific example of the heat flow calorimeter is the Calvet calorimeter used in this study. The principle of the heat flow calorimeter was developed by Calvet and Pratt [86].

3.4.2 High Temperature Inverse Drop Calorimeter

Enthalpy increment measurements on all the compounds under study have been carried out in a high-temperature inverse drop calorimeter (SETARAM, model MHTC-96) [86]. The general principle of drop calorimeter is discussed as follow.

This calorimeter is isoperibol type and it involves the isothermal measurement of heat content of material under quasi adiabatic condition. Conventionally, the enthalpy content is used to be measured by heating a sample to the desired temperature and after equilibration at this temperature for some fixed time the sample is dropped in to a well-equilibrated calorimeter block or bed that is maintained at fixed reference temperature. This type of calorimeter is called as direct drop calorimeter. In this type of calorimeter the differential rise in the temperature of the calorimeter with respect to the sample is being measured. The temperature difference between calorimeter and sample causes the heat transfer under

externally insulated conditions and this can be converted into enthalpy with proper calibration. The measured rise in the temperature can be correlated to heat flow (Q_S) in the following standard relation.

$$Q_S = m_S \times C^S_P \times \Delta T \tag{3.3}$$

Where m_S the mass and C^S_P are the heat capacity of the sample. The calibration is usually done by dropping the reference or calibrating sample of known mass and known enthalpy under identical experimental conditions and for reference.

$$Q^R = m_R \times C^R_P \times \Delta T \tag{3.4}$$

Where m_R and C^R_P are the mass and heat capacity of reference material, respectively. With the help of Eqs.(3.1 & 3.2) heat flow for unknown sample can be obtained. Further, the output of the drop calorimetry experiment, heat flow (Q) is related to enthalpy by the following equation.

$$Q = m \times C(T) \times (H_T - H_{298.15}) \tag{3.5}$$

where $C(T)$ is the calibration constant which is determined by calibration with a reference material like α-Al_2O_3. By determining $Q(T)$ as a function of temperature T, the enthalpy of the sample at various temperatures can be obtained. In an actual schedule of drop calorimetry measurements, temperature of sample is varied in discrete closely spaced steps and the experiments are repeated afresh at each new temperature with new sample. Despite the possibility that the successive drops can be performed at fairly closely spaced temperature intervals; the drop calorimetry offers only a set of closely spaced discrete data points rather continuous. The enthalpy increment ($H_T - H_{298.15}$) as a function of temperature is nonlinear in nature and it suffers a distinct change at phase transformation point. A schematic variation of enthalpy increment as function of temperature is shown in Fig. 3.8.

In the present study, inverse drop calorimeter has been employed and measurements are made in the inverse manner, i.e. the sample is dropped onto the hot calorimeter bed from the

is that the heat losses that are accrued in the normal mode of dropping the hot sample are minimized by resorting to dropping of cold samples. In accordance with this change, the instrument is also modified in its design in the appropriate manner [87]. Inverse drop calorimetry has some advantages; namely it can easily adopt small sample size, avoid any metastable phase retention from high temperature excursion and ability to study many different types of chemical reactions etc [88].
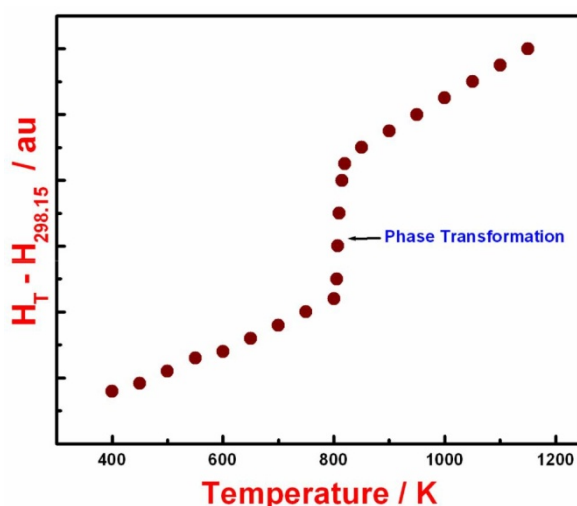

Fig. 3.8. Schematic of enthalpy increment variation with temperature

A *Setaram* multi HTC 96 inverse drop calorimeter used in the present study is shown in Fig. 3.9. A brief description of the component of drop calorimeter is given below [87].

(a) High temperature furnace

The high temperature furnace is suspended from the calorimeter cabinet's top plate. The heating element of the furnace is made of graphite tube which surrounds the experimental chamber of the calorimeter and is heated by resistance heating element up to a maximum temperature of 1773 K. A sealed alumina tube crosses the furnace through the centre of the heating element and insulates the experimental chamber from the furnace atmosphere.

Fig. 3.9. The inverse drop calorimeter

(b) Measurement head – drop Transducer

The measurement head itself is an integrated structure made of a cylindrical re-crystallized alumina tube in which two grooves are cut at its bottom to introduce the sample crucible. The crucible has a working volume of 5.3 cm^3. The measuring crucible's temperature is monitored by a thermopile made up of 28 B-type thermocouples distributed over the bottom and all over the side surface of the crucibles and it can be seen in Fig. 2.10 [87]. In addition, another dummy reference crucible having an identical thermopile 66 arrangement is kept underneath the sample crucible. This vertically aligned arrangement of both the sample and reference crucible is placed in the uniform temperature zone of the graphite furnace. Measurement of the sample and furnace temperatures is undertaken by two thermocouples of B type (PtRh-6% / PtRh-20%) [87].
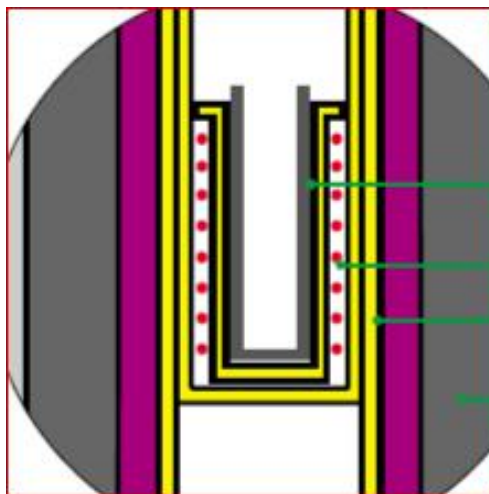
Fig. 3.10. Schematic representation of inverse drop calorimeter

(c) *Multi-sample introducer and the drop tube*

The multi sample introducer is equipped at the top portion of the experimental chamber and provides 23 slots to load samples in to it. The samples are being dropped manually from this introducer. Normally four to six samples are loaded for each measurement. For each sample, a reference sample is also loaded in to the adjacent slot. The sample from introducer are dropped to the alumina bed via guiding tube made of alumina known as drop tube.

(d) *Gas, vacuum, chill-water circuit and controller*

The equipment contains two separate gas circuits, one for the furnace and another for the analysis chamber to maintain the required inert gas atmosphere. An external rotary vacuum pump (EDWARDS®) supplied by *Setaram* is used for evacuating both the experimental and furnace chambers before starting the experiment. An external chill water supply with controlled flow (Julabo FC 1600 T) is provided for the furnace cooling. The heating schedule programming, the data acquisition and storage are performed through the CS 32 controller interfaced with the personal computer. The procedure for performing inverse drop calorimetric experiment is given below:

(e) Experimental procedure

The samples for drop calorimetry measurements were loaded in to the specimen slots of the multi sample introducer of *Setaram* multi HTC 96 inverse drop calorimeter. The standard or reference α–Al_2O_3 samples, supplied by Setaram drop were also loaded adjacent to the

sample used for the experiment. The sample crucible was filled with high pure alumina powder to 3/4th of its capacity and loaded in to the measurement head. After loading the samples and placing the working crucible in its position, both furnace and experimental chambers were evacuated using rotary pump. This was followed by purging both the experimental chamber and furnace with high purity argon gas (Iolar grade II) for few times and continuing with further evacuation. Once the evacuation process was completed both the chambers were allowed to fill with argon gas until the gas pressure level reaches one atmosphere pressure. An inert atmosphere was maintained throughout the experiment in order to prevent the evaporation of carbon from the graphite furnace at high temperature and also to avoid the oxidation of sample. The chill water supply was switched on before the furnace is started to heat. The furnace was gradually heated from 298.15 K to a desired temperature at the rate of 10 K/min. The surrounding graphite furnace heats the alumina bed. Once the pre-set value of the alumina bed temperature was reached within the accuracy of ± 0.1 K, the samples were dropped from the respective slot to the hot alumina bed through drop tube. The heat absorbed by the sample upon its drop from the ambient temperature into the hot alumina bed can be quantified by monitoring the change in temperature as a function of time t.

The net heat flow Q from the hot alumina bed to the cold sample was measured as area under the curve (V) *vs* time t [89] and can be represented by the following expression.

$$Q = C\,(T)\,x\,V\,x\,t \tag{3.6}$$

The dropping of the sample at a particular temperature was followed by the dropping of a standard or reference sample like α-Al_2O_3 with known enthalpy and mass at the same temperature in order to determine the calibration constant $C(T)$. Both dropping of the sample and reference were performed under identical conditions. The whole experiment other than the dropping of sample was controlled through a computer that is connected to the calorimeter by a proprietary interface module. The signals from the calorimeter are

digitalized and transferred to a computer *via* a CS 232 series interface. The data acquisition period for each drop was maintained for about 20-25 minutes in the present study. Once the data acquisition was completed for one experiment, a gap of about 20 minutes was kept before dropping the next sample so that the alumina bed regain its thermal equilibrium. Fresh samples were used for each drop experiment. In the present study, the drop experiments for U_2Ti and ZrCo alloys were performed in the temperature range of 299-1169 K and 642-1497 K, respectively. After the experiment, the samples were weighed to check any loss or gain due to reaction or due to oxidation. The weight change was found to be less than 1 mg. The isothermal drop experiment is performed at successively higher temperatures with approximate temperature step of 50 K.

(f) *Temperature and heat calibration of drop calorimeter*

Prior to the experiment the calorimeter has been calibrated for temperature and the peak area which is referred as heat flow (Q). The temperature calibration has been carried out with melting points of pure element such as In, Sn, Al, Ag, Au and Cu. The resulting error in the measured temperature was found to be ± 2 K. The heat flow (Q) has been calibrated by dropping α-Al_2O_3, the reference material into the hot alumina bed set at different temperatures during enthalpy measurement of unknown samples.

(g) Estimation of enthalpy

The raw data which obtained from the output of experiment is basically the heat flow Q (mV.s) for both sample and reference. Assuming negligible heat loss due to radiation and quasi adiabatic condition in the experimental chamber, $Q_s(T)$, the heat energy transported from the bed to the sample may be written as follows [90-91].

$$Q_s (T) = C (T) \times (m_s/M_s) \times (H_T - H_{298.15}) \tag{3.7}$$

In the above expression, m_S is the mass of the sample, M_S its molecular weight and $H_T H_{298.15}$ is the measured enthalpy increment with respect to reference temperature 298.15 K (25 ^{0}C)

and C(T) is a temperature dependent calibration constant. The calibration constant can be obtained from the heat change measured for the standard alumina reference (Q_R) and from the knowledge of its assessed enthalpy increment data [92]. Thus

$$Q_R(T) = C(T) \times (m_R/M_R) \times (H_T - H_{298.15})_R \tag{3.8}$$

In the above equation m_R is the mass of the reference sample and M_R is its molecular weight which is taken to be 101.96 kg m^{-3} [92]. Once the calibration constant C(T) is obtained as a function of temperature from *Eq*. (3.8), the enthalpy for the unknown sample can be calculated using Eq. (3.7) as a function of temperature.

(h) Few aspects of result of drop calorimeter

It is generally assumed that the drop calorimetry measurements are carried out at thermally equilibrium conditions. As a result, a reliable and consistent thermodynamic data are obtained with static calorimetric measurements. The enthalpy variation with temperature measured at discrete temperature increments is used to derive heat capacity by fitting the temperature variation of enthalpy to a suitable analytical representation. In principle, it is desirable to have as large a number of data points as is possible for obtaining reliable conversion of enthalpy into specific heat [92]. This is especially true for characterizing the thermal property variation in the phase transformation domain. In drop calorimetry, when adequate precautions are ensured such as temperature stability high purity argon atmosphere etc., it is possible to achieve reproducible experimental data points, especially since a high level of accuracy in measuring and maintaining temperature stability is possible. In the present study, we have allowed enough equilibration time so as to achieve a temperature stability of ±0.1 K. The accuracy of temperature measurement is ±2 K. In order to avoid the effect of thermal gradients in the sample affecting the attainment of true equilibrium, a slow heating rate of 5 K min^{-1} and a reasonable sample mass of 50 to 75 mg are adopted in this study. Too large a sample mass, while contributing to signal strength also add up to data scatter as the noise

level is also raised in general. In view of such careful measures adopted in the present study, it is assured that drop calorimetry technique has yielded reliable thermodynamic quantities.

CHAPTER 4

Theoretical and Experimental Study of U$_2$Ti Alloy

4.1 *Ab-initio* Study of U$_2$Ti

4.1.1 Computational Details

The computational details for this study are already described in section 2.9.1 of chapter 2.

4.1.2. Results and Discussion

a) Structural Properties

Before calculating the ground state properties of the U$_2$Ti alloy, which is the main purpose of this paper, we determine the ground state properties of U and Ti and compare them with available experimental results. The crystal structure of α-uranium is face-centered orthorhombic (*Cmcm*) at low temperature and pressure (Fig.4.1).
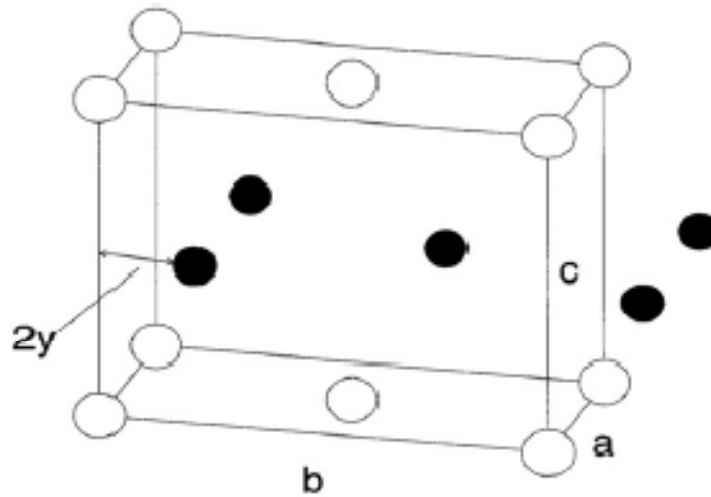
Fig. 4.1: Crystal structure of α-uranium

This structure can be described with two U atoms per unit cell. To obtain the ground state structural parameters, the total energy has been calculated by varying the cell volume as well as the lattice parameters independently. The total energy versus volume plot is shown in Fig. 4.2.
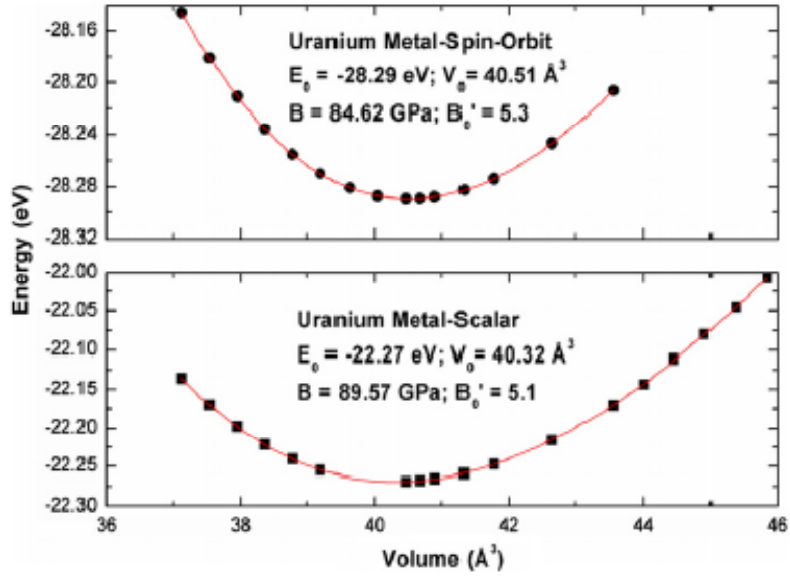
Fig. 4.2: Variation in total energy as a function of cell volume for α-U

The parabolic *E-V* plot is then fitted to the Murnaghan equation of state to determine the equilibrium lattice constants and bulk moduli (B_0). The optimized lattice constants and internal parameters are presented in Table 4.1.

Table 4.1: Crystal structure data of α-U, Ti and U₂Ti

System	Crystal System	Space Group	Calculated (0 K) from *E* Vs *V* graph		Expt. (298 K) [Ref.]
α-U	Orthorhombic	*Cmcm* (63)	a(Å)	2.831	2.854 [93]
			b (Å)	5.823	5.870 [93]
			c (Å)	4.915	4.955 [93]
			y	0.105	0.105 [93]
			V_0 (Å³)	40.51	41.50 [93]
Ti	Hexagonal	*P6₃/mmc* (194)	a (Å)	2.915	2.951 [96]
			c (Å)	4.629	4.686 [96]
			V_0 (Å³)	34.04	35.34 [96]
U₂Ti	Hexagonal	*P6/mmm* (191)	a (Å)	4.773	4.828 [97]
			c(Å)	2.815	2.847 [97]
			V_0 (Å³)	55.54	57.47 [97]

It is clear from this table that the calculated values are in good agreement with the experimental results [93]. I a previous work Söderlind et al. reported the bulk modulus of α-U 133 GPa using the full potential version of the linear muffin-tin orbital (FP-LMTO) method with generalized gradient approximation (GGA). In another theoretical study, Adak et al. reported similar bulk modulus value using pseudopotential method with GGA. Recently Bihan et al. carried out the diamond-anvil cell experiment using angle-dispersive X-ray diffraction with a synchrotron source and calculated the bulk modulus of α-uranium B_0= 104 GPa with $B_0' = 6.2$ GPa [94]. Further they claimed that these values are more precise than the previous values because of the precise data and use of different media for the pressure transmission. In the present study we have used plane wave-pseudopotential method with GGA and spin-orbit coupling term in the total energy calculation. The bulk modulus is found to be 84.6 GPa, which is in good agreement with the recent experimental work by Bihan etal. [94] and Kittel [95]. Apart from the limitations of DFT based calculation, the primary reason for such difference in the bulk modulus is attributed to the different theoretical techniques applied in these works. In this context it should be mention that no significance difference in terms of lattice parameters has been found between the scalar relativistic and relativistic spin-orbit calculations.

At room temperature and ambient pressure, Ti stabilizes into a hexagonal crystal structure with space group symmetry of $P6_3/mmc$ (194). In line with U calculations, the total energy of Ti is calculated by changing the lattice parameters as shown in Fig. 4.3.
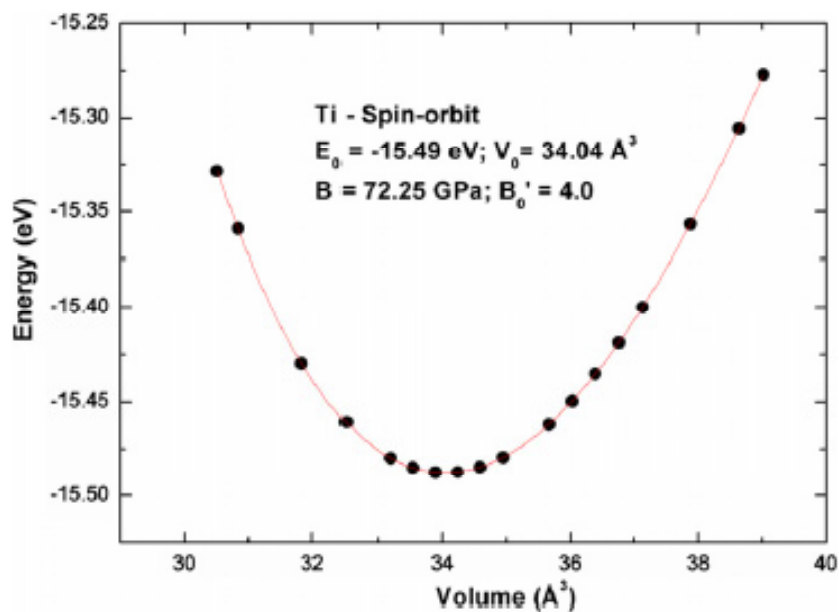
Fig. 4.3: Variation in total energy as a function of cell volume for Ti

The *E-V* plot has been fitted to the Murnaghan equation of state. The estimated lattice parameters are found to be a = 2.915 Å and c = 4.629 Å, which are in good agreement with the experimental values [96].

After establishing accurate structural parameters of U and Ti using the plane wave based PAW method, we have optimized the structural parameters of U_2Ti. From the experiment [97] it is reported that U_2Ti crystallizes into a hexagonal structure with space group symmetry of *P6*/*mmm* (191) as shown in Fig. 4.4.
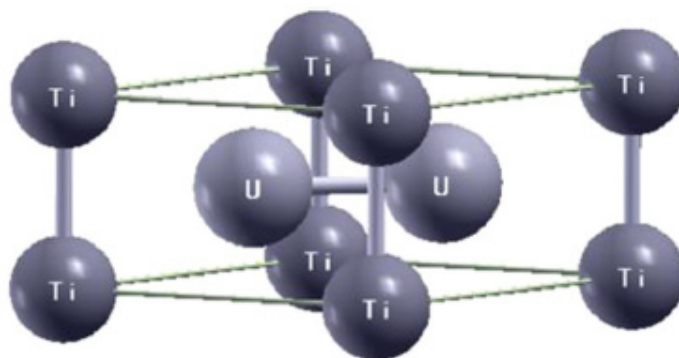
Fig. 4.4: The crystal structure of U_2Ti

The Ti atom occupies $1a$ site and two U atoms occupy $2d$ sites; the *P6/mmm* space group fixes the fractional coordinates of all three positions [98-100]. Now we repeat the same method of calculation as described for U and Ti. The variation in the total energy as a function of cell volume has been plotted in Fig. 4.5.
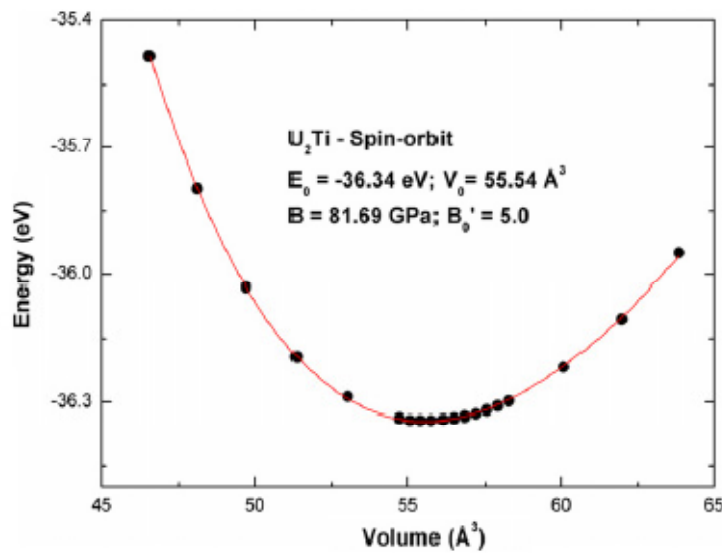

Fig. 4.5: Variation in total energy as a function of cell volume for U$_2$Ti

The lattice parameters of U$_2$Ti are found to be a= 4.773 Å, c= 2.815 Å. These results are in good agreement with the experimentally observed values of a = 4.828 Å and c = 2.847 Å with equilibrium volume V_0= 57.47 Å^3.

b) Energetics

Due to the recent advent of *ab-initio* calculations, a large number of studies concerning the formation energy at T= 0 K in metallic systems have been investigated. But notably, very few calculations have been performed for lanthanide and actinide based alloys. Although one of the aspects of finding the formation energy of metals is to verify the accuracy of theoretical methods, the most important one is to understand the stability and alloying behavior of binary or ternary systems. In Table 4.2 we have summarized the total energies E_{tot}, and bulk moduli of U, Ti and U$_2$Ti.

Table 4.2: Total energies (E_{tot}) and bulk moduli (B_0) of U_2Ti, α-U and Ti

System	E (eV/f.u.)	B_0 (GPa)	
		Calculated	Experiment [Ref.]
U_2Ti	-36.34	81.69	-
α-U	-14.14	84.62	98.7 [95]
Ti	-7.74	72.25	105 [95]

It is clear from this table that our calculated values are in good agreement with experimental observations. On the basis of these total energies the formation energy of U_2Ti is estimated to be -0.32 eV/f.u. or -30.84 kJ/mol (Eq. (1)).

To underscore the effect of spin-orbit coupling, we have compared the total density of state (DOS) for U_2Ti, U and Ti before and after inclusion of the spin-orbit (SO) term in the total energy calculation as shown in Fig. 4.6.
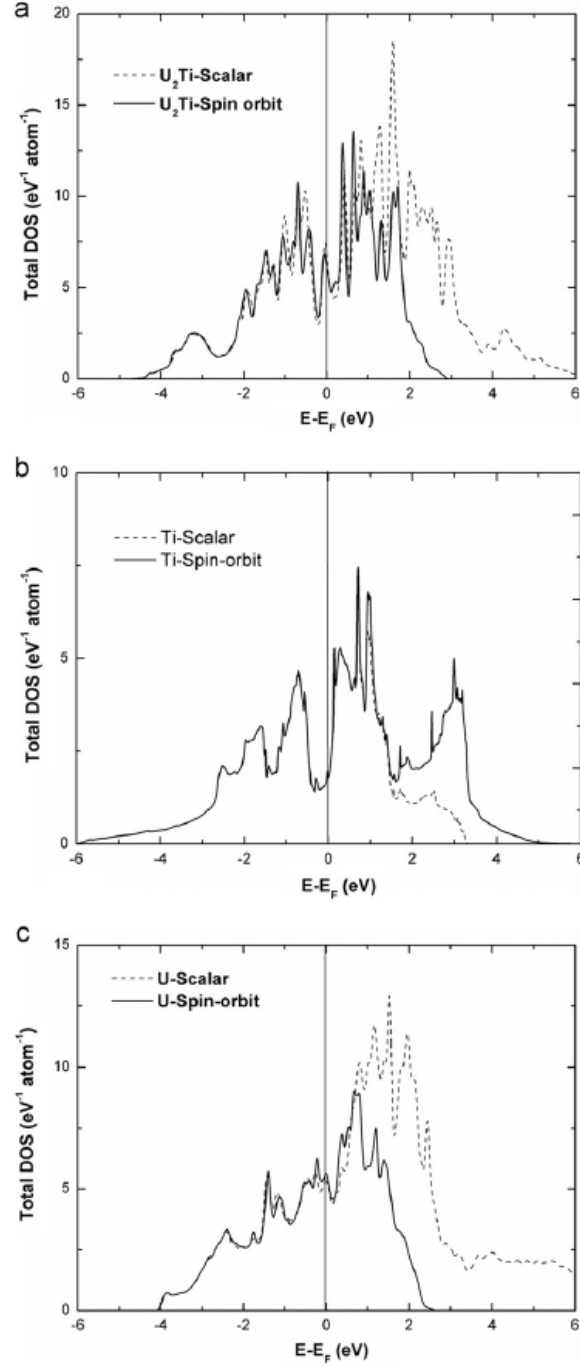
Fig. 4.6: The total density of states (DOS) for; (a) U$_2$Ti; (b) Ti and (c) α-U

The dotted and solid lines represent the DOS obtained from scalar relativistic and spin-orbit calculation, respectively. The energies are shifted in such a way that the Fermi level is aligned to zero for all cases. It is seen from the figure that for both U and U$_2$Ti, the nature of the DOS spectrum is similar below the Fermi level. However, a substantial difference in the DOS spectrum is observed using SO and NSO approach above the Fermi level. For both α-U

and U$_2$Ti, the inclusion of spin-orbit effect results in narrowing the band width and this effect is more prominent above the Fermi level. Unlike this, the DOS of Ti does not show any significant effect due to SO incorporation. This feature infers the significance of spin-orbit interaction over the scalar relativistic calculations in such systems.

A test to check the accuracy of the density of states is deriving the specific heat of the system. The coefficient of the electronic specific heat (γ) is calculated as

$$\gamma = \left(\pi^2/3\right) k_B^2 n(E_f) \tag{4.1}$$

where K_B is Boltzmann's constant. The coefficient of electronic specific heat for α-U and Ti are found to be 13.11 and 4.22 mJ ol (f.u.)$^{-1}$ K^{-2}, respectively. These are in good agreement with the experimental observations [95,101]. For U2Ti, the DOS at the Fermi energy is found to be $n(E_f) = 6.3$ states/eV f.u. and the corresponding coefficient of specific heat is calculated to be 14.75 mJ mol (f.u.)$^{-1}$ K^{-2}.

Now to understand the chemical interaction of U and Ti in the U$_2$Ti alloy, we compare the split DOS of U$_2$Ti as shown in Fig. 4.7.
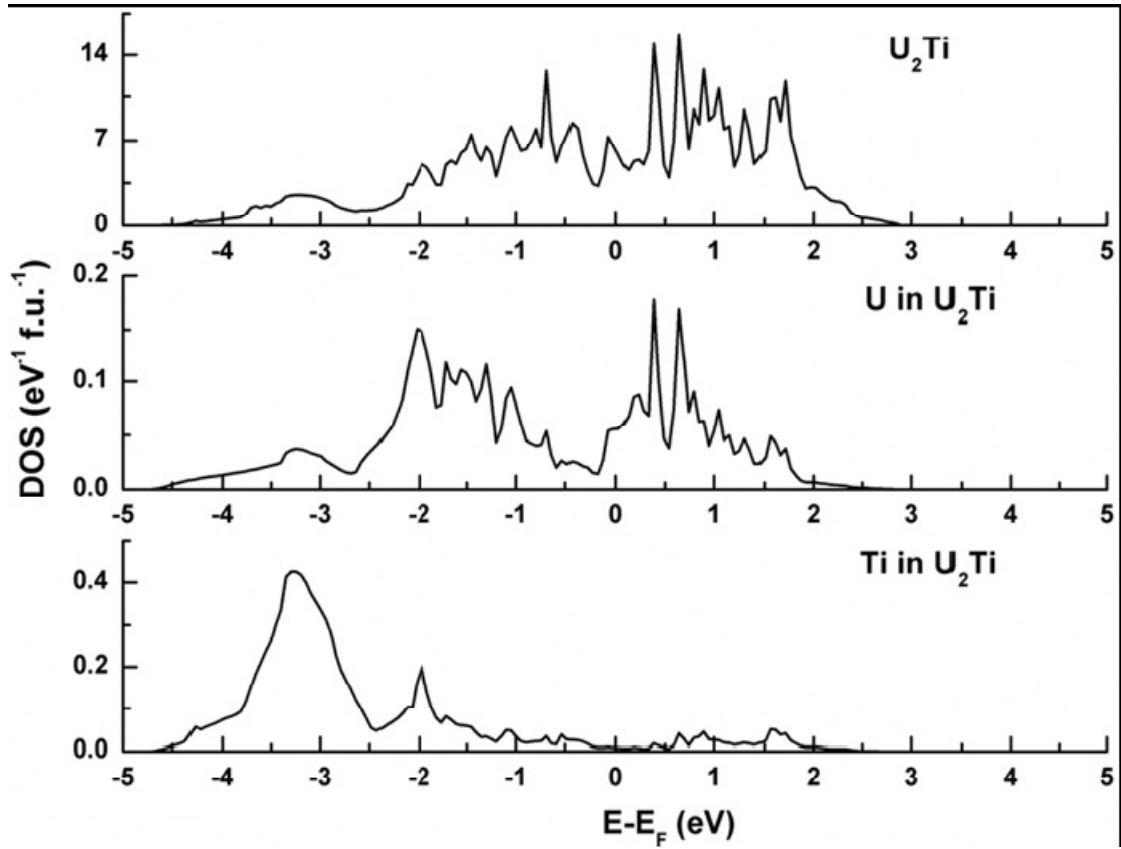
Fig. 4.7: A comparison of split DOS spectra (SO) for U₂Ti, U in U₂Ti and Ti in U₂Ti

It is clear from this figure that the nature of U_2Ti DOS and U DOS are very similar. However, the energy levels of Ti lie much lower in the DOS spectrum. Due to the predominant presence of U at the Fermi energy, it may be inferred that the inclusion of Ti will not affect the hydrogenation behavior of U, but it will help to prevent the pyrophoricity of U.

4.2 Enthalpy Increment Study of U_2Ti

4.2.1 Materials Preparation and Characterization

The preparation of the U_2Ti alloy is already described in section 3.2.3 (a) of chapter 3. The XRD pattern shown in Fig. 4.8 was recorded with 2θ range of 15^0-80^0 degree using monochromatized Cu-Kα_1 ($\lambda = 1.5406$ Å) radiation.
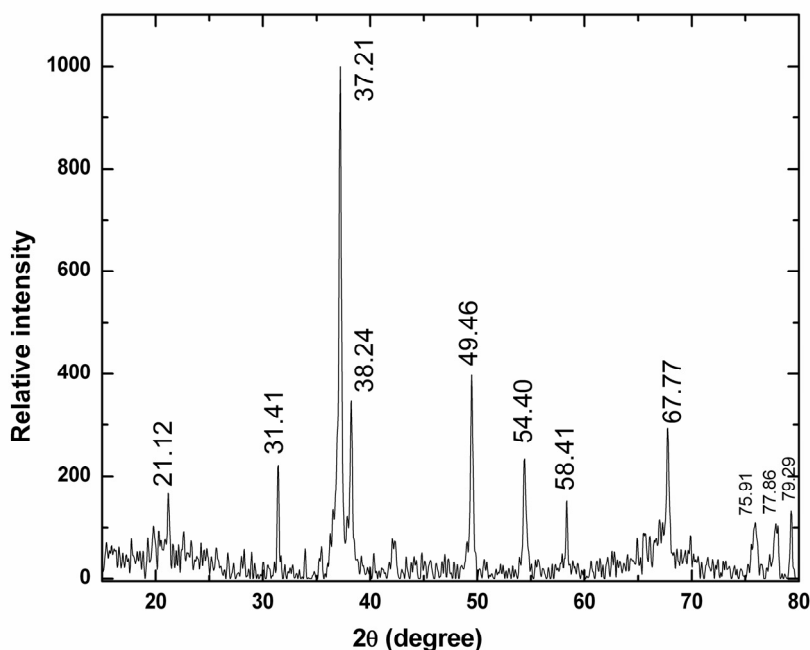

Fig. 4.8: XRD pattern of U_2Ti

The formation of the alloy phase was confirmed by comparing the obtained XRD pattern obtained in this study (Fig. 4.8) with that reported in the Joint Committee on Powder Diffraction Standards (JCPDS) file no: 07-0176 [102]. The impurities present in U_2Ti alloy was measured by XRF and ICPMS, and the results are given in Table 4.3.

Table 4.3: The impurities present in U_2Ti

S. No.	Impurity	Quantity/ppm
Metallic impurities/XRF		
1.	Fe	<25
2.	Ni	<10
3.	Zr	<10
4.	V	<15
Non-metallic impurities/ICPMS		
5.	C	<15
6.	O	<40
7.	N	<20
8.	S	<15

4.2.2 High Temperature Enthalpy Increment of U_2Ti

Fig. 4.9 shows DSC profiles of U_2Ti recorded in heating mode usingmulti-HTC. The five phase transitions at 944, 963, 990, 1165 and 1563 K were observed in U_2Ti.
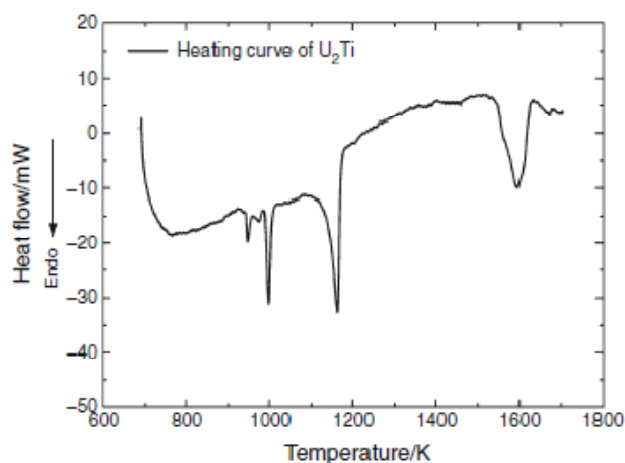
Fig.4.9: DSC profile of U_2Ti in heating mode

The experimentally determined enthalpy increment data acquired by drop mode of multi-HTC were shown in Fig. 4.10. The enthalpy increment data below the first transition temperature were given in Table 2.
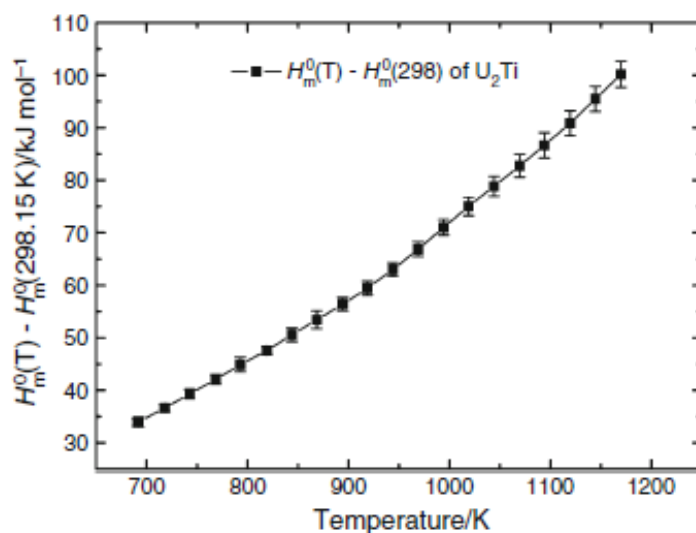
Fig. 4.10: Measured enthalpy increment of U$_2$Ti as a function of temperature

Table 4.4 Enthalpy increment data along with fit values of U$_2$Ti

T/K	$H_m^0(T) - H_m^0(298.15\ K)/$ J mol^{-1} experimental	$H_m^0(T) - H_m^0(298.15\ K)/$ J mol^{-1} calculated	% difference
691.1	33,872 ± 690	33,908	0.11
692	33,963 ± 932	33,999	0.11
718	36,638 ± 716	36,668	0.08
742.7	39,307 ± 883	39,263	-0.11
768.6	42,080 ± 891	42,048	-0.08
792.9	44,901 ± 1,395	44,719	-0.41
819.2	47,579 ± 727	47,676	0.20
843.9	50,575 ± 1,268	50,515	-0.12
868.6	53,439 ± 1,675	53,415	-0.04
894.3	56,379 ± 1,275	56,497	0.21
918.7	59,465 ± 1,325	59,485	0.03

% difference = 100(calc. -exp.)/exp.

These values were least square fitted in the temperature range of 691-918 K into polynomial

equation using Shomate method [102] with constraints (i) $H_m^0(T) - H_m^0(298.15\ K) = 0$ at

298.15 K and (ii) $C_{p,m}^0(298.15\ K) = 79.0$ (taken from room temperature DSC data). The fitted polynomial expression obtained for $U_2Ti(s)$ in the temperature range of 691-918.7 K is given as

$$H_m^0(T) - H_m^0(298.15\ K)(J\ mol^{-1}) = 23.236(^T/_K) + 53.292 \times 10^{-3}(^T/_K)^2 - 21.294 \times$$

$$10^5(^K/_T) - 4523 \tag{4.2}$$

The heat capacity expression of $U_2Ti(s)$ was obtained by differentiating above enthalpy increment expression with respect to temperature. The heat capacity expression obtained from multi-HTC data can be given as

$$C_{p,m}^0(J\ K^{-1}\ g^{-1}) = 23.236 + 10.6584 \times 10^{-2}(^T/_K) + 21.294 \times 10^5(^K/_T)^2\ (300 \leq$$

$$^T/_K \leq 900) \tag{4.3}$$

The molar heat capacity at constant pressure $(C_{p,m}^0)$ of U_2Ti as a function of temperature is plotted in Fig. 4.11.
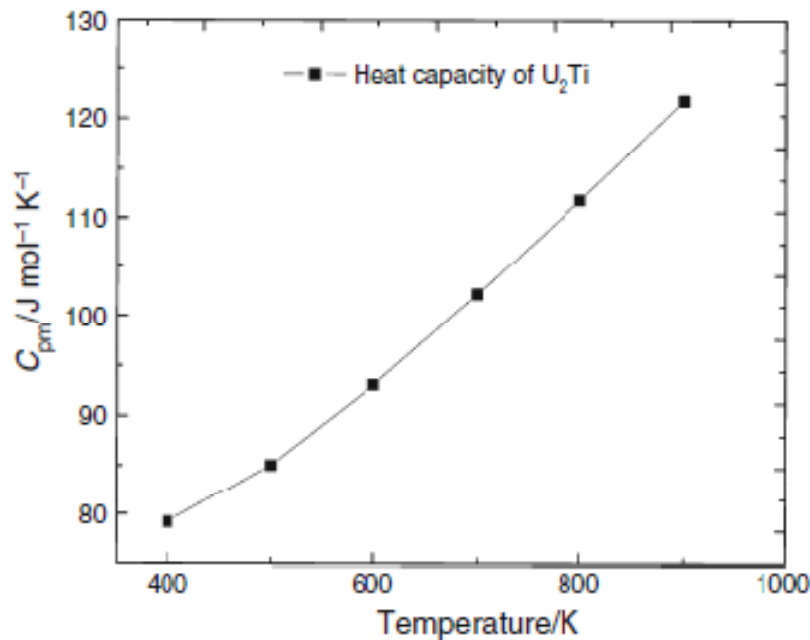

Fig. 4.11: Variation of molar heat capacity at constant pressure (C^0$_{p,m}$) of U$_2$Ti as a function of temperature

4.2.3 Thermodynamic Functions of U$_2$Ti

Enthalpy increment values for U$_2$Ti(s) have not been previously reported in the literature to compare. In order to generate thermodynamic functions for U$_2$Ti(s) from enthalpy increment data, $\Delta_f H_m^0(298.15\ K)$ and $S_m^0(298.15\ K)$ values are required. Recently, present authors [103] computed $\Delta_f H_m^0(U_2Ti, s, 0\ K) = -30.84\ kJ\ mol^{-1}$ from first principles calculations. Bajaj et al. [105] calculated U–Ti phase diagram that was consistent with experimental phase diagram and thermodynamic data (enthalpy of formation of δ-U2Ti and γ(bcc)-U–Ti alloys as a function of Ti) from DFT. Authors [104] obtained accurate phase stabilities of U$_2$Ti phase in U–Ti system by taking its enthalpy of formation to be -35.86 kJ mol^{-1} at 298.15 K. This value is selected in this study for the calculations of thermodynamic functions of U$_2$Ti.

For the calculation of entropy of U$_2$Ti(s) at 298.15 K, $C_{p,m}^0(T)$ values in the temperature range of 0–298.15 K are required. These values for U$_2$Ti(s) have been estimated from low temperature heat capacity data of α-U and Ti, the calculated S_m^0 (U$_2$Ti,s,298.15) was 131 J K^{-1} mol^{-1}.

The self consistent thermodynamic functions like $S_m^0(T)$, $C_{p,m}^0(T), \{H_m^0(T) - H_m^0(298.15\ K)\}, \varphi_m^0(T) = \{-(G_m^0(T) - H_m^0(298.15))/T\}, G_m^0(T)$, $\Delta_f H_m^0(T)$ and $\Delta_f G_m^0(T)$ have been calculated in the temperature range 298.15-900 K using $\Delta_f H_m^0(298.15\ K)$, $S_m^0(298.15\ K)$, and heat capacity data of U$_2$Ti(s). The relations used for calculations are as follows:

$$H_m^0(T) - H_m^0(298.15) = \int_{298.15}^{T}\left(C_{p,m}^0\right) dT \tag{4.4}$$

$$S_m^0(T) = S_m^0(298.15\ K) + \int_{298.15\ K}^{T}\left(\frac{C_{p,m}^0(T)}{T}\right) dT \tag{4.5}$$

$$\varphi_m^0 = -\left(\frac{(G_m^0(T) - H_m^0(298.15))}{T}\right) = S_m^0(T) - \frac{\left(H_m^0(T) - H_m^0(298.15)\right)}{T} \tag{4.6}$$

$$\Delta_f H_m^0(T) = \Delta_f H_m^0(298.15\ K) + \int_{298.15\ K}^{T} \Delta C_{p,m}^0\ dT \tag{4.7}$$

$$\Delta_f G_m^0(T) = \Delta_f H_m^0(T) - T\Delta_f S_m^0(T) \tag{4.8}$$

The calculated thermodynamic functions are given in Table 4.5.

Table 4.5: Thermodynamic functions of U$_2$Ti ($C_{p,m}^0(T), S_m^0(T), \varphi_m^0(T)$ in J mol^{-1}K^{-1} and $H_m^0(T) - H_m^0(298.15), H_m^0(T), G_m^0(T), \Delta_f H_m^0(T), \Delta_f G_m^0(T)$ in kJ mol^{-1}) calculated from equation (1)

T/K	$C_{p,m}^0(T)$	$S_m^0(T)$	$H_m^0(T) - H_m^0(298.15)$	$\varphi_m^0(T)$	$H_m^0(T)$	$G_m^0(T)$	$\Delta_f H_m^0(T)$	$\Delta_f G_m^0(T)$
298.15	79.0	131.0	0.0	131.0	-35.9	-74.9	-35.9	-35.8
300	79.0	131.5	0.1	131.2	-35.8	-75.2	-35.9	-35.8
400	79.2	154.0	8.0	134.0	-27.9	-89.5	-36.3	-35.7
500	85.0	172.2	16.2	139.8	-19.7	-105.9	-37.0	-35.4
600	93.1	188.4	25.1	146.6	-10.8	-123.9	-37.6	-35.0
700	102.2	203.5	34.8	153.8	-1.1	-143.6	-38.0	-34.5
800	111.8	217.7	45.5	160.8	9.6	-164.7	-38.2	-34.0
900	121.8	231.5	57.2	167.9	21.3	-187.1	-38.4	-33.6

CHAPTER 5

Theoretical and Experimental Study of Zr-based Compounds

5.1 *Ab-initio* Study of ZrX$_2$ (X= H, D and T) Compounds

5.1.1 Computational Details

The computational details for this study are already described in section 2.9.2 of chapter 2.

5.1.2 Results and Discussion

a) Crystal Structure

The crystal structure of α-Zr is hexagonal closed pack (hcp) with space group *P63/mmc*. The hydrogenation of α-Zr produces different hydrides like ζ-Zr$_2$H, γ-ZrH, δ-ZrH$_{1.5}$ and ε-ZrH$_2$ at different conditions. As reported by Flotow *et. al* [105], at 25 ^{0}C the ZrH$_2$ compound exists both as face-centered tetragonal (fct) and body centered tetragonal (bct) crystal structure. We have optimized the bct structure with lattice constants a = 3.518 Å and b = 4.447Å as shown in Fig. 5.1.
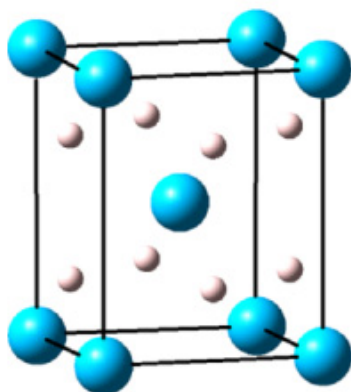
Fig. 5.1: Crystal structure of ZrH$_2$ (big spheres for Zr and small spheres for H)

In the unit cell the Zr and H atoms are placed in the Wyckoff position 2a (0, 0, 0) and 4d (0, 0.5, 0.25), respectively. In this structure (Fig. 1) each Zr atom is surrounded by eight H atoms forming a tetragonal moiety and each H connects with four Zr atoms to build a tetrahedron. To obtain the ground state structural parameters, the total energy calculation were carried out by varying the cell volume as well as the lattice parameters independently. Based on these energies, the energy vs. volume plot (*E-V*) of the ZrH$_2$ is shown in Fig. 5.2.
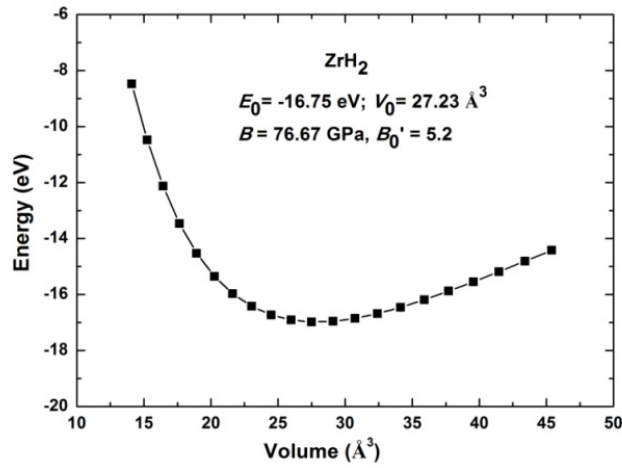
Fig. 5.2: Energy-volume graph of ZrH$_2$

The parabolic E-V graph is fitted with the Murnaghan equation of state [84] to determine the

equilibrium lattice constants and bulk moduli (B_0). The bulk modulus of the ZrH$_2$ is found to

be 76 GPa which is lower than that of α-Zr (85 GPa). This suggests that hydrogenation of α-

Zr reduces the fracture strength of α-Zr. The optimized lattice parameters along with their

experimental values for α-Zr and ZrH$_2$ are summarized in Table 5.1.

Table 5.1: Optimized lattice constants along with the available experimental values (in Å) for α-Zr and ZrH$_2$

System	this work (at 0 K)		Expt. (at 298 K)		previous work (at 0 K)	
	a	*c*	*a*	*c*	*a*	*c*
α- Zr	3.230	5.169	3.233[a]	5.150[a]	3.223[c]	5.157[c]
			3.231[b]	5.147[b]		
ZrH$_2$	3.538	4.442	3.518[d]	4.447[d]	-	-

[a] Reference [107], [b] Reference [108], [c] Reference [109], [d] Reference [106].

The calculated values are found to be within ±1% of the corresponding experimental values

[106-109]. The closeness of calculated values of the lattice parameters obtained in this study

with the experimental reported values in the literature establishes the accuracy and reliability

of the present computational method. Hence, the computed values in this study form the basis

for further calculations in the subsequent sections described below.

b) Energetics and Electronic Structure

In order to describe the nature of chemical bonding in the ZrH_2, the orbital projected density of states (DOS) of ZrH_2 have been calculated and shown in Fig. 5.3 which depicts that $4d$-orbital of Zr and $1s$-orbital of hydrogen are mainly participating in the bonding of ZrH_2.
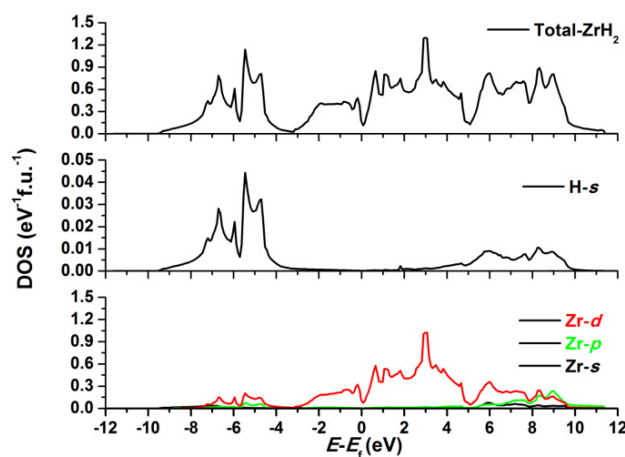

Fig. 5.3: Split density of state (DOS) of ZrH_2

Furthermore, $1s$-orbital spectrum of hydrogen is more localized (mainly ranging from -3 to -9 eV) compared to the d-orbital spectrum of Zr, which is more delocalized over a wide range from -8 to 10 eV. It is seen that at the Fermi level of ZrH_2, the d-orbital contribution of Zr is dominant whereas the s-orbital of hydrogen is contributing mainly below the Fermi energy. The presence of finite DOS at Fermi level in ZrH_2 signifies that it is retaining the metallic nature even after the hydrogenation of metallic zirconium. The calculated total DOS of ZrH_2 at the Fermi level is $N(E_f) = 0.0813$ states per eV-f.u. The coefficient of electronic specific heat is calculated as $\gamma = (\pi^2/3) \cdot k_B^2 \cdot N(E_f)$, where k_B is the Boltzmann's constant. Using this relation γ value of ZrH_2 is found to be 0.0317mJ/mol-K^2. The understanding of chemical bonding in ZrH_2 have been further described by the charge density distribution and electron localization function (ELF) as shown in Fig. 5.4 and Fig. 5.5.
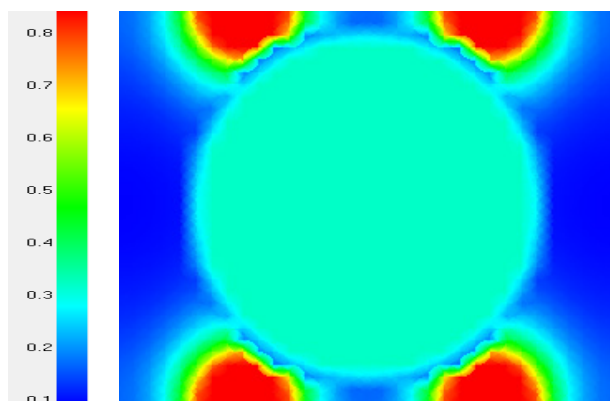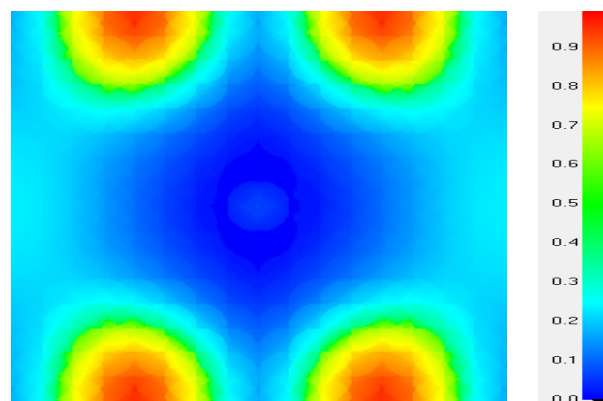
Fig. 5.4: Charge density contour of ZrH₂   **Fig. 5.5: Electron localization function of ZrH₂**

The color bar graph shows relative electron density across the figures. In Fig. 5.4, it is seen that more electronic charges are localized at H sites which have been donated by Zr atoms resulting the hydride to be metallic in nature. A different perspective on bond character can be depicted by the ELF, which has been described to be very useful in revealing atomic shell structure and bond charge in crystal systems [110-112]. The ELF is a position dependent function the values of which vary within the range $0 \leq ELF \leq 1$. The ELF value of 0.5 signifies the electron-gas like pair probability. In Fig. 5.5, the ELF value reaches its highest values of ~0.9 (red) in the vicinity of 1s core state of H atoms. The ELF values decrease in the order ~0.9 (red)<~0.75 (yellow) < ~0.65 (green) < ~0.3 (sky) < ~0.05 (blue) as we move from H sites to Zr sites. The ELF of ZrH_2 shows that there is significant charge transfer from Zr to H atoms indicating more ionic bond character which is also consistent with the charge density contour given in Fig. 5.4. Although the electronic structure is unable to distinguish ZrH_2 from its isotopic analogues ZrD_2 and ZrT_2, but it provides in depth information about the nature of chemical bonding of ZrH_2. After establishing the electronic structure of ZrH_2, the isotopic effect on the ZrX_2 (X=H, D and T) compounds has been described in terms of vibrational and thermodynamic properties in the proceeding sections.

95

c) Vibrational Properties

According to lattice vibration theory [113], vibrational frequency ω is a function of both direction and magnitude of wave vector q, which is described by the dispersion relation:

$$\omega = \omega_j(q) \tag{5.1}$$

The subscript j is the branch index. A crystal lattice with n atoms per unit cell has 3n branches, three of which are acoustic modes and the remainders are optical modes. The dispersion curve exhibits symmetry properties in q-space, which enables us to restrict consideration to the first Brillouin zone only. The lattice vibration mode with $q \approx 0$ plays a dominant role for Raman scattering and infrared absorption [114]. For this reason, the vibrational frequency with $q = 0$, *i.e.* at the centre Γ point of the first Brillouin zone, is called as normal mode of vibration. Since the tetragonal structure of ZrX_2 (X= H, D, T) contains 3 atoms per unit cell, so there are nine normal modes of vibrations, which includes three low frequency acoustic modes and six high frequency optical modes. The light atom H has larger displacement amplitude which corresponds to high frequency optical modes and the slow moving heavy atom Zr corresponds to low frequency optical modes. According to group theory [115], the irreducible representations of normal modes at Brillouin zone centre (Γ point) can be expressed as

$$2a: \Gamma_{aco} = 2E_u(IR) + A_{2u}(IR) \text{ (for Zr)} \tag{5.2}$$

$$4d: \Gamma_{opt} = 2E_u(IR) + A_{2u}(IR) + 2E_g(R) + B_{1g}(R) \text{ (for H)} \tag{5.3}$$

where (IR) and (R) stand for infra red active and Raman active modes respectively; subscript u and g represents antisymmetric and symmetric modes respectively with respect to the center of inversion. The calculated phonon frequencies at the Γ point of ZrX_2(X= H, D and T) are listed in Table 5.2.

Table 5.2: Phonon frequency at the Γ point of ZrH$_2$

Branch			Wyckoff	Mode	Multiplicity	Frequency (THz)	Active mode
ZrH$_2$	*Acoustic*		2a (Zr)	E_u	2	-0.343	Infrared
				A_{2u}	1	-0.121	Infrared
	Optical		4d (H)	E_u	2	31.866	Infrared
				A_{2u}	1	33.645	Infrared
				E_g	2	36.744	Raman
				B_{1g}	1	39.364	Raman
ZrD$_2$	*Acoustic*		2a (Zr)	E_u	2	-0.340	Infrared
				A_{2u}	1	-0.120	Infrared
	Optical		4d (D)	E_u	2	22.774	Infrared
				A_{2u}	1	24.049	Infrared
				E_g	2	25.982	Raman
				B_{1g}	1	27.834	Raman
ZrT$_2$	*Acoustic*		2a (Zr)	E_u	2	-0.336	Infrared
				A_{2u}	1	-0.119	Infrared
	Optical		4d (T)	E_u	2	18.790	Infrared
				A_{2u}	1	19.845	Infrared
				E_g	2	21.214	Raman
				B_{1g}	1	22.727	Raman

The phonon dispersion curves show how the phonon energy depends on the q-vectors along the high symmetry directions in the Brillouin zone. This information can be obtained experimentally from neutron scattering experiments on single crystals. The phonon dispersion curves and corresponding phonon density of states (PHDOS) at 0 K for ZrX$_2$ (X= H, D, T) have been obtained by plotting vibrational frequencies along the high symmetry directions, which are shown in Figs. 5.6-5.8.
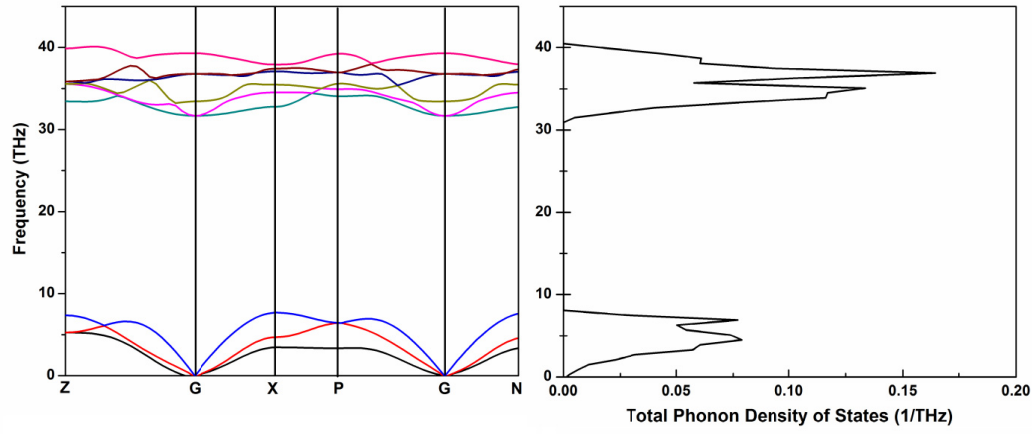
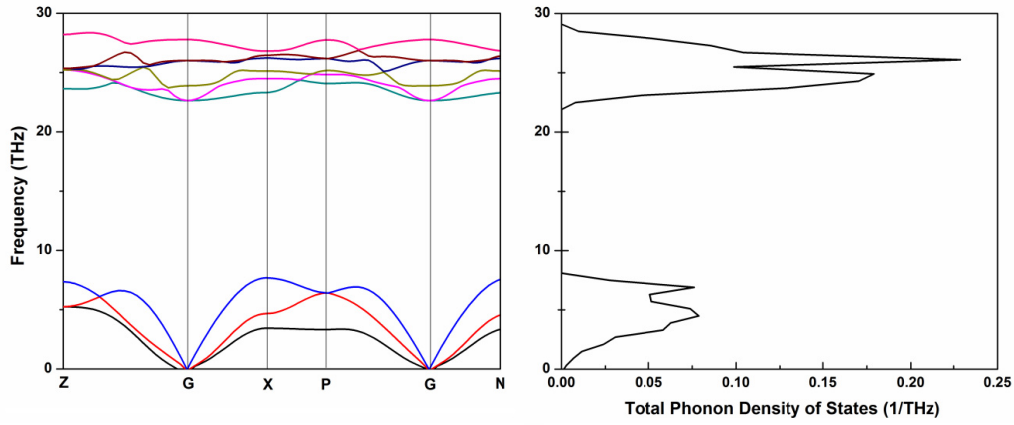**Fig. 5.6: Phonon dispersion graph and phonon density of states of ZrH$_2$**

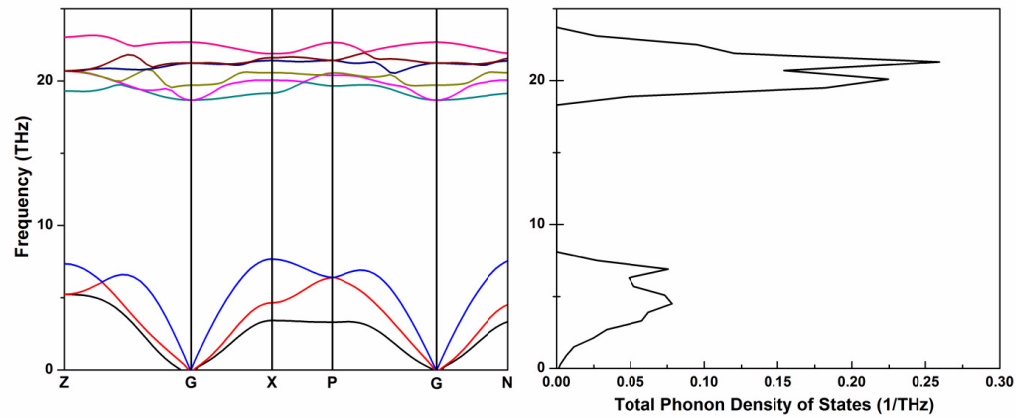**Fig. 5.7: Phonon dispersion graph and phonon density of states of ZrD$_2$**

Fig. 5.8: Phonon dispersion graph and phonon density of states of ZrT$_2$

It is shown that the dispersion curves and corresponding PHDOS resemble each other for ZrH$_2$, ZrD$_2$ and ZrT$_2$ compounds. The acoustic frequencies of ZrX$_2$ (X= H, D, T) are

imaginary and the optical phonon frequencies are positive. This indicated that the tetragonal structure of ZrX_2(X= H, D, T) is dynamically unstable which is in accordance with the previous studies [116]. Despite some differences in the exact position of the optical modes among the ZrX_2 (X = H, D, T) compounds, the spectral feature of the phonon dispersion curves and PHDOS show similar pattern. It is known that the mass difference between the constituent elements of the compound strongly affects the maximum and minimum values of the acoustic and optical branches. Thus a frequency gap between these two branches is formed, as can be seen in Figs. 5.6-5.8. It is observed that the gap between the high frequency optical modes and low frequency acoustic modes decreases as heavier isotopes are substituted in ZrX_2. The range of the frequency gap varies from ~24 THz (ZrH_2) to ~15 THz (ZrD_2) to ~11 THz (ZrT_2). However, the PHDOS frequency of Zr for all the three compounds remains constant in the range ~0 to 7 THz.

d) Thermodynamic Properties

Thermodynamic properties, particularly, zero point energy is another important parameter to describe the isotopic effect on the ZrX_2 (X=H, D and T) compounds. Here in this section, the isotopic effect has been described in terms of thermodynamic properties of the compounds. The temperature-dependent thermodynamic functions of a crystal, such as the internal energy (E), entropy (S), Helmholtz free energy (F) and constant volume heat capacity (C_V) are calculated from their phonon density of states as a function of frequencies

The variation of F, E, S, C_V are shown in Fig. 5.9 (a-d) upto 800 K, which is below the decomposition temperature of ZrH_2.
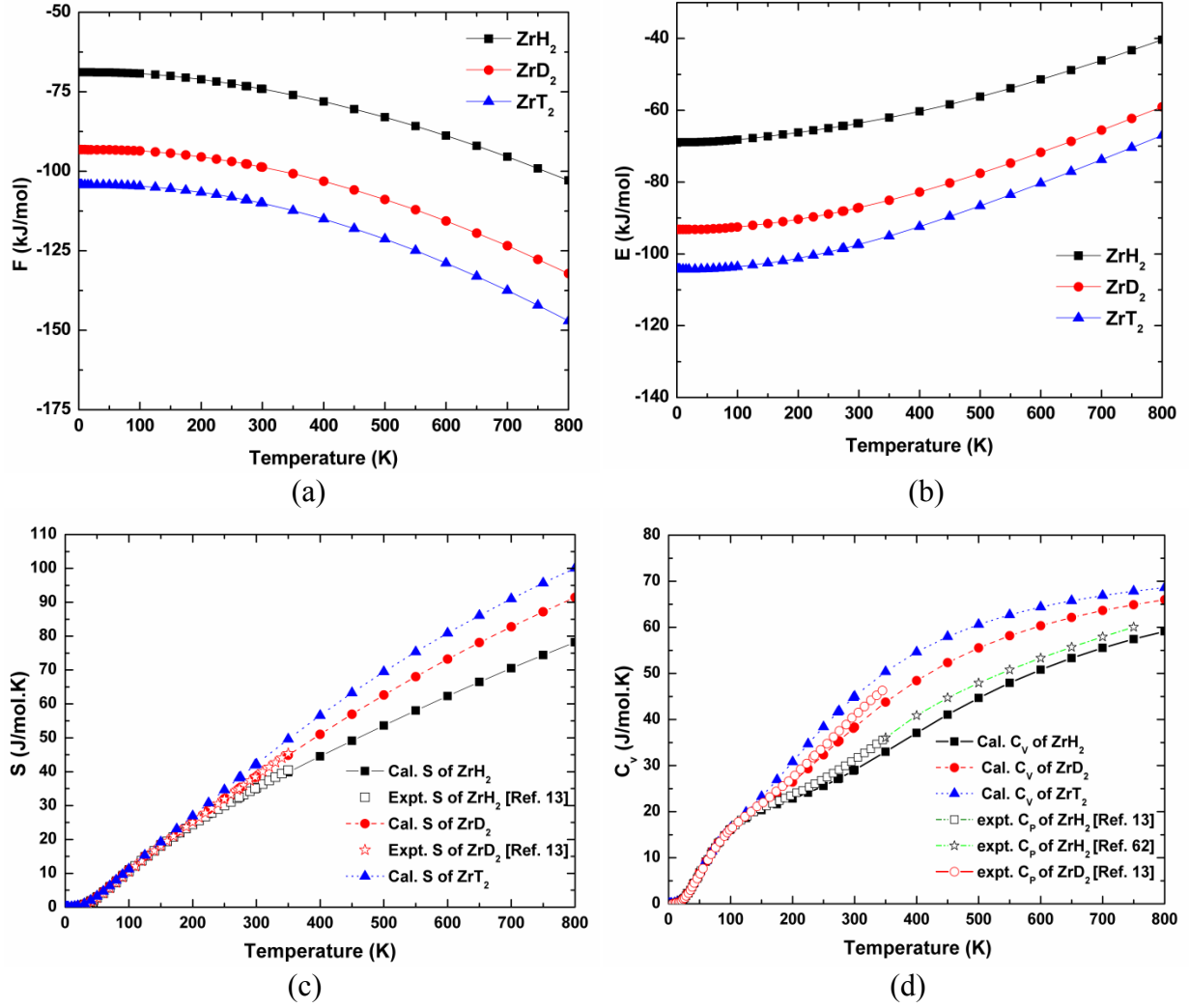
Fig. 5.9: Calculated thermodynamic functions of ZrX$_2$ (X= H, D and T) compounds

It may be noted that the *F* and the *E* at 0 K represents the zero point energy, which can be calculated from the expression as $F_0 = E_0 = 3nN \int_0^{\omega_{max}} \left(\frac{\hbar\omega}{2}\right) g(\omega)d\omega$, where *n* is the number of atoms per unit cell, *N* is the number of unit cells, ω is the phonon frequencies, ω_{max} is the maximum phonon frequency, and g(ω) is the normalized phonon density of states with $\int_0^{\omega_{max}} g(\omega)d\omega = 1$.

The formation of ZrX$_2$ from its constituent elements is described by the chemical reaction:

Zr(s) + X$_2$(g) = ZrX$_2$(s)   (X = H, D, and T)   (5.4)

Hence, the enthalpy of formation of ZrX$_2$from the elements at any temperature (*T*) can be calculated using the following equation [117]:

$$\Delta_f H \ (ZrX_2, \ T) = (E_{tot} \ (ZrX_2, \ T) + ZPE \ (ZrX_2)) - (E_{tot} \ (Zr, \ T) + ZPE \ (Zr)) - (E_{tot} \ (X_2, \ T) + ZPE$$

$$(X_2)) \hspace{2cm} (ZPE = \text{zero point energy}) \hspace{3cm} (5.5)$$

The calculated zero point energies (ZPE) are 45.08, 33.29 and 27.75 kJ/mol for ZrH_2, ZrD_2

and ZrT_2, respectively. For the constituent element Zr, the calculated ZPE is 2.67 kJ/mol and

for X_2 (X= H, D, and T), the calculated ZPEs are 26.3, 18.7 and 15.3 kJ/mol X_2, respectively.

The enthalpy of formation ($\Delta_f H$) at 0 K for ZrH_2 is found to be -159.79 kJ/mol without ZPE

contribution. After including the ZPE corrections, the heat of formation of ZrH_2 changes

from -159.79 to -143.68 kJ/mol. Similarly, ZPE corrected $\Delta_f H$ for ZrD_2 and ZrT_2 are -147.87

and -150.01 kJ/mol, respectively. Sieverts $et. \ al$ [118] and Flotow $et. \ al$ [105] reported the

enthalpies of formation of ZrH_2 and ZrD_2 are -169.65 and -173.84 kJ/mol, respectively at 298

K. However, they did not include the ZPE correction. It is interesting to mention that,

although ZrH_2 and its isotopic analogues ZrD_2 and ZrT_2 have the same crystal and electronic

structure, ZrT_2 and ZrD_2 are more stable than ZrH_2. This is in line with the prediction made

by Hu et al. [119] and Frankcombe et al. [120]. Fig. 5.9(a) shows that the free energy (F) for

all three hydrides decreases gradually with increase in temperature. In contrast, the internal

energy E and entropy S increases with increase in temperature as shown in Fig. 5.9(b) and

5.9(c). Moreover, a good agreement between the experimental and calculated values of

entropy (S) was obtained for ZrH_2 and ZrD_2. After establishing the accuracy of the calculated

entropy for ZrH_2 and ZrD_2, it can be argued that the calculated entropy of ZrT_2, for which

experimental data is not available, will be reasonably accurate.

We have also calculated the heat capacities of ZrX_2 (X = H, D, and T), which is an

interesting parameter to understand the thermodynamic stability of solids. The temperature

dependence of heat capacity (C_V) of ZrX_2 (X= H, D, T) is shown in Fig. 5.9(d). It is seen that

at low temperature, upto 600 K, the heat capacities of ZrX_2(X = H, D, and T) increase rapidly

with increase in temperature and thereafter increases slowly up to 800 K, and attain the

saturation value of ~70 J/mol.K. This is the Dulong-Petit classical limit. From the fig. 5.9(d) it is seen that upto 100 K, the variation of C_V versus T curve follows the same trend for all ZrX$_2$ compounds, but above 100 K it shows different trend: $C_V(ZrT_2) > C_V(ZrD_2) > C_V(ZrH_2)$. In addition, the heat capacity plot shows a broad hump around 100 K for all three compounds. This is in agreement with the previously reported results of Flotow and Osborne [105]. At low temperature, below 100 K, the acoustic modes in which the Zr and H atoms are vibrating 'in-phase' dominate the heat capacity contribution. At higher temperature, above 100 K, the optical modes of vibration in which the light H atoms vibrate against the heavy and almost stationary Zr atoms, dominates the heat capacity. Hence, around 100 K, this transition from predominant acoustic vibration to optical vibration cause a change in heat capacity function thus showing a broad hump. Now we compare the calculated heat capacity with the available experimental results. As it is not possible to measure the C_V directly from experiments, so the calculated C_V was compared with the experimentally reported C_P values. In this context, it needs to be mentioned that although C_p values are available for ZrH$_2$ and ZrD$_2$, no experimental results are available for ZrT$_2$. For solids, the relation between C_P and C_V is $C_P - C_V = \alpha^2 TVB$, where α is the thermal expansion coefficient, V is the molar volume, and B is the bulk modulus of the system. It is reported that the difference between C_P and C_V is on the order of a few percent of C_V [121]. Since the data of C_V calculated from phonon DOS represents only the vibrational contribution, the calculated C_V data of ZrH$_2$ from 0-20 ^{0}K have been fitted with the equation $C_V = 1943.9 \left({T}/{\theta_D} \right)^3$ where θ_D is the Debye temperature. The Debye temperature θ_D obtained by fitting the C_V versus T graph of ZrH$_2$ is 324.4 K, which is in good agreement with the experimentally reported value of 311.4 K for ZrH$_2$ [13]. The calculated C_V and S values of ZrH$_2$ and ZrD$_2$ at 298 K are compared with the experimental data in Table 5.3.

Table 5.3: The calculated and experimental specific heat and entropy of ZrH$_2$, ZrD$_2$ and ZrT$_2$

System	Calculated (J mol^{-1}K^{-1})		Experimental (J mol^{-1}K^{-1})	
	C_V (at 298 K)	S (at 298 K)	C_P (at 298.15 K)	S (at 298.15 K)
ZrH$_2$	28.88	34.87	30.98 ± 0.06[a], 30.96[b]	34.83±0.08[a], 35.02[b]
ZrD$_2$	38.10	38.27	40.34±0.08[a]	38.40±0.08[a]
ZrT$_2$	44.76	41.93	-	-

[a]Ref. [105], [b]Ref. [122]

Although the calculated C_V is marginally different than the experimental C_P values, but the calculated S values are in excellent agreement with the experimental data. The difference between the calculated and experimental values of heat capacity at high temperature is attributed to two reasons; (i) the anharmonicity effect and (ii) electron phonon coupling.

5.2 *Ab-initio* Study of ZrCo and ZrCoX$_3$ (X= H, D and T) Compounds

5.2.1 Computational Details

The computational details for this study are already described in section 2.9.3 of chapter 2.

5.2.2 Results and Discussion

a) Crystal structure

The ground state crystal structures data and the optimized lattice parameters of α-Zr, Co, ZrCo and ZrCoH$_3$ are summarized in Table 5.4.

Table 5.4: Crystal structure data of α-Zr, Co, ZrCo and ZrCoH$_3$

System	Crystal system	Space group	Calc. lattice parameters (at 0 K)	Expt. (at 298 K) [Ref.]
α-Zr	hcp	*P63/mmc*	a (Å) = 3.230	3.233 [109]
			c (Å) = 5.169	5.150
			V_0 (Å^3) = 46.62	46.70
Co	hcp	*P63/mmc*	a (Å) = 2.484	2.507 [123,95]
			c (Å) = 4.039	4.070
			V_0 (Å^3) = 21.59	22.15
ZrCo	bcc	*Pm-3m*	a (Å) = 3.181	3.196 [124,125]
			V_0 (Å^3) = 32.19	32.65
ZrCoH$_3$	orthorhombic	*Cmcm*	a (Å) 3.531	3.527 [126,127]
			b (Å) 10.395	10.463
			c (Å) 4.311	4.343
			V_0 (Å^3) 79.11	80.13

The lattice parameters are found to be within ± 1% accuracy from the experimental data. The good agreement between calculated and experimental values provides confidence for further the calculations of the ground state properties of ZrCo and ZrCoH$_3$. The crystal structure of ZrCo is CsCl-type cubic (bcc) with lattice parameter a = 3.196 Å [124,125] as shown in Fig. 5.10. The hydride of ZrCo, i.e.; ZrCoH$_3$ favors a simple orthorhombic ZrNiH$_3$-type crystal structure as shown in Fig. 5.11 with the room temperature lattice parameters listed in Table 5.4 [126,127].
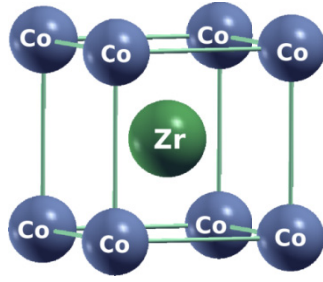
Fig. 5.10: Unit cell of ZrCo
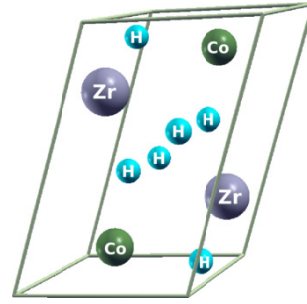
Fig. 5.11: Unit cell of ZrCoH₃

The crystal structure shown in Fig. 5.11 contains two unit cell of $ZrCoH_3$. During hydrogenation, the crystal structure of the intermetallic compound ZrCo (CsCl type) undergoes reconstruction into orthorhombic structure of $ZrCoH_3$. The present computational approach predicts a volume expansion of ZrCo due to hydrogenation to be 22.9% whereas the reported value by Gupta using LMTO-ASA approach along with LDA is 21.8%. These two results compare well within ±5% [128].

To obtain the ground state structural parameters, the atomic and electronic structure of the ZrCo was optimized by varying the cell volume as well as the lattice parameters independently. The energy vs. volume plots (*E-V*) of the ZrCo and ZrCoH3 are shown in Fig. 5.12.
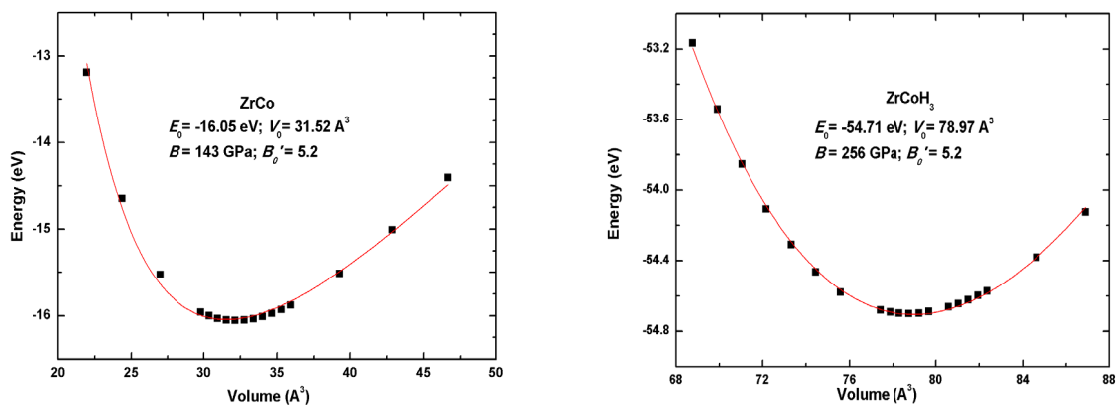
Fig. 5.12: Energy-Volume graph of ZrCo and ZrCoH₃

The parabolic *E-V* plot is fitted with Murnaghan equation of state to determine the equilibrium lattice constants and Bulk moduli (B_0) [84]. The calculated and experimental

bulk moduli for these compounds and their constituent elements α-Zr and Co are listed in Table 5.5 [124, 129-133].

Table 5.5: Total energies (E_{tot}) and bulk moduli (B_0) of ZrCoH₃, ZrCo, α-Zr and Co

System	E (eV)	E (eV)	B_0 (GPa)	
	Ionic opt.	E-V plot	Calculated	Experimental [Ref.]
ZrCoH₃	-55.50	-55.71	256	
ZrCo	-16.25	-16.05	143	140 [129]
α-Zr	-17.09	-16.88	85	92 [130], 96 [131], 97 [132], 83.3 [95]
Co	-14.23	-14.01	185	195 [133]
H₂	-6.725			

A very good agreement between the calculated and the experimental values of the structural parameters and bulk moduli for ZrCo and ZrCoH₃ reaffirms the reliability of the present computational method.

b) Energetics and electronic properties

The enthalpy of formation of ZrCo and ZrCoH₃ are calculated using the following relations:

$$\Delta_f H \text{ (ZrCo, 0 K)} = E_{tot} \text{ (ZrCo)} - E_{tot} \text{ (Zr)} - E_{tot} \text{ (Co)} \tag{5.6}$$

$$\Delta_f H \text{ (ZrCoH}_3\text{, 0 K)} = E_{tot} \text{ (ZrCoH}_3\text{)} - E_{tot} \text{ (ZrCo)} - 1.5 E_{tot} \text{ (H}_2\text{)} \tag{5.7}$$

On the basis of the total energy values of each constituent species, the formation energies of ZrCo and ZrCoH₃ compounds have been estimated to be -55 kJ/mol and -91 kJ/mol of H₂ respectively, using equations (1) and (2). This suggests that ZrCoH₃ is thermodynamically more stable than ZrCo, which favors the formation of hydride from the intermetallic compound ZrCo. The total energies for the compounds under study along with the constituent

elements are listed in Table 5.5. The estimated values are compared with the available experimental data and shown in Table 5.6 [43-47].

Table 5.6: Enthalpy of formation of ZrCo and ZrCoH₃

System	Enthalpy of formation at 0K (calculated in this study)	Enthalpy of formation at 298 K (experimental values)	Enthalpy of formation by Miedema model
ZrCo	-55 kJ/mol	-35.8±0.7 kJ/mol [134] -42.2±1.0 kJ/mol [135]	-60.0 kJ/mol [136]
ZrCoH₃	-90 kJ/mol of H₂	-86.2 [137], -97.8 [138]	

To best of our knowledge there are no other reported literature data on enthalpy of formation of ZrCo and ZrCoH₃ either by experiment or by theory to compare with our calculated data. However, the data presented here is at 0 K. In practice, the hydrogenation of ZrCo takes place at higher temperature. In order to know the thermodynamic parameters like enthalpy and entropy of hydrogenation reaction of ZrCo, it is necessary to know these thermodynamic parameters of ZrCo and ZrCoH₃ as a function of temperature. This information can be generated if the enthalpy of formation at 0 K is combined with the heat capacity data of these compounds. Once these high temperature thermodynamic data for individual reactant and products are available, one can calculate the equilibrium dissociation pressure using the van't Hoff equation.

In order to underscore the chemical bonding in the ZrCo we have compared the total density of states spectrum of ZrCo and its constituent elements as shown in Fig. 5.13.
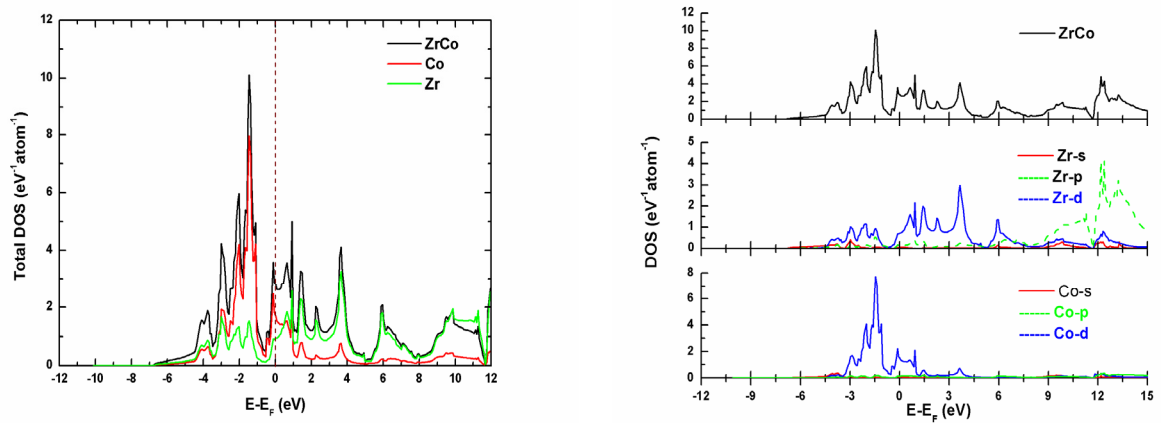
Fig. 5.13: Total and split density of state of ZrCo

It is seen that for both Zr and Co, the d-orbital electrons are contributing at the Fermi energy. Moreover, the d-orbital spectrum of Co is more localized (ranging from 1 to -4 eV) in comparison to that of d-orbital spectrum of Zr which is more delocalized over a wide range (from 12 to -4 eV) and at the fermi energy of ZrCo, the d-orbital contribution of Co is more than Zr. The calculated total DOS of ZrCo at the fermi energy is $N(E_F)$= 2.763 states per eV-formula unit. The coefficient of electronic specific heat γ is estimated to be 6.505 mJ/ mol–K^2, which is in line with the reported value of 7.44 mJ/ mol–K^2 [139]. The overlap of *d*-states of both Zr and Co at fermi energy ensures the metallic nature of the ZrCo compound. After analyzing the DOS of the ZrCo intermetallic we examined the effect of hydrogenation on its electronic structure. For this purpose we have plotted the total and orbital projected DOS of the ZrCoH$_3$ as shown in Fig. 5.14.
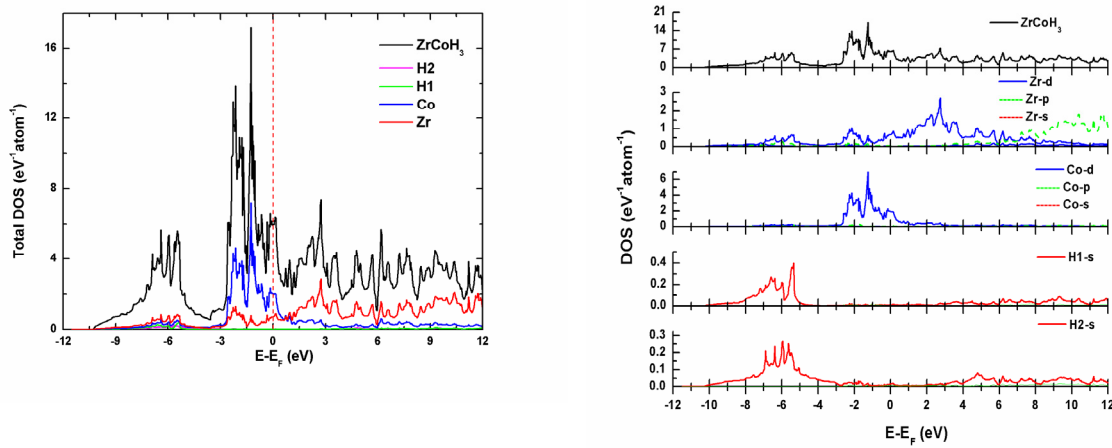
Fig. 5.14: Total and split density of state of ZrCoH₃

It is clear from these figures that the 4d and 3d orbitals of Zr and Co have contributed significantly to the fermi energy. Below the fermi energy (in the range of -6 to -12 eV), two new peaks are found in the density of states spectrum of ZrCoH₃ in comparison to ZrCo. These new peaks are due to two types of hydrogen atoms H1 (4c) and H2 (8f) in the ZrCoH₃. The Fermi energy of the ZrCoH₃ is 0.336 eV lower than the intermetallic ZrCo. The lowering of the fermi energy (E_F) is attributed to the hydrogenation of ZrCO, which induces lattice expansion, and the higher chemical stability of the hydride. The total DOS at E_F of ZrCoH₃ is 2.982 states per eV-f.u. in ZrCoH₃. The coefficient of electronic specific heat (γ) calculated from the total DOS at E_F is estimated to be 7.021 mJ/ K²-mol.

The understanding of the chemical bonding in ZrCo and ZrCoH₃ was further substantiated by comparing the charge density distribution between these two compounds as shown in Fig. 5.15.
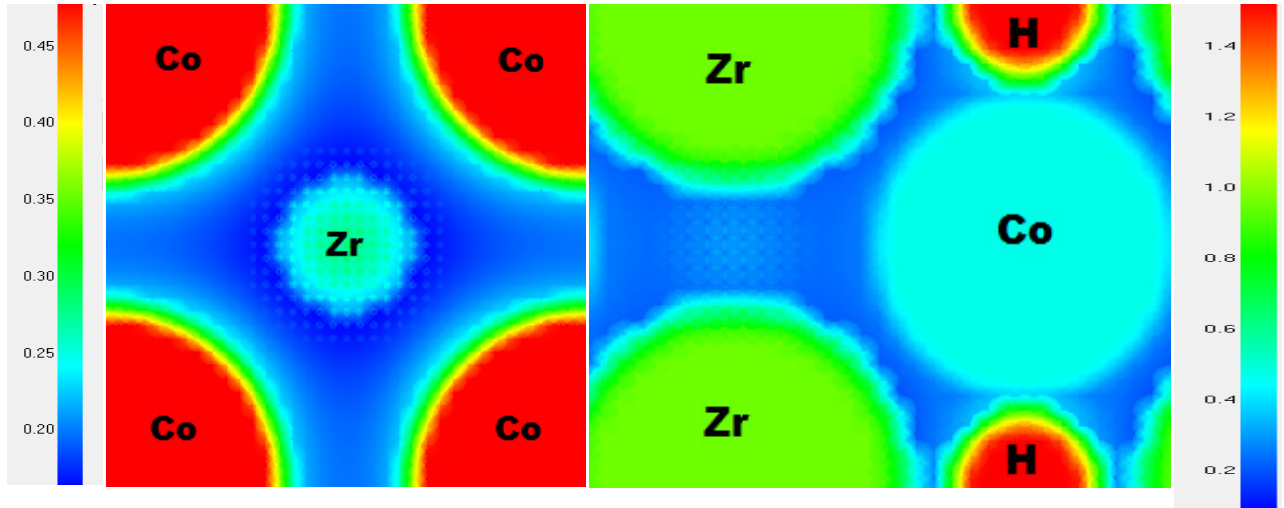
Fig. 5.15: Charge density contours of ZrCo and ZrCoH₃

The color bar graph shows relative electron density across the figure. For ZrCo, it is seen that more electronic charges are localized at the Co than Zr, thus polarizing the Zr-Co bond. It has been observed that for $ZrCoH_3$, the electronic charges are localized in the decreasing order of H, Zr and Co, respectively.

c) Vibrational Properties

The dispersion relation between vibrational frequency ω and wave vector q can be expressed as [115]:

$$\omega = \omega_j(q) \tag{5.8}$$

The subscript j is the branch index. Generally, a crystal lattice with n atoms per unit cell has 3n branches, three of which are acoustic modes and the remainders are optical modes. The lattice vibration mode with $q \approx 0$ plays an important role for Raman scattering and infrared absorption [116]. So, the vibrational frequency with $q = 0$, *i.e.* at the centre Γ point of the first Brillouin zone, is called as normal mode of vibration. The crystal structure of ZrCo contains 2 atoms per unit cell, so there are six normal modes of vibrations, which includes three low frequency acoustic modes and three high frequency optical modes. As the $ZrCoX_3$ (X= H, D and T) compounds contains two unit cell having total number of 10 atoms, there are 30

normal vibrational modes among which three are acoustic and the remainder are optical modes. The light atom H has larger displacement amplitude which corresponds to high frequency optical modes and heavy atoms Zr and Co corresponds to low frequency optical modes. According to group theory [117], the irreducible representations of normal modes at Brillouin zone centre (Γ point) for ZrCo can be expressed as

$$\Gamma_{aco} = 3T_{1u}(IR), \quad \Omega_{acu} = 0.012 \text{ THz} \tag{5.9}$$

$$\Gamma_{opt} = 3T_{1u}(IR), \quad \Omega_{opt} = 5.318 \text{ THz} \tag{5.10}$$

Similarly, the phonon frequencies at Brillouin zone centre (Γ point), the IR and Raman active modes of ZrCoX$_3$ (X= H, D and T) are given in Table 5.7.

Table 5.7: Phonon frequency (in THz) at the Γ point (Ω) of ZrCoX$_3$ (X= H, D and T)

ZrCoX$_3$ (X = H, D and T)											
IR				Raman				Silent			
	H	D	T		H	D	T		H	D	T
Mode	Ω	Ω	Ω	Mode	Ω	Ω	Ω	Mode	Ω	Ω	Ω
B2u	img	img	0.196	B1g	4.158	4.141	4.153	Au	30.682	21.696	18.466
B1u	img	img	img	B1g	4.343	4.331	4.505				
B3u	0.198	0.196	0.209	Ag	4.413	4.401	4.383				
B3u	5.000	4.979	5.311	B3g	4.578	4.557	4.650				
B1u	5.018	5.001	5.220	B3g	6.392	6.364	6.617				
B2u	5.055	5.042	4.838	Ag	6.756	6.730	6.931				
B3u	28.957	20.669	17.393	B1g	29.262	20.767	17.295				
B1u	28.967	20.508	16.533	B3g	30.050	21.300	17.582				
B1u	29.147	20.734	17.505	B3g	30.296	21.447	17.849				
B2u	30.021	21.309	18.512	Ag	30.615	21.686	18.609				
B3u	31.713	22.521	18.793	B2g	32.566	23.028	19.764				
B2u	32.940	23.397	18.640	Ag	32.912	23.283	19.109				
B1u	41.494	29.517	19.721	B1g	33.759	23.950	20.254				
B2u	43.462	30.876	21.384	B3g	42.756	30.394	20.391				
				Ag	44.569	31.647	21.911				

img = imaginary

The (IR) and (R) stand for infra red active and Raman active modes respectively; subscript u and g represents antisymmetric and symmetric modes respectively with respect to the center of inversion.

The phonon dispersion curves show how the phonon energy depends on the q-vectors along the high symmetry directions in the Brillouin zone. This can be compared with the experimental graph obtained from the neutron scattering experiments on single crystals. The phonon dispersion curves at 0 K for ZrCo and ZrCoX$_3$ (X= H, D, T) have been obtained by plotting vibrational frequencies along the high symmetry directions, as shown in Figs. 5.16-5.19.
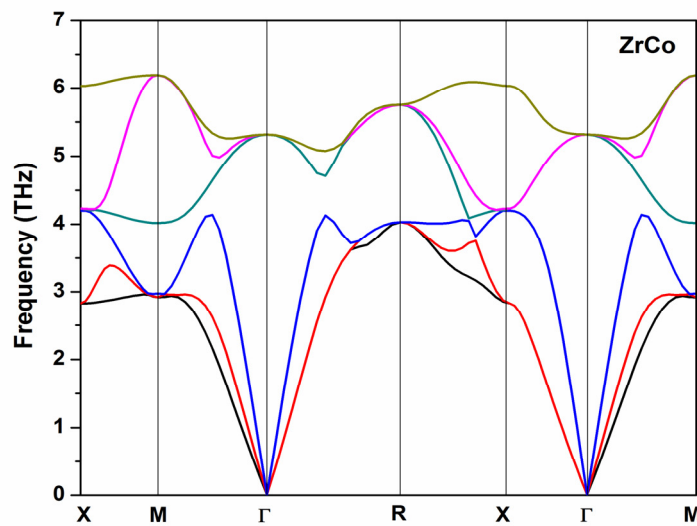
Fig. 5.16: Phonon dispersion graph of ZrCo
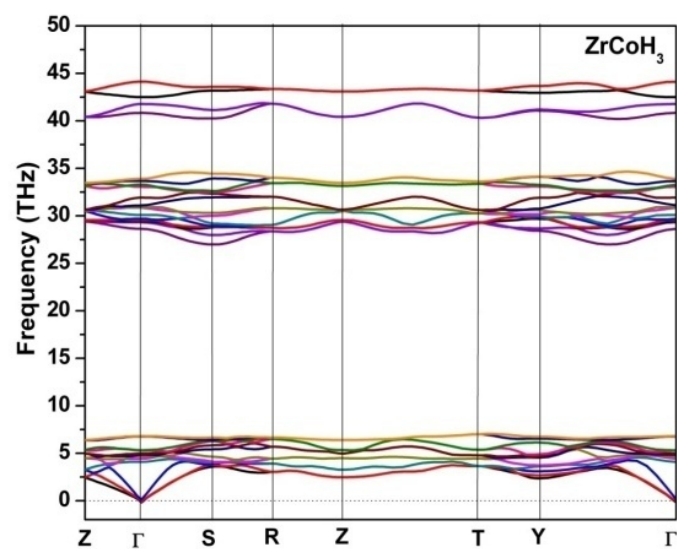
Fig. 5.17: Phonon dispersion graph of ZrCoH₃
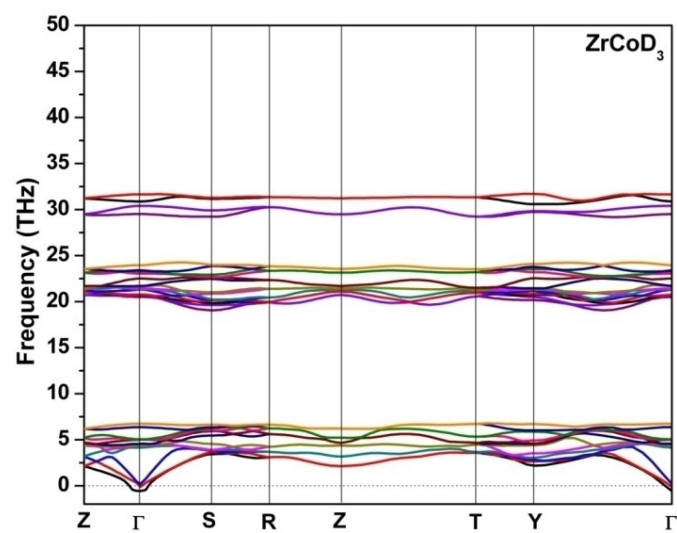
Fig. 5.18: Phonon dispersion graph of ZrCoD₃

113
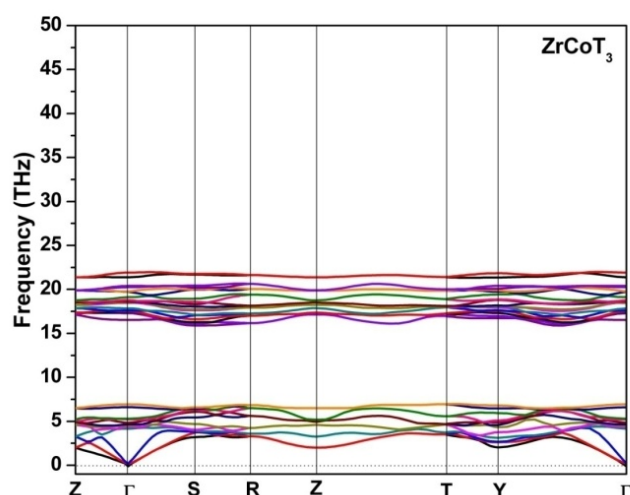
Fig. 5.19: Phonon dispersion graph of ZrCoT$_3$

For dynamical stability of a compound, the phonon frequencies for all the wave vectors should be positive. However, in computational calculations, if a particular calculation gives an imaginary frequency for any of the wave vectors, the compound is treated as dynamically unstable. Since, in this present study, all the acoustic and optical frequencies for ZrCo are positive, it can be inferred that this compound is dynamically stable. However, the B2u acoustic mode of ZrCoH$_3$ and ZrCoD$_3$ and B1u acoustic mode of ZrCoX$_3$ (X= H, D and T) are imaginary as shown in Table 5.7 and Figs. 5.17-5.19. Hence these three hydrides are dynamically unstable. The phonon dispersion curves of ZrCoH$_3$ and its analogue are almost similar but there are some distinct features in which they actually differ. The mass difference between the constituent elements of the compound significantly affects the maximum and minimum values of the acoustic and optical branches, and a clear gap is formed between them, as can be seen in Figs. 5.16-5.19. The gap between the high frequency optical modes and low frequency acoustic modes decreases by isotopic substitution in ZrCoX$_3$ from ~22 THz (ZrCoH$_3$) to ~16 THz (ZrCoD$_3$) and ~11 THz (ZrCoT$_3$). The higher frequency peaks come closer to Zr and Co peaks as we substitute H of ZrCoH$_3$ with the isotopes D and T which is attributed to the increase in mass.

114

d) Thermodynamic Properties

The calculated zero point energies (ZPE) are 5.01, 43.7, 32.1 and 26.2 kJ/mol for the ZrCo, ZrCoH$_3$, ZrCoD$_3$ and ZrCoT$_3$, respectively. The enthalpy of formation of ZrCo (at 0 K) changes from -55.9 kJ/mol to -51.0 kJ/mol after ZPE correction. The enthalpy of formation ($\Delta_f H$) at 0 K for ZrCoH$_3$ is -190.3 kJ/mol without considering ZPE. After including the ZPE correction, the heat of formation of ZrCoH$_3$ changes from -190.3 to -146.7 kJ/mol. Similarly, ZPE corrected $\Delta_f H$ at 0 K for ZrCoD$_3$ and ZrCoT$_3$ are -158.3 and -164.1 kJ/mol, respectively. It is interesting to note that, although ZrCoH$_3$ and its isotopic analogues ZrCoD$_3$ and ZrCoT$_3$ have the same crystal and electronic structure, ZrCoT$_3$ and ZrCoD$_3$ are more stable than ZrCoH$_3$. The variation of F, E, S and C_v are shown in Fig. 5.20(a-d) upto 600 K, which is below the decomposition temperature of ZrCoX$_3$ (X= H, D, and T).
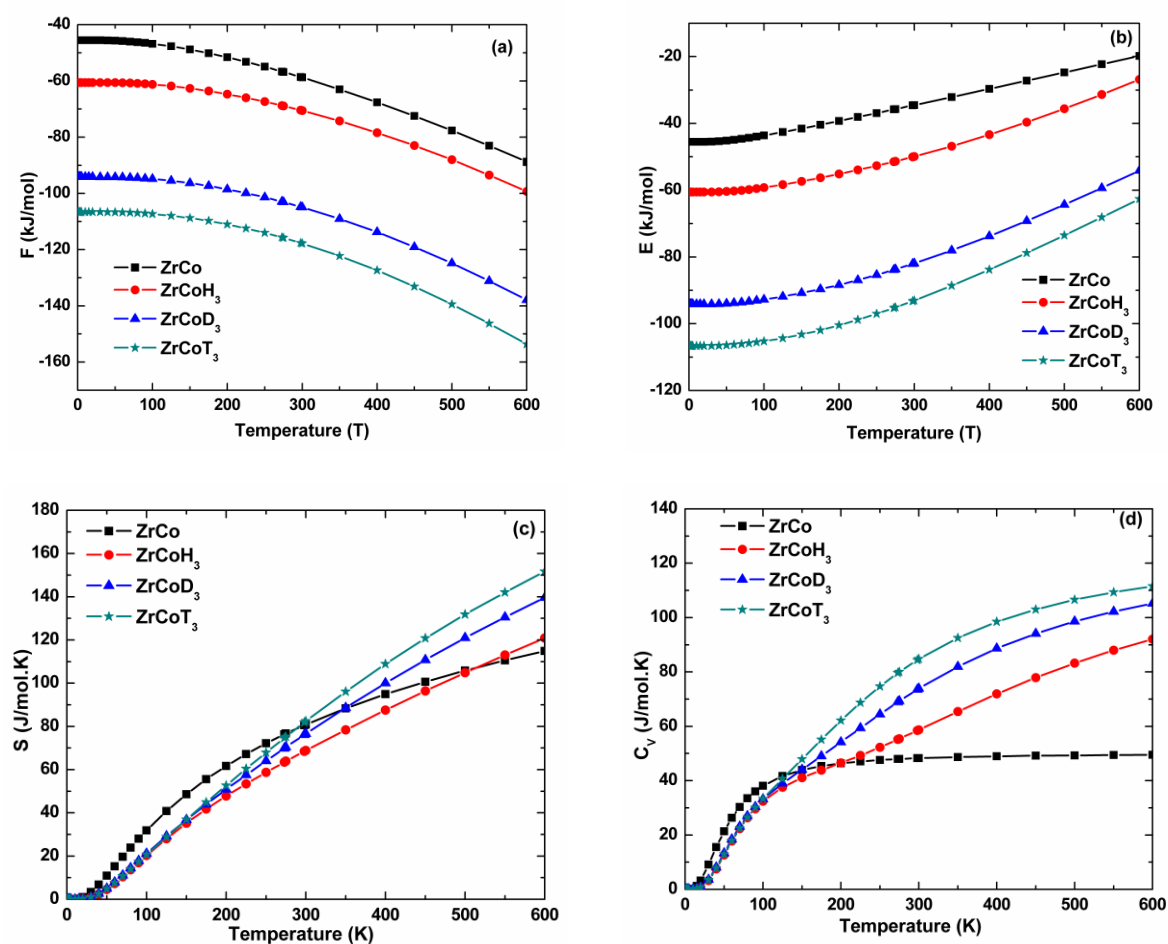
Fig. 5.20(a-d): Thermodynamic functions as a function of temperature

Fig. 5.20(a) shows that the Helmholtz free energy (F) for all three hydrides decreases gradually with increase in temperature. In contrast, the internal energy E and entropy S increases with increase in temperature as shown in Fig. 5.20(b) and 5.20(c).

Heat capacity of a solid is an important thermodynamic parameter which depicts the behavior of that material in different thermal conditions. We have also calculated the heat capacities of ZrCo and ZrCoX$_3$ (X = H, D, and T). The temperature dependent heat capacity (C_v) of ZrCo and ZrCoX$_3$ (X= H, D, T) is shown in Fig. 5.20(d). It is observed that the C_v of ZrCo increases rapidly upto 100 K and gradually attains a constant value of ~ 49 J/mol K. The calculated specific heat of ZrCo is found to be 2.8 x 10^{-3} J/mol K. This is in good agreement with the experimental value of 2.45 x 10^{-3} J/ mol K at 3 K [133]. It is also seen that at low temperature, upto 300 K, the heat capacities of ZrCoX$_3$ (X = H, D, and T) increase rapidly with increase in temperature and thereafter increases slowly up to 600 K, and attain the saturation value which is known as Dulong-Petit classical limit. From the fig. 6(d) it is seen that upto 100 K, the variation of C_v versus T curve follows the same trend for all ZrCoX$_3$ compounds, but above 100 K it shows different trend: C_v (ZrCoT$_3$) > C_v (ZrCoD$_3$) > C_v (ZrCoH$_3$). The heat capacities of hydrides are higher compared to its precursor alloy ZrCo. It is due to the contribution of high frequency optical modes of X$_2$ (X= H, D and T) to the C_v of hydrides. In addition, the heat capacity plot shows a broad hump around 100 K for all three compounds. At low temperature, below 100 K, the acoustic modes, in which the Zr, Co and H atoms are vibrating 'in-phase', dominate the heat capacity contribution. At higher temperature, above 100 K, the optical modes of vibration, in which the light H atoms vibrate against the heavy and almost stationary Zr and Co atoms, dominates the heat capacity. Hence, around 100 K, a transition from predominant acoustic vibration to optical vibration cause a change in heat capacity function leading to a broad hump.

e) Elastic Properties

The mechanical properties of solids are very important for various reasons, particularly, it depicts the behavior of a material under different stress and strain conditions [140]. The structural and mechanical stability, deformations, phase transformations, bonding characteristics, melting point etc. can be described by elastic stiffness parameters. The elastic constants of a solid are also related to mechanical properties such as bulk modulus, shear modulus, Young's modulus, poison's ratio and elastic anisotropy. The elastic constants are also useful to determine Debye temperature. Investigation of elastic contribution to the hydrogen-hydrogen interaction energy in metal hydrides [141] requires adequate knowledge of elastic constants. To investigate the mechanical stability of ZrCo and its hydride $ZrCoH_3$, a set of zero pressure elastic constants have been determined from the stress-strain approach [142] as implemented in the VASP code. The calculated single crystal elastic constants of ZrCo and its hydride $ZrCoH_3$ are listed in Table 5.8.

Table 5.8: Calculated elastic constants C_{ij} (in GPa) of ZrCo and $ZrCoH_3$

System		C11	C12	C13	C22	C23	C33	C44	C55	C66
ZrCo	This Study	174	134	-	-	-	-	36	-	-
$ZrCoH_3$	This Study	243	124	159	257	93	241	68	78	79

For body centered cubic (bcc) symmetry, there are three independent elastic constants, namely, C_{11}, C_{12} and C_{44}. The conditions for mechanical stability of cubic crystals are: $C_{11}-C_{12} > 0$, $C_{11} > 0$, $C_{44} > 0$, $C_{11}+2C_{12} > 0$, $C_{12} < B < C_{11}$ [143]. The calculated elastic constants (C_{ij}) of ZrCo alloy satisfy all of these conditions, hence it can be said that ZrCo is mechanically stable at ambient pressure. Similarly, for mechanically stable orthorhombic crystal, nine independent elastic constants C_{ij} should satisfy the following criteria [143]:

$C_{11} > 0, C_{22} > 0, C_{33} > 0, C_{44} > 0, C_{55} > 0, C_{66} > 0$ (5.11)

$[C_{11} + C_{22} + C_{33} + 2(C_{12} + C_{13} + C_{23})] > 0$ (5.12)

$(C_{11} + C_{22} - 2C_{12}) > 0$ (5.13)

$(C_{11} + C_{33} - 2C_{13}) > 0$ (5.14)

$(C_{22} + C_{33} - 2C_{23}) > 0$ (5.15)

In this study, the calculated elastic constants C_{ij} of orthorhombic $ZrCoH_3$ satisfy above conditions. Hence, $ZrCoH_3$ is mechanically stable at ambient pressure. In ZrCo, $C_{11} > C_{12} > C_{44}$, indicates that the bonding strength is strongest in (100) direction. In case of $ZrCoH_3$, it is seen that C_{11} and C_{33} have, almost, same value, which indicates that the atomic bonding between nearest neighbors along the (100) and (001) planes, have the same strength. However, $C_{22} > C_{33}$ for $ZrCoH_3$ implies that the atomic bonds along (010) planes between nearest neighbors are stronger than those along the (001) plane. This may be attributed to the bond formation between Co and H atoms in the (010) plane. Comparison of the elastic constants for the precursor alloy and its hydride indicates that the hydride is more resistant to both compressions in the a- and c-directions and especially to shear deformation, as C_{11}, C_{12} and C_{44} of $ZrCoH_3$ are higher than that of ZrCo. For ZrCo and $ZrCoH_3$, $C_{11} > C_{44}$, So deformation in the perpendicular direction to a-axis is easier than along c-axis. The shear elastic constants C_{44}, C_{55} and C_{66} are indicative of resistance to shear deformation whereas C_{11}, C_{22} and C_{33} are related to the unidirectional compression along the principal crystallographic directions. The calculated result shows that C_{44}, C_{55} and C_{66} values are more than 50% lower than that of C_{11}, C_{22} and C_{33}. This depicts that $ZrCoH_3$ has weak resistance to shear deformation compared to that of the unidirectional compression.

The elastic moduli of polycrystalline materials are generally calculated by two approximations, namely, Voigt [144] and Reuss [145] in which uniform strain or stress are assumed throughout the polycrystal. Later, Hill [1461] proposed that the actual elastic moduli

is the arithmetic mean of the Voigt and Reuss values, which is known as the Voigt-Reuss-Hill (VRH) value. The details of the calculations for the bulk and shear moduli is given in somewhere else [147,148] and therefore not recalled here. The Young's modulus and the Poisson's ratio can be obtained from the bulk and shear moduli [148]. The Cauchy pressure σ, Zener anisotropy factor A, Poisson's ratio ν and Young's modulus Y, which are important elastic parameters, are calculated using the following relations [149]:

$$\sigma = (C_{12} - C_{44}) \tag{5.16}$$

$$A = \frac{2C_{44}}{C_{11} - C_{12}} \tag{5.17}$$

$$\nu = \frac{3B - 2G}{2(3B + G)} \tag{5.18}$$

$$Y = \frac{9GB}{G + 3B} \tag{5.19}$$

where $G = (G_V + G_R)/2$ is the isotropic shear modulus, G_V is Voigt's shear modulus corresponding to the upper bound of G values, and G_R is Reuss's shear modulus corresponding to the lower bound of G values.

The Zener anisotropy, bulk modulus, shear modulus, Young's modulus and Poisson's ratio have been estimated from the calculated single crystal elastic constants, and are given in Table 5.9.

Table 5.9: Calculated elastic moduli (in GPa), Zenar anisotropy (A), Poisson's ratio (ν), ratio of B/G of ZrCo and ZrCoH₃

System		B	G	L	Y	A	ν	B/G
ZrCo	This Study	145.7	45.0	182.1	122.4	1.80	0.36	3.24
	[a]Reported	140.0	49.2	-	132	-	0.34	2.85
ZrCoH₃	This Study	162	63	246	168	*A1* = 1.64	0.33	2.57
						A2 = 1.0		
						A3 = 1.25		

[a]Ref [129]

Pettifor [150] and Johnson [151] suggested that ductile or brittle behavior of a material can be predicted by the Cauchy Pressure (C_{12}-C_{44}). For ductile material, Cauchy pressure is positive, while for brittle material, it is negative. For ZrCo, Cauchy pressure was found to be positive which indicates that ZrCo is ductile in nature. The Zener anisotropy factor (A) represents the degree of elastic anisotropy in solids. The A takes the value of 1 for a completely isotropic material. If the value of A is smaller or greater than unity it shows the degree of elastic anisotropy. The calculated Zener anisotropy factor for ZrCo is 1.80 at 0 GPa, which indicates that the compounds are entirely anisotropic. The shear anisotropic factors of different Miller planes express the degree of anisotropy in atomic bonding in those planes. The shear anisotropic factors are expressed as follows:

$$A_1 = \frac{4C_{44}}{C_{11}+C_{33}-2C_{13}} \qquad \text{for the 100 plane} \qquad\qquad (5.20)$$

$$A_2 = \frac{4C_{55}}{C_{22}+C_{33}-2C_{23}} \qquad \text{for the 010 plane} \qquad\qquad (5.21)$$

$$A_3 = \frac{4C_{66}}{C_{11}+C_{22}-2C_{12}} \qquad \text{for the 001 plane} \qquad\qquad (5.22)$$

The calculated A_1, A_2 and A_3 of $ZrCoH_3$ are 1.64, 1.0 and 1.25 respectively. For an isotropic crystal, the factors A_1, A_2 and A_3 must be equal to 1, while any value smaller or greater than 1 represents varying degree of anisotropy. The calculated results indicate that $ZrCoH_3$ is isotropic in (010) plane while anisotropic in (100) and (001) planes.

The average bond strengths between the atoms in a crystal can be predicted by knowing its bulk modulus [152]. The calculated bulk modulus of $ZrCoH_3$ is 162 GPa which is higher than that of ZrCo (146 GPa). This suggests that hydrogenation of ZrCo resulting $ZrCoH_3$ increases the fracture strength of ZrCo. The resistance of a material to size and shape change can be measured by the bulk modulus B and shear modulus G, respectively. The calculated results show that $ZrCoH_3$ is more resistant to size and shape changes than its precursor alloy ZrCo. Young's modulus indicates the resistance against uniaxial tensions and is indicative of stiffer

material. Accordingly, the high Young modulus value of ZrCoH$_3$ compared to ZrCo suggests that this hydride is stiffer than its precursor alloy. Poisson's ratio is the ratio of transverse contraction strain to longitudinal extension strain under a stretching force. It is also related to the bonding properties of materials. Poisson's ratio varies in different materials depending on the nature of bonding present in those materials. As for covalent materials, the value of ν is small (typically $\nu = 0.1$) whereas for ionic and metallic materials, the typical value of ν are 0.25 and 0.33, respectively [153]. The Poisson's ratio of ZrCo is 0.34, which indicate that it is metallic in nature. The lower limit and upper limit of Poisson's ratio ν are given 0.25 and 0.5, respectively, for central forces in solids [154]. In solids, most of the measured values fall in the range of 0.28 - 0.42. Our calculated values show that the interatomic forces in the ZrCo and ZrCoH$_3$ are predominantly central in nature. It is important to know the brittle and ductile behavior of metals, alloys and their hydrides. Pugh suggested that the ratio of bulk (B) to shear modulus (G) *i.e.* B/G is an important criteria to predict the brittle or ductile properties of a material [155]. A high value of B/G > 1.75 is responsible for the ductility; otherwise the material behaves as brittle. The ratio for ZrCo is larger than 1.75, and the results suggest that the ZrCo phase is ductile in nature which is supported by the calculated Cauchy pressure in this study. It has recently been reported that elastic properties, specially ductility, bulk to shear modulus ratio (B/G), Poisson's ratio (ν) etc., are related to the initial hydriding mechanism [156]. In this present study, the B/G value of ZrCoH$_3$ has been calculated and compound with those of other hydrides available in literature [157-161] are listed in Table 5.10.

Table 5.10: Comparison of bulk modulus (B), shear modulus (G), B/G ratio for different hydrides

Hydride	Method	B (GPa)	G (GPa)	B/G	Ductile/Brittle
α-UH$_3$	Theory[a]	97	74	1.31	brittle

Cubic MoH	Theory[b]	182	151	1.21	brittle
Cubic TcH	Theory[b]	189	150	1.26	brittle
Cubic RuH	Theory[b]	199	158	1.26	brittle
ZrCoH$_3$	This study	162	63	2.57	ductile
fct ZrH$_2$	Theory[c]	130	29	4.48	ductile
PtH	Theory[d]	294	120	2.45	ductile
IrH	Theory[d]	273	100	2.73	ductile
α-MPd$_3$H$_{0.5}$	Theory[e]	136.96	47.38	2.89	ductile

[a]Ref [157], [b]Ref [158], [c]Ref [159], [d]Ref [160], [e]Ref [161]

It is observed that B/G value of ZrCoH$_3$ is very high suggesting its ductile nature compared to the brittle hydrides having B/G < 1.75.

The elastic moduli of a solid are also related to the thermal properties of solid through the Debye theory. The Debye temperature (θ_D) is related to many important physical properties such as specific heat, elastic constants, and melting point [162]. The Debye temperature and mean, transverse, longitudinal sound velocities have been calculated using the following well-known relations [163]:

$$\theta_D = \frac{\hbar}{k}\left[\frac{3n}{4\pi}\left(\frac{N_A\rho}{M}\right)\right]^{1/3} v_m \qquad (5.23)$$

where $\hbar$ is the Planck's constant, k is Boltzman's constant, N_A is Avogadro's number, n is the number of atoms per formula unit, ρ is the density and M is the molecular weight.

Mean(v_m), transverse (v_t) and longitudinal (v_l) sound velocities are given, respectively, as

$$v_m = \left[\frac{1}{3}\left(\frac{2}{v_t^3} + \frac{1}{v_l^3}\right)\right]^{1/3} \qquad (5.24)$$

$$v_t = \left(\frac{G}{\rho}\right)^{1/2} \qquad (5.25)$$

$$v_l = \left(\frac{3B+4G}{3\rho}\right)^{1/2} \qquad (5.26)$$

The calculated elastic constant can be used to determine the melting temperature T_m of solids. The melting temperature of (T_m) has been estimated using an empirical relation [164],

$$T_m(K) = 553 + (591/MBar)C_{11} \pm 300 \tag{5.27}$$

Using the equation (5.27), the melting point of ZrCo is calculated to be 1581.3 ± 300 K which is agreement with the experimental value melting point (1622 K) of ZrCo [165]. All calculated quantities from Eq. (5.23 - 5.27) are listed in Table 5.11.

Table 5.11: Calculated sound velocities (m/s) and Debye temperature (K) of ZrCo and ZrCoH₃

System		V_l (m/s)	V_t (m/s)	V_m (m/s)	θ_D (K)	T_m (K)
ZrCo	This Study	4785	2433	2785	259.3	1581.3 ± 300
	[a]Reported	5338	2640	2960	281.3	-
ZrCoH₃	This Study	6191	3139	3593	315.8	-

[a]Ref [129]

The calculated Debye temperature (θ_D) of ZrCo agrees well with the experimental value of 281.3 K [129]. It is seen from the Table 5.11 that, Debye temperature of ZrCo is lower than ZrCoH₃. As Debye temperature of a solid represents the interatomic force, the high θ_D value of ZrCoH₃ compared to its ZrCo indicates that ZrCoH₃ has stronger bonds than ZrCo.

5.3 Enthalpy Increment Study of ZrCo

5.3.1 Material Preparation and Characterization

The preparation of the ZrCo alloy is already described in section 3.2.3 (b) of chapter 3. The polished specimen of synthesized intermetallic was characterized by X-ray powder diffraction method. X-ray diffraction measurements were carried out using a diffractometer (theta–theta geometry) supplied by GNR Analytical Instruments Group, Italy (Model: EXPLORER) with Cu Ka (l = 1.5418 Å) radiation at 40 kV and 30 mA.

The X-ray diffraction pattern of $Zr_{0.5}Co_{0.5}(s)$ was shown in Fig. 5.21.
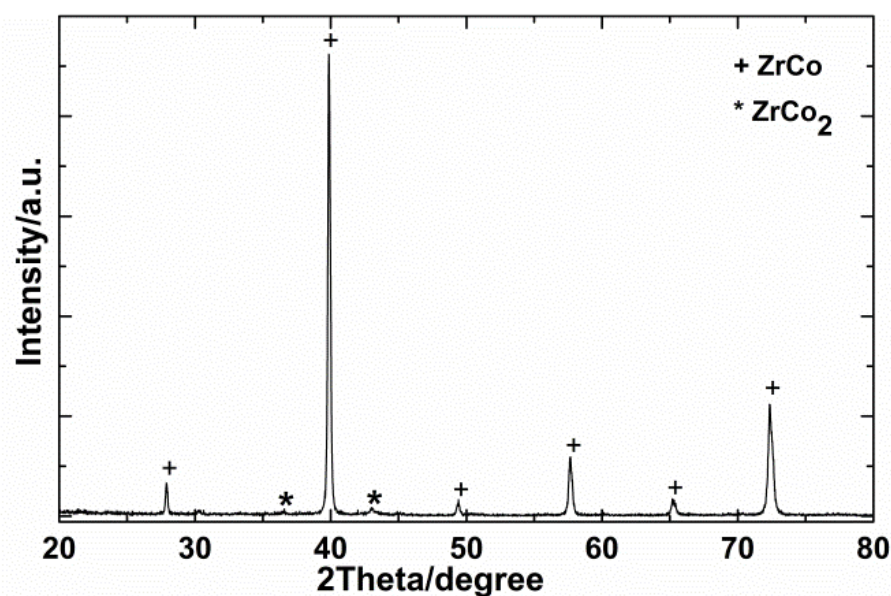
Fig. 5.21: XRD pattern of $Zr_{0.5}Co_{0.5}$ (s)

The formation of ZrCo phase (cubic structure) was confirmed by comparing XRD pattern obtained in this study with that reported in the JCPDS file no: 18-0436 [166]. It is evident from fig. 5.1 that a trace amount of $ZrCo_2$ phase is present. A Rietveld analysis of XRD pattern confirms the phase fraction of $ZrCo_2$ to be around 2 volume %. The contribution of enthalpy increment due to this impurity phase is within the measurement error and hence, will not affect the final tabulated values of thermodynamic functions.

5.3.2 Computational Details

The computational details for this study are already described in section 2.9.3 of chapter 2. The quasi-harmonic Debye model was used to calculate the thermodynamic functions of the compounds [167- 169].

5.3.3 High Temperature Enthalpy Increment of ZrCo

The experimentally determined enthalpy increment data acquired by drop mode of multi-HTC are given in Table 5.12 and shown in Fig. 5.22.

Table 5.12: Enthalpy increment data along with fit values of $Zr_{0.5}Co_{0.5}(s)$

T/K	$H^o_m(T)-H^o_m(298.15\ K)$ $J\ mol^{-1}$ Experimental	$H^o_m(T)-H^o_m(298.15\ K)$ $J\ mol^{-1}$ Calculated	% difference[*]
642.0	9369	9401	-0.33
692.9	10809	10886	-0.69
743.6	12304	12384	-0.63
794.3	13858	13900	-0.27
844.0	15409	15402	0.07
893.9	16990	16928	0.39
943.5	18570	18461	0.62
994.0	20196	20037	0.82
1043.8	21764	21608	0.75
1095.9	23399	23269	0.72
1144.3	24991	24826	0.66
1194.8	26555	26467	0.33
1245.1	28227	28118	0.39
1295.3	29772	29780	-0.03
1345.3	31408	31452	-0.14
1397.0	32980	33196	-0.65
1446.8	34645	34892	-0.71
1497.2	36371	36623	-0.69

[*]% difference = {(Exp.-Cal.)./Exp}·100
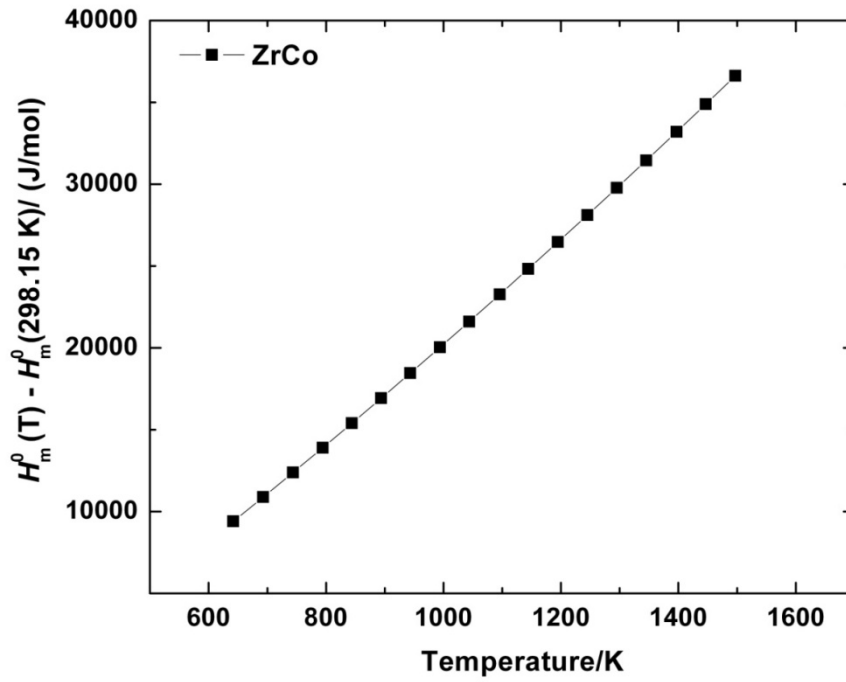
Fig. 5.22: Enthalpy increment of Zr$_{0.5}$Co$_{0.5}$ (s)

Enthalpy increment values were least squared fitted in the temperature rang 642-1,497 K (before melting) into polynomial equation using Shomate method [102] with constraints, i) $H_m^0(T) - H_m^0(298.15\ K) = 0$ at 298.15 K and ii) $C_{p.m}^0$ (298.15 K) = 25.0 J K^{-1}mol^{-1}. $C_{p.m}^0$ (298.15 K) value was estimated from the heat capacity of component elements. The polynomial expression obtained for Zr$_{0.5}$Co$_{0.5}$(s) in the temperature range 642-1497 K is given as:

$$H_m^0(T) - H_m^0(298.15\ K)(J \cdot mol^{-1}) = 25.682 \cdot \left(\frac{T}{K}\right) + 29.807 \cdot 10^{-4} \cdot \left(\frac{T}{K}\right)^2 +$$

$$2.1864 \cdot 10^5 \cdot \left(\frac{K}{T}\right) - 8655.5 \tag{5.28}$$

The heat capacity expression of Zr$_{0.5}$Co$_{0.5}$(s) was obtained by differentiating above enthalpy increment expressions with respect to temperature. The heat capacity expression obtained from Multi HTC data can be given as:

$$C_{p.m}^0(J \cdot K^{-1} \cdot mol^{-1}) = 25.682 + 5.961 \cdot 10^{-3} \cdot \left(\frac{T}{K}\right) - 2.1864 \cdot 10^5 \cdot \left(\frac{K}{T}\right)^2 \tag{5.29}$$

In order to generate thermodynamic functions for $Zr_{0.5}Co_{0.5}$(s) from enthalpy increment data; $\Delta_f H_m^0(298.15\,K)$ and $S_m^0(298.15\,K)$ values are required. Gachon et al. measured the enthalpies of formation of four phases $Co_{0.33}Zr_{0.67}$, $Co_{0.5}Zr_{0.5}$, $Co_{0.67}Zr_{0.33}$ and $Co_{0.8}Zr_{0.2}$ by direct reaction calorimeter [170]. The measured $\Delta_f H^o{}_m$(298.15 K) of $Zr_{0.5}Co_{0.5}$ was determined to be -42.2±1 kJ mol^{-1} at 1512 K. Chart and Putland [171] estimated enthalpy of formation of Zr-Co phases from the experimentally determined phase diagram by Bataleva et al. [172]. Authors [171] estimated enthalpy values of Zr-Co alloys from the enthalpy of formation of the Laves phase Co_2Zr (-88 kJ mol^{-1}) derived from critically assessed data for Laves phases and other structurally related binary compounds of Ti, V, Zr, Nb, Mo and Ta with Cr, Fe, Co and Ni. This parameter was measured using direct reaction calorimetry, to be -90.3 ± 9 kJ mol^{-1} at 773 K. Miedema [173] estimated $\Delta_f H^o{}_m$(298.15 K) of $Zr_{0.5}Co_{0.5}$ to be -60 kJ mol^{-1}. The discrepancy among the three sets of data reported in the literature is large. However, the enthalpy of formation of $Zr_{0.5}Co_{0.5}$ calculated from the quasi harmonic approximation in this study is -27.98 kJ mol^{-1} which is agreeing reasonably well with that (-26.75 kJ mol^{-1}) of Chart and Putland [171]. The enthalpy of formation of $Zr_{0.5}Co_{0.5}$ at 298.15 K calculated in this study has been selected for computation of high temperature thermodynamic functions. The $S^o{}_m(Zr_{0.5}Co_{0.25}$, 298.15 K) has been calculated from the component elements and assuming ideal entropy of mixing of the components.

5.3.4 Thermodynamic Functions of ZrCo

The thermodynamic functions like $S_m^0(T)$, $C_{P,m}^0(T)$, $\{H_m^0(T) - H_m^0(298.15\,K)\}$, $\varphi_m^0(T)\{-(G_m^0(T) - H_m^0(298.15))/K\}$ have been calculated in the temperature range 298.15-1500 K using $\Delta_f H_m^0(298.15\,K) \approx$ -27.98 kJ mol^{-1} and $S^o{}_m(Zr_{0.5}Co_{0.5}$,298.15 K) = 40.2 J mol^{-1} K^{-1} and measured heat capacity data in this study. The calculated thermodynamic functions are given in Table 5.13.

Table 5.13: High temperature thermodynamic functions of Zr$_{0.5}$Co$_{0.5}$

T /K	$C_{p,m}^{o}(T)$ /J·mol^{-1}·K^{-1}	$H_m^{o}(T)-H_m^{o}(2$ /kJ·mol^{-1}	$S_m^{o}(T)$ /J·mol^{-1}·K^{-}	$H_m^{o}(T)$ /kJ·mol^{-1}	$G_m^{o}(T)$ /kJ·mol^{-1}	$\Delta_f H_m^{o}(T)$ /kJ·mol^{-1}	$\Delta_f G_m^{o}(T)$ /kJ·mol^{-1}
298.15	25.00	0.0	40.2	-27.98	-39.97	-27.98	-29.69
300	25.04	0.0	40.4	-27.98	-40.10	-28.03	-29.76
400	26.70	2.6	47.8	-25.38	-44.50	-27.99	-30.32
500	27.79	5.4	53.9	-22.58	-49.53	-27.87	-30.84
600	28.65	8.2	59.0	-19.78	-55.18	-27.86	-31.44
700	29.41	11.1	63.5	-16.88	-61.33	-27.82	-32.06
800	30.11	14.1	67.5	-13.88	-67.88	-26.51	-32.62
900	30.78	17.1	71.1	-10.88	-74.87	-26.56	-33.24
1000	31.42	20.2	74.3	-7.78	-82.08	-26.66	-33.72
1100	32.06	23.4	77.4	-4.58	-89.72	-26.83	-34.29
1200	32.68	26.6	80.2	-1.38	-97.62	-29.05	-34.68
1300	33.30	29.9	82.8	1.92	-105.72	-29.26	-34.91
1400	33.92	33.3	85.3	5.32	-114.10	-29.60	-35.12
1500	34.53	36.7	87.7	8.72	-122.83	-30.26	-35.40

Molecular weight= 75.1016 g

Temperature dependent thermodynamic functions such as the heat capacity, enthalpy, entropy, and Helmholtz energy were also calculated using the Debye-Grüneisen quasi-harmonic approximation. The calculated thermodynamic functions of ZrCo alloy have been shown in Table 5.13. In table 5.13, $E_m^0(T) - E_m^0(0)$ is the change in vibrational internal energy from 0 K, the vibrational entropy at temperature T is $S_{v,m}^0(T)$, the electronic plus

vibrational energy of formation $E_m^0(T)$, is equal to the summation of electronic energy, zero point energy and the change of vibrational internal energy from 0 K. $A_m^0(T)$ is the electronic plus vibrational Helmholtz free energy. The calculated internal energy of formation $\Delta_f E_m^0(T)$, and Helmholtz free energy of formation of ZrCo have also been given in Table 5.14. The zero point energy of ZrCo alloy has been computed to be 5.06 kJ mol^{-1}.

Table 5.14: Low temperature thermodynamic functions of ZrCo

T /K	$C_{v,m}^o(T)$ /J·mol^{-1}·K^{-1}	$E_m^o(T)$-$E_m^o(0)$ /kJ·mol^{-1}	$S_{v,m}^o(T)$ /J·mol^{-1}·K^{-}	$E_m^o(T)$ /kJ·mol^{-1}	$A_m^o(T)$ /kJ·mol^{-1}	$\Delta_f E_m^o(T)$ /kJ·mol^{-1}	$\Delta_f A_m^o(T)$ /kJ·mol^{-1}
1	0.0002	0	0.0001	-50.26	-50.26	-57.52	-57.52
2	0.0016	0	0.0009	-50.26	-50.26	-57.52	-57.52
3	0.0053	0	0.0031	-50.26	-50.22	-57.52	-57.52
4	0.0126	0	0.0074	-50.26	-50.26	-57.52	-57.52
5	0.0246	0	0.0144	-50.26	-50.26	-57.52	-57.52
10	0.1969	0.0005	0.1149	-50.26	-50.26	-57.52	-57.52
15	0.6644	0.0025	0.3876	-50.26	-50.26	-57.52	-57.52
20	1.5714	0.0079	0.9174	-50.25	-50.27	-57.52	-57.52
30	5.0477	0.0391	2.9918	-50.22	-50.31	-57.50	-57.54
40	10.314	0.1149	6.3688	-50.14	-50.40	-57.46	-57.58
50	16.120	0.2471	10.540	-50.01	-50.54	-57.41	-57.64
60	21.523	0.4359	14.994	-49.82	-50.72	-57.33	-57.71
70	26.147	0.6749	19.419	-49.58	-50.94	-57.24	-57.78
80	29.955	0.9561	23.667	-49.30	-51.20	-57.14	-57.86
90	33.044	1.2717	27.684	-49.00	-51.48	-57.04	-57.93
100	35.542	1.615	31.458	-48.64	-51.79	-56.95	-58.01
125	39.935	2.5631	39.915	-47.69	-52.68	-56.73	-58.22
150	42.653	3.598	47.199	-46.66	-53.74	-56.55	-58.46
175	44.421	4.6879	53.571	-45.57	-54.95	-56.40	-58.73

200	45.626	5.8144	59.226	-44.44	-56.29	-56.28	-59.02
225	46.479	6.9663	64.306	-43.29	-57.76	-56.17	-59.33
250	47.103	8.1364	68.916	-42.12	-59.35	-56.09	-59.65
275	47.572	9.3201	73.136	-40.94	-61.05	-56.01	-60.00
298	47.908	10.418	76.725	-39.84	-62.70	-55.96	-60.32

Molecular weight =150.2032 g

In order to check the reliability of low temperature thermodynamic functions, the calculated low temperature heat capacities of ZrCo was plotted along with that of high temperature experimental data in Fig. 5.23. It shows reasonable agreement between high and low temperature $C_{p,m}^0(T)$ data. Similarly, low and high temperature $S_m^0(T)$ of ZrCo have been compared in Fig. 5.24, which also show reasonable agreement.
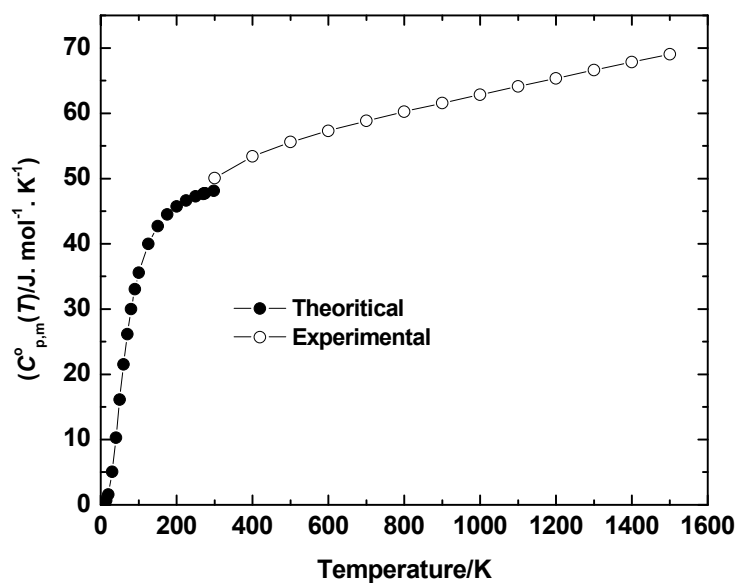
Fig. 5.23: Comparison of low temperature and high temperature molar heat capacity of ZrCo(s)
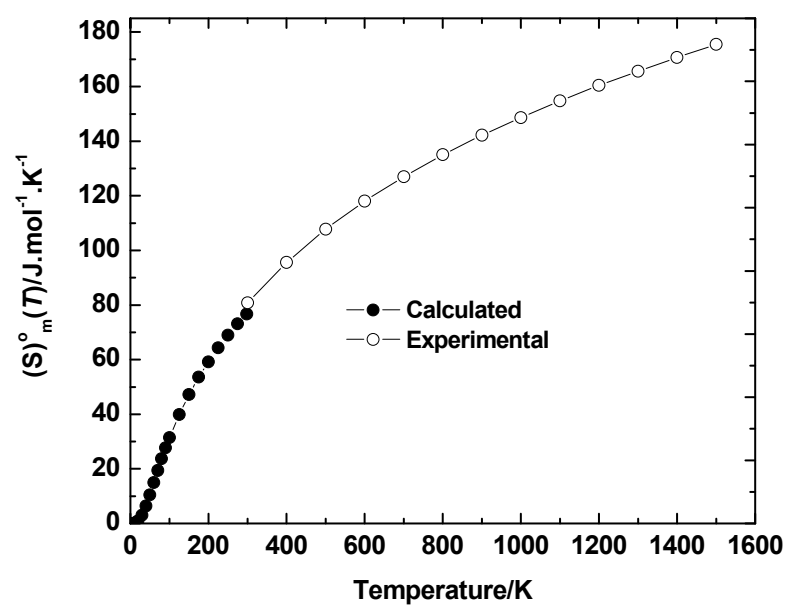
Fig. 5.24: Comparison of low temperature and high temperature molar entropy of ZrCo(s)

CHAPTER 6

First Principles Study of Hydrogen Interaction with ZrCo Surface and Clusters

6.1 ZrCo Surface

6.1.1 Computational Details

The computational details for this study are already described in section 2.9.4 of chapter 2.

6.1.2 Results and Discussion

a) H$_2$ Adsorption and Decomposition on ZrCo (110) Surface

For H adsorption, ZrCo (110) surface is modeled with a six layers slab of (3×2) super-cell. The top view of the super-cell is presented in Fig.6.1.
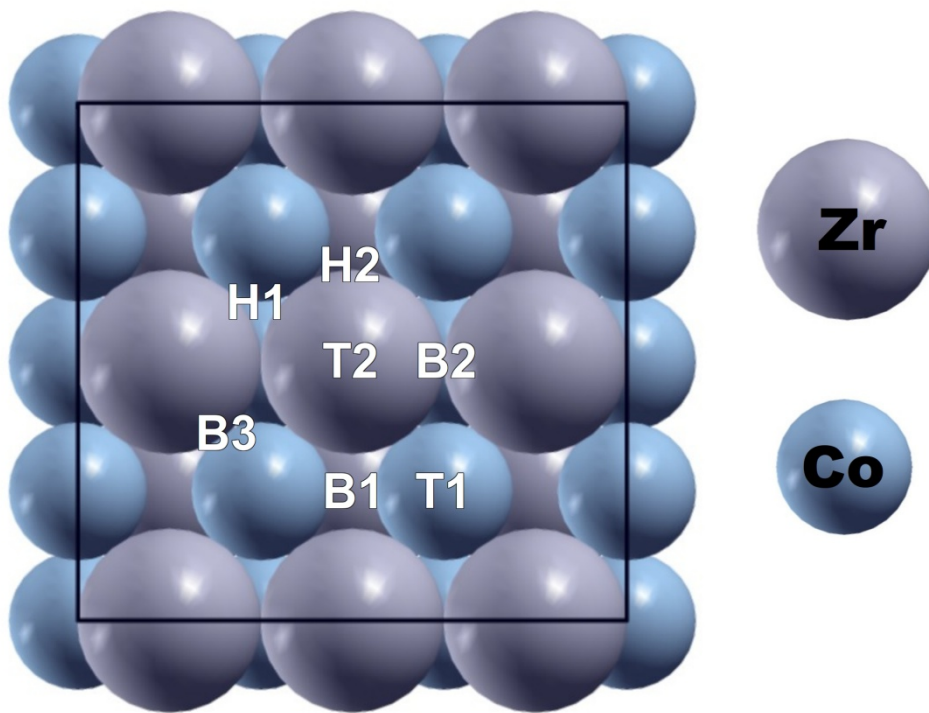
Fig. 6.1: Top view of ZrCo (110) surface. The adsorption sites considered for H adsorption are marked. T-on top adsorption, B-bridge site connecting two atoms and H-hollow site connecting three atoms

The bottom three layers are fixed at the bulk positions and top three layers are allowed to relax. The adsorption energy of hydrogen molecule on ZrCo surface has been calculated using the formula:

$$E_{ads} = E_{slab+nH} - E_{slab} - n\frac{1}{2}E_{H_2}$$

(6.1)

Where, $E_{slab+nH}$ is total energy of the slab with hydrogen adsorbed on it, E_{slab} is total energy

of the bare slab, E_{H_2} is total energy of the gas phase hydrogen molecule and n is the number of hydrogen atoms adsorbed on surface. E_{H_2} was calculated by taking a H_2 molecule in a cubic-cell having a length of 15Å. The H-H bond length is obtained as 0.75 Å with a binding energy of -4.52 eV for H_2 molecule. The calculated values are in good agreement with the experimental data of 0.74 Å and -4.75 eV [174].

In this section, we report the adsorption properties of H_2 molecule on ZrCo (110) surface and the dissociation mechanism. The adsorption sites we considered for the adsorption of H_2 are the on-top site, bridge site and hollow site presented in Fig. 6.1. On the (110) surface there are two different top sites, on top of Co and Zr, respectively denoted by T1 and T2. Three bridge sites are possible they are denoted by B1, B2 and B3. Here, B1, B2 are respectively the bridge site between two Co, two Zr and B3 is the bridge site between a Co and Zr. Two types of hollow sites are present and denoted by H1 and H2.

In initial configurations for calculating H_2 adsorption on ZrCo (110) surface, the H_2 molecule is placed parallel to the surface at a distance of 3Å along Z-axis. The adsorption energy of H_2 molecule on top of Zr is calculated to be -0.28 eV, indicating the adsorption of H_2 occurs on top of Zr. In contrast, the hydrogen molecule on other sites is unstable. While, a H_2 molecule is placed on top of Co at the same distance of 3Å along Z-axis, the molecule has been decomposed into two H atoms without an activation barrier and the two H atoms are finally staying at two B1 sites connected to the Co atom. However when we placed H_2 on bridge sites, it has been decomposed into two H atoms and these H atoms are finally staying at two hollow sites. This finding indicates that H_2 decomposition can easily take place on top of Co and in the bridge sites.

Molecular hydrogen adsorbed on top of Zr is considered as the initial configuration for the hydrogen dissociation (marked as IS-1 in Fig. 6.2). To find the final configuration, we placed two hydrogen atoms at various possible adsorption sites like bridge between two Zr,

bridge between two Co and the hollow sites. We found that in the most stable geometry two hydrogen atoms adsorbed on two nearby hollow sites (H1), in which the hollow site connect two Zr and one Co (marked as FS-1 in Fig. 6.2).
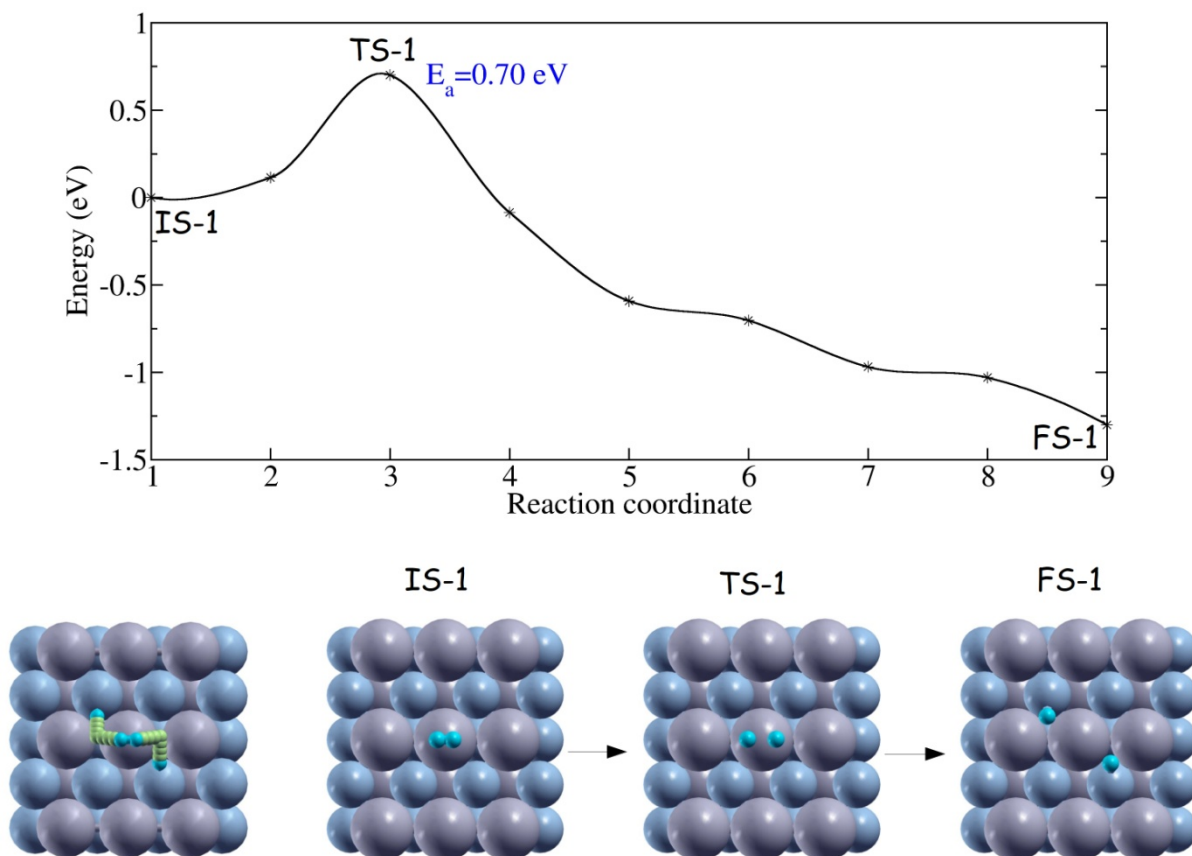
Fig. 6.2: Hydrogen dissociation on ZrCo (110) surface

We setup a NEB calculation to find the dissociation barrier for the hydrogen dissociation starting from H_2 adsorbed on top of Zr to two H atoms adsorbed on hollow sites. This process has been decoupled into two steps. In the first step H_2 adsorbed on top of Zr dissociate to a meta-stable state in which two hydrogen atoms are adsorbed on two Zr bridge sites (Fig. 6.2). This has an energy barrier of 0.70 eV. In the next step the hydrogen atoms diffuses to the most stable hollow site with a negligible barrier. This indicates that the hydrogen decomposition on top of Zr is less favorable compared to on top of Co. It is of great interest to know how the hydrogen adsorption behavior changes in ZrCo surface compare to the

surface of its constituent elements. From the first principles study Zhang *etal*. have found that the adiabatic dissociation process of H_2 on Zr (0001) surface is an activated type but with a small energy barrier, which is well consistent with the macroscopic phenomena that the zirconium metal is easily hydrogenated [175]. Whereas, Huesges etal. have studied the interaction of hydrogen with the Co(0001) surface using ultra high vacuum between 90 and 500 K by means of low energy electron diffraction (LEED), temperature-programmed thermal desorption (TPD) and work function change measurement. They have reported that hydrogen adsorbs spontaneously and dissociatively in two atomic binding states with a high sticking probability [176]. From the above discussion it is notified that pure Zr and Co surfaces are having smaller barriers for hydrogen decomposition than ZrCo alloy. It is also clear that the H_2 decomposition involves a barrier only on top of Zr.

b) H Adsorption on ZrCo (110) Surface

The adsorption energy associated with the various binding sites on the surface of a material strongly depends on the H-atom coverage. By adding the H-atoms to the surface one at a time, filling first the strongest binding sites and ending with the weakest ones, the energy per atom can be calculated from the adsorption energy. To find the stability of the atomic hydrogen on ZrCo (110) surface, we have considered one H in a super-cell corresponds to the H coverage (θ_H) of 0.16 ML. We have calculated the adsorption energy using Eq.(6.1) and presented in Table 6.1.

Table 6.1: Adsorption energy (or binding energy) (E_{ads}), Zr-H and Co-H bond distances (d_{Zr-H} and d_{Co-H}, respectively) after H atom adsorption on ZrCo(110) at 0.16 H coverage

Adsorption site	E_{ads}/H eV	d_{Zr-H} Å	d_{Co-H} Å
T1	-0.43	-	1.55
T2	0.28	1.90	-
B1	-0.58	-	1.76, 1.76
B2	-0.46	2.03, 2.03	-
H1	-0.79	2.21, 2.21	1.64
S1-Oh1	-0.16	2.21, 2.38	1.70, 1.66
S2-Oh1	-0.38	2.28, 2.25	1.80, 1.80
Oh1 (bulk ZrCo)	-0.38	2.26, 2.26	1.80, 1.80

It is seen from the table that atomic hydrogen adsorption is exothermic on this surface, except on atop site on Zr. In general, the stability of H atom on ZrCo surface follows the order hollow > bridge > atop. The most stable adsorption site is (H1) hollow site. Adsorption energy of H at this site is -0.79 eV/H. The next stable site is the bridge sites, B1 and B2 respectively have adsorption energy -0.58 and -0.46 eV/H. We also placed the H at B3, this site is not stable for H adsorption, as H moves to the most stable H1 site. Among atop sites the adsorption energy of H at T1 is similar to the bridge site has a value of -0.43 eV/H, whereas the adsorption on T2 is very weak and endothermic about 0.28 eV/H.

The effect of pre-adsorbed hydrogen on the surface is important to estimate the adsorption energy of upcoming H. To study this, two H atoms are taken in a (3×2) super-cell corresponds to θ_H=0.33 ML, in which one H placed at a most stable H1 site. Now, for the other H we have seven possibilities to place. We studied all these possibilities and obtained

the maximum adsorption energy -1.59 eV/2H when the two H atoms are at a distance of 4.49 Å. The lowest adsorption energy obtained at θ_H=0.33 was the case where the two H atoms are at a distance of 2.69 Å. All other cases have a adsorption energy between -1.52 to -1.59 eV/2H given in Fig. 6.3(a). This above result suggest that the effect of H adsorbed on surface to the adsorption energy of upcoming H is very small compared the adsorption energy.

At a low coverage of θ_H=0.33 ML, may be the effect of pre-adsorbed H on adsorption energy is small but at increased θ_H this may change. To address this we have studied the H adsorption up to θ_H=1 ML, and to understand the effect more clearly the differential adsorption energy was also calculated. The differential adsorption energy was calculated as,

$$\Delta E_{ads} = E_{slab+nH} - E_{slab+(n-1)H} - \frac{1}{2}E_{H_2}$$ (6.2)

Here, ΔE_{ads} is differential adsorption energy of H and all the term in the right hand side are the total energy of the respective system. Adsorption energy and differential adsorption energy of H as a function of θ_H are given in Fig. 6.3(b).

(a)   (b)
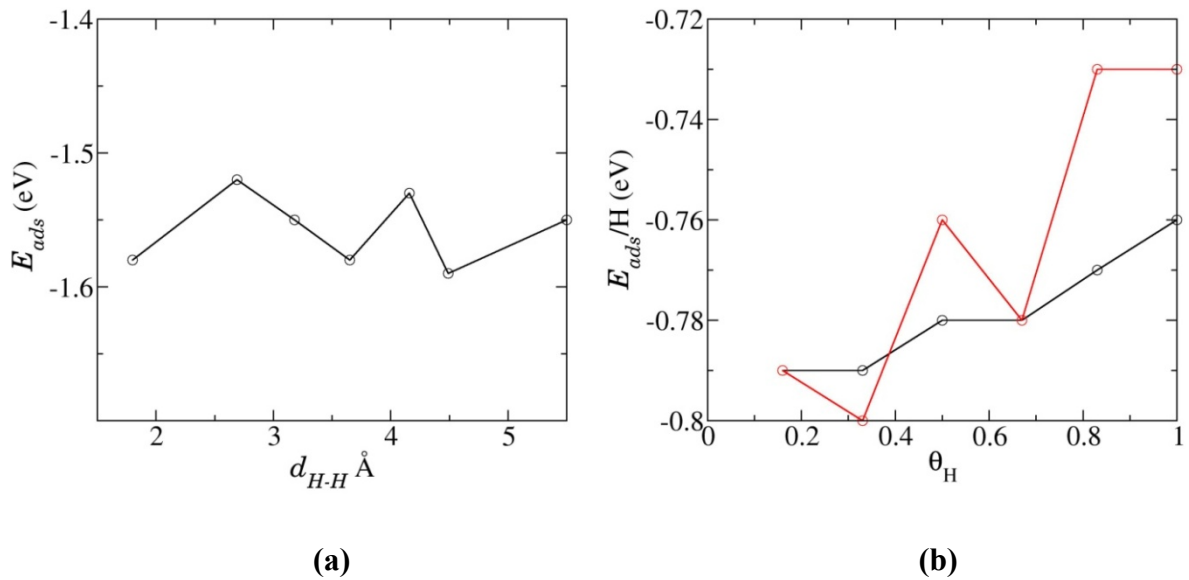
Fig. 6.3: (a) Adsorption energy of H at θ_H = 0.33 ML on ZrCo(110) as a function of d_{H-H}, (b) Adsorption energy of H as a function of θ_H. Black circles – adsorption energy calculated using Eq.(2) and red circles – differential adsorption energy calculated using Eq.(3)

With increase in θ_H the adsorption energy decreases, whereas the differential adsorption energy does not follow any trend with θ_H. However, the change in the differential adsorption energy of H is very small.

c) H Binding in Subsurface and Bulk ZrCo

Adsorption of H in subsurface is important, since it is the intermediate state for the diffusion of H from the surface to the bulk. Similar to the bulk ZrCo, three inequivalent interstitial sites are presented in subsurface, shown in Fig. 6.4.
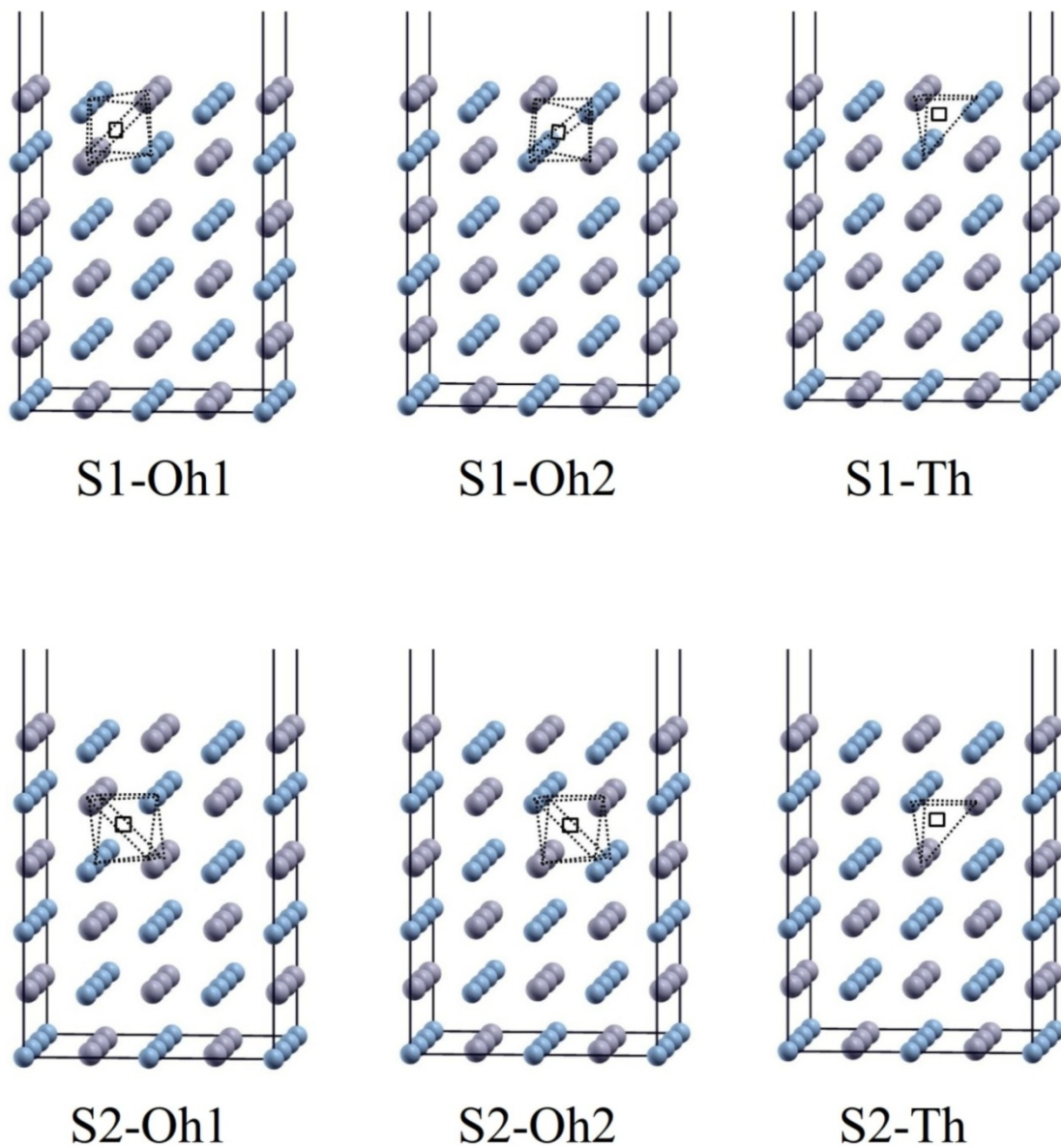
Fig. 6.4: High symmetry interstitial sites present in ZrCo subsurface, which are considered for H adsorption. Oh- octahedral site, Th- tetrahedral site

The subsurface adsorption sites are denoted with a prefix S1, S2 and S3 corresponding to the first second and third subsurface layer. Similar to bulk ZrCo, adsorption of H in the subsurface is stable only at Oh1 site. The binding of H is exothermic at this site. Octahedral site present in the first subsurface layer S1-Oh1 has a binding energy of -0.16 eV/H. This is very weak compared to the adsorption energy of H on surface. However, this is weaker than the binding of H in bulk ZrCo. The binding energy saturates in the second subsurface layer and S2-Oh1 has binding energy of -0.38 eV/H. This value is equal to the binding energy of H in bulk ZrCo. This result is an indication that H at the first subsurface is less stable and will diffuse to either to bulk or surface depending on the barrier associated with the process.

Typically in bulk metals and intermetallics, the H atom prefers to stay at the interstitial sites, since the size of the H atom is much smaller than that of the metal atoms. There are three inequivalent high symmetry interstitial sites present in bulk ZrCo shown in Fig. 6.5., i.e., two octahedral sites (Oh) and one tetrahedral site (Th).

Oh1   Oh2   Th
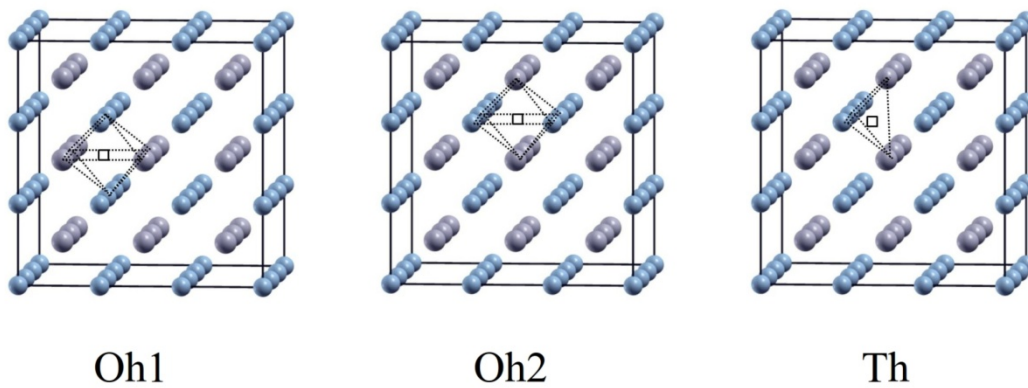
Fig. 6.5: High symmetry interstitial sites present in bulk ZrCo which are considered for H adsorption. Oh- octahedral site, Th- tetrahedral site

To study the binding of H in the bulk of ZrCo, th system was modeled by using a 3x3 supercell. The binding energy was calculated using a equation similar to Eq.(2), here instead of the total energy of the slab and corresponding system with H, we used the total energy of the bulk ZrCo supercell and the corresponding systems with H. The results show that H is

stable only on Oh1 site with adsorption energy of -0.38 eV/H. We also placed H on other sites, however during relaxation it moves to the most stable Oh1 site. The binding energy of H at the most stable site in bulk ZrCo is about 0.41 eV higher than that of H at the most stable site on the surface. This indicates that H atom prefers to stay on the surface than the bulk. From the energetic and structural properties, it is clear that the H atom binds more tightly to Co atom and with more number of Zr atom, the Oh1 is stable whose nearest neighbors are four Zr and two Co. This is also true for ZrCo (110) surface, in the most stable adsorption site H atom is bound with two Zr and one Co.

d) Diffusion of H on ZrCo (110) Surface and Bulk

We have considered six different possible paths for H diffusion on ZrCo(110) surface, in all the cases bond breaking and bond making between the H and metal atom (either Co or Zr) takes place. Four of these paths are simple translational diffusion, i.e., two along X direction, two along Y direction and two paths involve circular motion of H.

In the first two cases, we consider H diffusion along X direction. One H atom adsorbed at B1site is the initial state for the first path. This is about 0.21eV less stable compared to H at the most stable H1 site. H diffuses to the next B1 site through T1 site. Diffusion of H along this path requires activation energy of 0.36 eV and H adsorbed at T1 is the saddle point. The diffusion path and the structures are presented in Fig. 6.6. The second case is also similar to the first path, in which the initial state for this is one H atom adsorbed at B2 site, which is 0.32 eV less stable compared to the most stable H1 site. This H diffuses to the next B2 site along X direction through T2site. This has a large energy barrier of 0.74 eV and H adsorbed at T2site is the saddle point. The diffusion path and structures are presented in Fig. 6.7. These results suggest that the translational diffusion of H along X direction needs minimum activation energy of 0.15 eV. This small value is an indication for ready diffusion of H on ZrCo surface along X.
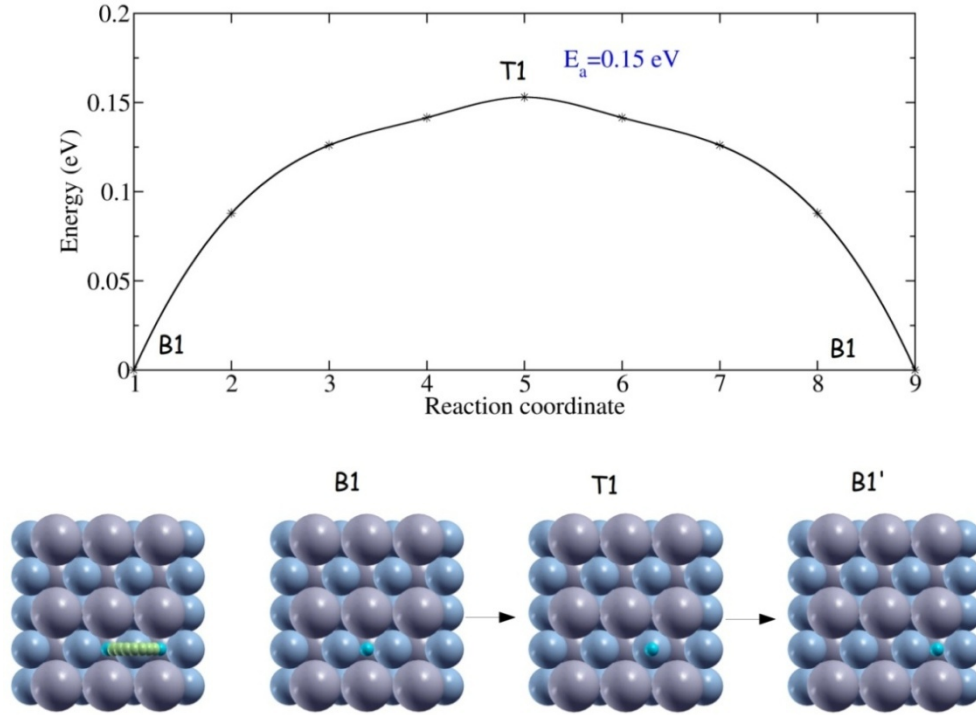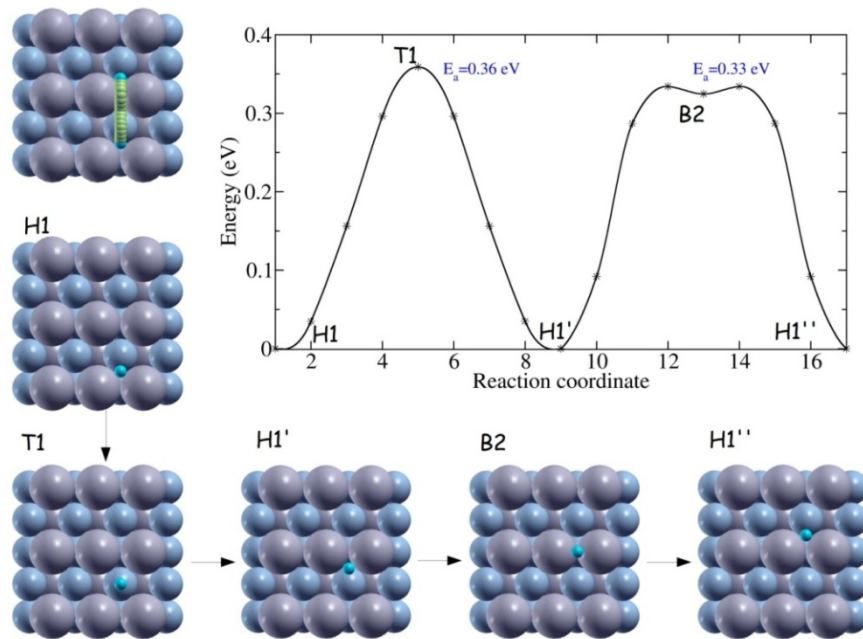
Fig. 6.6: Potential energy surface for H diffusion on ZrCo (110), starting from B1 to next B1 through T1 along X direction. This requires activation energy 0.15 eV
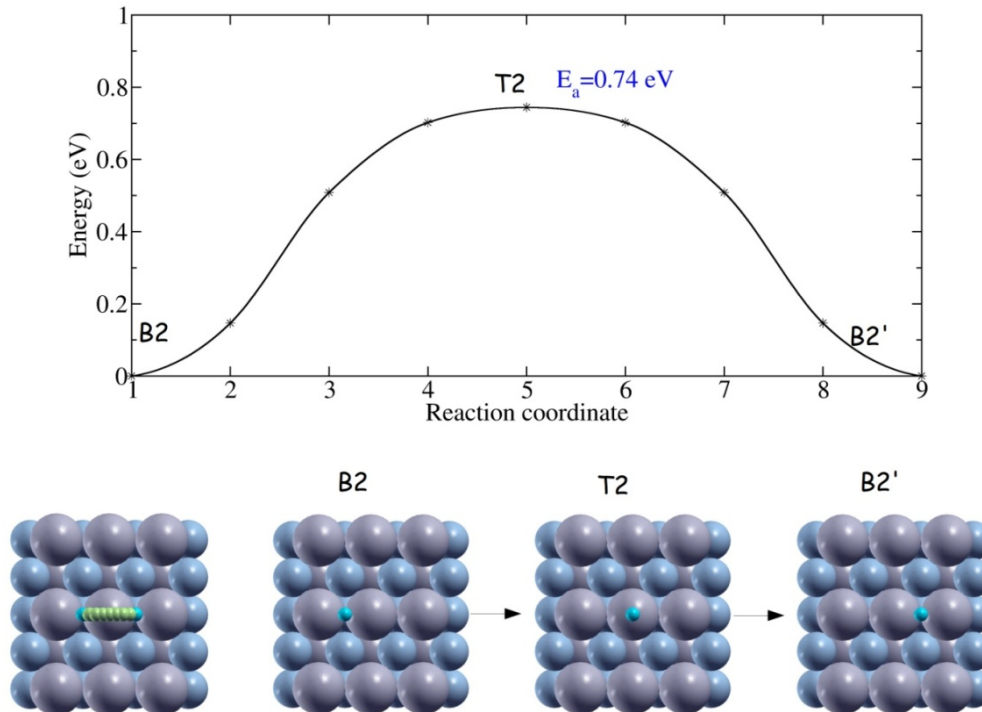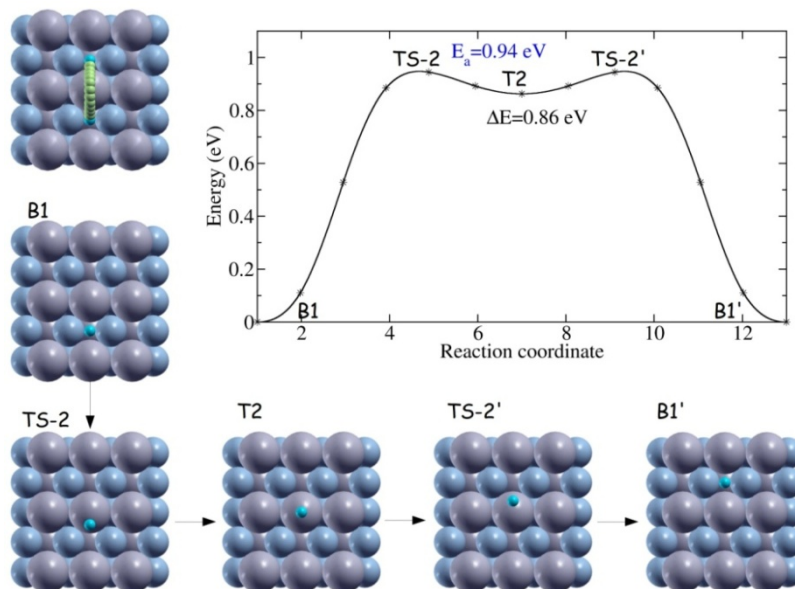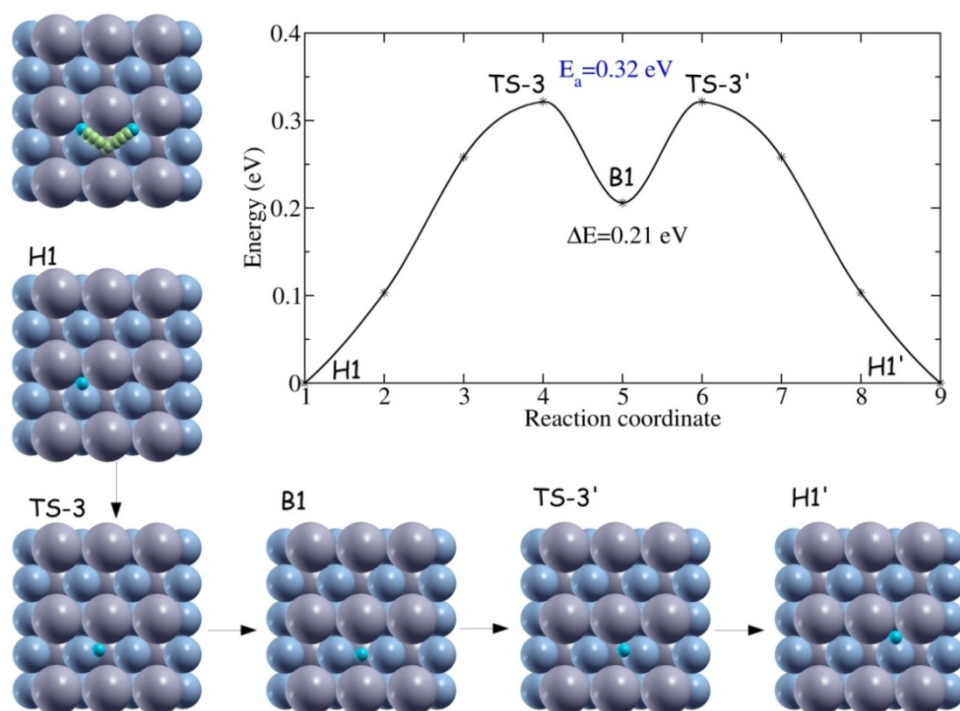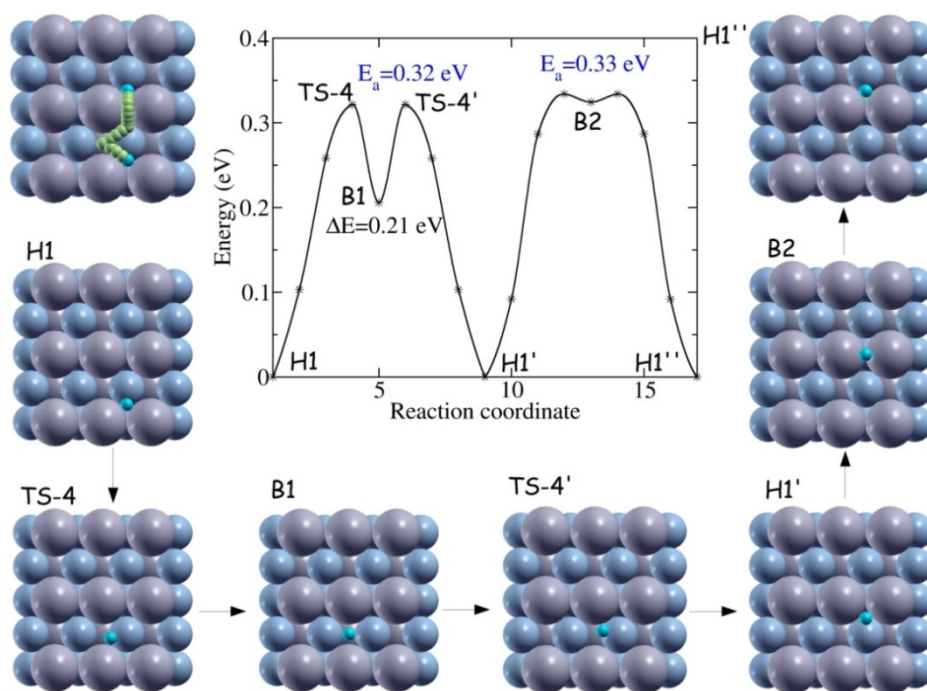

Fig. 6.7: Potential energy surface for H diffusion on ZrCo (110), starting from B2 to next B2 through T2 along X direction. This requires activation energy 0.74 eV

Third and fourth cases are also similar to the first two cases, in these cases we consider the H diffusion along Y direction. The initial state for third case is the one in which the H is adsorbed at the most stable H1 adsorption site. This H diffuses to the next equivalent H1 site along Y direction. This diffusion path involves three intermediate stable states namely T1, H1 and B2. In the first step H present in the H1 site diffuses to the next H1 site through T1 site. This requires an activation barrier of 0.36 eV and H at T1 is the saddle point. In the next step, H present at the H1 site diffuses to the final H1 site through B2, requires an activation energy of 0.32 eV and H adsorbed at B2 site is the saddle point for this. Overall barrier for diffusion of H along this path is 0.36 eV. The complete path is given in Fig. 6.8. Considering fourth case, at the initial state H atom adsorbed at B1 site and diffuses to the next B1 site along Y direction through an intermediate state in which H adsorbed at T2 site. This requires higher activation energy of 0.94 eV and the path is given in Fig. 6.9. These above results suggest that the translational diffusion of H along Y needs minimum activation energy of 0.36 eV.

The last two paths are the diffusion of H atom in a circular path, in the fifth path H diffuses along X and in the sixth path H diffuses along Y. The initial state for the fifth path is same as the initial state for third path. H atom adsorbed at H1 diffuses to the next H1 site through an intermediate state B1. The intermediate state is about 0.21eV less stable compared to the initial state. The diffusion path is given in Fig. 6.10. This circular diffusion requires slightly higher activation energy of 0.32 eV compared to other paths along X, i.e., 0.15 and 0.74 eV for first and second paths respectively. The sixth path is similar to the third path. Only the first step is slightly different, the H atom adsorbed at H1 diffuses to the next H1 through an intermediate state in which H atom adsorbed at B1. The next step is same as the third path. The first step has the same activation energy of 0.32 eV as fifth path. The path is presented in Fig. 6.11.

From the above results of the diffusion barriers for H on ZrCo(110) surface, it is clear that the minimum energy paths for the H diffusion on ZrCo(110) surface is involving circular diffusion of H. However, translational diffusion of H along Y is also having very close barrier of 0.36 eV compared to the circular diffusion barrier of 0.32 eV. This suggests that H atoms will readily diffuse on ZrCo surface.

To understand the penetration of H into the bulk ZrCo from the surface, the H diffusion from the surface to the subsurface has been investigated. In the first step to this approach, the stable configuration of H atom, i.e., H atom adsorbed at H1 has been considered as initial state whereas the final state is H adsorbed at interstitial octahedral site of the first subsurface of ZrCo (S1-Oh1). The H atom diffuses vertically from the surface to the first subsurface. The H diffusion path is shown in Fig. 6.12. The diffusion barrier for this is 0.79 eV, which is larger than that of H diffusion on surface. The high diffusion barrier corresponds to the penetration of H atom to the first subsurface from surface. After H atom gets into the subsurface, it can diffuse further and ultimately reach a bulk environment. In the next step, the H diffusion from first subsurface to second subsurface has been investigated and shown in Fig. 6.13. The activation energy for this diffusion is calculated to be 0.53 eV. This value is less than the diffusion barrier associated with the H diffusion from surface to first subsurface. It indicates that once H atom penetrates into the first subsurface it can easily further diffuse into bulk.

From the previous result it is seen that octahedral hole is more stable for interstitial H atom. The H diffusion from one octahedral hole to near neighbor octahedral hole inside the bulk has also been studied using the NEB method. The diffusion path is shown in Fig. 6.14. The diffusion proceeds through a trigonal transition state, in which H is connected with two Zr and one Co. d_{Zr-H} and d_{Co-H} at the transition state are 1.98Å and 1.56Å, respectively. The activation energy required for this diffusion is found to be 0.61 eV. Once, H atom penetrates

the surface and reaches the first subsurface, it does not require very high energy to reach the bulk.

Fig. 6.8: Potential energy surface for H diffusion on ZrCo (110), starting from H1 to next H1 through T1, H1 and B2 along Y direction. Diffusion of H from H1 to next H1 through T1 requires activation energy 0.36 eV and diffusion of this H to next H1 through an intermediate state B2 requires activation energy 0.32 eV

Fig. 6.9: Potential energy surface for H diffusion on ZrCo (110), starting from B1 to next B1 through T2 along Y direction. The intermediate T2 state is 0.86 eV higher in energy than the initial state. This diffusion requires activation energy 0.94 eV

Fig. 6.10: Potential energy surface for rotational H diffusion on ZrCo (110), starting from H1 to next H1 through B1 along X direction. The intermediate B1 state is 0.21 eV less stable than initial state. This rotational diffusion requires activation energy 0.32 eV

Fig. 6.11: Potential energy surface for H diffusion on ZrCo (110), starting from H1 to next H1 through B1, H1 and B2 along Y direction. Both rotational diffusion of H from H1 to H1 through intermediate B1 and translational diffusion of H from H1 to next H1 through B2 require activation energy 0.32 eV
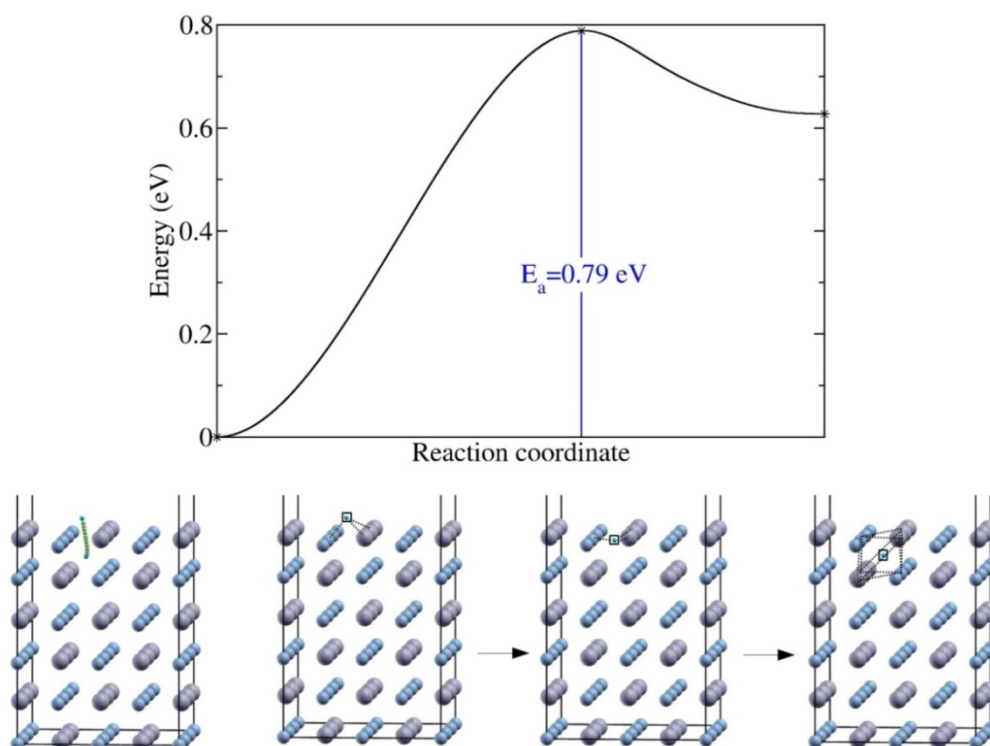
Fig. 6.12: Potential energy surface for penetration of H from ZrCo (110) surface to the first subsurface. This requires activation energy 0.79 eV
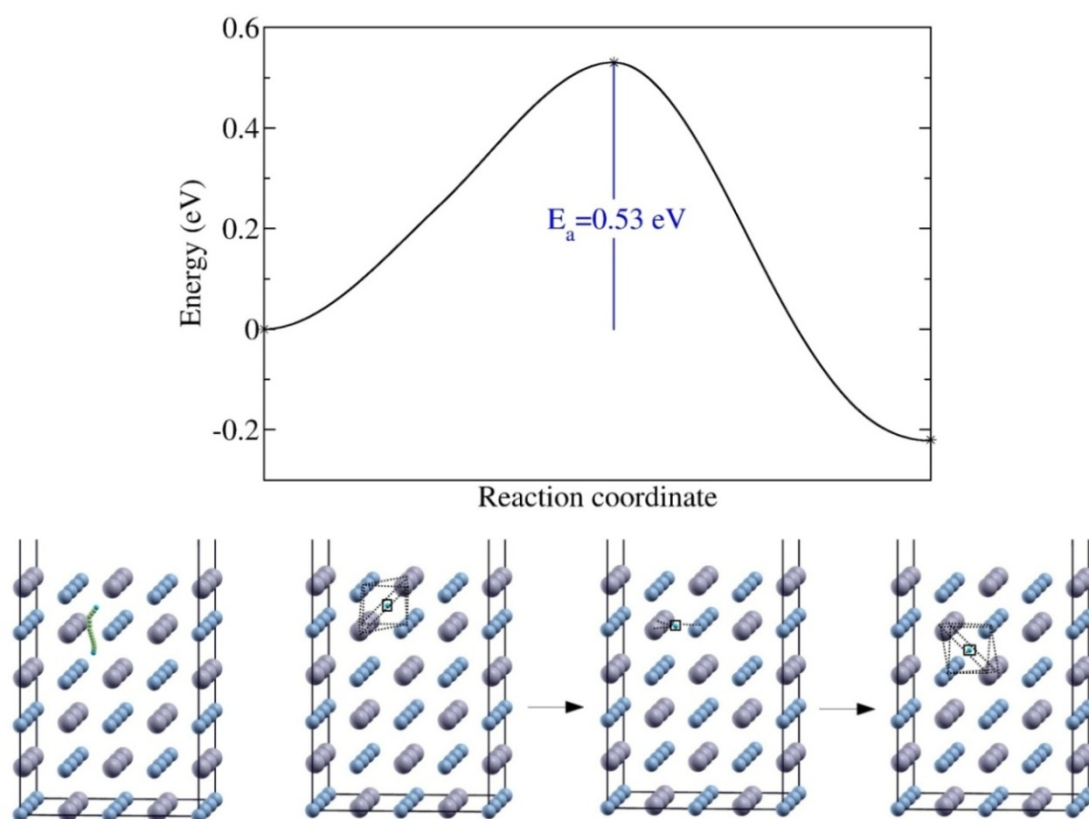
Fig. 6.13: Potential energy surface for H diffusion on ZrCo (110), starting from first subsurface to second subsurface. This diffusion requires activation energy 0.53 eV

146
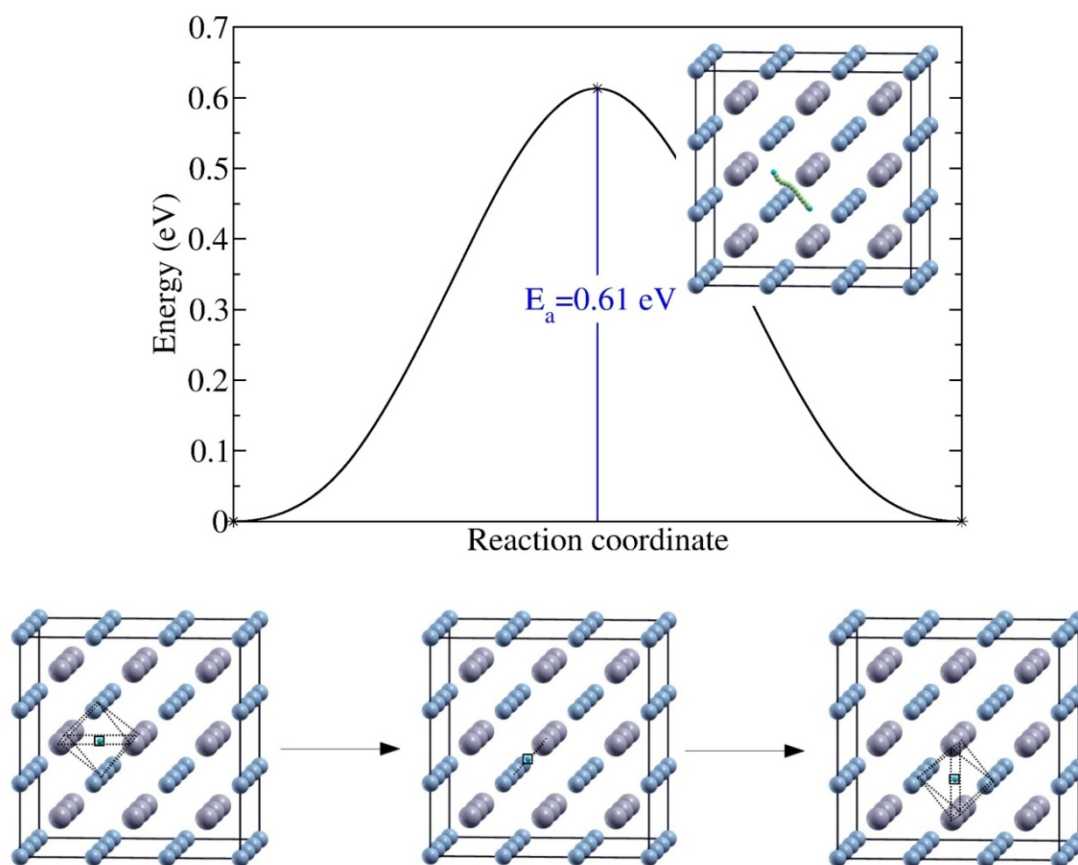
Fig. 6.14: Potential energy surface for H diffusion in bulk ZrCo, starting one octahedral hole (Oh1) to next Oh1. This requires activation energy 0.61 eV

e) Electronic Properties

In order to understand the chemical bonding of hydrogen with ZrCo we have compared the density of states spectrum and its constituent elements as shown in Fig.6.15. It has been shown that in bulk ZrCo, the *d*-orbital electrons of Zr and Co are contributing at the Fermi level [177]. The *d*-orbital spectrum of Co is more localized compared to the Zr. The overlap of d states of both Zr and Co at Fermi energy ensures the metallic nature of ZrCo. The contribution of Co states at the Fermi is almost double the times that of Zr states. For the clean (110) surface, the DOS of the Zr and Co atoms in the topmost layer is shown. The states are more localized for the surface atoms (from -4 to 2 eV) in comparison with the bulk ZrCo (from -6 to 6 eV). Moreover the contribution of Co states at Fermi is significantly reduced and the peak of the *d* states also up shifted to -1 eV from -1.5 eV.

After analyzing the DOS of the ZrCo (110) surface we examined the bonding nature of molecular and atomic hydrogen on this surface. Molecular hydrogen binds on top of surface Zr. To understand the chemical interaction of H_2 and Zr we have plotted the DOS of Zr atom and H_2 after interaction. New peaks which are located at -8.2 eV is coming from the interaction of Zr with hydrogen molecule, whereas the other features are not affected much. To study the chemical interaction with atomic hydrogen the most stable H1 configuration is considered, in which H atom binds with two Zr and a Co. DOS of surface Zr, Co and adsorbed H atom are plotted in order to understand the chemical bonding. The newly generated peaks, in the range -6.5 eV to -4.5 eV are the characteristic peaks due to the interaction with atomic H. The interactions are mainly coming from the *s*-orbital of H with *s*-orbitals of Zr and Co.
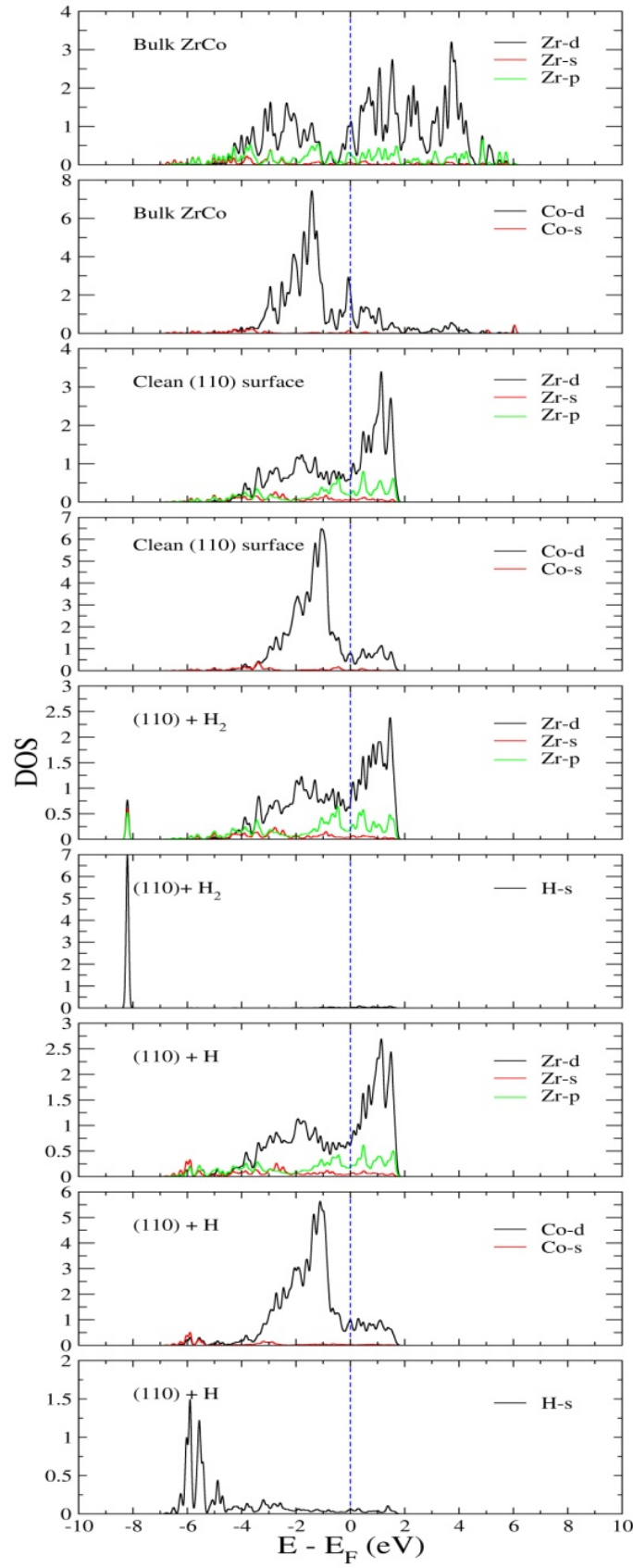
Fig. 6.15: Projected density of states of bulk ZrCo, clean, H₂ and H covered ZrCo (110) surface. The Fermi level is set to 0

6.2 ZrCo Clusters

6.2.1 Computational Details

The computational details for this study are already described in section 2.9.4 of chapter 2.

6.2.2 Results and Discussions

a) Dimer

First, we have calculated the binding energy and bond length of all constituent dimmers viz. Zr_2, Co_2 and ZrCo with and without spin-orbit coupling scheme. This is required to compare the accuracy of the theoretical method of the total energy calculation and the reliability of the pseudopotential used in the study. The calculated results with PBE are summarized in Table 6.2 and compared with the reported experimental and theoretical values [178-180].

Table 6.2: Calculated and experimental binding energies and bond lengths of Zr_2, ZrCo and Co_2 dimers

Cluster	Binding energy (eV/atom)		Bond length (Å)	
	Calculated	Reported	Calculated	Reported
Zr_2	-1.57	-1.53[a]	2.64	2.30[b]
ZrCo	-2.06	-	2.02	-
Co_2	-1.51	-1.72[c]	1.96	2.31[c]

[a]Ref: [178], [b]Ref: [179], [c]Ref: [180]

It is seen from Table 6.2 that the calculated results with PBE agree well with the reported experimental and theoretical values. It is also observed that the binding energy of ZrCo dimer is higher in comparison Zr_2 and Co_2 dimers. The higher binding energy of ZrCo cluster compare to the dimers of their constituent elements indicate stronger Zr-Co bond compare to Zr-Zr and Co-Co bond present in Zr_2 and Co_2 dimers, respectively. It is also reported earlier that a strong overlap of $4d$ orbital of Zr and $3d$ orbital of Co is responsible for the high bond strength in ZrCo bulk [177]. After establishing the ZrCo dimer, the total energy and binding energy of different Zr_mCo_n (m+n = 4, 6 and 8) clusters are calculated. A large number of

geometrical isomers for each composition of Zr_mCo_n (m+n = 4, 6 and 8) are shown in Table 6.3-6.5.

Table 6.3: Geometric isomers of Zr_4, Zr_mCo_n (m+n = 4) and Co_4 clusters (pink ball = Zr, gray ball = Co)
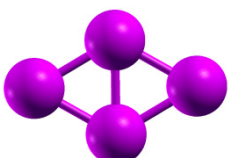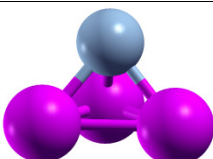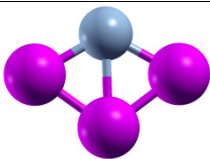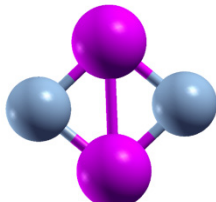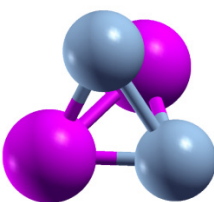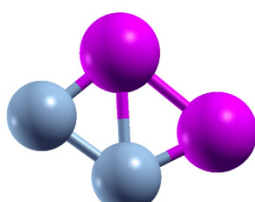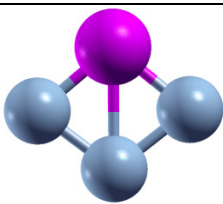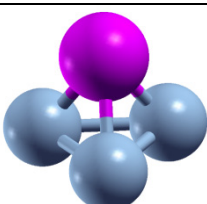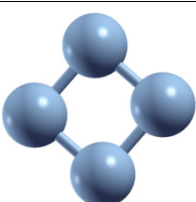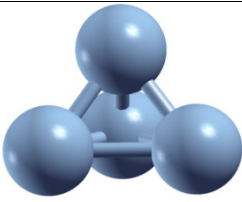
Cluster			
Zr_4	ΔE=0	0.91 eV	
Zr_3Co	ΔE=0	0.96 eV	
Zr_2Co_2	ΔE=0	0.42 eV	1.50 eV
$ZrCo_3$	ΔE=0	0.21	
Co_4	ΔE=0	0.55	

Table 6.4: Geometric isomers of Zr$_6$, Zr$_m$Co$_n$ (m+n = 6) and Co$_6$ clusters (pink ball = Zr, gray ball = Co)
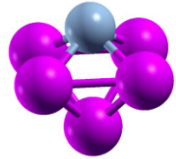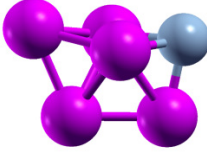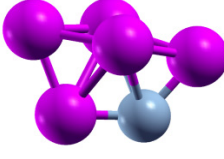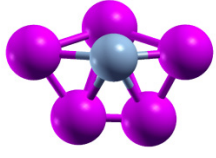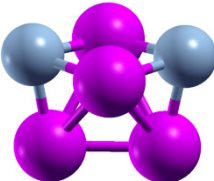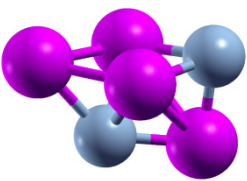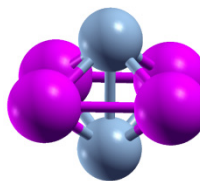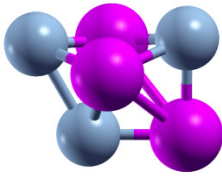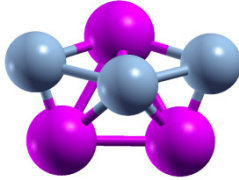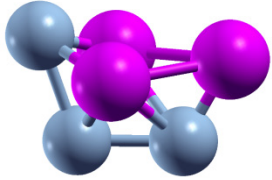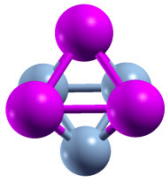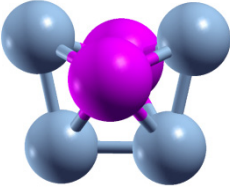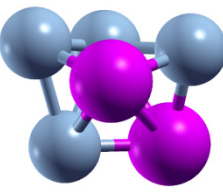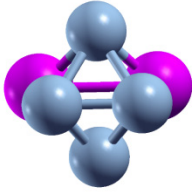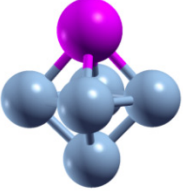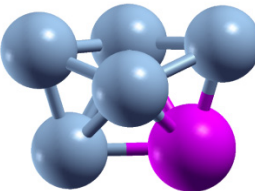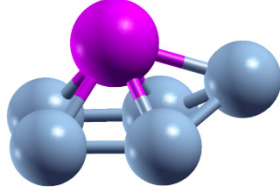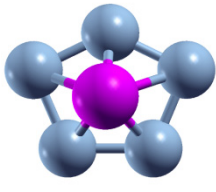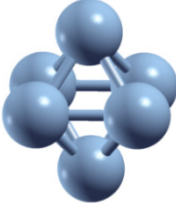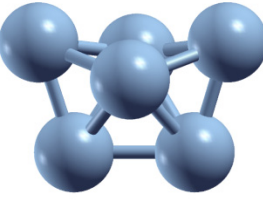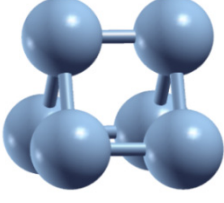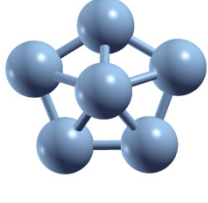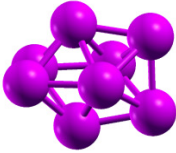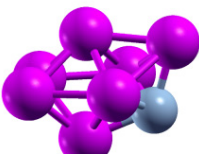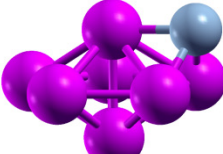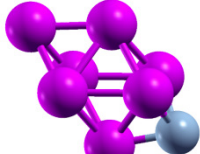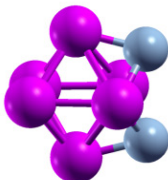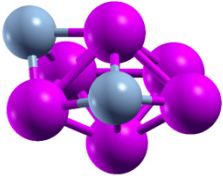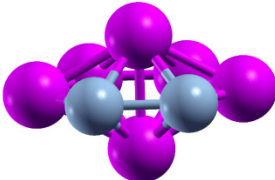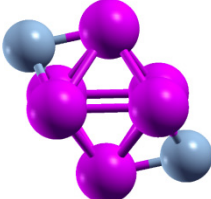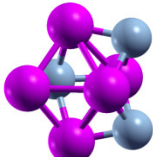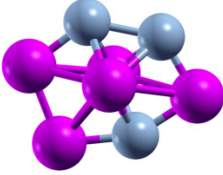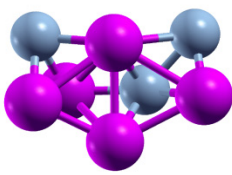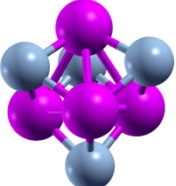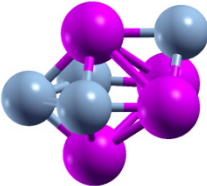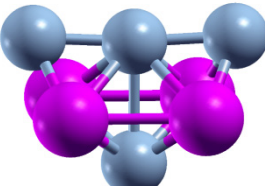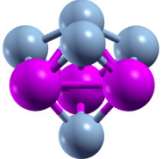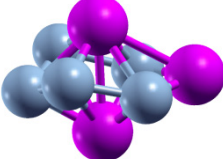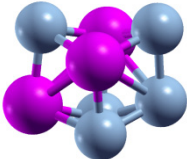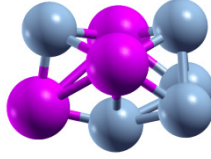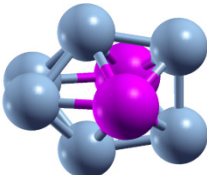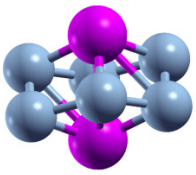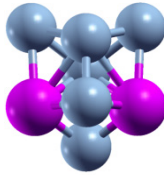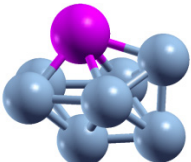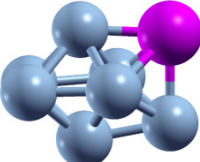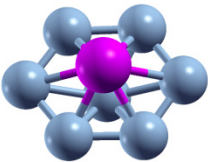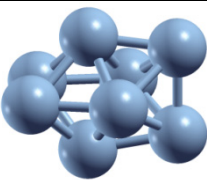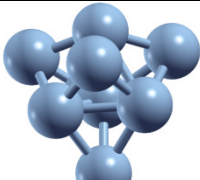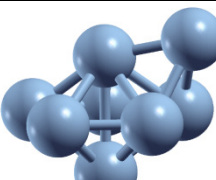
Clusters				
Zr$_6$	ΔE=0	0.09 eV		
Zr$_5$Co	ΔE=0	0.25 eV	0.62 eV	1.42 eV
Zr$_4$Co$_2$	ΔE=0	0.79 eV	1.03 eV	
Zr$_3$Co$_3$	ΔE=0	0.91 eV	1.24 eV	1.52 V
Zr$_2$Co$_4$	ΔE=0	0.35 eV	0.40 eV	
ZrCo$_5$	ΔE=0	0.89 eV	0.95 eV	1.49 eV
Co$_6$	ΔE=0	1.03 eV	1.12 eV	1.66 eV

Table 6.5: Geometric isomers of Zr$_8$, Zr$_m$Co$_n$ (m+n = 8) and Co$_8$ clusters (pink ball = Zr, gray ball = Co)

Clusters				
Zr$_8$	ΔE=0			
Zr$_7$Co	ΔE=0	0.28 eV	0.92 eV	1.45 eV
Zr$_6$Co$_2$	ΔE=0	0.04 eV	0.11eV	0.47 eV
Zr$_5$Co$_3$	ΔE=0	0.49 eV	1.31 eV	1.05 eV
Zr$_4$Co$_4$	ΔE=0	0.74 eV	1.46 eV	
Zr$_3$Co$_5$	ΔE=0	0.51 eV	0.59 eV	0.93 eV
Zr$_2$Co$_6$	ΔE=0	0.12 eV	0.15 eV	

ZrCo7: ΔE=0, 0.53 eV, 0.71 eV

Co8: ΔE=0, 0.41 eV, 0.53 eV

The results reveal that small ZrCo clusters favor 1:1 composition (e.g. – ZrCo, Zr_2Co_2, Zr_3Co_3 and Zr_4Co_4) as the most stable moiety. The ground state geometric configuration for each composition of Zr_mCo_n clusters are shown in Fig. 6.16.

(a) (b) (c) (d)
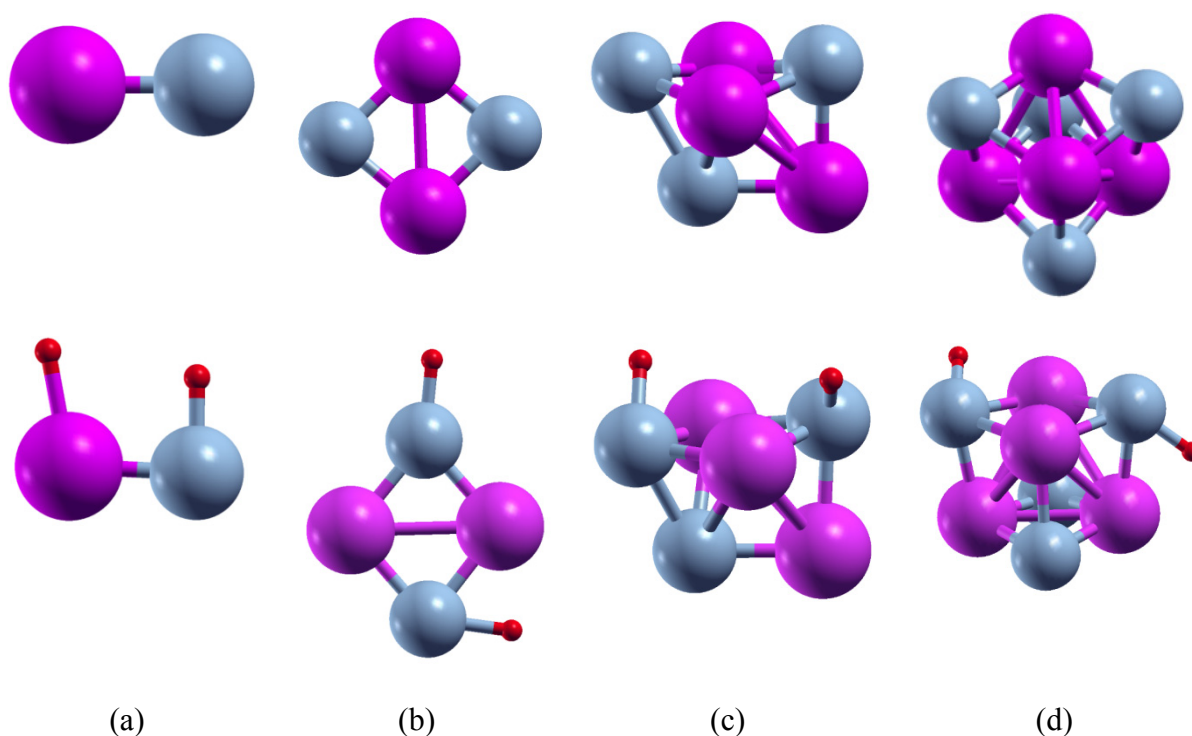
Fig. 6.16: Stable isomers of Zr_mCo_n (m+n = 2, 4, 6 and 8) clusters and their hydrogen adsorbed counter parts (pink ball = Zr, gray ball = Co and red ball = H). (a) ZrCo and ZrCo-2H, (b) Zr_2Co_2, Zr_2Co_2-2H, (c) Zr_3Co_3, Zr_3Co_3-2H and (d) Zr_4Co_4, Zr_4Co_4-2H

b) Tetramer

The structure of a tetramer cluster is important as this is the smallest size where a cluster can choose between planar and non-planar structure, which in turn provide initial clue about the

154

growth pattern of larger clusters. For tetramer (m+n = 4) alloy clusters, three compositions (1:3, 2:2, 3:1), apart from homoatomic clusters, are possible. Accordingly, we have optimized various possible isomeric structures of Zr_4, Co_4, Zr_3Co, Zr_2Co_2 and $ZrCo_3$ clusters. The results (average bond length, average binding energy and magnetic moment) are summarized in Table 6.6.

Table 6.6: Average bond length, average binding energy, magnetic moment of Zr_mC_n (m+n = 4, 6 and 8) clusters

Number of atoms (n)	System	Ave. Zr-Co Bond Length (Å)	Ave. Binding Energy (eV/atom)	Magnetic Moment (μ_B)
n=4	Zr_4	-	-3.18	4
	Zr_3Co	2.40	-3.09	3
	Zr_2Co_2	2.26	-3.14	0
	$ZrCo_3$	2.24	-2.73	5
	Co_4	-	-2.31	10
n=6	Zr_6	-	-3.73	2
	Zr_5Co	2.42	-3.77	1
	Zr_4Co_2	2.37	-3.80	2
	Zr_3Co_3	2.34	-3.86	1
	Zr_2Co_4	2.45	-3.47	4
	$ZrCo_5$	2.43	-3.24	9
	Co_6	-	-2.99	14
n=8	Zr_8	-	-4.05	4
	Zr_7Co	2.44	-4.06	1
	Zr_6Co_2	2.39	-4.08	0
	Zr_5Co_3	2.40	-4.10	1
	Zr_4Co_4	2.44	-4.16	4
	Zr_3Co_5	2.52	-3.79	3
	Zr_2Co_6	2.55	-3.56	8
	$ZrCo_7$	2.49	-3.35	11
	Co_8	-	-3.13	16

The binding energy of Zr_mCo_n clusters along with their hydrogenated species is shown in Fig. 6.17(a) and 6.17(b).

(a)   (b)
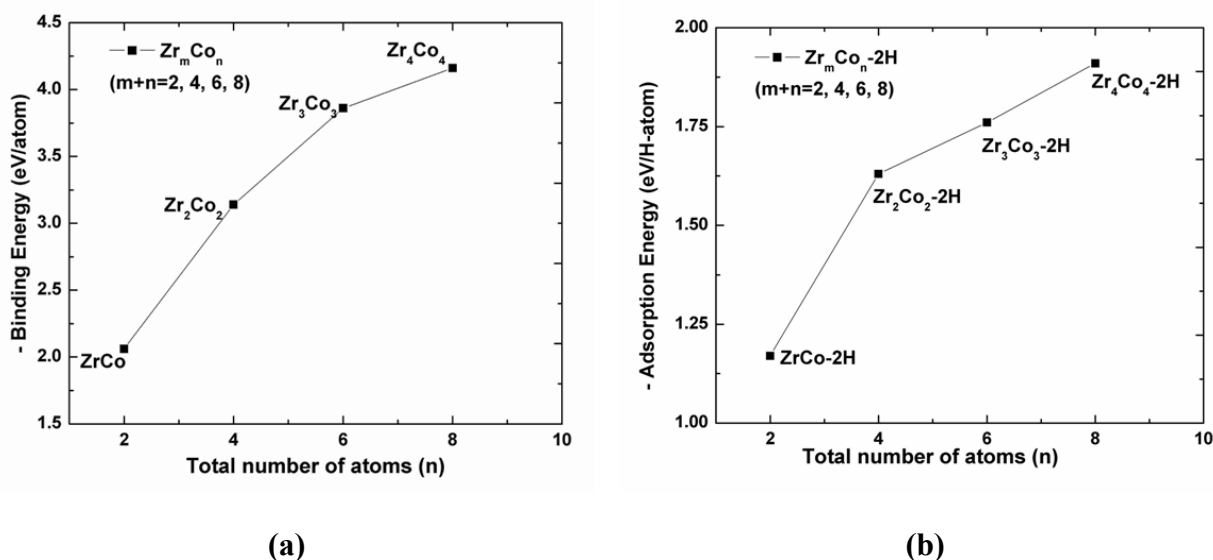
Fig. 6.17: Binding energy of (a) Zr_mCo_n clusters and hydrogen adsorption energy of (b) Zr_mCo_n-2H (m+n = 2, 4, 6 and 8) clusters as a function of cluster size

It is seen that Zr_2Co_2 is most the stable among all the Zr_mCo_n (m+n = 4) clusters with binding energy -3.14 eV/atom. It is seen from Table 6.3 that Zr_4 forms a triangular pyramid as lowest energy structure with average Zr-Zr bond length of 2.77 Å. The substitution of a single Zr by Co atom in Zr_4 resulting Zr_3Co does not change the geometry as well as binding energy much. Further substitution of a Zr atom in Zr_3Co forming Zr_2Co_2 changes the 3-dimensional triangular pyramid into square planar structure with average Zr-Co bond length of 2.26 Å. The further substitution of Zr atoms in Zr_2Co_2 resulting $ZrCo_3$ and Co_4 does not change the square planar geometry. The Zr_2Co_2 cluster can be visualized as a combination of maximum of two ZrCo dimer moieties which gives stability to Zr_2Co_2 whereas in Zr_3Co and $ZrCo_3$ only one ZrCo dimer moiety is present. The magnetic moment of Zr_4 and Co_4 clusters are calculated to be 4 and 10 μ_B, respectively. The substitution of Zr atom in Zr_4 cluster and Co atom in Co_4 cluster reduces the magnetic moment upto Zr_2Co_2 composition. The Zr_2Co_2 was found to be paramagnetic in nature.

c) Hexamer

For hexamer Zr_mCo_n clusters (m+n= 6) clusters, we have investigated all compositions starting from Zr_6 to Co_6 by substituting one atom at a time *viz.* Zr_5Co, Zr_4Co_2, Zr_3Co_3, Zr_2Co_4, $ZrCo_5$. For each cluster we have optimized a large number of isomers generated using *cascade* genetic algorithm scheme. The relative stability of various isomers (within 1 eV difference of energy with respect to lowest energy isomer) is listed in the Table 6.4). Both homoatomic clusters, Zr_6 and Co_6, favors high symmetry octahedral geometry with Zr-Zr and Co-Co bond lengths 2.93 Å, and 2.27 Å, respectively. The substitution of one Zr by Co atom in Zr_6 cluster does not show any significant deviation from the octahedral structure for of the Zr_5Co cluster. In the next step when two Zr atoms are replaced by Co atoms, the resulting Zr_4Co_2 cluster adopts distorted octahedron like envelope structure. Subsequent substitution of Zr atoms by Co retains the structural motif of envelop like structure for Zr_3Co_3 and Zr_2Co_4 clusters but $ZrCo_5$ adopts octahedral geometry as shown in Table 6.4. A comparison of binding energy for all these hexamer clusters shows the highest stability of Zr_3Co_3 cluster. The binding energy of Zr_3Co_3 is estimated to be -3.86 eV/atom and the smallest bond length of Zr-Co is 2.34 Å. In Fig. 6.16(c), the structure of the Zr_3Co_3 cluster can be viewed as bicapped rhombus formed by the fusion of Zr_2Co_2 and $ZrCo$ clusters so that the Zr-Co bonds are maximized in the structure. Thus the stability of Zr_3Co_3 cluster is attributed to the highest number of Zr-Co bonds as compared to the other hexamer clusters. The total magnetic moment of Zr_6, Co_6 and Zr_mCo_n (m+n = 6) clusters is listed in Table 6.6. The homoatomic Zr_6 and Co_6 clusters have magnetic moments 2 and 14 μ_B, respectively. In general, for alloy clusters, while Zr rich clusters show lower magnetic moment, the Co rich clusters have higher magnetic moment. The magnetic moment of Zr_3Co_3 cluster is reduced to 1 μ_B.

d) Octamer

The atomic and electronic structure of Zr_mCo_n (m +n = 8) has been investigated through all composition range. For ionic optimization, several initial structures were generated using cascade genetic algorithm. Based on the comparison of relative energies, the homoatomic Zr_8 and Co_8 clusters are found to favor bicapped octahedron structures as shown in Table 6.5. The smallest bond lengths of Zr-Zr and Co-Co is 2.88 Å and 2.32 Å, respectively. The geometry of other low-lying isomers, close to the lowest energy isomer, along with bond lengths and magnetic moments are listed in the Table 6.5 and Table 6.6. For alloy clusters, although the lowest energy isomers favor distorted bicapped octahedron moiety and the amount of distortion depends on the ratio of constituents. For example, the lowest energy isomer of the Zr_5Co_3 cluster can be viewed as tricapped triangular bypiramid, where the trigonal bi-pyramid (TBP) is formed by five Zr atoms and three Co atoms cap three trigonal faces. For equiatomic Zr_4Co_4 cluster, a compact geometry with tetracap tetrahedron structure is found to be the most stable configuration, where Zr and Co atoms are placed at alternate positions. From the binding energy point of view the Zr_8 is more stable than Co_8 cluster by 0.92 eV. In general, alloy clusters show higher stability as compared to the homoatomic clusters. In particular, the alloy cluster with equiatomic composition showed the highest stability. Accordingly, the binding energy of the Zr_4Co_4 cluster, which is 4.16 eV/atom, is the highest among all the compositions for octamer alloy clusters. The higher stability of this cluster is attributed to the largest number of Zr-Co bonds. From the spin distribution point of view all Zr_mCo_n (m+n= 8) clusters have spin polarization except Zr_6Co_2. The magnetic moment of Zr_8 and Co_8 is 4 and 16 μ_B, respectively. The substitution of Zr in Co_8 quenches magnetic moments to 11, 8, 3, 4 μ_B, for $ZrCo_7$, Zr_2Co_6, Zr_3Co_5 and Zr_4Co_4, respectively.

e) Electronic structure and hydrogenation of the *Zr_mCo_n (m+n = 2, 4, 6 and 8) clusters*

After establishing the stable isomers of Zr_mCo_n clusters, we have investigated the chemical reactivity of these clusters. ZrCo intermetallic compounds are known to be promising for hydrogen isotope (tritium) storage. Thus we have evaluated the interaction behavior of ZrCo clusters with molecular and atomic hydrogen.

First, we have performed the H_2 molecule adsorption on the lowest energy structures of Zr_mCo_n (m+n = 2, 4, 6 and 8) clusters. The hydrogen adsorption energy, hydrogen-metal bond length and magnetic moments of hydrogenated clusters are shown in Table 6.7.

Table 6.7: Hydrogen adsorption energy, H-metal atom bond length (D_{H-M}) and magnetic moment of Zr_mCo_n -2H (m+n = 2, 4, 6 and 8) clusters

Cluster	Adsorption energy (eV/H-atom)	D_{H-M} (Å)	Magnetic Moment (μ_B)
ZrCo-2H	-1.17	Zr-H = 1.86	1
		Co-H= 1.52	
Zr_2Co_2-2H	-1.63	Co-H = 1.62	0
Zr_3Co_3-2H	-1.76	Co-H = 1.62	1
Zr_4Co_4-2H	-1.91	Co-H = 1.61	2

The results showed that molecular hydrogen adsorption is stable on Zr_mCo_n clusters. The estimated interaction energy varies from 0.52 eV to 1.23 eV depending on the size of the cluster. In general hydrogen molecule prefers to bind on the Co site with elongation of the H-H bond upto 0.82 Å. The activation of the hydrogen bond indicates the possibility of rupturing the bond and adsorption of hydrogen in the atomic form is feasible. Thus we have performed additional calculations considering atomic hydrogen adsorption. Indeed, it is found that atomic hydrogen adsorption on Zr_mCo_n (m+n=2, 4, 6 and 8) clusters is thermodynamically favorable than molecular hydrogen. In line with previous results here also hydrogen atoms prefer Co site over the Zr site. Fig. 6.16 shows the lowest energy structure of

all these hydrated complexes. The interaction energy per H-atom varies from 1.17 to 1.91 eV. The H-Co bond distances are found to be 1.62, 1.62 and 1.61 Å for Zr_2Co_2-2H, Zr_3Co_3-2H, Zr_4Co_4-2H species, respectively. The magnetic moment of Zr_mCo_n (m+n= 2, 4 and 6) clusters has not been quenched except Zr_4Co_4 clusters.

In order to underscore the nature of chemical bonding present in Zr_mCo_n (m+n= 2, 4, 6 and 8) clusters and their hydrogenated species , the density of states (DOS) spectra and charge density contours have been calculated as shown in Fig. 6.18-6.21 and 6.22, respectively. From these figures it is clear that for ZrCo clusters the 4d and 3d orbitals of Zr and Co, respectively contributing to the total DOS. While 3d orbitals of Co are dominating below the Fermi level (E_F), above E_F, 4d orbitals of Zr are contributing.

In the DOS of ZrCo-2H, two new peaks at around -5 eV are present which corresponds to two hydrogen atoms adsorbed by ZrCo dimer. The Fermi level of ZrCo dimer is lowered by 0.41 eV after hydrogenation and indicates higher stability of the hydrogenated species compared to its dimer. Similar phenomena have been observed in the DOS of Zr_2Co_2, Zr_3Co_3 and Zr_4Co_4 clusters and their hydrogenated species which are shown in Fig. 6.18-6.21.

The charge distribution among different atoms in the system is an important parameter to get insight about the nature of bonding. The charge density contours of ZrCo dimer and its hydrogenated species (ZrCo-2H) are shown in Fig. 6.22. It is seen that in ZrCo dimer the electron density is higher in between Zr and Co, indicating covalent bonding between them. In contrast, a significant charge is transferred from Zr to Co in Zr_2Co_2, Zr_3Co_3 and Zr_4Co_4 clusters (as shown in Fig. 6.22) indicating partial ionic character to these Zr-Co bonds. For ZrCo-2H, electronic charge is transferred from Zr and Co to the H atoms. For other hydrogenated clusters, electronic charge enriched Co atom donates charge to two

attached H atoms as shown in Fig 6.22. This is also supported by the DOS spectra of ZrCo clusters and their hydrogenated species which is discussed above.
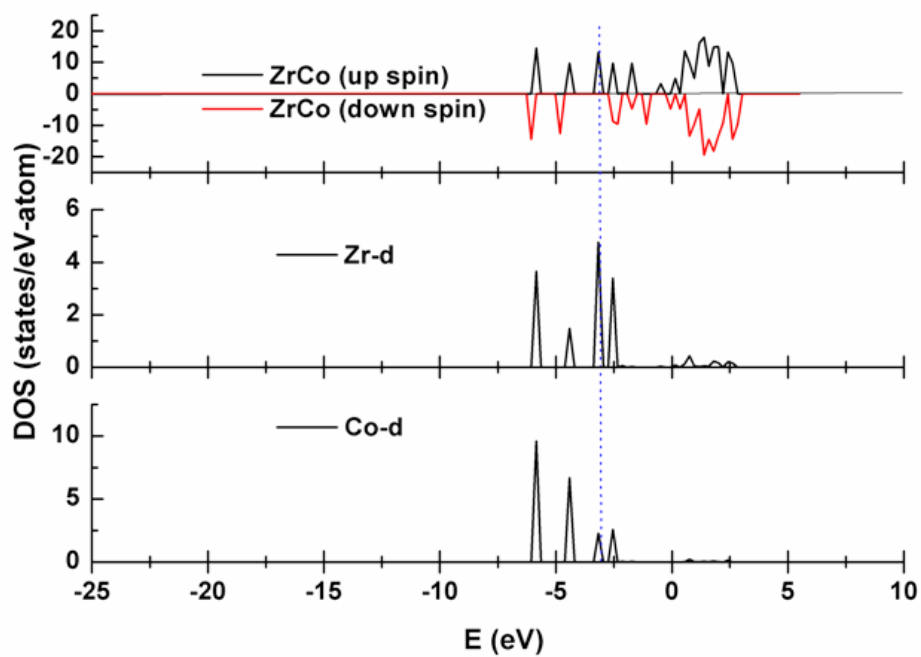
(a)
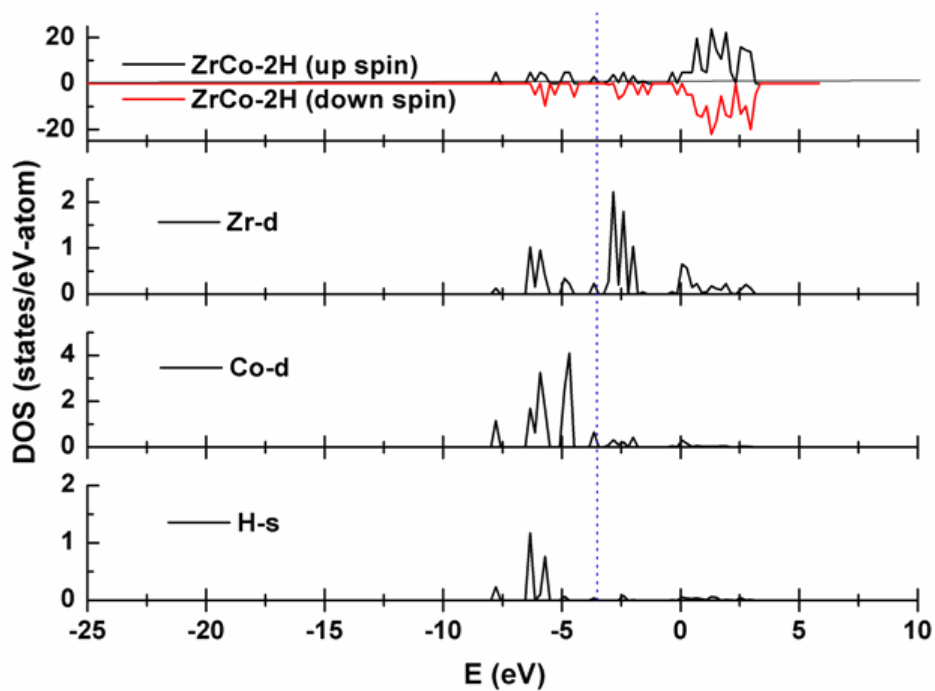
(b)

Fig. 6.18: Partial density of states of (a) ZrCo and (b) ZrCo-2H clusters
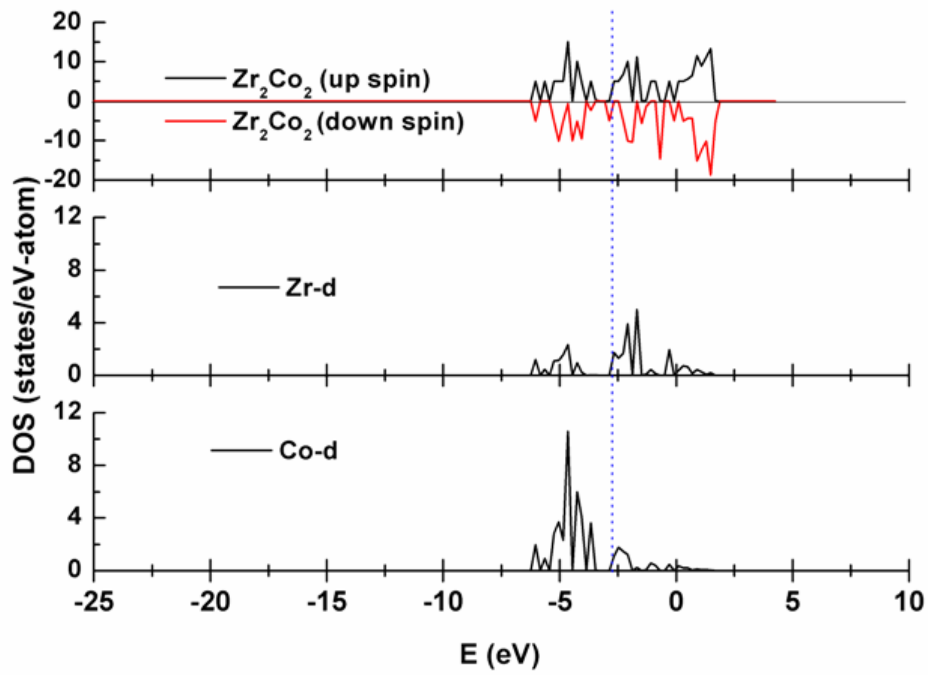
(a)
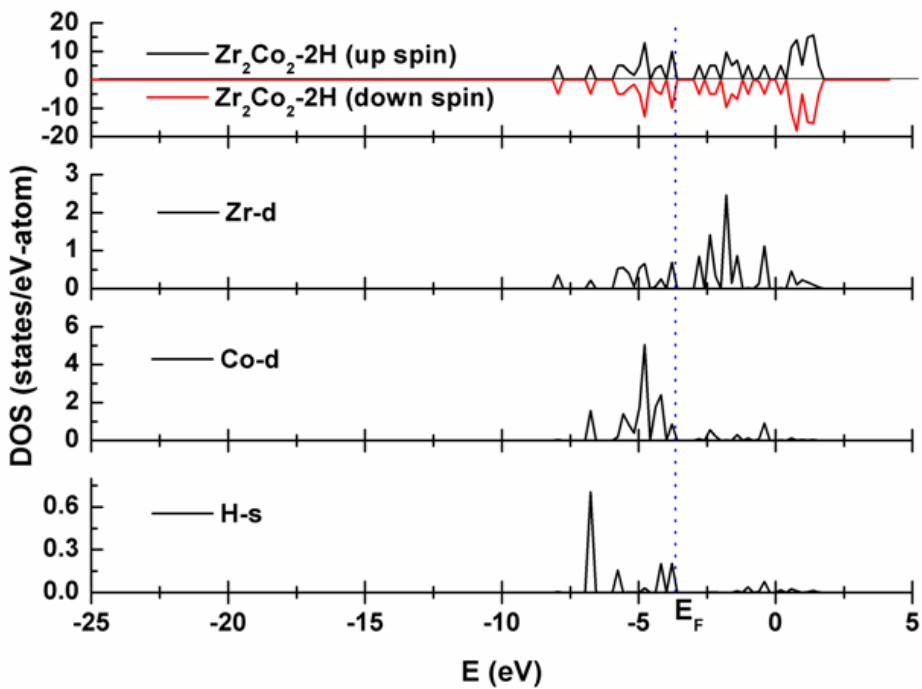
(b)

Fig. 6.19: Partial density of states of (a) Zr_2Co_2 and (b) Zr_2Co_2-2H clusters
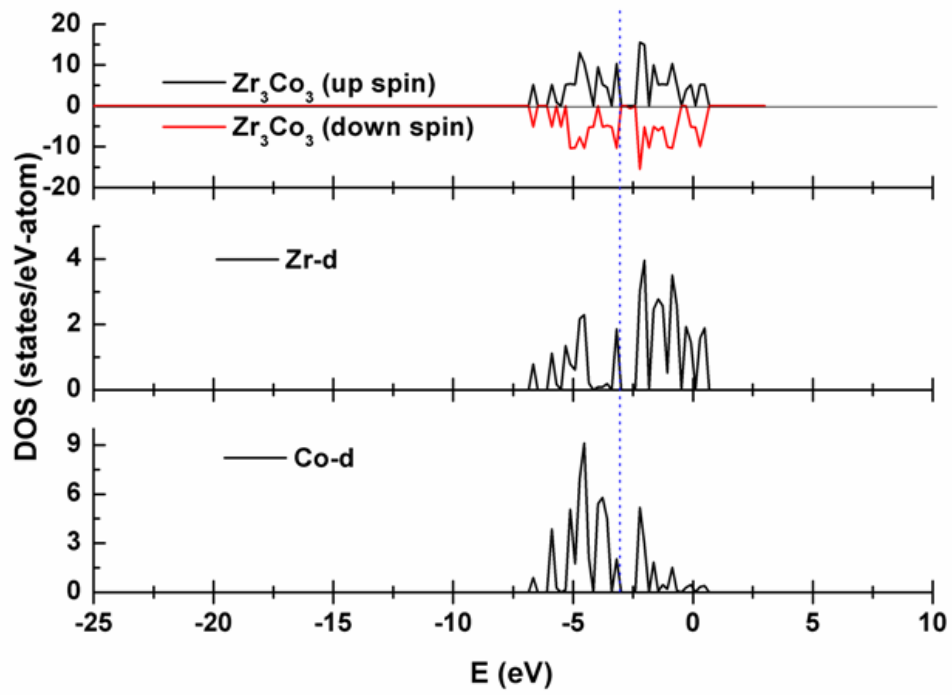
(a)
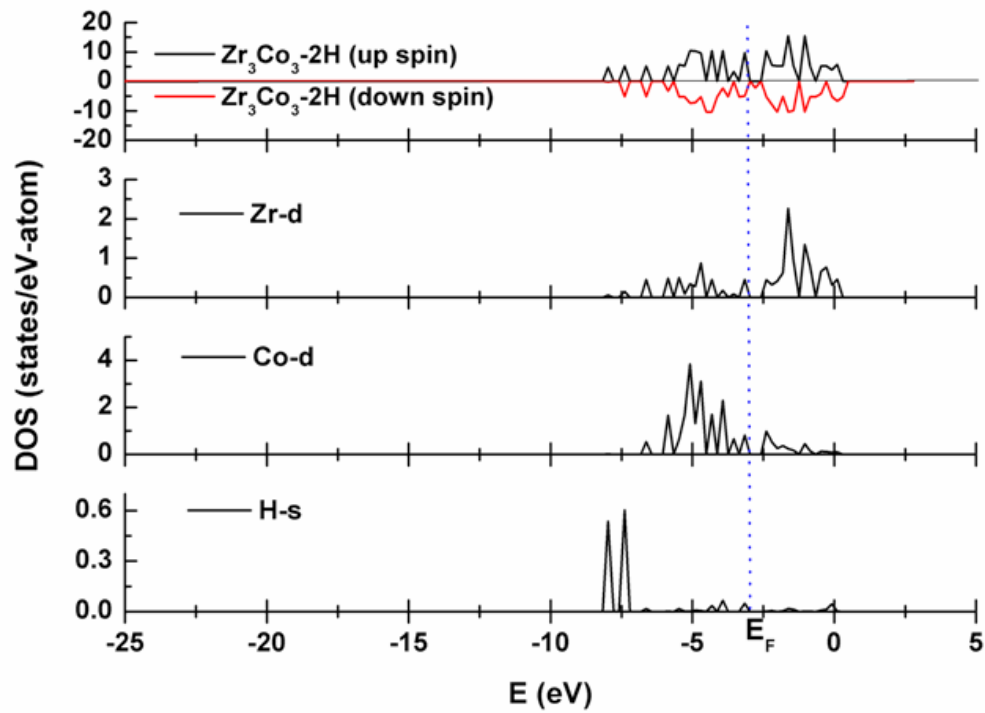
(b)

Fig. 6.20: Partial density of states of (a) Zr₃Co₃ and (b) Zr₃Co₃-2H clusters
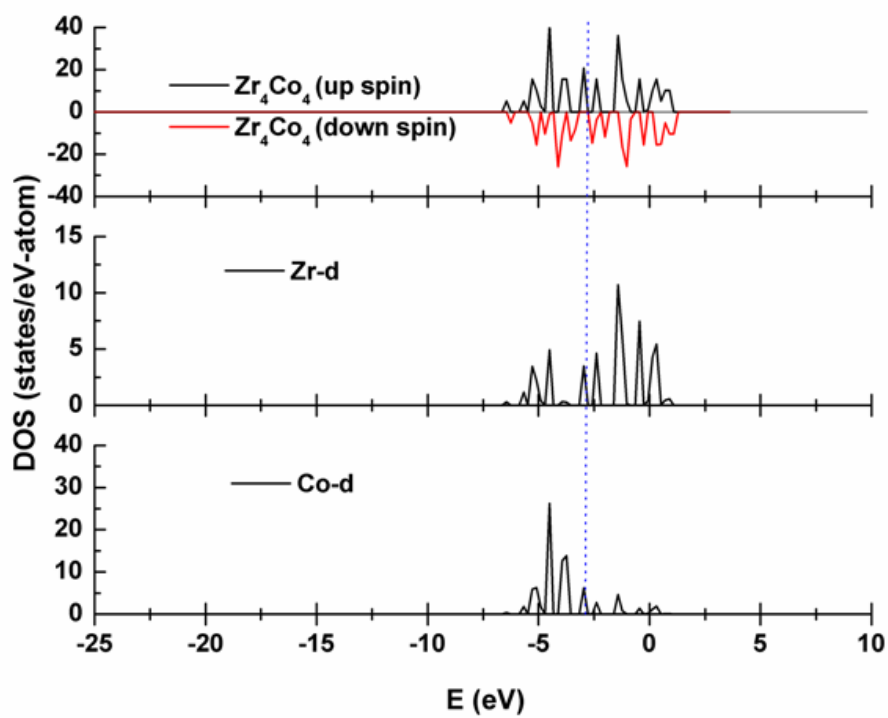
(a)
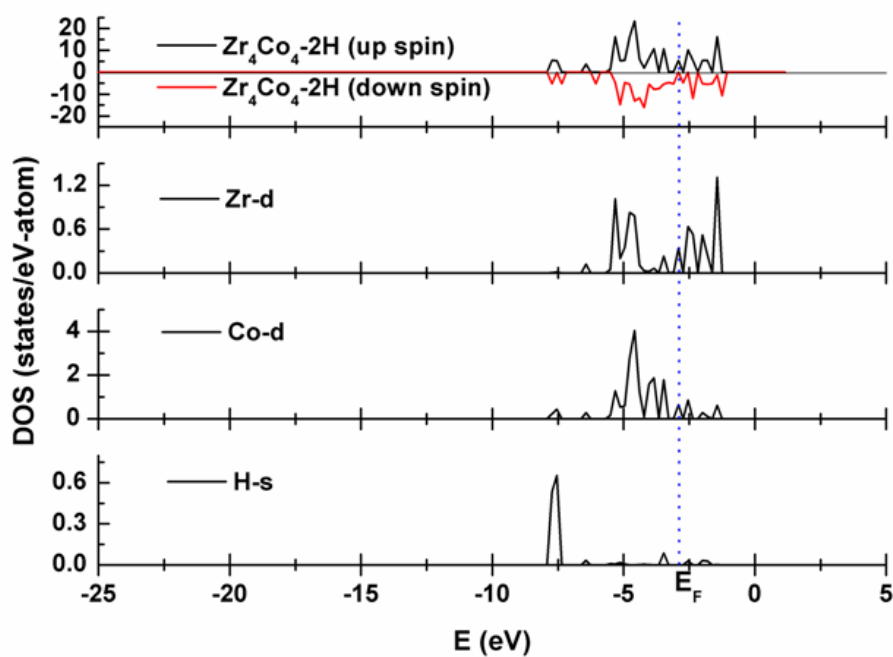
(b)

Fig. 6.21: Partial density of states of (a) Zr_4Co_4 and (b) Zr_4Co_4-2H clusters
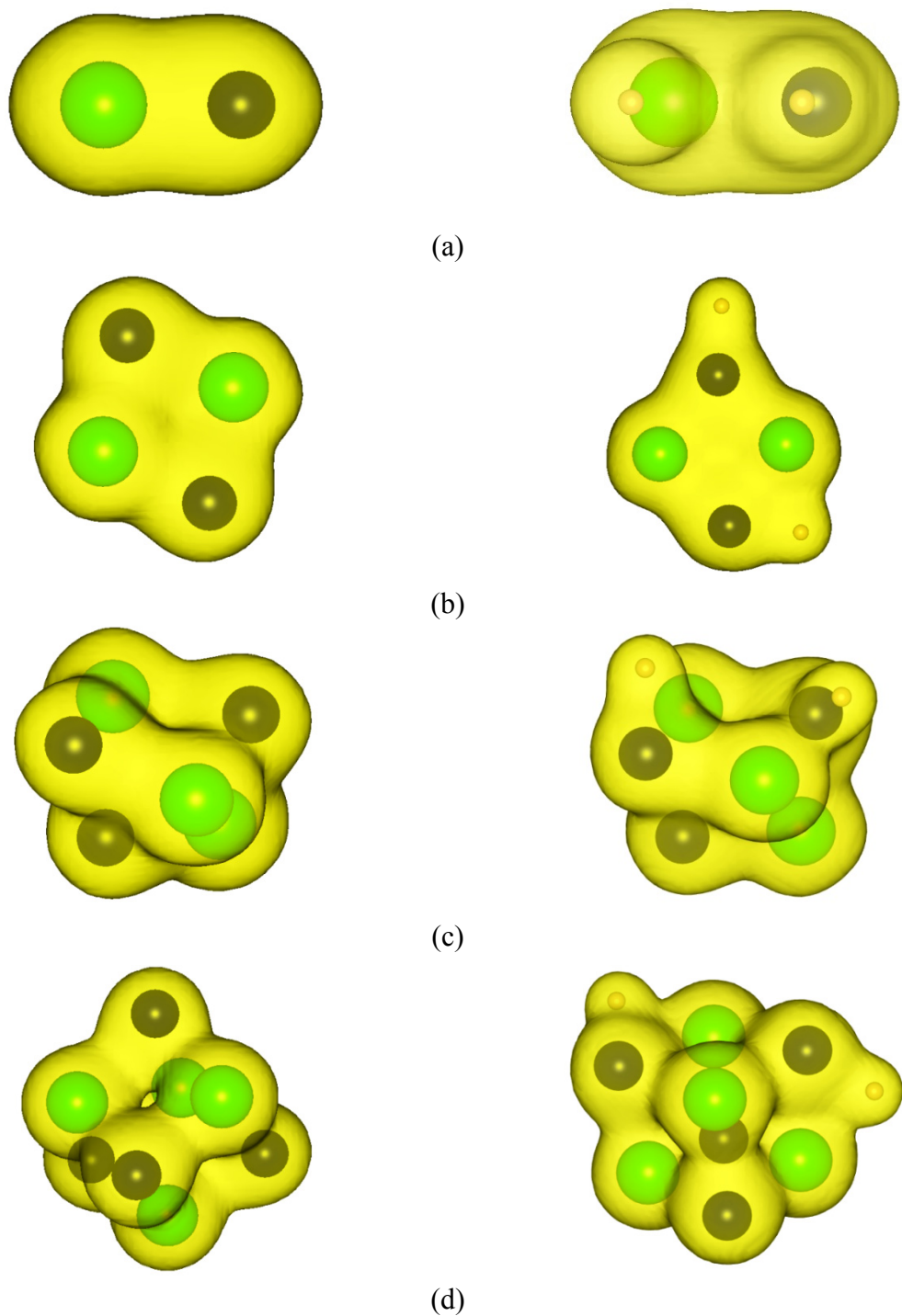
Fig. 6.22: The charge density contour of Zr_mCo_n and Zr_mCo_n-2H (m+n= 2, 4, 6 and 8) clusters. The green balls correspond to Zr atoms and gray balls correspond to Co atoms and white balls correspond to H atoms. (a) ZrCo and ZrCo-2H, (b) Zr_2Co_2, Zr_2Co_2-2H, (c) Zr_3Co_3, Zr_3Co_3-2H, and (d) Zr_4Co_4, Zr_4Co_4-2H

CHAPTER 7

Conclusions

7.1 Conclusions

It has been noticed that both uranium and zirconium based alloys are potential candidates for storage of hydrogen isotopes. Among various alloys, U_2Ti and ZrCo have been studied more in literature compared to other alloys. Alhough both alloys have their own advantages and disadvantages, scientific community is yet to converge on one of them to be used as tritium storage materials. In this competition, ZrCo alloy is few step ahead due to its few favourable properties like it is a non-nuclear material and its hydride is not pyrophoric. To understand the behavior of those alloys and the effect of hydrogenation, it is important to study the fundamental physico-chemical properties of alloy-hydrogen systems. This will not only provide us the behavior of these alloys and their hydrides but also help us to overcome their drawbacks related to tritium storage. For this purpose, computational and experimental study of these systems have been carried out which is the main objective of this thesis. The computational study has helped us to unravel the physico-chemical properties and isotope effect of $ZrCoX_3$ (X=H, D and T) compounds. In particular, how the hydrogenation behavior evolves with change in dimension of the alloy ZrCo, have been studied and reported in this thesis. Another important aspect of hydrogen storage is the investigation of hydrogen diffusion in the alloy. The hydrogen diffusion path, mechanism, activation barrier, temperature dependent diffusion coefficient etc are investigated theoretically and reported in this thesis. A summary of present study is discussed below.

Followed by uranium, its alloy U_2Ti has been found to be a better material for hydrogen isotope storage. Therefore, we felt a need to explore the fundamental properties of U_2Ti compound before it can be really used for the purpose of tritium storage. With this motive, we have calculated the structural and electronic properties of U, Ti and U_2Ti under the framework of spin polarized density functional theory. It was that the plane wave pseudopotential method coupled with spin-orbit interaction term as implemented in VASP is

capable of describing the ground state properties quite accurately. It was found that the structural parameters like lattice constants, bulk moduli, the formation energy, and the electronic specific heat calculated in this work are in good agreement with available experimental values. The estimated lattice parameters are found to be within 1.0 % from the experimental data. The nature of chemical interaction in these systems has been derived by comparing the DOS spectrum of U, Ti and U_2Ti. Moreover, the inclusion of spin-orbit effects results in narrowing the band width above the Fermi level. Finally, the results obtained in this study is giving encouragement that the state-of-the-art computational techniques based on density functional theory can be meaningful in several respects to research on heavy metal based hydrogen storage materials.

Thermodynamics of alloys play a crucial role for its selection as a tritium storage material. As a part of experimental study, the enthalpy increments of U_2Ti alloy were measured using drop calorimeter. A set of self consistent thermodynamic functions of U_2Ti were computed using enthalpy increment data obtained in this study. The Gibbs energy of formation values calculated in this study could be used for calculation of equilibrium pressures of hydrogen isotopes in hydriding and dehydriding cycles. The thermodynamic functions of U_2Ti obtained in this study would be very much useful for the understanding various reactions of U_2Ti alloy.

Before proceeding to the study of ZrCo and its hydride, we have studied the physico-chemical properties of ZrH_2 using *ab-initio* method. The electronic, vibrational, and thermodynamic properties of zirconium hydrides, ZrX_2 (X = H, D, T), with a focus on the effect of isotopic substitution was investigated theoretically. The nature of chemical bonding was analyzed through charge density distribution, electronic density of states, and electron localization function. The results showed significant electronic charge transfer from Zr to the X site, indicating ionic bond character. The phonon frequencies, phonon density of states and

phonon dispersion curves were obtained using the direct super-cell method and the Raman and infrared active modes of all the compounds were assigned. Using the phonon frequencies, the thermodynamic functions were determined within the framework of harmonic approximation. A good agreement was found between the experimental results and the calculated values. On the basis of the ZPE corrected enthalpies of formation ($\Delta_f H$ at 0 K) for all three compounds, it is found that the thermodynamic stabilities vary as: $ZrT_2 > ZrD_2 > ZrH_2$. Thus the effect of atomic mass of different isotopes on the thermodynamic properties was established. Based on the results, it is envisaged that the ZPE corrected enthalpy of formation data at 0 K coupled with the high temperature data of ZrX_2 (X= H, D, T) will help us to calculate the equilibrium dissociation pressure of X_2 (X= H, D, T) for practical applications. This computational study provided immense confidence for similar study on ZrCo and its hydride which is the main motif of this thesis.

As mentioned earlier, ZrCo and its hydride $ZrCoX_3$ (X= H, D and T) are potential system for tritium storage and its fundamental properties are of great importance. A comprehensive study on ZrCo and $ZrCoX_3$ (X = H, D and T) compounds is performed to explore its structural, electronic, vibrational, thermodynamic and elastic properties using first principles approach. The calculated lattice parameters of ZrCo and $ZrCoH_3$ are found to be within ± 1% of the reported experimental data. The volume expansion upon hydrogenation of ZrCo was found to be 22.9%. The formation energies of ZrCo and $ZrCoH_3$ compounds have been estimated to be -56 kJ/mol and -91 kJ/mol of H_2 respectively. The formation enthalpy data at 0 K can be coupled to high temperature thermodynamic data of ZrCo and $ZrCoH_3$ to calculate the equilibrium dissociation pressure of hydrogen for practical application. The role of Zr and Co in $ZrCoH_3$, in terms of bonding with H, is described through the density of states spectrum and the charge distribution analysis. The frequencies and dispersion curves of phonon are obtained using the frozen phonon approach and the Raman and infrared active

modes are also assigned. Using the calculated phonon frequencies, the thermodynamic functions are determined within the harmonic approximation. The ZPE corrected enthalpies of formation ($\Delta_f H$ at 0 K) for $ZrCoX_3$ (X = H, D, T) are -146.7, -158.3 and -164.1 kJ/(mole of $ZrCoX3$) for X = H, D and T, respectively. This suggests that $ZrCoT_3$ and $ZrCoD_3$ are more stable than $ZrCoH_3$. The isotope effect is also reflected on the thermodynamic properties of these compounds. The ZPE corrected enthalpy of formation data at 0 K coupled with the high temperature data of $ZrCoX_3$ (X = H, D, T) will help to calculate the equilibrium dissociation pressure of X_2 (X = H, D, T) for practical applications. In addition to the dynamical and thermodynamic properties, the effect on elastic properties upon hydrogenation of ZrCo is also explored in this study. The results show that both ZrCo and $ZrCoH_3$ are mechanically stable. On the basis of elastic properties it is also envisaged that both ZrCo and $ZrCoH_3$ are ductile in nature.

Thermodynamics of alloy is important for its use as tritium getter bed. It is important to investigate the thermodynamic properties of the alloy theoretically and validate that with experiment or vice versa. For this purpose, the enthalpy increments of $Zr_{0.5}Co_{0.5}(s)$ intermetallic were measured using inverse drop calorimeter. The thermodynamic functions of ZrCo (s) were estimated using enthalpy increment data obtained in this study. The Gibbs energy values calculated for ZrCo (s) could be used for calculation of equilibrium pressure of hydrogen isotopes in hydriding and dehydriding cycles. The thermodynamic functions obtained experimentally and theoretically would be very much useful for the understanding of various thermal reactions of ZrCo intermetallic. The computed temperature dependent thermodynamic functions may provide critical insight into temperature dependent effects of ZrCo alloy.

The change in dimension of the tritium storage material may have an impact on its storage behavior. Thus, it is interesting to study how hydrogen interacts with ZrCo in

different dimensions like bulk, surface and nanoclusters. With this scope, after studying the bulk ZrCo and ZrCoH$_3$, the adsorption and diffusion of H on ZrCo (110) surface and in the bulk have been investigated using the DFT calculations. The results show that the decomposition of H$_2$ molecule on ZrCo (110) can easily occur and the largest barrier of H$_2$ decomposition is 0.70 eV. The adsorption of H$_2$ molecule is weak with adsorption energy of 0.28 eV/H$_2$, where as the adsorption of H atom is strong and the maximum adsorption energy was found to be -0.79 eV at hollow site. The adsorption energy of H atom increases with increase in hydrogen coverage. The adsorptions of H atom on ZrCo (110) surface, subsurface and bulk are exothermic with respect to gas phase H$_2$ molecule. The stability order for H adsorption is surface > bulk > subsurface. The energy barriers for H diffusion on surface are in the range 0.15-0.94 eV, however the minimum energy barrier is only 0.15 eV, indicating that H can easily diffuse on surface. The energy barrier for the penetration of H from surface to the bulk is 0.79 eV. Further, the energy barrier for the diffusion of H in bulk ZrCo is 0.61 eV. Here, the entire process of molecular hydrogen adsorption, decomposition, atomic hydrogen diffusion on ZrCo surface, subsurface and inside the bulk has been depicted using the *ab-initio* method. This study on hydrogen interactions with ZrCo surface is important for the fundamental understating of this alloy-hydrogen system and it may help to overcome the disadvantages of this alloy related to hydrogen isotope storage.

After establishing the hydrogen interaction with ZrCo bulk and surface, it is of great interest to study that with ZrCo nanoclusters. For that, the growth behaviors, stabilities, magnetic and electronic properties of small-sized Zr$_m$Co$_n$ (m+n = 2, 4, 6 and 8) clusters are investigated using GGA-PBE under DFT. The higher binding energy of ZrCo dimer compare to Zr$_2$ and Co$_2$ indicates stronger Zr-Co bond compare to Zr-Zr and Co-Co bond. From the binding energy calculation it has been found that Zr$_2$Co$_2$ (for tetramer), Zr$_3$Co$_3$ (for hexamer) and Zr$_4$Co$_4$ (for octamer) are the most stable isomers. Molecular hydrogen adsorption on the

stable Zr_mCo_n (m+n = 2, 4, 6, 8) clusters has also been studied. It has been found that in case of ZrCo dimer, two H atoms of H_2 molecule get adsorbed on Zr and Co atoms independently. Whereas, in higher order Zr_mCo_n (m+n = 4, 6 and 8) clusters, the two H atoms get adsorbed by two different Co atoms present in those clusters. The electronic structures of Zr_mCo_n clusters along with their hydrogen adsorbed species are described in terms of density of state spectra and charge density contours. The magnetic moment of the Zr_mCo_n (m+n = 2, 4, 6 and 8) clusters and their hydrogenated species are also reported.

7.2 Future Scope

Though ZrCo is a promising material for tritium storage, it has one drawback. $ZrCoH_3$ undergoes disproportionation reaction on repeated hydrogen absorption-desorption resulting to the formation of stable hydride ZrH_2 and hydrogen non-absorbing phase $ZrCo_2$. Due to this disproportionation reaction the hydrogen storage capacity of ZrCo decreases. Recent experimental studies suggest that this drawback can be reduced or eliminated by ternary alloying of ZrCo. It is expected that our comprehensive study on ZrCo and ZrCoH3 will definitely help in choosing the ternary alloy. The basic fundamental properties of ZrCo alloy reported in this thesis will be useful for the investigation of ternary alloys related to tritium storage.

Experimental study of tritides requires a special and safe facility as tritium is radioactive in nature. The calculated properties of ZrX_2 and $ZrCoX_3$ (X= H, D and T) and determined isotope effects will hopefully be useful in further experimental studies. Hydrogen diffusion on the ZrCo surface, surface to bulk and inside the bulk has been carried out using ab-initio method and reported in this thesis. Deuterium and tritium are heavier than hydrogen and diffusion process depends on the mass of the diffusing species. Hence, there is a scope of studying how the diffusion behavior changes with deuterium and tritium in place of hydrogen.

Another serious issue in tritium storage is tritium aging. Tritium has radiological half life of 12.3 years. Tritium decays into helium-3 by beta decay. Due to long term storage, there is accumulation of helium in the tritides matrix. This tritium aging will reduce the tritium storage properties of the material. It is required that the storage material should have a good helium retention capacity. Hence, there is a scope to reduce the tritium aging effect of the existing tritium storage materials or find out a material with good helium retention capacity through theoretical and experimental studies. The reported data in this thesis on both uranium and zirconium based alloys will hopefully help in tritium storage projects.

References

1. Omar Ellabban, Haitham Abu-Rub, Frede Blaabjerg, Renewable and Sustainable Energy Reviews 39 (2014) 748–764.

2. The ITER project, EFDA, European Fusion Development Agreement, 2006.

3. T. Nagasaki, S. Konishi, H. Katsuta, Y. Naruse, Fusion Technol. 9 (1986) 506-509.

4. Anjan Chaki; R.K. Purohit, R. Mamallan, Energy Procedia. 7 (2011) 153–157.

5. Turan Unak; Prog. Nucl. Energ. 37 (2000) 137-144.

6. J. G. Coller, G. F. Hewitt, Introudction to Nuclear Power, Hemisphere Publishing Coroporation, USA.

7. J. Byrne, Neutrons, Nuclei, and Matter, Dover Publications, Mineola, NY, 2011, p. 259, ISBN 978-0-486-48238-5.

8. R. Vandenbosch and J. R. Huizenga, Nuclear Fission, Academic Press, New York, 1973.

9. R. D. Evans, The Atomic Nucleus, Tat-McGraw-Hill Book Co., New York, 1978.

10. I. Kaplan, Nuclear Physics, 2nd Ed., Addision Wesley, Cambridge, Massachusetts, 1963.

11. G. I. Bell and S. Glasstone, Nuclear Reactor Theory, Van Nostrand, Reinhold, New York, 1970.

12. A. M. Jacobs, Basic Principles of Nuclear Science and Reactors, Van Nostrand Princeton, New Jersey, 1960.

13. H. A. Bethe, Energy production in stars, Phys. Rev. 55 (1939) 434-456.

14. A. Beiser, Perspectives of Modern Physics, McGraw-Hill, 14th printing, 1984

15. Dan O'Leary, The deeds to deuterium, Nature Chemistry, 4 (2012), 236.

16. Nuclear Chemistry, Vols. 1 and 2, Editor L. Yaffe, Academic Press, New York, 1968.

17. W. Wenzl, K.H. Klatt, The Use of FeTi-Hydride for Production and Storage of Supra Pure Hydrogen, Hydrides for Energy Storage, Pergamon, 1978, p. 323.

18. J.J. Reilly, R.H. Wiswall, Inorg. Chem. 13 (1974) 218-222.

19. H. van Mal, K. Buschow, A.R. Miedema, J. Less-Common Mets. 35 (1975) 65-76.

20. M. S. Ortman, L.K. Heung, A. Nobile, R. L. Rabun, , J of Vacuum Science & Technology A 8(3) (1990) 2881-2889.

21. T. Motyka, Fusion Technol. 21 (1992) 247-252.

22. H. Dim, A. Percheron-Guegan, J.C. Achard, Int. J. of Hydrogen Energy 4 (1979) 445-454.

23. A. Nobile, Fusion Technol. 20 (1991) 186-199.

24. M.S. Ortman, T. J. Warren, D. J. Smith, Fusion Technol. 8 (1985) 2330-2336.

25. E.H.P Cordfunke, The chemistry of uranium, Amsterdam: Elsevier, 1969.

26. J.J. Katz, E . Robinowich, The chemistry of uranium, New York, Dover Publication, 1951.

27. G.R. Longhurst, Fusion Technol. 14 (1988) 750–755.

28. T. Yamamoto, T. Supardjo, T. Terai, F. Ono, S. Tanaka, M. Yamawaki, Fusion Technol. 14 (1988) 764–768.

29. T. Yamamoto, S. Tanaka, M. Yamawaki, J Nucl. Mater. 170 (1990) 140–146.

30. T. Yamamoto, T. Yoneoka, S. Kokubo, M. Yamawaki, Fusion Eng. Des. 7 (1989) 363–367.

31. S. Konishi, T. Nagasaki, N. Yokokawa, Y. Naruse, Fusion Eng. Des. 10 (1989) 355-358.

32. E. Willin, M. Sirch, Fusion Technol. 14 (1988) 756-763.

33. R.D. Penzhorn, M. Devillers, M. Sirch, J. Nucl. Mater. 170 (1990) 217-231.

34. M.V. Šušic´ , Int. J. Hydrogen Energy 13 (1988) 173-179.

35. W.T. Shmayda, A.G. Heics, N.P. Kherani, J. Less-Comm. Met. 162 (1990) 117-127.

36. B. Sakintuna, F. Lamari-darkim, M. Hirscher, Int. J. Hydrogen Energy 32 (9) (2007) 1121-1140.

37. H.J. Wenzl, Int. Met. Rev. 27 (1982) 140-168.

38. R. M. Martin. Electronic structure: Basic theory and practical methods, Cambridge University Press, 2004.

39. E. Schrödinger, Phys. Rev. 28 (1926) 1049–1070.

40. M. Born, J. R. Oppenheimer. Zur quantentheorie der molekeln. Ann Physik, 84 (1927) 457-484.

41. D. R. Hartree. Proc. Cam. Phil. Soc. 24 (1928) 89–110.

42. J. C. Slater. Phys. Rev. 34 (1929) 1293–1322.

43. C. Møller, M. S. Plesset. Phys. Rev. 46 (1934) 618–622.

44. C. D. Sherrill and H. F. Schaefer III. The configuration interaction method: Advances in highly correlated approaches. volume 34 of *Advances in Quantum Chemistry*, pages 143 – 269. Academic Press, 1999.

45. H. Kummel. Theoretica chimica acta, 80(2-3) (1991) 81–89.

46. P. Hohenberg, W. Kohn, Phys. Rev. 136 (1964) B864–B871.

47. W. Kohn, L. J. Sham, Phys. Rev. 140 (1965) A1133–A1138.

48. P. A. M Dirac. Proceedings of the Cambridge Philosophical Society, 26 (1930) 376-385.

49. J. P. Perdew, Y.Wang. Phys. Rev. B, 45 (1992) 13244–13249.

50. J. P. Perdew. Int. J. of Quant. Chem. 30(3) (1986) 451–451.

51. C. S. Wang, B. M. Klein, and H. Krakauer. Phys. Rev. Lett. 54 (1985) 1852–1855.

52. J. P. Perdew, K. Burke, M. Ernzerhof. Phys. Rev. Lett. 77 (1996) 3865–3868.

53. H. J. Monkhorst, J. D. Pack. Phys. Rev. B, 13 (1976) 5188–5192.

54. K. Laasonen, A. Pasquarello, R. Car, C. Lee, D. Vanderbilt, Phys. Rev. B, 47 (1993) 10142-10153.

55. P. Schwerdtfeger. Chem. Phys. Chem. 12(17) (2011) 3143–3155.

56. P. E. Blöchl. Phys. Rev. B, 50 (1994) 17953–17979.

57. G. Kresse, J. Furthmüller, Comput. Mater. Sci. 6 (1996) 15-50.

58. G. Kresse, J. Hafner, Phys. Rev. B 49 (1994) 14251-14269.

59. G. Kresse, J. Furthmüller, Phys. Rev. B 54 (1996) 11169-11186.

60. P. Giannozzi, S. Baroni, N. Bonini, M. Calandra, R. Car, C. Cavazzoni, D. Ceresoli, G. L. Chiarotti, M.Cococcioni, and I. Dabo *et al.* J. Phys. Cond. Matter, 21 (2009) 395502-1-19.

61. K. Parlinski, Z.Q. Li, Y. Kawazoe, Phys. Rev. Lett. 78 (1997) 4063-066.

62. O.K. Andersen, Phys. Rev. B 12 (1975) 3060-3083.

63. D. Vanderbilt, Phys. Rev. B 41 (1990) 7892-7895.

64. G. Kresse, D. Joubert, Phys. Rev. B 59 (1999) 1758-1775.

65. P.E. Blöchl, O. Jepsen,O.K. Andersen,Phys.Rev.B 49(1994) 16223-16233.

66. H. Hellman, Introduction to Quantum Chemistry, Deuticke, Leipzig, 1937.

67. R.P. Feynman, Phys. Rev. 56 (1939) 340-343.

68. F.D. Murnaghan, Proc. Natl. Acad. Sci. 30 (1944) 244-247.

69. Y. Le Page, P. Saxe, Phys. Rev. B 65 (2002) 104104-1-14.

70. N. Marzari, D. Vanderbilt, A. D.Vita, M.C. Payne, Phys. Rev. Lett. 82 (1999) 3296-3299.

71. I.R. Harris, D. Hussain, and K.G. Barraclough, Scripta Metallurgica 4 (1970) 305-308.

72. G. Henkelman, B.P. Uberuaga, H.A. Jónsson, J. Chem. Phys. 113 (2000) 9901-9904.

73. V. Blum, R. Gehrke, F. Hanke, P. Havu, V. Havu, X. Ren, K. Reuter and M. Scheffler; Comp. Phys. Comm. 180 (2009) 2175-2196.

74. S. Bhattacharya, S. Levchenko, L. Ghiringhelli, M. Scheffler, Phys. Rev. Lett. 111 (2013) 135501-135505.

75. S. Bhattacharya, S. Levchenko, L. Ghiringhelli, M. Scheffler, New J. Phys. 16 (2014) 123016-1-34.

76. A. V. Krukau1, O. A. Vydrov, A. F. Izmaylov and G. E. Scuseria J. Chem. Phys. 125 (2006) 224106-1-5.

77. Kuang-Oscar Yu , Modeling for Casting & Solidification Processing, CRC, 1st edition; October 15, 2001; ISBN 0-8247-8881-8.

78. B. D. Cullity; Elements of X-ray diffraction, Addison-Wesley publishing company, (1978).

79. H. P. Klug, L.E. Alexander; X-ray diffraction procedures, Wiley-Interscience Publication, NY, (1974).

80. R. Jenkins, X-ray Fluorescence Spectrometry, Wiley, ISBN 0-471-29942-1.

81. A. Montaser, D. W. Golightly, Inductively Coupled Plasmas in Analytical Atomic Spectrometry, VCH Publishers, Inc., New York, 1992.

82. Alan Newman, Elements of ICPMS, Analytical Chemistry 68 (1996) 46A-51A.

83. R. Hultgren, P. D. Desai, D. T. Hawkins, M. Gleigev, K. K. Kelley, Selected values of the thermodynamic properties of the elements. Metal Park, Ohio (1973).

84. R. Capelli, R. Ferro, A. Borsese, Thermochim Acta 10 (1974) 13-21.

85. E. Calvet, H.Pratt, Traite de Microcalorimetric, Paris (1956).

86. http://www.setaram.com/MHTC-96-Accessories.htm.

87. Multi HTC-96, Setaram Installation Guide and Manual (1997).

88. K. D. Maglic, A. Cezairliyan, V. E. Peletsky (Eds.), Compendium of Thermophysical Property Measurement Techniques, vol**.** 2, Plenum Press, NewYork**, (**1992).

89. Yoichi Takahashi and Yuji Kohsaka, J. Nucl. Mater. 130 (1985) 109.

90. J. Leitner, A. Strejc, D. Sedimidubsky, and K. Ruzicka, Thermochim. Acta 401 (2003) 169.

91. D. G. Archer, J. Phys. Chem. Ref. Data 22 (1993) 1441.

92. M. Nevriva, D. Sedimidubsky, J. Leitner, Thermochim. Acta 347 (2000)123-128.

93. C.S. Barrett, M.H. Mueller, R.L. Hitterman, Phys.Rev. 129 (1963) 625-629.

94. T. Le Bihan, S. Heathman, M. Idiri, G.H. Lander, J.M. Wills, A.C. Lawson, A. Lindbaum, Phys.Rev.B 67 (2003) 134102-1-6.

95. C.Kittel, Introduction to Solid State Physics, sixth edition, John Wiley, 1986.

96. R.T. Downs, M. Hall-Wallace, Am. Mineral. 88 (2003) 247-250.

97. A.G. Knapton, Acta Crystallogr. 7 (1954) 457-458.

98. W.B. Pearson, Lattice Spacings and Structures of Metals and Alloys, Pergamon, NewYork, 1958, p.874.

99. J.H. Wernick ,in: J.H. Westbrook (Ed.) Intermetallic Compounds, Wiley, New York, 1967.

100. W.P. Ellis, G.L. Powell, Surf. Sci. 115 (1982) L165-L171.

101. J.E. Gordon, H. Montgomery, R.J. Noer, R.Tobon, Phys.Rev. 152 (1966) 432-1-7.

102. C.H. Shomate, J. Phys. Chem. 58 (1954) 368–372.

103. D. Chattaraj, S.C. Parida, C. Majumder. Phys. B. 406 (2011) 4317–4321.

104. S. Bajaj, A. Landa, P. Söderlind, P.E.A. Turchi, R. Arroyave. J. Nucl. Mater. 419 (2011)177–185.

105. H.E. Flotow, D.W. Osborne. J. Chem. Phys.34 (1961) 1418-1425.

106. K. Niedzwiedz, B. Nowak, O.J. Zogal, J. Alloys Compd. 194 (1993) 47-51.

107. R.B Russel, J. Appl. Phys. 24 (1953) 232-233.

108. S.K. Sikka, Y.K. Vohra, R. Chidambaram, Prog. Mater. Sci. 27 (1982) 245-310.

109. W. Zhu, R. Wang, G. Shu, P. Wu, H. Xiao, J. Phys. Chem. C 114 (2010) 22361-22368.

110. A.D. Becke, K.E. Edgecombe. J. Chem. Phys. 92 (1990) 5397-5403.

111. B. Silvi, A. Savin, Nature 371 (1994) 683-686.

112. A. Savin, R. Nesper, S. Wengert, T.F Fa ssler, Angew. Chem. 36 (1997) 1808-1832.

113. M.A. Omar, Elementary solid state physics: principles and applications. Massachusetts: Addision-Wesley Publishing Company; 1975.

114. G.Y Zhang, G.X. Lan, Lattice vibration spectroscopy, Beijing, High Education Press, 1991.

115. T. Hahn, International tables for crystallography, Space group symmetry, vol. A., Dordrecht, Reidel, 1983.

116. P. Zhang, B. Wang, C. He, P. Zhang, J. Comp. Mat. Sci. 50 (2011) 3297-3302.

117. Jr. L.G. Hector, J.F. Herbst, J. Phys. Condens matter 20 (2008) 064229-064239.

118. A. Siverts, A. Gotta, S. Halberstadt, J. Inorg. Chem. 187 (1930) 155-164.

119. C.H. Hu, D.M. Chen, Y.M. Wang, K. Yang, J. Alloys Compd. 450 (2008) 369-374.

120. T.J. Frankcombe, G.J. Kroes, Chem. Phys. Lett. 423 (2006) 102-105.

121. X.Z. Ke, I. Tanaka, Phys. Rev. B, 71 (2005) 024117-024132.

122. C.W. Bale, P. Chartrand, S.A. Decterov, G. Eriksson, K. Hack, R.B. Mahfoud, J. Melancon J, A.D. Pelton, S. Petersen, "FactSage thermochemical software and databases", version 6.3, 1976-2012.

123. A. Taylor, R.W. Floyd, Acta Crystallographica, 3 (1950) 285-289.

124. I.R. Harris, D. Hussain, K.G. Barraclough, Scr. Metall. 4 (1970) 305-308.

125. O.S. Ivanova, A.S. Adamova, E.M. Tararaeva, Tregubov, Structure of zirconium

alloys. Moscow: Izd. Nauka; 1973.

126. A.V. Irodova, V.A. Somenkov, S.S. Shilshtein, L.N. Padurets, A.A. Chertkov, Soviet Phys. Crystallogr. 23 (1978) 591-592.

127. S.W. Peterson, V.N. Sadana, W.L. Korst, J. Phys. 25 (1964) 451-3.

128. M. Gupta, J. Alloys Comp. 293 (199) 190-201.

129. D.S. Agosta, J.E. Hightower, K. Foster, R.G. Leisure, Z. Gavra, J. Alloys Comp. 346 (2002)1-5.

130. C. Domain, R. Besson, A. Legris. Acta Materialia, 50 (2002) 3513-3526.

131. W. Zhu, R. Wang, G. Shu, P. Wu, H. Xiao, J. Phys. Chem. C, 114 (2010) 22361-22368.

132. E.S. Fisher, C.J. Renken, Phys. Rev. 135 (1964) A482-494.

133. R. Ramji Rao, A. Ramanand,26(3/4) (1977) 365-377.

134. Q. Guo, O.J. Kleppa, J. Alloys Compd. 269 (1998) 181-186.

135. J.C. Gachon, N. Selhaoui, B. Aba, J. Hertz, J. Phase Equilib. 13 (1992) 506-511.

136. A.R. Miedema, A.K. Niessen, F.R. de Boer, R. Boom, W.C.M. Mattens. Cohesion in Metals: Transition Metal Alloys. Amsterdam: Elsevier: 1989.

137. V. Felicia, A. Preda, S. Ioan, D. Claudia, Asian J. Chem. 22(6) (2010) 4291-4294.

138. T. Gongli, L. Xiaopeng, J. Lijun, W. Shumao, L. Zhinian, L. Hualing,17 (2007) 949-953.

139. R. Kuentzler, A. Amamou, R. Clad, P. Turek, J. Phys. F: Met Phys. 17 (1987) 459-74.

140. J.F. Nye, Physical properties of crystals, Clarendon Press, Oxford, 1985.

141. Y. Fukai, The Metal-Hydrogen System, Springer, Berlin, 1993.

142. Y. Le Page, P. Saxe, Phys. Rev. B 65 (2002) 104104-104117.

143. M. Born, On the stability of crystal lattices, I math. Proc Cambridge Philos Soc 36 (1940) 160-172.

144. W. Voigt, Lehrbuch de Kristallphysick, Terubner, Leipzig, 1928.

145. A. Reuss, Angew Z, Math. Mech. 9 (1929) 49-58.

146. R. Hill, Proc. Phys. Soc. London A 65 (1952) 349-354.

147. X.M. Tao, P. Jund, C. Colinet, J.C. Tedenac, Phys. Rev. B 80 (2009) 104103-104112.

148. Z.J. Wu, E.J. Zhao, H.P. Xiang, X.F. Hao, X.J. Liu, J. Meng, Phys. Rev. B 76 (2007) 054115-054129.

149. C. Zener, Elasticity and Anelasticity of Metals, University of Chicago Press, Chicago, 1948.

150. D.G. Pettifor, Mater. Sci. Technol. 8 (1992) 345-349.

151. R.A. Johnson, Phys. Rev. B 37 (1988) 3924-3931.

152. A.A. Maradudin, E.W. Montroll, G.H. Weiss, I.P. Ipatova, Theory of Lattice Dynamics in the Harmonic Approximation, second ed., Academic Press., New York, London, 1971.

153. J. Haines, J.M. Leger, G. Bocquillon, Annu. Rev. Mater. Res. 31 (2001) 1-23.

154. H. Fu, X.F. Li, W.F. Liu, Y. Ma, T. Gao, X. Hong, Intermetallics 19 (2011) 1959-1967.

155. S.F. Pugh, Philos. Mag. 45 (1954) 823-843.

156. J. Bloch, M. Brill, Y. ben-Eliahu, Z. Gavra, J. Alloys Comp. 267 (1998) 158-166.

157. C. Zhang, H. Jiang, H.L. Shi, G.H. Zhang, Y.H. Su, J. Alloys. Comp. 604 (2014) 171-174.

158. G. Sudhapriyanga, A.T. Asvinimeenaatci, R. Rajeswarapalanichamy, K. Iyakutti, Trans. Nonferrous Met. Soc. China 23 (2013) 2700-2707.

159. P. Zhang, B.T. Wang, C.H. He, P. Zhang, Comp. Met. Sci. 50 (2011) 3297-3302.

160. G. Sudhapriyanga, A.T. Asvinimeenaatci, R. Rajeswarapalanichamy, K. Iyakutti, J. At. Mol. Sci., 5 (2014) 64-80.

161. D.H. Wu, H.C. Wang, L.T. Wei, R.K. Pan, B.Y. Tang, J. Mag. Alloys 2 (2014) 165-177.

162. E. Screiber, O.L. Anderson, N. Soga, Elastic Constants and Their Measurement, first ed., McGraw-Hill, New York, 1973.

163. O.L. Anderson, J. Phys. Chem. Solid 24 (1963) 909-917.

164. M.E. Fine, L.D. Brown, H.L. Marcus, Scr. Metall. 18 (1984) 951-956.

165. H. Okamoto, J Phase Equilib. Diff. 32 (2011) 169-170.

166. PCPDFWIN version 2.2, 2001, JCPDS-ICDD.

167. F. Peng, H. Fu, X. Yang, Physica B 403 (2008) 2851-2855.

168. M.A. Blanco, E. Francisco, V. Luana, Comput. Phys. Comm. 158 (2004) 57-72.

169. O. L. Anderson, Equations of state of solids for geophysics and ceramic science, Oxford University Press, New York, 1995, p.34.

170. J.C. Gachon, M. Dirand, J. Hertz, , J. Less-Com Met. 85 (1982) 1-9.

171. T. Chart, F. Putland, CALPHAD 3 (1979) 9-18.

172. S.K. Bataleva, V.V. Kuprina, V.V. Burnashova, V.Ya. Markiv, G.N. Ronami, S.M. Kuznetsova, , Moscow Univ. Chem. Bull. 25 (1970) 37–40.

173. A.R. Miedema, K.H.J. Buschow, H.H. Van Mal, J. Less-Com Met. 49 (1976) 463-472.

174. K.P. Huber, G. Hertzberg, *Molecular Spectra and Molecular Structure IV: Constants of Diatomic Molecules*, Van Norstrand Reinhold, New York, 1979.

175. P. Zhang, S. Wang, J. Zhao, C. He, and P. Zhang, J. Nucl. Mater. 418 (2011) 159-164.

176. Z. Huesges, K. Christmann, Z. Phys. Chem. 227 (2013) 881-899.

177. D. Chattaraj, S.C. Parida, Smruti Dash, C. Majumder, Int. J. Hydrogen Energy 37 (2012) 18952-18958.

178. C.A. Arrington, T. Blume, M.D. Morse, M. Doverstal, U. Sassenberg, J. Phys. Chem.

98 (1994) 1398-1406.

179. C. Wang, J. Zhao, J. Han, J. Chem. Phys. 124 (2006) 194301-1-8.

180. B. Kant, J. Strauss, J. Chem. Phys. 41 (1964) 3806-3808.